Measurement Techniques to Characterize Bubble Motion in Swarms

Claudio Abraham Acuña Pérez

Department of Mining and Materials Engineering
McGill University,
Montreal, Canada

A thesis submitted to the Faculty of Graduate Studies and Research
in partial fulfillment of the requirements of the degree of
Doctor of Philosophy

June 2007

Your file Votre référence
ISBN: 978-0-494-50762-9
Our file Notre référence
ISBN: 978-0-494-50762-9

Dedicated to the greatest women in my life.

Constanza, Carla, Isolina and Mercedez

ABSTRACT

A technique was developed to study the effect of surfactant (frother) on individual bubble motion in swarms. The technique was based on high speed cinematography and tracking of multiple moving objects. Image processing algorithms were implemented in Matlab to isolate and measure geometric properties of the bubbles in image sequences recorded at 1 ms interval; and these properties were compiled into a data structure. To track a bubble, the geometric properties and a matching criterion were applied on consecutive pictures to identify the bubble. The bubble trajectory was reconstructed from the data structure for the matched objects. To maximize the number of bubbles identified from an image, de-clustering algorithms were developed and validated. A new shape factor model for ellipsoidal objects and a correction model for pixelation effect were developed. To characterize the level of bubble interaction in a swarm, a technique for measuring average dimensionless bubble inter-distance was developed. To characterize the effect of frother type on bubble surface a new technique for measuring surface flows (Marangoni effect) on a bubble blown in air was developed. The results provided experimental evidence of the mechanisms by which surfactants dampen bubble oscillation and reduce bubble terminal rise velocity and helped to interpret the frother type effect.

Experiments to determine the effect of surfactant (concentration and type), bubble interactions and bubble size distribution type on bubble velocity in swarms were conducted using the bubble tracking technique in a rectangular transparent column (12x5x140 cm) with an inclined top section (15^{o}). A flat bubble swarm was generated combining a slot (60 mm x 60 μm) and porous-slot (60 x 1.1 mm) spargers. These combinations allowed the generation of bubble size distributions similar to those in industrial flotation machines. Bubble images were collected at three locations (near the point of generation, the top of the straight section and in the inclined section) to track the impact of surfactant accumulation. The results showed that the presence of surfactant reduced bubble coalescence and breakage and stabilized the bubble

surface. As a consequence, the bubble size distribution remained stable as the swarm rose.

Experimental measurements of bubble motion in the presence of surfactants showed for both single bubbles and swarms, that surfactant accumulation occurs as the bubbles detach from the generating point, and the impact occurs gradually, determined by the subsequent evolution of bubble aspect ratio. The bubble tracking measurements revealed a velocity-size profile, which was determined by: the predominant bubble size class, bubble interactions (dimensionless bubble inter-distance), and the surfactant type and concentration. The surfactant type seems to be a factor in determining bubble rise velocity for bubbles below 0.8 mm, despite the theory that surface mobility for such small bubbles in unaffected by surfactants. It is thus proposed that surface viscosity plays a role on bubble motion.

The new techniques for bubble motion and surface characterization were tested for bubble swarms in presence of Polyglycol and Pentanol. Two contributions to the knowledge emerging from this phase of the work are: a) bubble motion in swarm describes a bubble velocity-size profile with a high dependency on the bubble distribution type, and b) surfactant type influences bubble rise velocity for bubbles in range 0.1 to 4 mm.

RÉSUMÉ

Une technique fut développée pour l'étude de l'effet des agents de surface (moussants) sur les mouvements de bulles individuelles dans les essaims. La technique fut basés sur la cinématographie de haute vitesse et la poursuite en simultané de plusieurs objets. Des algorithmes de traitement d'image se furent implantés avec Matlab pour isoler et mesurer les attribues géométriques des bulles en images séquentiels enregistrées en intervalles de 1 ms, et ces attribues se furent compilés en structures informatiques. Afin de poursuivre une bulle, les attribues géométriques et un critère d'assortiment se furent appliqués sur des images consécutives pour identifier la bulle. Le trajet se fut reconstruit utilisant la structure informatique des objets couplés. Pour maximiser la quantité de bulles identifiée dans une image, un algorithme de dégroupement fut développé et validé. Un nouveau modèle de facteurs géométriques pour des objets ellipsoïdaux et un modèle pour la correction des effets de pixellisation se développèrent. Pour caractériser le niveau d'interaction de bulles dans un essaim, une méthode pour prendre la moyenne de l'inter-distance non dimensionnelle de bulles se développa. Pour caractériser l'effet du type de moussant sur la surface des bulles, une nouvelle méthode pour mesurer les flux superficielles (l'effet Marangoni) pour une bulle gonflée dans l'air fut développée; les résultats justifièrent expérimentalement les mécanismes par lesquels les agents de surface atténuent les oscillations de bulle et réduisent la vitesse terminale ascensionnelle de bulles.

Des expériences déterminant l'effet des agents de surface (concentration et type), des interactions de bulles et de la distribution de diamètres sur la vitesse de bulles en essaims, s'administrèrent utilisant la méthode de poursuite dans une colonne rectangulaire et transparente (12x5x140 cm) ayant une inclination en haut (15°). Un essaim de bulles en forme plate se fut généré avec la combinaison d'une fente (60mm x 60µm) et quelques arroseurs à fente poreux (60 x 1.1 mm). Ces combinaisons permirent la génération de distributions de diamètres de bulle

comparable à ceux des machines de flotte industrielle. Des images de bulles se furent collectées dans trois endroits (proche du point de génération, en haut de la section droite et dans la section inclinée) pour observer l'impact de l'accumulation d'agent de surface. Les résultats démontrèrent que la présence des agents de surface réduit la coalescence et la cassure de bulles et stabilisa les surfaces de bulles. En conséquence, la distribution des diamètres de bulles demeura stable durant la montée de ces essaims.

Les observations expérimentales des mouvements de bulles dans la présence d'agent de surface démontrèrent également pour de bulles isolées et pour des essaims, que l'accumulation se passe lorsque les bulles se détachent du point de génération, et l'effet se prononce graduellement par l'évolution du rapport largeur/hauteur. Les mesures provenant de la poursuite de bulles révélèrent un profile vitesse-diamètre déterminé par: le classement volumétrique de bulle prédominant, des interactions de bulles (inter-distance non dimensionnelle de bulles), et la quantité et le type d'agent de surface. Il semble que le type d'agent de surface soit un facteur déterminant la vitesse terminale ascensionnelle de bulles inferieurs à 0.8 mm, malgré la théorie que la mobilité superficielle de ces petites bulles soit inaffecté par les agents de surface. Il est donc proposé que la viscosité superficielle joue un rôle dans les mouvements de bulle.

ACKNOWLEDGEMENTS

I wish to express my gratitude and appreciation to Professor J.A. Finch for his invaluable guidance, constant encouragement and unconditional support.

This work was made possible by the financial support of Universidad Católica del Norte and MECESUP project UCN-104. I want to express special thanks to my colleagues in the UCN Chemical Engineering Department for their continuous motivation and friendship.

I want to thank Dr. Ram Rao, Dr. Cesar Gomez, Dr. H. Mustafa Tarkan, Mr. Jan E. Nesset for their friendship and fruitful discussion about bubbles and practical aspects of flotation.

Special thanks to my friends and colleagues at McGill University for their help: Jason Doucet, Alessandro Navarra, Ray Langois, Ralph Dhalke, Jarrett Quinn, Vera Gella, Fariba Azgomi, Luis Calzado, Elvi Delgard, Ana Becerra, Frank Rosemblun, Davin Knutila, Annie Wang, Willy Kracht, Dominique Lascelles, Dr. Stephanie Gelinas, Dr. Stephanie Somot, Kevin Robertson, Pamela Moyo, Helin Girgin, Dr. Mitra Mirnezami.

Finally, I want express my heartfelt gratitude to my beloved wife Carla Pesce, who has been my best friend and constant support living this adventure outside our homeland.

TABLE OF CONTENTS

ABSTRACT i

RÉSUMÉ iii

ACKNOWLEDGEMENTS v

TABLE OF CONTENTS vi

NOMENCLATURE x

LIST OF FIGURES xi

LIST OF TABLES xv

CHAPTER 1: Role of bubbles and frothers in flotation 1

1.1- Thesis Objectives 5

1.2- Thesis scope 6

1.3- Thesis structure 9

CHAPTER 2: Bubble swarm characterization 11

2.1- Bubble swarm velocity and surfactant type influence 12

2.2- Characterization of bubble swarm motion. 14

2.3- Individual bubble measurement techniques in bubble swarms. 17

CHAPTER 3: Development of technique to track bubble motion in a swarm ...19

3.1- High speed cinematography and uneven light compensation 21

3.2- Bubble image processing and data structure conversion 25

3.2.1- image thresholding 27

3.2.2- image segmentation and filtering 32

3.2.3- blob features: measurement and data structure 34

3.2.4- shape factor and selection criteria for single bubbles 37

3.2.5- shape factor model for ellipsoidal objects 41

3.2.6- de-pixelation correction for bubble perimeter calculation 44

3.2.7- bubble cluster separation 47

3.2.8- enhanced algorithm benchmarking and validation 51

3.3- Tracking of multiple moving objects technique 56

3.4- Bubble trajectory reconstruction technique 63

3.4.1- bubble matching technique validation 66

3.5- Generation of a flat front of bubbles 70

3.5.1- bubble size distribution type with slot spargers 74

3.6- Bubble surface mobility measurement 77

3.6.1- effect of frother on static bubble blown in air 77

3.6.2- bubble surface motion (velocity) measurement 79

3.7- Bubble interaction characterization technique 81

3.7.1- area fraction of gas and inter-bubble distance relationship 81

3.7.2- area fraction of gas and volumetric fraction of gas relationship 83

3.7.3- dimensionless inter-bubble inter distance 86

3.7.4- model validation 88

3.8- Conclusions 91

CHAPTER 4: Frother effect on bubble behavior: experimental results 93

4.1- Effect of frother on single bubbles 93

4.2- Effect of frother on bubble swarms 99

4.2.1- bubble size distribution stabilization in presence of frother 99

4.2.2- bubble shape distribution stabilization in presence of frother 100

4.3- Frother type effect on bubble surface mobility 104

4.4- Conclusions.....107

CHAPTER 5: Tracking bubble velocity in swarms: experimental results.....109

5.1- Surfactant effect on bubble velocity reduction in swarms.....110

5.1.1- effect of bubble shape on bubble oscillation and bubble path..... 112

5.1.2- effect of surfactant accumulation time 115

5.1.3- effect of surfactant concentration..... 118

5.2- Effect of bubble inter-distance and BSD type on bubble swarms.....121

5.2.1- comparison of similar BSDs at two level of interactions..... 121

5.2.2- comparison of a narrow and a wide bubble size distribution..... 123

5.2.3- comparison of a narrow and a bimodal bubble size distributions..... 126

5.2.4- bubble inter-distance and gas holdup relationship validation..... 129

5.3- Effect of frother type on bubble motion in swarms 130

5.3.1- effect of Polyglycol and n-Pentanol solutions on bubble motion at the same superficial gas velocity and D_{32} ~3 mm..... 130

5.3.2- effect of Polyglycol and n-Pentanol solutions on bubble motion at same dimensionless bubble inter-distance (d*) D_{32} ~0.4 mm..... 133

5.4- Conclusions.....137

CHAPTER 6: Conclusions, contributions and future work.....139

6.1- Conclusions.....139

6.2- Claims to original research.....143

6.3- Contribution to knowledge.....144

6.4- Recommendations 145

REFERENCES.....146

APPENDIX 1: Calculations, tables and plots 154

Appendix 1.1: Volumetric fraction of gas and inter-bubble distance for ellipsoidal bubbles in an ideal dispersion. 157

Appendix 1.2: Volumetric fraction of gas and bubble and area fraction of gas relationship for random dispersions.....159

Appendix 1.3: Effect of surface tension on bubble size generated on slot sparger. 160

APPENDIX 2: Software: description, codes, manuals references.....161

APPENDIX 3: Hardware specifications and equipment setup.....163

APPENDIX 4: Experimental results.....167

NOMENCLATURE

A	mm^2	Projected area bubble
a	mm	Bubble major axis
AR	-	Bubble aspect ratio (b/a)
BSD		Bubble size distribution
b	mm	Bubble minor axis
D_{32}	mm	Sauter mean diameter, total volume of the bubbles divided by total surface of the bubbles
D_{10}	mm	Mean bubble diameter
d	mm	bubble inter distance
d*	-	Dimensionless bubble
E_g	-	Gas hold-up, volumetric fraction of gas
E_g^{2D}		Fraction area of bubbles in a picture
J_g	m/s	Superficial gas velocity, volumetric gas flow rate divided by cross sectional area of the reactor
J_l	m/s	Superficial liquid velocity, volumetric liquid flow rate divided by cross sectional area of the reactor
P		Bubble perimeter
r	mm	Bubble radius
SF		Shape factor or the reciprocal of the roundness
u_s	m/s	Superficial gas velocity in a slot sparger
u_{sp}	m/s	Superficial gas velocity in a porous slot sparger
u_{sb}	m/s	Bubble swarm velocity
u_t	m/s	Terminal bubble rise velocity

Greek letters

ρ_g	Kg/m^3	Gas density
ρ	Kg/m^3	Liquid density
σ	N/m	Surface tension
μ	Pa s	Fluid viscosity (1 mPa s = 1 cP)
ψ	%	Similitude value for two bubbles base on a, b, A

LIST OF FIGURES

Figure 1.1: Weber number as a function of bubble spherical equivalent diameter. 3
Figure 1.2: Pictographic representation of the studies in bubble hydrodynamics. 6
Figure 1.3: Operating ranges for industrial flotation machines. 7
Figure 1.4: The three common bubble size distribution type found in industrial flotation machines .8
Figure 2.1: Negative images of a bubble front at 100 ms interval. 14
Figure 3.1: Examples of high speed cinematography used in (a) bubble motion and (b) shape 21
Figure 3.2: High speed camera set up 23
Figure 3.3: Uneven illumination compensation algorithm 24
Figure 3.4: Typical image used in bubble size measurement 25
Figure 3.5: Image intensity frequency histogram 28
Figure 3.6: Image intensity variation across bubble border 28
Figure 3.7: Picture average intensity variation during plant measurement. 29
Figure 3.8: Calzado-Acuna thresholding function 31
Figure 3.9: Image thresholding algorithms 32
Figure 3.10: Image segmentation using 8 directions 33
Figure 3.11: Reduction in processing time by applying an image filter 33
Figure 3.12: Effect of magnification factor on image digitation 34
Figure 3.13: Data structure for bubble geometric parameters 36
Figure 3.14: Aspect ratio frequency distribution (613 industrial cell measurements) 38
Figure 3.15: Low selectivity using shape factor criterion 38
Figure 3.16: Shape factor values and the effect of frother 39
Figure 3.17: Actual bubble area and its corresponding convex area 40
Figure 3.18: Area bubble to convex area ratio selection criteria comparison 40
Figure 3.19: Plant and lab ellipsoidal bubbles. 41
Figure 3.20: Shape factor for ellipsoidal bubbles 42
Figure 3.21: Global shape for ellipsoids 43
Figure 3.22: Perimeter underestimation using image processing software 45
Figure 3.23: Shape factor and perimeter bias for pixelation effect 45
Figure 3.24: Proposed model to correct pixelation effect 46
Figure 3.25: Selected bubbles and frequency number distribution 47
Figure 3.26: Area fraction of bubbles accepted using isolated bubbles 48
Figure 3.27 Intensity image showing touching and neighbor bubbles 49
Figure 3.28: Image de-clustering example 50
Figure 3.29: Area fraction of detected bubbles 51

Figure 3.30: Bubble area acceptance (moving average 30 pictures) 52
Figure 3.31: Bias measurement in five selected plant test measurements 53
Figure 3.32 Simulated bubble size distributions 53
Figure 3.33: Effect of bubble area fraction sampled on D_{10} accuracy 54
Figure 3.34: Frequency distribution of average bubble area detected from 480 tests on individual flotation cells 55
Figure 3.35: Incidence value for two consecutive images. 56
Figure 3.36: Incidence value and displacement for matching bubbles 57
Figure 3.37: Incidence value comparison for ellipsoids 58
Figure 3.38: Incidence value and bubble for two consecutive images. 58
Figure 3.39: Changes in incidence value for wobbling object tracked manually 60
Figure 3.40: Bubble velocity-size profile for two bubble size distributions 61
Figure 3.41: Bubble size distribution corresponding to Figure 3.40 61
Figure 3.42: Repeat measurements of bubble velocity-size profiles 62
Figure 3.43: Bubble trajectory reconstruction from an image sequence 63
Figure 3.44: Bubble velocity trajectory mapping 64
Figure 3.45: Bubble trajectory reconstruction for bubble swarms 65
Figure 3.46: Bubble identification based on color "marking" technique 66
Figure 3.47: Bubble tracking using color "marking" technique 67
Figure 3.48: Bubble trajectory reconstruction for crowded system 68
Figure 3.49: Effect of tolerance on the number of matching bubbles. 69
Figure 3.50: Top view and schematic of bubble generating devices 70
Figure 3.51: Bubble size distributions generated using flat slot sparger 71
Figure 3.52: Bubble column and sampling points 72
Figure 3.53: Generation of a flat front of bubbles (slot sparger) 73
Figure 3.54: Coalescence by bubble collision during generation 74
Figure 3.55: Effect of surfactant on bubble size in slot spargers 75
Figure 3.56: Effect of superficial gas velocity on bubble size distributions 75
Figure 3.57: Stabilization of bubble size distribution at gas velocities above 1.6 m/s 76
Figure 3.58: Example of bubble surface texture identifying liquid packets. 79
Figure 3.59: Tracking of bubble surface motion on a bubble blown in n-Pentanol 80
Figure 3.60: Trajectories of selected liquid packets on a bubble surface 80
Figure 3.61: Illustration of bubble interaction distance and fraction of gas relationship 82
Figure 3.62: Volumetric fraction of gas based on area fraction 84
Figure 3.63: Example of random dispersion of bubbles 85
Figure 3.64 Bubble inter-distance 86
Figure 3.65: Inter-bubble distance computation example 87

Figure 3.66: Area fraction of bubbles as a function of inter-bubble distance 88
Figure 3.67 Volumetric fraction of gas and relationship to inter-bubble distance 89
Figure 4.1: Surfactant effect on bubble shape and surface oscillation 94
Figure 4.2: Surfactant effect on bubble shape and surface oscillation (10 ms) 96
Figure 4.3: Salt effect on bubble oscillation 97
Figure 4.4: Effect of frother on bubble rise velocity 98
Figure 4.5: Bubble coalescence and breakage events in tap water 99
Figure 4.6: Evidence of bubble size distribution stabilization in presence of surfactant 100
Figure 4.7: Evidence of bubble stabilization in shape in presence Polyglycol 101
Figure 4.8: Effect of frother type on aspect ratio of bubbles in swarms 102
Figure 4.9: Effect of Polyglycol concentration on aspect ratio of bubble swarms 102
Figure 4.10: Surface tension of Polyglycol and n-Pentanol in tap water (20°C) 104
Figure 4.11: Surface texture and tracking for different "liquid packets" on bubbles blown in air (and remaining in contact with solution below) 105
Figure 4.12: Effect of surfactant on average surface velocity 106
Figure 5.1: Bubble velocity-size profile for tap water and Polyglycol solution 110
Figure 5.2: Bubble size distribution for Polyglycol solution and tap water 111
Figure 5.3: Bubble AR frequency distribution for Polyglycol solution and tap water 113
Figure 5.4: Bubble trajectory mapping in Polyglycol solution (0.2 mmol/L) 114
Figure 5.5: Bubble trajectory mapping in tap water 114
Figure 5.6: Horizontal velocity frequency distribution for bubbles in Polyglycol solution and tap water 115
Figure 5.7: Evidence of surfactant accumulation reducing bubble rise velocity. 116
Figure 5.8: Evidence of surfactant conferring bubble shape stability as swarm rises 117
Figure 5.9: Evidence of surfactant changing bubble shape (AR) as swarm rises 118
Figure 5.10: Evidence of surfactant concentration reducing bubble rise velocity 119
Figure 5.11: Evidence of surfactant accumulation effect on BSD. 120
Figure 5.12: Effect of bubble interaction on bubble velocity-size profile (similar BSD) 121
Figure 5.13: BSD at two levels of bubble interactions 122
Figure 5.14: Bubble AR frequency distributions at two levels of interactions 122
Figure 5.15: Bubble velocity-size profile comparison for narrow and wide BSDs 124
Figure 5.16: Wide and narrow BSDs at two levels of superficial gas velocity 124
Figure 5.17: Bubble AR frequency distributions for wide and narrow BSDs 125
Figure 5.18: Image examples of narrow and wide BSDs 125
Figure 5.19: Bubble velocity-size profile comparison for narrow and bimodal BSDs 127
Figure 5.20: Narrow and bimodal bubble size distributions 127
Figure 5.21: Bubble AR frequency distributions for narrow and bimodal BSDs 128
Figure 5.22: Image example of narrow and bimodal BSDs 128

Figure 5.23: Dimensionless bubble inter-distance and area fraction of gas relationship for Polyglycol solutions 129

Figure 5.24: Bubble velocity-size profile for rising bubbles in Polyglycol and n-Pentanol solutions (same superficial gas velocity and sparger type). 130

Figure 5.25: Frequency size distributions for bubbles in Polyglycol and n-Pentanol solutions 131

Figure 5.26: AR frequency distributions for bubbles in Polyglycol and n-Pentanol solutions (same Us). 131

Figure 5.27: Horizontal velocity frequency distributions for rising bubbles in Polyglycol and n-Pentanol solutions 132

Figure 5.28: Bubble velocity-size profile for rising bubbles in Polyglycol and n-Pentanol solutions (same superficial gas velocity, bubble inter-distance and BSD). 134

Figure 5.29: Frequency size distributions for bubbles in Polyglycol and n-Pentanol solutions (same d*) 134

Figure 5.30: AR frequency distributions for bubbles in Polyglycol and n-Pentanol solutions (same d*). 135

Figure 5.31: Image example of narrow and bimodal BSDs 135

Figure A1.1: Terminal velocity of a single bubble as a function of the spherical equivalent diameter 154

Figure A1.2: Wobbling zone for single bubble 155

Figure A1.3: Ideal dispersion of ellipsoidal bubbles of aspect ratio AR 157

Figure A3.1: Mass flow meter calibrations 164

Figure A3.2: Double chamber slot sparger details 165

Figure A3.3: Surface mobility equipment setup and specification 166

Figure A4.1: Comparison of bubble shape stabilization at 3, 50, and 90 cm above the sparger for tap water, Pentanol (0.2 mmol/L) and Polyglycol (0.2 mmol/L). 170

LIST OF TABLES

Table 3.1: High speed camera configurations 22
Table 3.2: Image processing software tested 26
Table 5.1: Effect of surfactant on bubble rise velocity profile 120
Table A1.1: Research groups in gas dispersion measurements 156
Table A1.2: 95% Confidence interval 156
Table A2.1: Matlab routines implement for image analysis 161
Table A2.2: Visual basic code to export images into Power Point 161
Table A2.3: Data structure parameters 162
Table A3.1: High speed camera specifications 163
Table A3.2: Macro lens specifications 164
Table A3.3: Mass Flow meter controller specifications 164
Table A4.1: Experimental result summary (test #7 -#30) 167
Table A4.2: Experimental result summary (test #31 -#70) 168
Table A4.3: Bubble surface velocity results 169
Table A4.4: Test #7, Polyglycol 0.2 mmol/L, Us = 0.9 m/s (3 cm) 171
Table A4.5: Test #10, Polyglycol 0.2 mmol/L, Us = 3.4 m/s (3 cm) 172
Table A4.6: Test #11, Polyglycol 0.2 mmol/L, Us=0.9 m/s (50 cm) 173
Table A4.7: Test #12, Polyglycol 0.2 mmol/L, Us=2.0 m/s (50 cm) 174
Table A4.8: Test #13, Polyglycol 0.2 mmol/L, Us=3.4 m/s (90 cm) 175
Table A4.9: Test #18, Polyglycol 0.01 mmol/L, Us=0.9 m/s (50 cm) 176
Table A4.10: Test #25, Tap water, Us=3.4 m/s (3 cm) 177
Table A4.11: Test #28, Tap water, Us=0.9 m/s (50 cm) 178
Table A4.12: Test #30, Tap water, Us=3.4 m/s (90 cm) 179
Table A4.13: Test #41, n-Pentanol 0.2 mmol/L, Us=2.0 m/s (50 cm) 180
Table A4.14: Test #49, Polyglycol 0.04 mmol/L, Us=0.2 m/s (6 cm) 181
Table A4.15: Test #51, Polyglycol 0.04 mmol/L, Us=1.0 m/s (6 cm) 182
Table A4.16: Test #64, Polyglycol 0.14 mmol/L, Usp=0.03 m/s (90 cm) 183
Table A4.17: Test #65, n-Pentanol 0.2 mmol/L, Us=3.7 m/s (90 cm) 184
Table A4.18: Test #66, n-Pentanol 0.2 mmol/L, Usp=0.03 m/s (90 cm) 185
Table A4.19: Test #68, Polylycol 0.1 mmol/L, Us=1.9 m/s (90 cm) 186
Table A4.20: Test #69, Polyglycol 0.14 mmol/L, Us=3.7 m/s (90 cm) 187

CHAPTER 1: Role of bubbles and frothers in flotation

Froth flotation is a separation process that selectively collects target particles y attachment to bubbles injected into a solid-liquid dispersion (pulp or slurry). Bubbles collide with, attach to and collect hydrophobic particles from mineral ores and other systems (e.g., de-inking recycled paper pulp). The particles are often previously treated with specific reagents, called collectors, that have the property to make selected particles non-wettable or hydrophobic (Rao, 2003). Hydrophobic particles attach to air bubbles, forming a bubble-particle aggregate, allowing the selected particles to be collected (recovered) and separated from hydrophilic particles, which remain in the pulp. The aggregates rise by buoyancy to the surface where they accumulate to produce a stable froth. To help create small bubbles and form a stable froth, surface active reagents, called frothers, are added to the pulp.

The use of frothers and the separation of particles make the flotation process different from the gas slurry reactors described in the chemical engineering literature (Mudde, 2005). In contrast to that large body of hydrodynamic information, little research into the hydrodynamics of flotation systems has been conducted. Most of the modern work has focused on measurements (superficial gas velocity, volumetric content of air, and mean bubble size), conducted by five research groups: HUT, McGill, JK-MRC, UTFSM and UCT (references in Table A1.1). These measurements are predominantly being used to correlate with metallurgical performance in order to improve the efficiency of the process.

Fundamental flotation models are restricted to single bubble or a mono-sized distribution (Tao, 2004; Nguyen and Schulze, 2004). But, in reality, bubbles are present as different sizes and shapes in a swarm, and in some cases bubble size distribution evolves (Colella et al., 1999; Laakkonen, 2002; Polli et al., 2002). In addition, particles and bubbles are often dispersed unevenly in flotation machines (Barigou and, 1992; Doucet et al., 2006). These characteristics make it particularly

complex to develop fundamental models that reflect the actual flotation process. There is general agreement that bubble size distribution and gas flow rate are among the more important aspects governing flotation performance (Ahmed and Jameson, 1984; Gorain et al., 1995; Gomez et al., 2006). To understand fundamentally the flotation process, bubble motion in swarms has to be addressed.

Individual bubble motion and bubble interactions in swarms in the presence of frothers (which modify bubble surface characteristics) are largely neglected areas of research, mainly due to the lack of measurement and characterization tools. There are a few studies concerning bubble motion in swarms under flotation-related conditions (Shen and Finch, 1996) and on the role of bubble swarms on flotation efficiency (Nguyen-Van and Kmet, 1994). Bubble motion may be fundamental to flotation performance. For example, after the particle-bubble aggregate is formed, changes in bubble motion may be sufficient to alter hydrodynamic conditions (Uribe-Salas et. al, 2003), and to detach collected particles (Cheng and Holtham, 1995).

Bubble motion refers to velocity trajectory patterns developed by a bubble as it rises by buoyancy. The pattern can take various forms (rectilinear, zigzag, helical, rocking), which depend on bubble size, bubble shape and liquid type. Motion of single bubbles has been studied over various size ranges and in diverse fluid types (Tsuge and Hibino, 1977; Sam et al., 1996; Tomiyama et al., 2002, Clift et al., 2005, Malysa et al., 2005).

Oscillation in bubble motion is the result of changes in bubble shape and bubble interaction in swarms. Depending on the bubble size and fluid characteristics, various bubble shapes can be generated (spherical, ellipsoidal, spherical cap, skirted, wobbling) (Guthrie and Bradshaw, 1973; Clift et al. 2005). As the bubble shape becomes less spherical, oscillations are present (Tsuge and Hibino, 1977). These shape variations are the result of forces acting on a bubble, principally inertial forces and surface tension forces. Inertial forces depend largely on bubble velocity and size; these forces generate a pressure across the bubble compressing and

flattening it. Surface tension forces, whose magnitude depend on surfactant type and concentration, confer bubble stability and create a "rigid" (non mobile) bubble surface, which opposes the deforming inertial force. As consequence of surface tension forces, bubbles tend to remain spherical, and the rise path tends to be rectilinear (Tomiyama et al., 2002). Bubble deformation and motion will depend on the ratio of these two acting forces. The ratio of inertial forces and surface tension forces is grouped in Weber's dimensionless number (Equation 1.1).

$$We = \frac{\rho \cdot u_b^2 \cdot d}{\sigma} \tag{1.1}$$

The Weber number indicates the predominant force regime, and may show if the bubble will be deformed, thus creating bubble oscillation as it rises. In Figure 1.1 Weber number is calculated as a function of size for contaminated water (presence of surfactant) and pure water for single bubbles. The terminal bubble rise velocity values to calculate the Weber number are obtained from Clift et al. (2005), (Appendix 1, Figure A1.1).

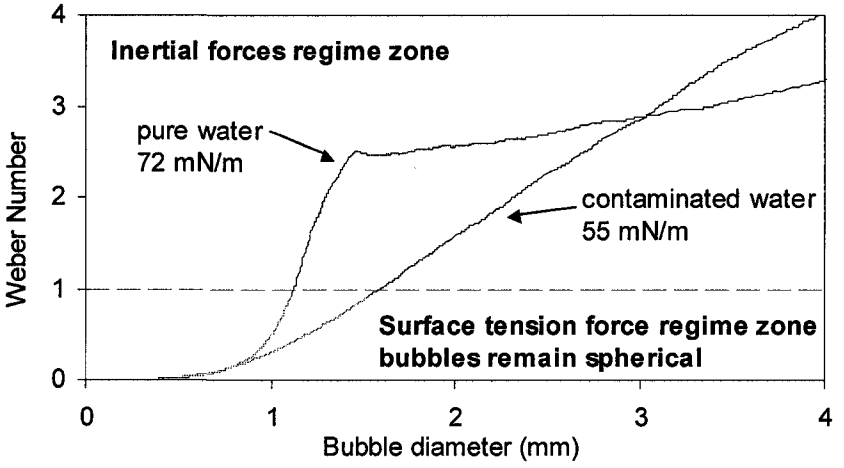

Figure 1.1: Weber number as a function of bubble spherical equivalent diameter.

A transition from the one force regime to the other for bubbles occurs above ca. 1.2 mm diameter in pure water and somewhat higher in the contaminated system (e.g. surface tension 55 mN/m). In flotation the common bubble size range is from 0.1 to 4

mm (Nesset et al., 2005). The fact that the bubble size range in flotation straddles the transition complicates fundamental modeling of flotation hydrodynamics.

In some cases, bubble wobbling (surface flexion) is observed (Nguyen and Schulze, 2004; Krasowska and Malysa, 2007). This phenomenon, which has not been studied extensively in regards to flotation systems, could be relevant for bubble-particle aggregate stability (Nguyen and Schulze, 2004). Surfactants play a significant role in both bubble shape stabilization and surface wobbling reduction.

Bubble motion and bubble surface stability may be further affected by the presence of other bubbles in the swarm, i.e., an inter-bubble effect. These characteristics, peculiar to flotation because of the presence of surface active agents, motivated the study of bubble motion in a swarm and the effect of frothers.

The aim of this research is the characterization of bubble motion in a swarm of bubbles under flotation-related conditions, i.e., presence of frothers and bubble sizes in the range 0.1 to 4 mm. To achieve these objectives required development of new measurement techniques including: tracking individual bubbles in a swarm of bubbles; measurement of bubble surface oscillations; characterization of bubble interactions; quantifying bubble surface flows (Marangoni effect); and evaluation of the effect of frother type on the above. These required development of appropriate image processing technique.

1.1- Thesis Objectives

The general objective is to characterize bubble motion in a swarm under flotation-related conditions. This required the following sub-objectives:

1- Development and validation of an on-line bubble size measurement technique able to:

Create standard images to evaluate image processing software.

Automate image digitization, and format conversion.

Develop software to compensate background intensities and masking.

Develop software to automate IMA parameter selection.

Develop algorithms to discriminate single bubbles and bubble clusters.

2- Development of bubble imaging techniques and software able to:

Measure individual bubble rise velocity in a swarm.

Establish frother type effect on bubble rise velocity.

Characterize bubble interaction (by measuring inter-bubble distance).

Characterize bubble surface mobility.

Decouple the effect of surfactant effect on generation, stabilization and motion.

1.2- Thesis scope

Bubble hydrodynamic studies have been conducted intensively for so-called bubble columns (Hibiki and Ishii, 2002; Mudde, 2005). But, for conditions relevant to flotation, very little research has been conducted. Figure 1.2 is a pictographic representation of the studies conducted on bubble columns, where operating ranges of mean bubble size and volumetric fraction of gas as a function of the superficial gas velocity are plotted. The operating conditions studied by several authors are depicted with the thick line rectangle showing the operating conditions typically found in industrial flotation columns (Finch and Dobby, 1990).

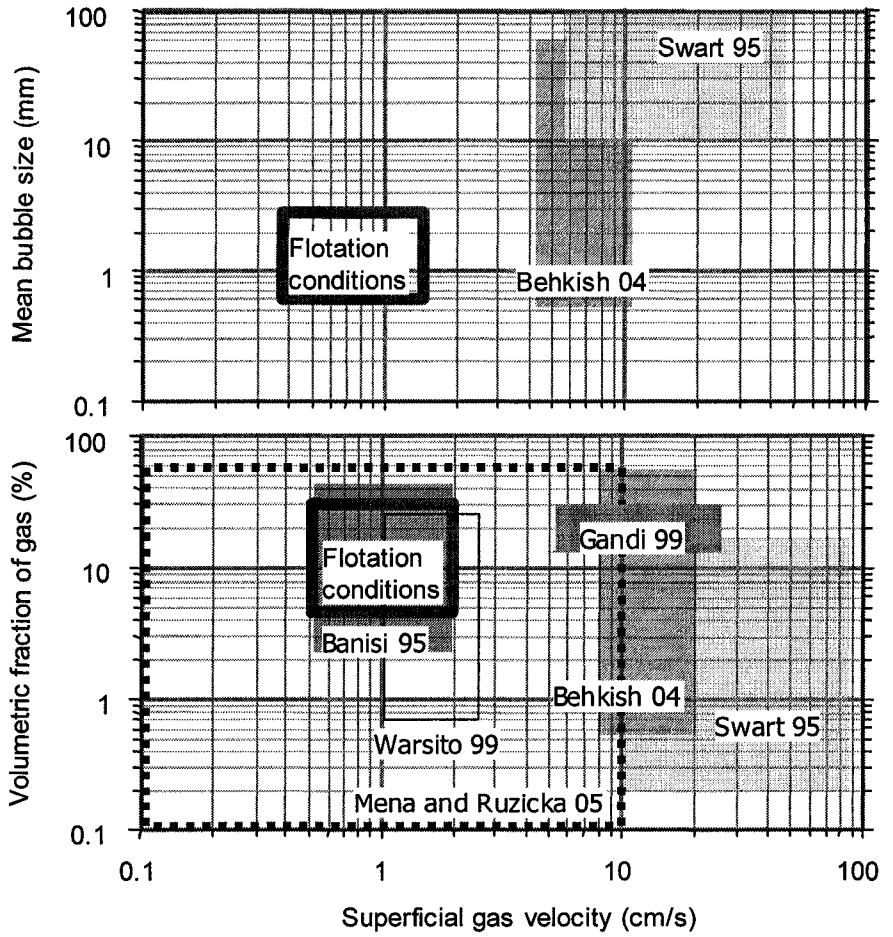

Figure 1.2: Pictographic representation of the studies in bubble hydrodynamics.

Despite that some of the operating conditions shown Figure 1.2 correspond to those in flotation only Banisi et al. (1995) used frother, and none of them measures directly individual bubble rise velocity. The inclusion of these characteristics makes the thesis original.

Operating conditions (mean bubble size, volumetric fraction of gas, and superficial gas velocity) typically found in industrial flotation machines are compiled in a data base created in this work from the author's and previous plant measurements. Figure 1.3 compiles the operating conditions for over 330 industrial cell measurements. Frother types commonly used are based on alcohols and glycols, in concentrations 0.01 to 0.6 mmol/L, depending on frother type (Azgomi et al., 2006). Some plants operate without frother but with high content of salts, which have surfactant-like properties (Quinn et al., 2006). The measurements were collected at six concentrators (in Canada, USA, Australia and Chile) using the McGill gas dispersion measurement technology (Gomez and Finch, 2002).

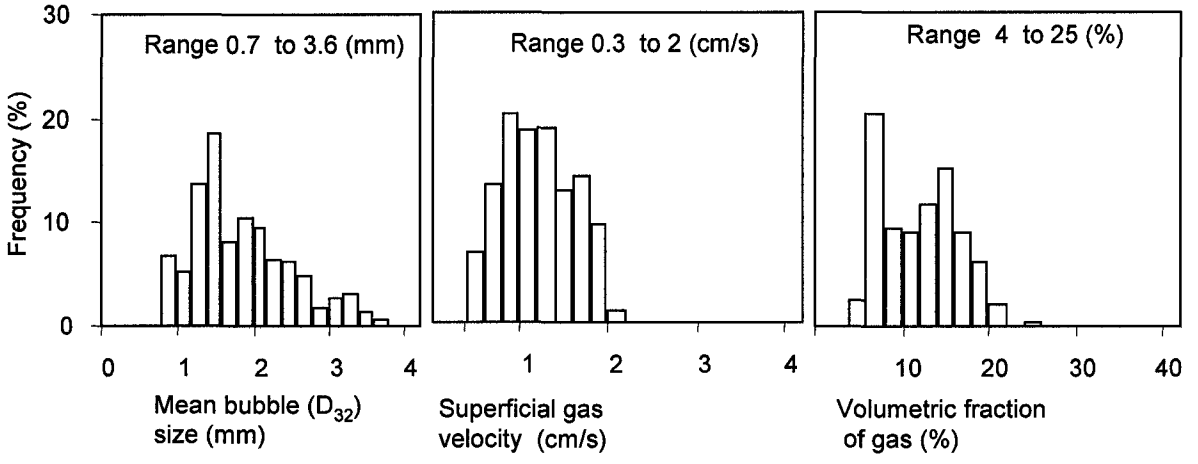

Figure 1.3: Operating ranges for industrial flotation machines.

Bubble size distributions vary depending on system chemistry, solid type and size distribution, and flotation machine type (Nesset et al., 2005). Mainly, three types of distribution have been found in industrial flotation machines (Figure 1.4): Narrow distributions, fine mean size (A); wide distributions, large mean size (B); and bimodal distributions (C). The measurements were collected in plant and processed by the

author. These three types of distribution will be reproduced to study the effect of distribution type on bubble motion in a swarm.

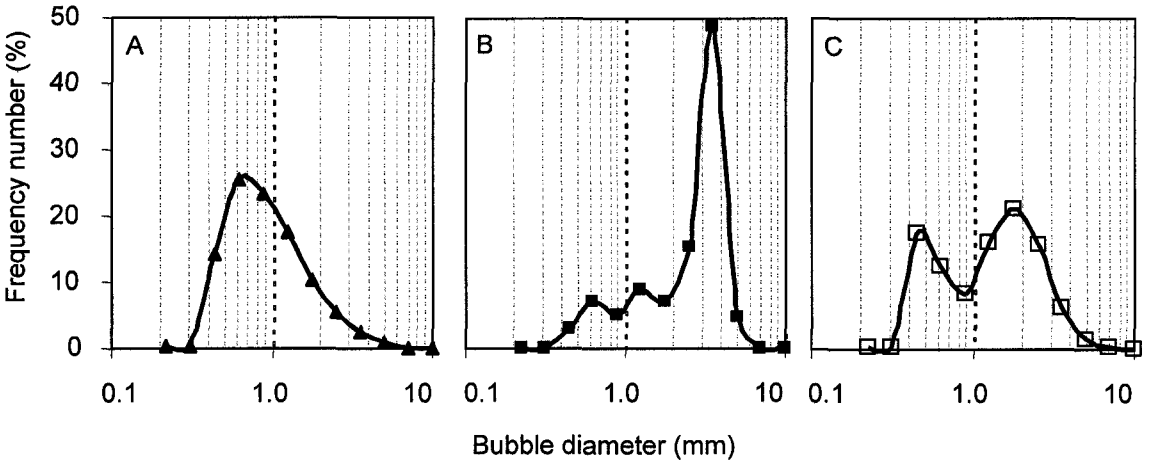

Figure 1.4: The three common bubble size distribution type found in industrial flotation machines

Using the McGill bubble size analyzer technique ("bubble viewer") (Hernandez-Aguilar et al., 2002) and settings for industrial measurements, the detectable bubble size range is between 0.1 to 4 mm. This detection limited is imposed by the magnification factor used and camera resolution (Gomez et al., 2006). The range is probably appropriate since smaller or bigger bubbles do not seem to be effective in flotation (Tao, 2004). The bubble sizes studied in this research cover this range (0.2 - 4 mm). In some experiments (to detect small bubble sizes generated by coalescence-mediated break-up (Tse et al., 2003)) the lower detection limit is set to 0.07 mm.

Individual bubble motion measurements in swarms are performed in laboratory bubble columns equipped with porous and slot sparger bubble generation devices, operated batch. Bubble images collected at intervals down to 0.5 ms are used to measure individual bubble rise velocity and inter-bubble distance (to quantify bubble interactions). Measurements are focused on 2D (or flat) swarms (volumetric fraction of gas 2 to 20%). The experiments are conducted under the hypothesis that the bubble size distribution is stabilized in the presence of surfactant.

1.3- Thesis structure

The thesis is organized in six chapters and four appendices. The structure of the thesis is as follows:

Chapter 1. Introduction: The flotation process and the role of frother are introduced. The thesis objectives and scope are presented.

Chapter 2. Literature review: Literature review on bubble swarm velocity measurements.

Chapter 3. Materials and methods: Description, development and validation of methods are presented for 7 techniques created or adapted to characterize bubble motion in swarms. These techniques are: high speed cinematography, conversion of bubble images into data structure, tracking of multiple moving objects, bubble trajectory reconstruction and bubble velocity measurements in swarms, generation of 2D bubble swarms, measurement of bubble surface flow velocity, measurement of bubble inter-distance in swarms.

Chapter 4. Experimental results of frother effect on bubbles: The effect of frother on the following is presented and analyzed: aspect ratio (single bubble and bubbles in swarms), rise velocity, surface oscillation, accumulation and distribution on bubble surface, coalescence and breakage events, size distribution stabilization, surface mobility. Experimental evidence to support the dynamic adsorption layer theory is described.

Chapter 5. Experimental results of frother effect on bubble motion in swarms: The effect of frother concentration and type (n-Pentanol and Polyglycol) on surfactant accumulation time, bubble inter-distance, bubble motion pattern and bubble size distribution type are evaluated.

Chapter 6. Conclusions: Conclusions and claims to original research are summarized and future research directions suggested.

Appendix 1. References: Calculations, demonstrations, reference tables and plots are presented to provide supporting information for the thesis body.

Appendix 2. Software: Software listings, software codes, data structure parameters.

Appendix 3. Hardware: Hi speed camera and lens specification; mass flow meter specification and calibration; slot sparger construction details, bubble surface mobility equipment set up.

Appendix 4. Experimental result tables: Bubble swarm velocity measurements at various operating conditions; surface mobility measurements (tap water, Polyglycol and n-Pentanol); bubble velocity-size profile and bubble size distributions for selected tests.

CHAPTER 2: Bubble swarm characterization

Bubble motion has long been an important field of study in fluid dynamics, heat and mass transfer, and its role in heterogeneous reactors, and adsorptive bubble separation process such as flotation. The studies have been focused on fundamental aspects of single bubble behavior (Sam, 1995; Tao, 2004; Clift et al.; 2005,) and bubble swarm hydrodynamic characterization (Lammers, 1994; Hibiki and Ishii, 2002; Mudde, 2005). In the latter, individual bubble motion is not considered and average properties of the swarm are measured, for example volumetric fraction of gas (Mena et al., 2005) or the average swarm velocity (Nicklin, 1962; Shen and Finch, 1996; Krishna et al., 1999). In contrast, characterization of individual bubble motion in swarms has seen little research (Cheng and Burkhardt, 2003; Zaruba, 2005), and there is no previous research on individual bubble characterization in bubble swarms in presence of surfactants (flotation-related conditions). Part of the reason for this lack is the difficulty to control production of known bubble size distributions and to decouple the effect of surfactants on generation and motion. Perhaps more important, the image analysis techniques require complex pattern recognition algorithms to identify and isolate bubbles from bubble-clusters or bubbles with flexing surfaces (Malysa et al., 2005). Current hardware limitations (image resolution and sampling rate) determine the capability to track bubbles over the range of size (0.1 mm to 4 mm), shape (spherical, oblate spheroid), surface wobbling (Nguyen and Schulze, 2004) and velocity relevant to flotation systems. Therefore, the development of techniques to measure and characterize bubble motion in swarms in the presence of surfactant requires integrating a broad range of skills (surface chemistry, fluid dynamics, instrumentation and image analysis programming).

2.1- Bubble swarm velocity and surfactant type influence

Bubble swarm velocity has been addressed as an average velocity of a package of bubbles in analogy to previous work on spherical particles settling in a fluid (Richardson and Zaki, 1954). This concept has been extensively used to model two-phase systems (solid-liquid and gas-liquid), using "simple one dimensional flow" (Wallis, 1969) or drift flux analysis. These early models are valid for mono-size distribution of the dispersed phase. To extend the model to distributions, Masliyah (1979) proposed a new model: "hindered settling in a multi-species particle system". These models were adapted for rising bubbles in swarms by Dobby et al. (1988), and establish a unique relationship between bubble size (d_b), superficial gas velocity (J_g), superficial liquid velocity (J_l) and gas holdup (E_g), as shown in Equation 2.1 and 2.2.

$$u_{sb} = \frac{J_g}{E_g} + \frac{J_l}{1-E_g} \tag{2.1}$$

$$u_{sb} = \frac{g \cdot d_b^2 \cdot (1-E_g)^{(1-m)} \cdot (\rho - \rho_g)}{18 \cdot \mu \cdot (1+0.15 \cdot E_g^{0.85})} \tag{2.2}$$

where m is function of Reynolds number

$$m = \left(4.45 + 18 \cdot \frac{d_b}{d_c}\right) Re_b^{-0.1} \qquad 1 < Re_b < 200 \tag{2.3}$$

$$m = 4.45 \cdot Re_b^{-0.1} \qquad 200 < Re_b < 500 \tag{2.4}$$

$$Re_b = \frac{u_t \cdot \rho \cdot d_b}{\mu} \tag{2.5}$$

The model, namely drift flux analysis (Banisi et al., 1994), has been used to predict mean bubble size based on gas holdup, superficial gas and liquid velocity in bubble columns in the presence of various frothers, and the results were compared with photographic bubble size measurements (Yianatos et al., 1988). This work (Table II, Yianatos et al., 1988) showed that the predicted bubble size using the drift flux analysis was underestimated for the Dowfroth 250C (polypropylene glycol methyl ether) in most of the tests, while for MIBC (methyl isobutyl carbinol) it was overestimated. Despite this observation going unrecorded by Yianatos et al., it can be inferred that the difference may be the consequence of a surfactant type effect on bubble rise velocity.

An effect of surfactant type on single bubble rise velocity was reported by Zhou et al. (1991) and recently by Azgomi et al. (2007), who observed bubbles in n-Pentanol appeared to rise at the same speed as bubbles twice as large in Polyglycol. A possible explanation is that frother type may have different effect on skin friction and/or bubble shape. Using the technique developed to test for a frother effect using n-Pentanol and Polyglycol became one focus of the thesis.

From Equation 2.2 it can be observed that the higher the gas holdup, the more packed the bubbles, increasing the extent of interaction and, as a consequence, swarm velocity is reduced. This interaction needs to be incorporated in predicting swarm behavior.

2.2- Characterization of bubble swarm motion.

A measurement technique to determine bubble swarm velocity in bubble columns was proposed by Nicklin (1962). The technique is based on a sudden interruption of the gas injection and the tracking of bubble front position. An example of a bubble front, after the gas injection valve was shut off, is shown in Figure 2.1. The resultant slope of the bubble front position and time correspond to the bubble swarm velocity or "the buoyancy velocity". Using this technique Nicklin developed a bubble swarm velocity model as a function of superficial gas velocity and volumetric content of gas assuming a mono-sized bubble size distribution in an air water system.

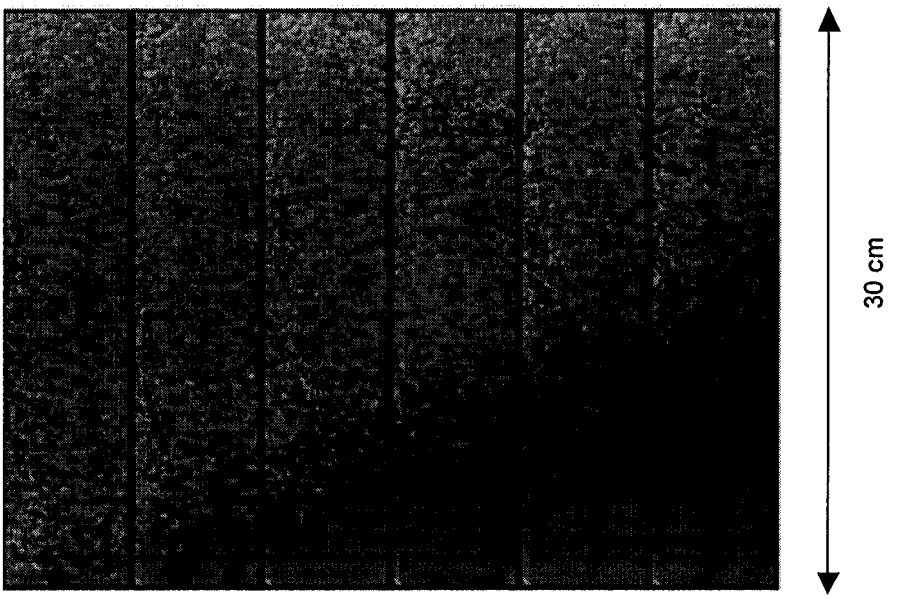

Figure 2.1: Negative images of a bubble front at 100 ms interval.
(Preliminary test conducted for this thesis)

To enhance the bubble swarm velocity measurement technique and the model derived by Nicklin, Shen et al. (1996) proposed a novel method based on the measurement of the volumetric fraction of gas in time (after the gas valve is shut off) using a fast-response conductivity meter. This technique, tested in a bubble column in the presence of frother, demonstrated a reduction in bubble swarm velocity when the gas holdup was increased. Shen interpreted the bubble swarm reduction as a

consequence of the bubble interactions, in analogy to the hindered effect on settling particles described by Masliyah (1979). However, the bubble front tracking technique did not provide information on bubble interaction to support the interpretation. Thus, measurement of bubble interaction on bubble motion became another focus of the thesis.

The rise of a bubble front, after the gas injection is shut off, creates dynamic bubble disengagement, i.e., bubbles rise at different velocities creating segregation along the column. This characteristic, studied by Siram and Mann (1976) tracking dynamic changes in gas holdup, helped interpret "bubble behaviour on bubble columns". According to Sriram and Mann the dynamic change in gas holdup was dependent on bubble size distribution, which seemed to determine bubble motion and interaction in a swarm. Complementing the previous technique with high speed cinematography and particle image velocimetry (PIV), Lee et al. (1999) observed bubble interactions on bimodal bubble size distribution using a 1.3 x 15 x 170 cm bubble column. The results showed that bubble interactions (bubble-bubble and bubble-fluid) produced both small bubbles pulled by faster bubbles and small bubbles hindered by others. These experiments were conducted without frother and coalescence was present, thus the bubble size distribution was not constant. The presence of surfactant seems to reduce coalescence and breakage once the bubble size distribution is generated (Schafer et al., 2002). In addition, the liquid motion generated while bubbles are disengaged does not correspond to the hydrodynamic condition in a bubble column operated with continuous gas injection. Therefore, the study of bubble motion in a bubble swarm requires the following aspects:

a) To assemble a device to generate different bubble size distributions (narrow, wide and bimodal) and to control the bubble-bubble inter-distance.

b) To produce a stable bubble size distribution (either sufficient frother concentration to reduce coalescence and breakage, or sufficient distance from the generating point to stabilize bubble size distribution).

c) To characterize bubble motion in a bubble column operated with continuous gas injection.

These aspects became another focus of the thesis.

Using a bubble column operated with continuous gas injection Becker et al. (1999) studied bubble swarm motion (bubble plume). The measurements were focused on the dynamics of circulation flows employing Laser Doppler Anemometry (LDA). Continuing with Becker's work, Pfleger et al. (1999) incorporated PIV and PTV (Particle Tracking Velocimetry) to characterize bubble plume oscillation. The techniques helped determine bubble plume behaviour, however no special attention was given to bubble interactions. PIV and LDA techniques are useful to track fluid motion (Deen et al., 2000; Buwa and Ranade, 2002) and to describe mixing characteristics in bubble columns (Lin et al., 1996; Mude, 2005), but shadows generated by bubbles make it difficult to track accurately the fluid motion, and the technique is limited to 1-4% volume fraction of the dispersed phase (Deen et al., 2002). Individual bubble tracking techniques became a focus of this thesis.

2.3- Individual bubble measurement techniques in bubble swarms.

Boyer et al. (2002) presented and classified characterization techniques for gas-liquid and gas-liquid-solid reactors. Some of these techniques have been proposed to detect and track individual bubbles in swarms. The techniques are mainly based on local probes (conductivity meters and optical fibre sensors), and recently high speed cinematography and image analysis have been incorporated.

Prasser et al., (2002) used a wire mesh sensor to measure individual bubble velocity on bimodal bubble size distributions. The bubble distributions were generated using two arrays of orifices on a perforated plate (the first array with 19 orifices of 0.8 mm and the second array with 8 orifices of 4 mm). The technique allowed the detection of individual bubbles (small and large bubbles) and helped "visualize the air-water flow". However the technique did not provided information on bubble velocities. A technique to measure individual bubble velocity and size, based on four conductivity needle probes, was proposed by Munholand and Soucy (2005). This technique helped measure individual bubble velocity and gas holdup, but for small bubble sizes it required smaller probes, which are less sensitive (low signal-to-noise ratio).

Risso and Ellingsen (2002) developed a small bubble velocity sensor (50 μm diameter) based on a double optical fibre probe. The instrument provided measurement of bubble velocity for bubble diameters of 2.4 mm and gas holdup 0.5 to 1.05%, however the level of dispersion on the velocity measurements was high. An enhanced probe, based on four point optic fibre, was proposed by Guet et al. (2003). This technique helped to measure individual bubble velocity in bubble columns with volumetric fraction of gas up to 30%.

Both techniques (conductivity and optic fibre sensors) can be used to measure individual bubble velocity and size, but bubble trajectory and bubble interaction

cannot be detected. High speed cinematography and image analysis seem to be the most appropriate techniques.

Miyahara et al., 1986, introduced imaging techniques to characterize bubble motion in a bubble column equipped with a sieve plate. However no techniques were developed to track individual bubbles (or transparent objects) until Nishino et al., (2000). Nishino introduced a technique, based on stroboscopic background illumination and stereo imaging, to track and size spherical glass dispersed in water. The result showed that stereo imaging helped reduce the depth of field distortion, but the uneven light distribution seemed to reduce the tracking capability. For bubbles in swarms Kluytmans et al. (2002) presented some image analysis techniques for measuring bubbles: size, velocity, interfacial area and coalescence behaviour in a 2D bubble column.

Cheng and Burkhardt (2003) introduced a technique, based on high speed cinematography and image analysis, to track vapour bubbles in image sequences. However, the background illumination, bubble reflections and bubble wobbling made it difficult to construct bubble trajectories. Zaruba et al. (2005) improved the illumination using an LED array and reduced the superimposed bubbles using a flat column (140x10x2 cm column). However bubble clusters (touching bubbles) were difficult to distinguish from ellipsoidal bubbles. To tackle this problem, Honkanen et al., (2005) proposed algorithms to recognize highly overlapping ellipse-like bubble images. Finally, Cheng and Burkhardt (2006) proposed a technique to identify and to track vapour bubbles in swarms. This technique is based on high speed cinematography and matching patterns ("templates" selected manually). However, uneven illumination, overlapped bubbles and bubble clusters remained, thus these difficulties became an additional aspect to be covered in this thesis.

CHAPTER 3: Development of technique to track bubble motion in a swarm

The technique is based on high speed cinematography and tracking of multiple moving objects in a sequence of images. Images, containing bubbles in a 2D plane, are generated from bubble swarms in a laboratory column. Images are recorded at intervals of 0.5 to 2 ms. Image processing algorithms are implemented to isolate and measure geometric properties of the bubbles. Images are converted into a data structure (Math Works Inc., 2003) containing geometric parameters for each bubble. The geometric parameters and a matching criterion, developed specifically for this work, are applied on consecutive data structures (converted pictures) to track matching bubbles using an incidence matrix (Corman et al. 2001). The individual bubble trajectory velocity is reconstructed from the data structure vector and the matched objects in the sequence of images.

Bubble swarms are generated using a double chamber sparger, with independent gas injection to each sparger, regulated by appropriate meters and controllers. The unit is assembled with a narrow slot sparger (Harris et al., 2005) and porous flat sparger (Southern and Wraith, 1990). This combination allows the generation of various bubble size distributions based on those found in industrial flotation machines (Figure 1.4). The experiments are conducted in a rectangular transparent column with an inclined top section (15^{o}) (shown in Figure 3.52). Bubble images are collected at three locations (near the point of generation, the top of the straight section and towards the top of the inclined section), in order to include the effect of surfactant accumulation on the bubble along the column. Both bubble-generating devices produce approximately a 2D (i.e., "flat") bubble swarm, which facilitates bubble tracking measurement in the first 50 cm of the column. After this distance, bubble oscillations, interactions and liquid re-circulation generate axial displacement of bubbles. As a consequence, a bubble plume starts to form (i.e., 3D swarm of bubbles), which makes it difficult to track trajectories. To try to limit this condition, the inclined section forces the plume to spread into single bubble layer again.

The technique allows the individual bubble motion to be studied under various operating conditions. In particular, the technique was developed to study the effect of surfactant type, which seems to influence bubble velocity in swarms (Azgomi et al., 2007; Zhou et al., 1991).

Many factors may influence bubble motion, as described in Chapter 2, which are magnified by bubble interactions. A novel measurement is derived from the bubble image to characterize the level of bubble interaction. The technique is based on determining inter-bubble distance.

Bubble size distribution, bubble tracking in a swarm, bubble trajectory reconstruction and bubble interaction measurement techniques require an effective image processing algorithm to maximize the number of bubbles identified from bubble swarm pictures. These pictures normally contain the following, which hamper identification: touching bubbles (bubble clusters), dark areas (due to uneven light distribution or presence of particles), and irregular bubble shapes. These characteristics make it difficult to identify and isolate individual bubbles, reducing the number of bubbles that can be analyzed. Typically only 2% to 30% of the area containing bubbles is used, requiring a large number of images to increase the total number of bubbles counted. This, however, does not solve the possible biasing that selecting only some of the bubbles in a picture may introduce.

The problems described above have been noted when the sampling for imaging technique is used (Grau and Heiskanen, 2002; Hernández-Aguilar, 2004a; Bailey, 2004; Gomez et al., 2006). In order to increase the number of bubbles counted, enhanced image processing software has been developed, based on intensity background compensation, the watershed algorithm to separate bubble clusters, and local thresholding to compensate the effect of dark areas or uneven light distribution. The techniques and the models developed are described in the following sections.

3.1- High speed cinematography and uneven light compensation

High speed cinematography allows the collection of image sequences of moving objects and/or objects changing in shape. These events can be tracked and measured in time. The present work requires the ability to track moving bubbles over at least 30 frames with a spatial resolution of a minimum of 35 pixels/mm. In addition, bubble surface oscillation or shape changes need to be tracked. Examples of high speed cinematography measurements conducted in this work are shown in Figure 3.1. Images are contrast enhanced to facilitate visual tracking.

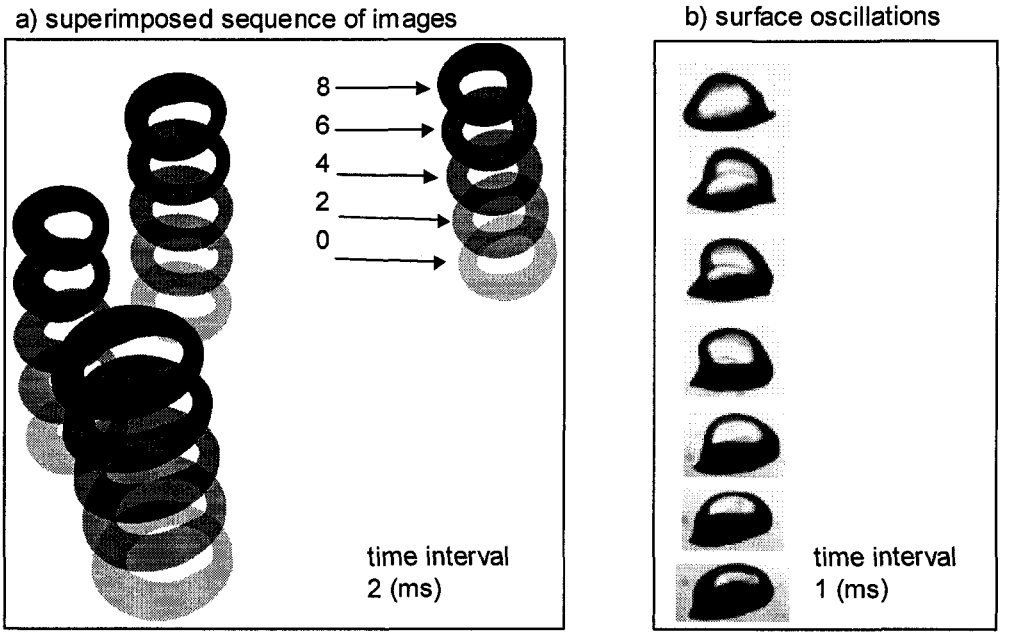

Figure 3.1: Examples of high speed cinematography used in (a) bubble motion and (b) shape

To meet the compromise of picture size, frame rate, magnification and viewing area, required for tracking bubbles and bubble surface oscillations, the camera is set to 500 pictures per second, image size is set to 1280x1024 pixels, and image resolution is set to 45 to 60 pixels/mm. For tracking bubble surface oscillation, where there is no available reference, images are collected at the maximum sampling rate determined by the hardware. To achieve these requirements, a digital high speed camera, model "Troubleshooter HR" (specifications in Appendix 3, Table A3.1), is used. The camera allows collecting sequences of images in AVI file format (audio video interleave), in 256 grey scale levels on a CMOS sensor (15.4 x 12.8 mm).

Different combinations of image size (number of pixels), and frame rate (number of pictures per second) can be configured. Exposure time or shutter speed is also configurable as a factor in the frame rate. Table 3.1 summarizes the configurations used in this research. A macro lens (Appendix 3, Table A3.2) is used and focal distance is set to 20 cm, to provide a depth of field of 5 mm. Figure 3.2 shows the camera set up.

Table 3.1: High speed camera configurations

Picture size (pixels)	Frame rate (fps)	Shutter speed (1/s)	Application
1240 x 1024	500 and 250	1/3000	Bubble velocity
320 x 240	2000	1/2000 -1/10000	Bubble surface oscillation

Once movies are recorded in a circular RAM memory (1 Byte), the AVI files are transferred to a computer where they are deployed into TIFF pictures (Tagged Image File Format). The deploying and naming process is implemented in a Matlab program (Appendix 2, Table A2.1). In order to manage the generated files, tag names based on date and time are created automatically to generate files and subfolders.

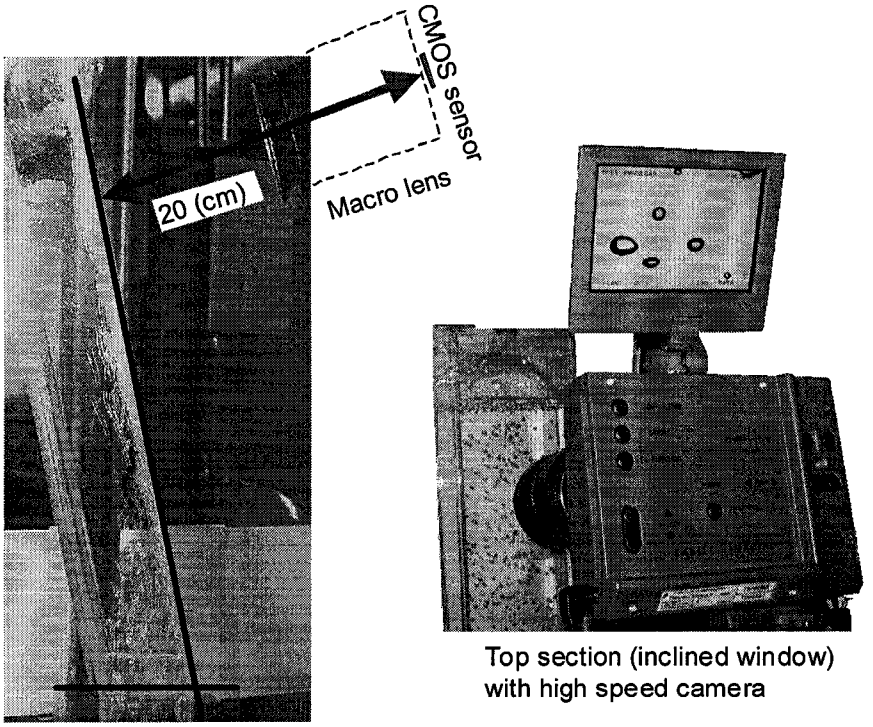

Figure 3.2: High speed camera set up

Backlighting is employed to produce bubble contours (Robinson, 1946); differentiating individual bubble groups from the liquid phase (Hernández-Aguilar et al., 2004). Halogen light of 1000 W is used for illumination, since high speed cinematography (shutter speed 3000 to 10000 (1/s)) requires high intensity lighting. The illumination system gives uneven light distribution producing dark areas, relative to the image center, where bubbles cannot be isolated (Gomez et al., 2006). Alternatively, uniform illumination can be obtained using light emission diodes (LED), as proposed by Grau (2006) in development of a similar bubble sizing technique. The light intensity required for high speed cinematography, however, cannot be obtained with the currently available LEDs.

In the present thesis, specific image processing software was developed to compensate uneven light distribution in images containing bubbles and dark objects (particles) (Appendix 2, Table A2.1). The algorithm is based on morphological opening (i.e., an erosion followed by a dilatation operation) using a 25 pixel disk as a structuring element (Math Works Inc., 2006b). The operation is applied on the image

complement (light spots are black, and bubble contours are white), shown in Figure 3.3(a), which has uneven light distribution, as shown in the corresponding intensity plot in Figure 3.3(b). The resulting operation generates the image background, shown in Figure 3.3(c). After "subtracting" the background image from the original complement image, this generates a "corrected" image. The corrected image is enhanced in contrast; the result is shown in Figure 3.3 (d).

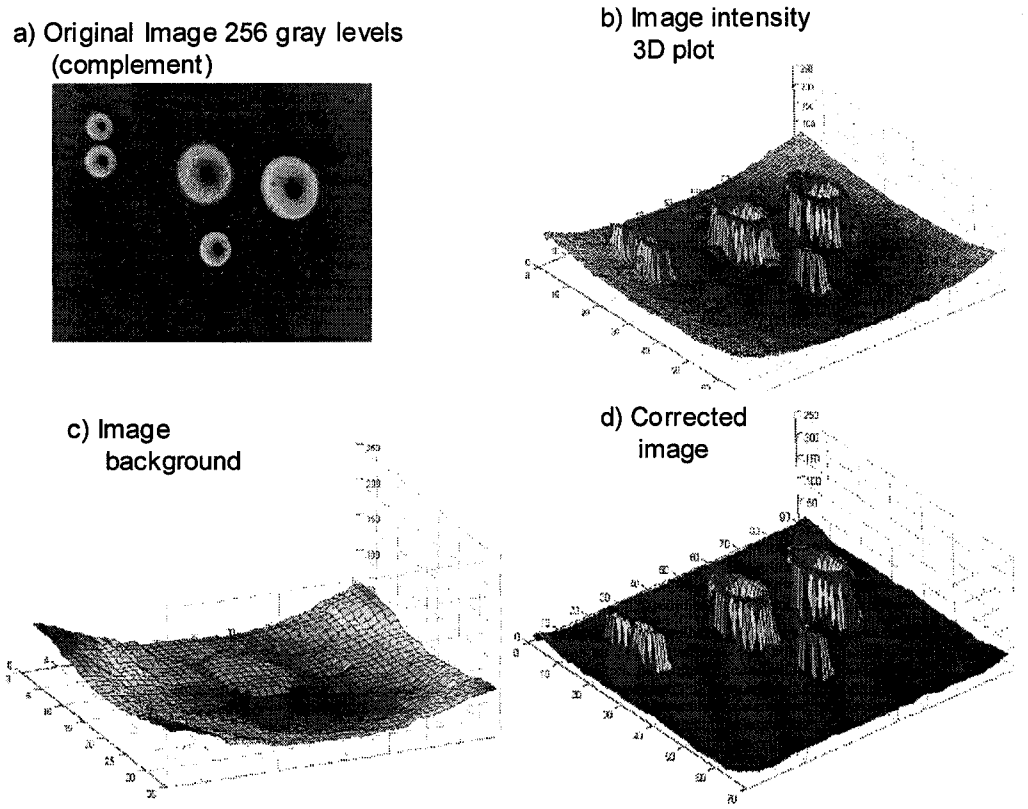

Figure 3.3: Uneven illumination compensation algorithm

Applying an illumination compensation algorithm, the number of bubbles detected is increased. This allows more bubbles to be tracked in image sequences. In some cases, the number of objects remains static in a sequence of images (bubbles or particles stuck to surfaces or image noise). This can significantly bias the measurement (e.g., 5 fixed objects on 35 bubbles per picture, on average, create a bias of 12%). To remove these objects specific routines have been developed (Appendix 2, Table A2.1).

After the bubble image sequence is deployed in grey scale files and corrected for uneven light illumination, image processing software is used to identify and to isolate individual bubbles. These isolated objects (sub pictures) are converted into a data structure containing bubble geometric properties such as area, perimeter, major axis and minor axis, among others.

3.2- Bubble image processing and data structure conversion

A bubble image is a set of dots (pixels) arranged in a matrix of m x n elements, each representing light intensity through a greyscale value going from the lowest 0 (black) to the highest, normally 255 (white). The 256 levels correspond to 8 bits intensity resolution (2^8 levels) or spectral resolution, where m x n pixels is the image size (Pratt, 2002). Figure 3.4 (a) shows a typical image, collected in a flotation system (Dahlke et al., 2004), used for bubble size measurement, and Figure 3.4 (b) shows the intensity levels for a section of the image.

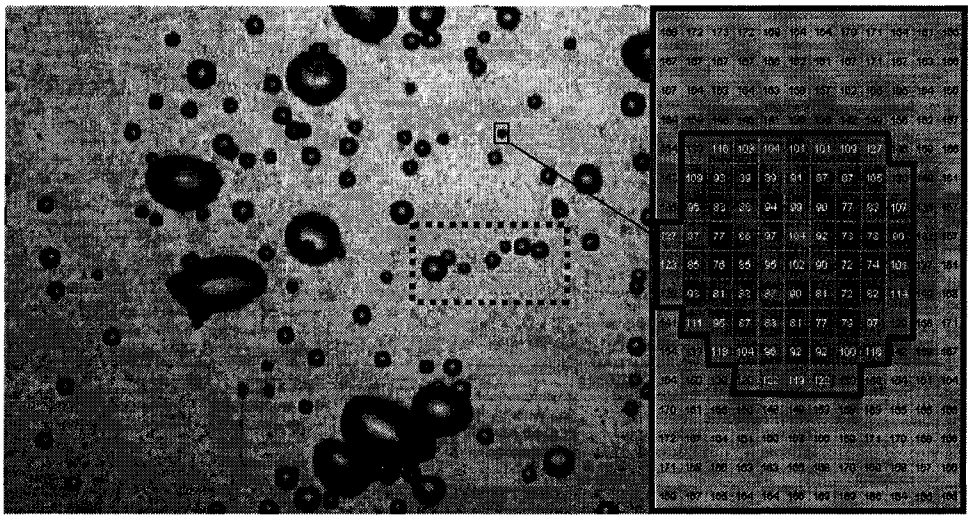

(a) 8 bit grey scale image (b) intensity levels

Figure 3.4: Typical image used in bubble size measurement
(*doted rectangle referenced in Figure 3.9)

Image processing operations are applied on the image intensity matrix in order to determine bubble geometric properties. Image processing consists of a series of matrix operations, for example: image contrast enhancement, filter operations (noise removal), edge detection, thresholding (Wang et al., 2002), morphology operations (erosion, dilatation, skeletonization) (Pratt, 2002), feature detection, and segmentation (Acharya and Ray, 2005). An extensive review, 1700 references, on image processing and computer vision is provided by Rosenfeld (2000).

Image processing routines are commonly used in various applications, but specifically for the current needs – bubble identification, tracking, inter-distance and surface mobility measurements – it is necessary to combine routines in specific programs capable of running multiple files (300 to 900) and creating data structures suitable for analysis.

Various image processing applications are available to implement routines. Four applications were evaluated in this research, summarized in Table 3.2, to determine which was the most suitable.

Table 3.2: Image processing software tested

Application name	Reference
Matlab and the image processing toolbox	Mathworks
Northern Eclipse	Empix imaging
UTHSCSA Image Tool	The University of Texas Health Science Center in San Antonio
Image J	National Institute of Health (USA)

These applications proved equivalent, except for perimeter measurement, which showed inconsistencies on standard images. Matlab gave results closer to the known perimeter, and was selected to develop all the applications required. Matlab image analysis toolbox programming (Mathworks Inc. 2003b) also showed more flexibility to combine algorithms, and all basic image-processing operations are

available. In addition, Matlab can create complex data structure, which is most advantageous for bubble tracking in a sequence of frames, but requires more programming skills.

To convert a sequence of images into data structure, five operations are performed. These operations detect and isolate bubbles and bubble clusters, generically called blobs, from a grey scale image generated by imaging with background light. Each object is converted into a binary matrix, where geometric properties are measured. The five operations are summarized as follows:

1- Thresholding: It differentiates blobs from background creating a binary image.

2- Segmentation: It isolates or separates blobs from a binary image.

3- Blob features measurement: It measures geometric properties for each segmented blob, creating a data structure.

4- Blob classification: It selects isolated bubbles based on geometric characteristics, and the remaining bubble clusters are stored.

5- Bubble cluster separation: It separates touching or super-imposed bubbles from the remaining non-selected bubbles. Its properties are added to the data structure.

3.2.1- image thresholding

The thresholding operation creates a binary image comparing an intensity value or threshold to the matrix pixel intensities; all pixels with greyscale values below the threshold are given a value of 1, while pixels with values above the threshold are given a value of 0. To determine a global threshold value, a variety of techniques have been proposed (Otsu, 1979; Tizhoosh, 2004; Chen and Wang, 2004; Huang et al., 2005). These techniques are based on the mean intensity value or picture intensity histogram. Image frequency intensity examples are shown in Figure 3.5, for a clear image (a) and a dark image (b), which were collected during an industrial

bubble size measurement trial. Both images correspond to the same measurement, but threshold values, for example using Otsu's algorithm, are different.

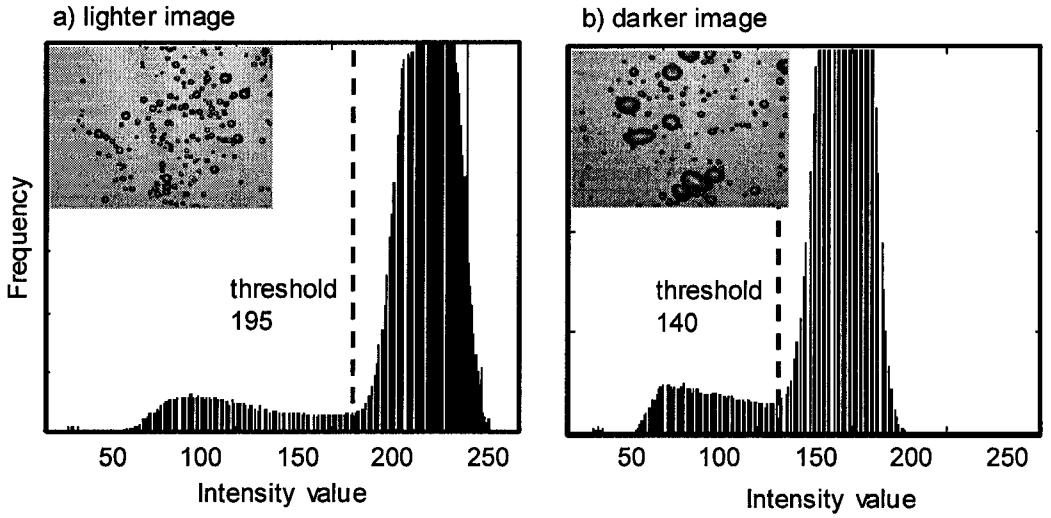

Figure 3.5: Image intensity frequency histogram

Bubble images generated using background light have a diffuse intensity gradient (Hernandez-Aguilar, 2005; Grau, 2006), which makes it difficult to identify bubble borders and can create under estimation by 15% in predicting bubble size (Leifter et al., 2003). Figure 3.6 illustrates image intensity in a given section: in this case a variation of threshold from 50 to 150 can create an error of 300%.

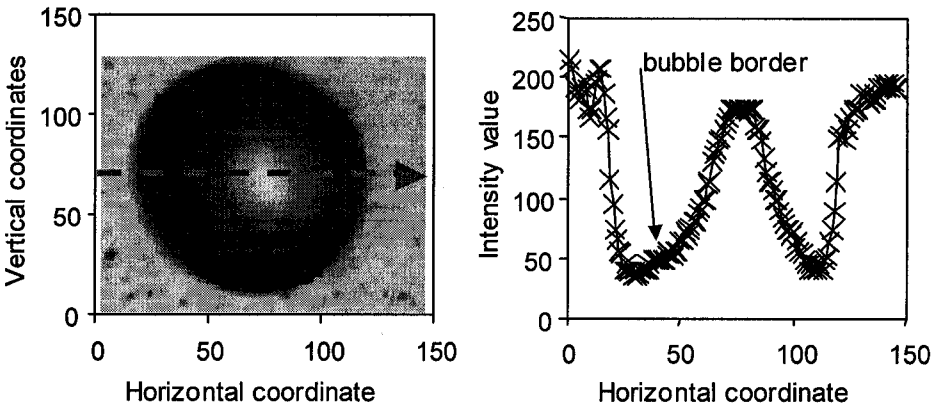

Figure 3.6: Image intensity variation across bubble border.

Bubble images collected in a flotation process vary in illumination intensity distribution due to the motion of bubbles and particles, the latter accumulating (and re-circulating) in the viewing section as bubbles burst and drop their particles.

Camera settings, shutter speed and aperture, are either manipulated to compensate changes in illumination intensity, or are kept constant. Examples of mean image intensity fluctuations, from tests conducted in plant by three operators, using the McGill Bubble Viewer, are presented in Figure 3.7. The figure shows the mean intensity value per picture, collected at intervals of 0.5 seconds. The sharp changes in intensity are due to camera setting changes, and the gradual changes are the consequence of solids accumulation. It is clear that average intensity cannot be used to set a global threshold.

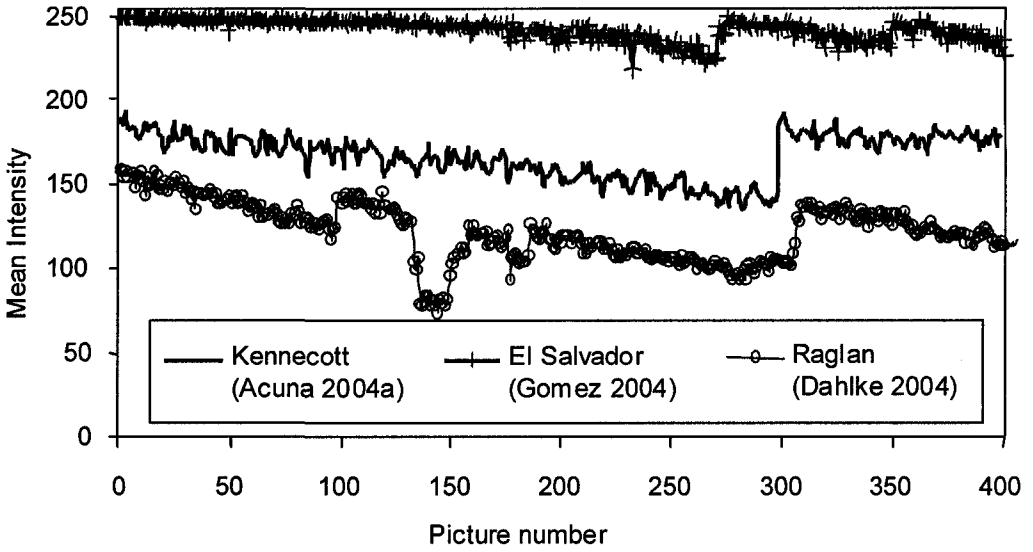

Figure 3.7: Picture average intensity variation during plant measurement.

A procedure to determine a threshold value for bubble images collected under plant conditions was proposed by Hernandez-Aguilar (2005), which is based on the mean intensity value of the last frame of a group of 50 consecutive frames. This value is used as a global threshold and the procedure repeated for the next 50 frames until completing the entire sequence of images. This approach requires: grouping images in sets of 50 pictures, processing in batches, and merging the results, which requires processing time. Also, setting the threshold value for fifty pictures may still incur bias.

In another approach, Grau (2006) revised threshold algorithms by simulating bubbles with glass micro spheres. Ignoring the fact that glass spheres do not have

the same optical properties as air bubbles, the result did show significant errors in the number of objects (micro spheres) counted and errors in D_{10} and D_{32} calculations if the threshold is set outside of an "optimum range".

One outcome of the Hernandez-Aguilar and Grau experiments is that a global threshold cannot be used, rather it must be calculated for each picture, using, for example, the classical Otsu algorithm (Otsu, 1979; Mathworks Inc, 2003b) or a novel algorithm, as developed in this work.

In order to reduce measurement bias and compensate intensity variation the following procedures are proposed: first, compensate light intensity using an automatic camera iris and a fixed shutter speed (1000 to 2000 1/s); second, correct background intensity if the images have uneven light distribution (Appendix 2, Table A2.1); and, finally, use the newly devised algorithm to assign the threshold value automatically in each picture. Thus, new algorithm is referred to the Calzado-Acuna algorithm after the co-developers.

The Calzado-Acuna algorithm uses the mean intensity value and an error function to calculate the threshold value, and iterates this value in order to maximize the number of bubbles detected per picture. The relationship between intensity value and threshold is presented in Figure 3.8.

This function was developed using results of a series of manual measurements made by an experienced operator. Basically, the threshold value is proportional to the mean intensity value with two slopes, one for clear images (mean intensity above 125) and another for dark images (intensity value below 80), as shown in Figure 3.8. The critical zone, in which images have a significant amount of dark objects, requires a non-linear relationship (error function). Normally, the calculation is iterated fewer than 3 times, based on a half interval algorithm, with the number of blobs identified as the objective function.

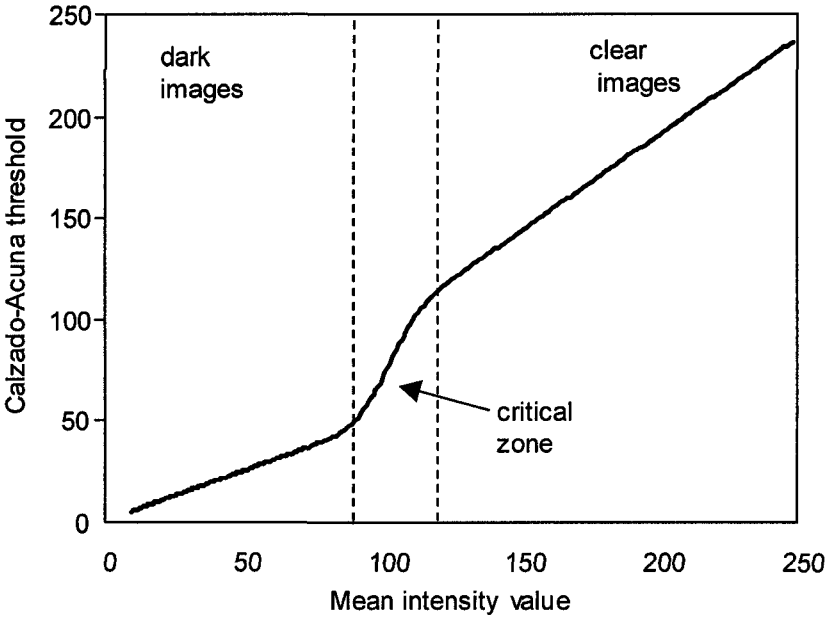

Figure 3.8: Calzado-Acuna thresholding function.

The Calzado-Acuna algorithm has demonstrated the ability to isolate more objects than conventional thresholding techniques, some 20% to 50% more than using the Otsu algorithm, for example. An illustration is shown in Figure 3.9 (image section taken from Figure 3.4): the Calzado-Acuna algorithm (d) finds more isolated elements than the other two. In addition, using mean intensity introduces noise (non-existing bubbles) shown in the two small dots towards the bottom of the picture (b). The original picture shows 7 bubbles, the Calzado-Acuna algorithm is able to identify the largest number of them.

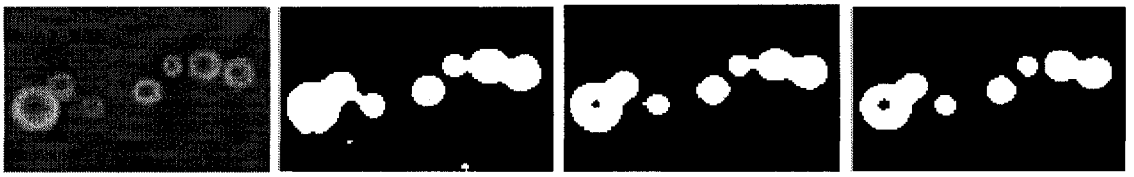

(a) Negative image (Figure 3.4 (A)) (b) Mean intensity (c) Otsu algorithm (d) Calzado-Acuna algorithm

Figure 3.9: Image thresholding algorithms

However, in some situations in which there are bubble clusters with diffuse borders (Figure 3.9 (a), left cluster), some bubbles are still excluded (rejected areas). To examine these rejected areas, local thresholding and de-clustering techniques are incorporated. These techniques are explained in section 3.2.7 (bubble de-clustering techniques).

After the threshold is applied a binary image is generated containing segments of isolated bubbles or bubble clusters (marked as 1) and black background (marked as 0). Image sub-regions are labeled, using a segmentation process (Pratt, 2005), and a series of matrices is extracted for each individual segment or blob, as described in the following section.

3.2.2- image segmentation and filtering

Individual objects within the image can be identified using "connected-component labeling" (Mathworks, 2003) or a segmentation process (Pratt, 2005). In this process, image sections, which are connected in four directions (N, S, W, E) or eight directions (N, NE, NW, S, etc), are marked with a correlative number, allowing matrix manipulation. A simplified example of a matrix containing 3 blobs segmented using 8 directions is shown in Figure 3.10. Objects labeled 2 in Figure 3.10b are connected, but if a 4 direction segmentation is used this blob will be split into three blobs. In bubble image segmentation, bubbles are rarely connected at one corner (0.8 %

found in a population of 11,000 bubbles), therefore 8-direction segmentation is applied which is faster than 4 directions.

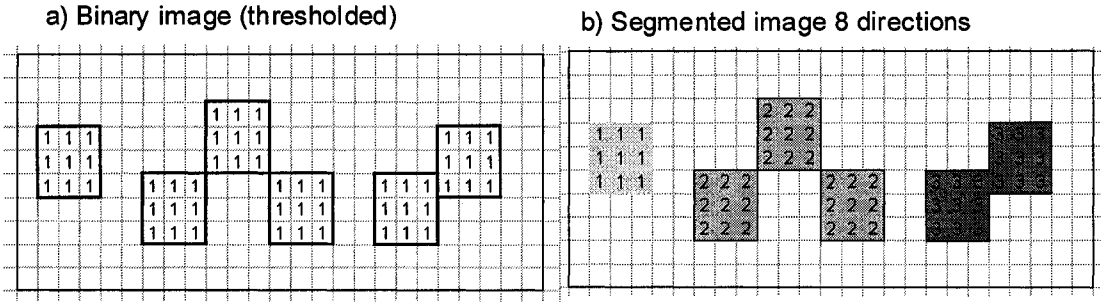

Figure 3.10: Image segmentation using 8 directions

To speed up the segmentation process, and later geometric measurements, small blob objects, most likely image noise or small uncompleted bubbles, are removed before segmentation. Small blobs are objects smaller than 5x5 pixels, which are not possible to distinguish as bubbles. To remove these objects a median filter operation of 4x4 pixels in size (Image Processing Toolbox User's Guide) is used to mask with 0 all sections in which there are segments of up to 4x4 pixels not touching other segments. Notably, for bubble images containing particles this operation reduces processing time significantly (by 75%). An example illustrating the process is shown in Figure 3.11.

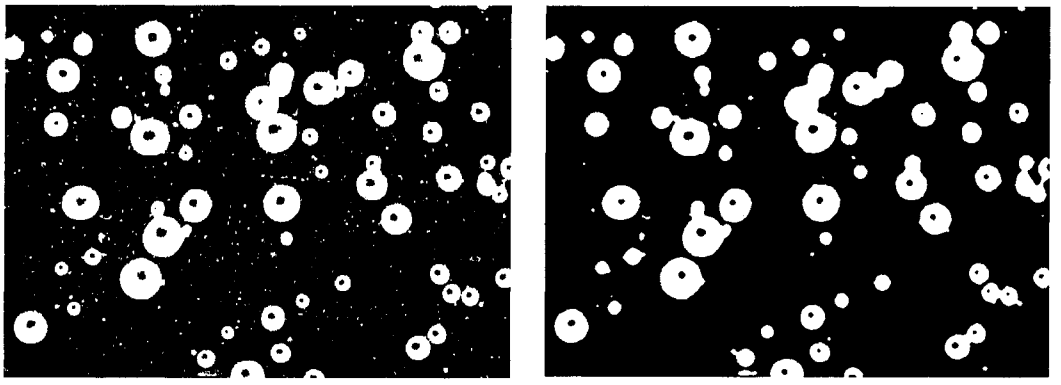

Non filtered image
Blobs = 741, processing time 2.01 (s)

Filtered image
Blobs= 76, processing time 0.48 (s)

Figure 3.11: Reduction in processing time by applying an image filter

Once the objects are segmented, blob measurements are applied to each object.

3.2.3- blob features: measurement and data structure

A segmented image contains isolated blobs in the form of a matrix. Each element in the matrix represents a square pixel. Pixel dimension depends on the image resolution and the magnification used. These two factors determine the pixel size (μm) or image resolution (pixels/mm). Figure 3.12 shows a sequence of pictures of a bubble using the same picture size (original image), but with different image resolution (pixel size). This example illustrates that magnification is crucial for bubble geometric properties measurement; for example F180 (Frennet diameter at 180° given below each image) is affected by the pixel size used. The smaller the pixel size the better the resolution. The pixel size used in this thesis is from 20 to 30 μm in images of 1280 x 1024 pixels. This particular aspect is not considered by some researchers and can create significant bias, excluding bubbles below certain size. For instance, De Swart et al. (1996) used a pixel size of 1000 μm and, in consequence, all bubbles below 1 mm were excluded.

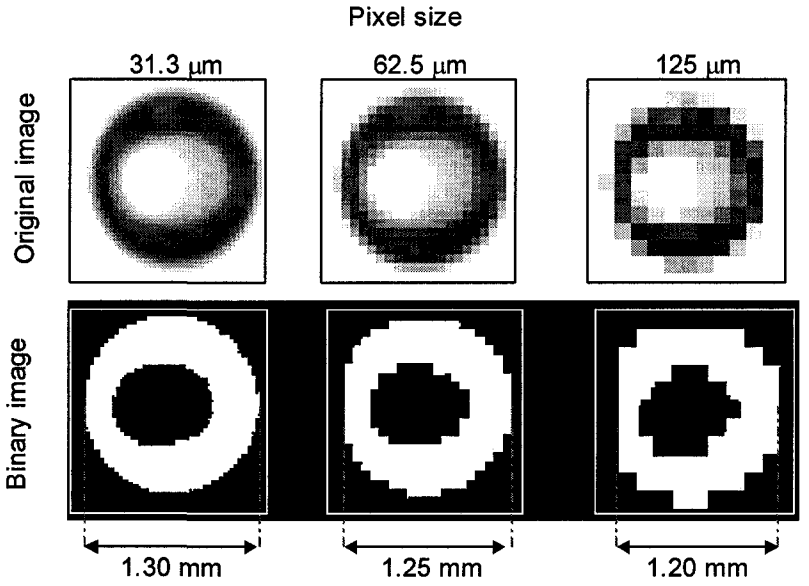

Figure 3.12: Effect of magnification factor on image digitation.

The pixel size aspect is particularly limiting when wide bubble size distributions are present as occurs, for example, when jetting spargers are used (Bailey et al., 2005). If the camera is set to measure large bubbles (3 to 5 mm), small bubbles cannot be

detected, but if camera resolution is increased to detect small bubbles, the viewing area is reduced and the chance to capture the whole of a large bubble is reduced. To resolve this situation high resolution (35 pixels/mm) and large viewing area (e.g., 150 mm by 120 mm) is required. However, increasing the resolution reduces the sampling rate, thus for the present task of tracking moving bubbles, image resolution and sampling rate become the limiting factors.

Blob geometric parameters (total filled area, major axis, minor axis, perimeter, etc) are measured and organized in a data structure, for each blob in a picture, for a sequence of images. Figure 3.13 shows the data structure developed for this work, and implemented in Matlab.

This structure allows the following: bubble classification (cluster bubbles and single bubbles), statistical computations such as bubble size distribution and aspect ratio distribution, and bubble tracking (section 3.3). Once the data structure is created bubble images are no longer required, i.e., no other image processing operation is needed. As a result data storage size is reduced by 95%. These characteristics convert an image processing problem into a data processing problem, speeding up analysis. This feature is exploited in this thesis.

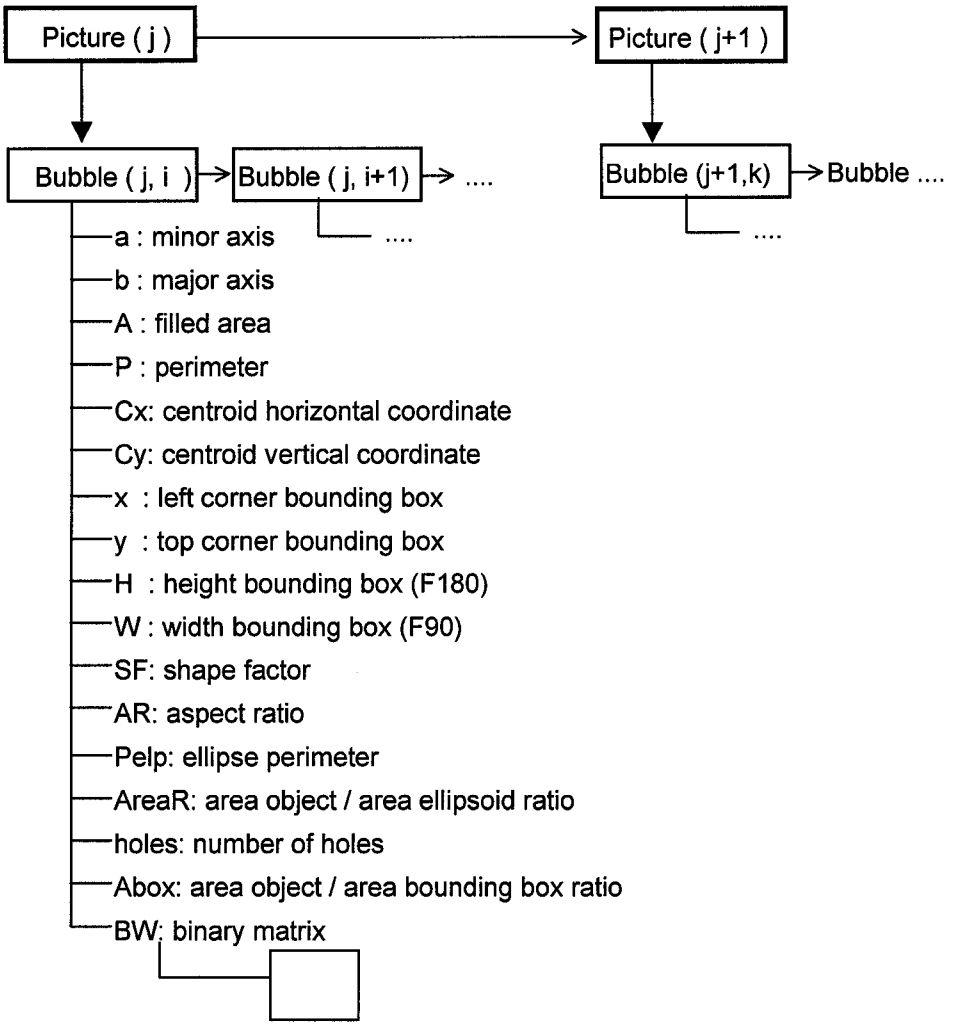

Figure 3.13: Data structure for bubble geometric parameters
(Parameter description in Appendix 2, Table A2.3)

Finally, elements of the data structure (bubbles per picture) are classified using selection criteria based on geometric properties for single isolated bubbles (accepted blobs) and bubble clusters (rejected blobs). Bubble clusters are separated using the watershed technique and local thresholding. The resultant isolated bubbles are merged with the previously accepted blobs to generate a final data structure with accepted bubbles. Typically up to 30% of the area containing bubbles is accepted as single objects, and after de-clustering this can go up to 90%, the remaining 10% corresponding to blobs overlapping the picture boundary, the presence of particles and image noise.

3.2.4- shape factor and selection criteria for single bubbles

A parameter commonly used to discriminate single bubbles from a bubble cluster is the shape factor (SF), defined in Equation 3.1, which is a measure of the circularity of an object:

$$SF = \frac{4\pi A}{P^2} \tag{3.1}$$

where, A and P are the area and the perimeter of the segment (bubble), respectively.

A shape factor of one indicates a circle, and as the value approaches zero, it indicates an increasingly elongated polygon (Bailey, 2004). The reciprocal of the shape factor is named compactness (Grau and Heiskanen, 2003) or roundness (Empix inc., 2002). A shape factor for circles (Equation 3.1) has been used to identify single bubbles from bubble clusters, based on the argument that bubbles under flotation conditions (presence of frothers) appear to be mostly spherical (Hernandez-Aguilar, 2004; Grau, 2006; Bailey, 2004; Gomez et al. 2005). However, evidence from over 600 measurements in industrial cells (over 4 million bubbles analyzed), using the McGill bubble sizing technique and the enhanced image processing algorithm described above, indicates that the average aspect ratio is 0.79, and that bubbles appear to be generally elliptical, as in Figure 3.14. These results show that a shape factor criterion should be defined for elliptical bubbles.

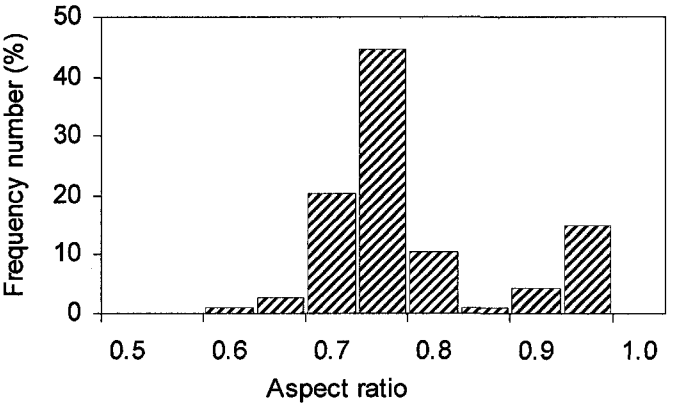

Figure 3.14: Aspect ratio frequency distribution (613 industrial cell measurements)

Normally for the McGill bubble sizing technique, the shape factor value (de-pixelation correction applied, section 3.2.6) is set to 0.90 to classify isolated bubbles. However, some bubble clusters can be accepted and some single bubbles rejected, as is illustrated in Figure 3.15.

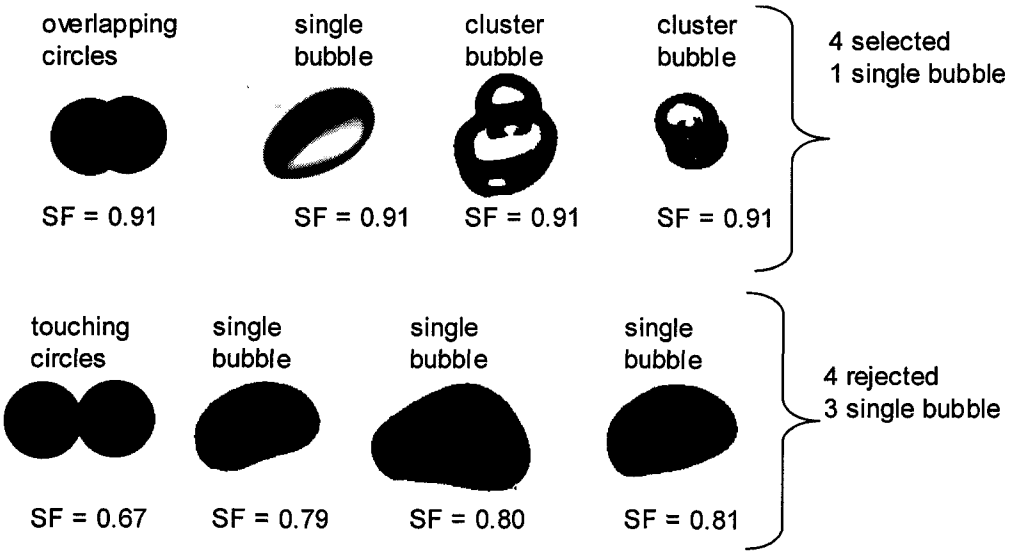

Figure 3.15: Low selectivity using shape factor criterion

As a consequence, a shape factor defined for circles does not appear to be the appropriate selection criterion. This may affect the accuracy of bubble size distribution measurement and, importantly in the present context, reduce the number of bubbles that are tracked. Figure 3.16 shows shape factor values for two sets of

data, in which bubbles were selected manually to ensure single bubbles. In presence of high concentration of frother bubbles tend to be spherical and then the acceptance is high, while without frother the criterion is not selective.

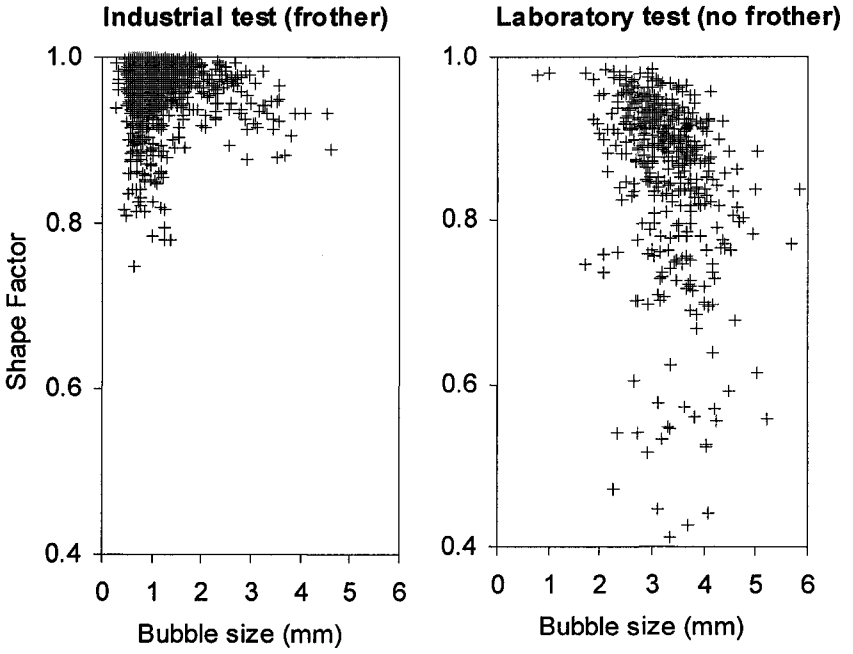

Figure 3.16: Shape factor values and the effect of frother

To avoid rejecting isolated bubbles and accepting bubble clusters other criteria have been proposed.

Bailey et al. (2004) evaluated a selection criterion based on number of holes (bright spot indicating bubble center), hole size and shape factor. This enhanced the accuracy of isolating single bubbles, but shape factor remained inappropriate to identify bubble from clusters.

Mena et al. (2005) proposed using the ratio of the area of the bubble to the convex area (concept illustrated in Figure 3.17). According to Mena et al. a factor 0.99 appeared to be a "good criterion" for ellipsoidal bubbles.

However, if the same isolated bubbles used in Figure 3.16 are taken and the bubble area and convex ratio are plotted, clearly this criterion also fails. In this case, for

spherical bubbles few have an area ratio above 0.99 (industrial test), as shown in Figure 3.18. The criteria proposed are valid over certain bubble size ranges, and it is required to use the criterion hierarchically.

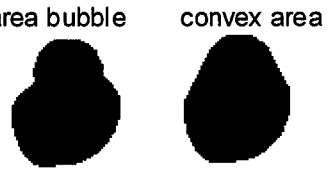

Figure 3.17: Actual bubble area and its corresponding convex area

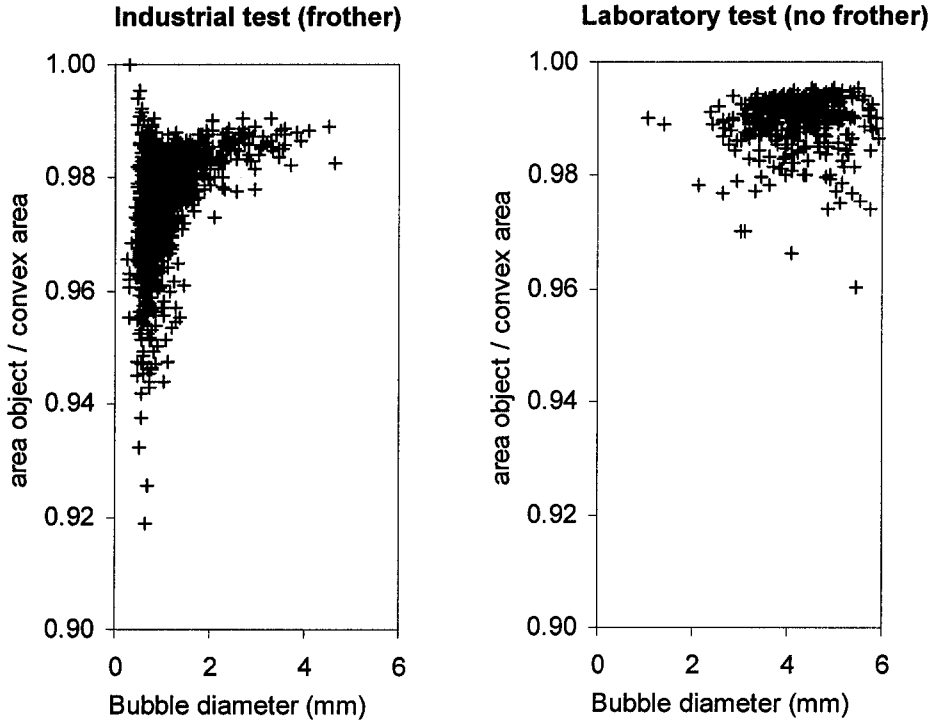

Figure 3.18: Area bubble to convex area ratio selection criteria comparison

To help improve the criteria, a model for SF for ellipsoidal objects is proposed and evaluated.

3.2.5- shape factor model for ellipsoidal objects

As bubbles above a diameter 1.4 mm tend to acquire an ellipsoidal shape (Clift et al. 2005), and because the dynamic forces tend to deform bubbles a shape factor based on of two semi ellipsoids with the same major axis is proposed. An example of bubbles from plant and lab measurements is shown in Figure 3.19 to illustrate bubble shape, which depends on bubble size and frother type/concentration. (This frother aspect is analyzed in section 4.)

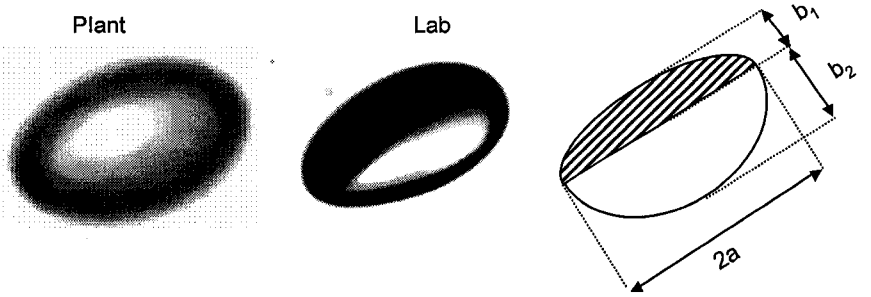

Figure 3.19: Plant and lab ellipsoidal bubbles.

For ideal ellipsoids shape factor is calculated as a function of aspect ratio and three minor axis ratios (E), as indicated in Figure 3.20. This plot shows that the shape factor for a circle has a low selection for ellipsoidal objects and, consequently, would reject the ellipsoidal bubbles in Figure 3.15.

For an ellipse, perimeter calculation uses a numerical approximation based on Equation 3.2, where b is the minor axis for a symmetric ellipse. Various approximations can be found in the literature (Barnard et al., 2001) for perimeter calculation; the approximation used in this work (Equation 3.2) has an error less than 1.7% for ellipses of aspect ratio 0.5.

$$P_{ellipse} = \pi \cdot \sqrt{2 \cdot \left(a^2 + b^2\right) - \frac{(a-b)^2}{2.2}} \tag{3.2}$$

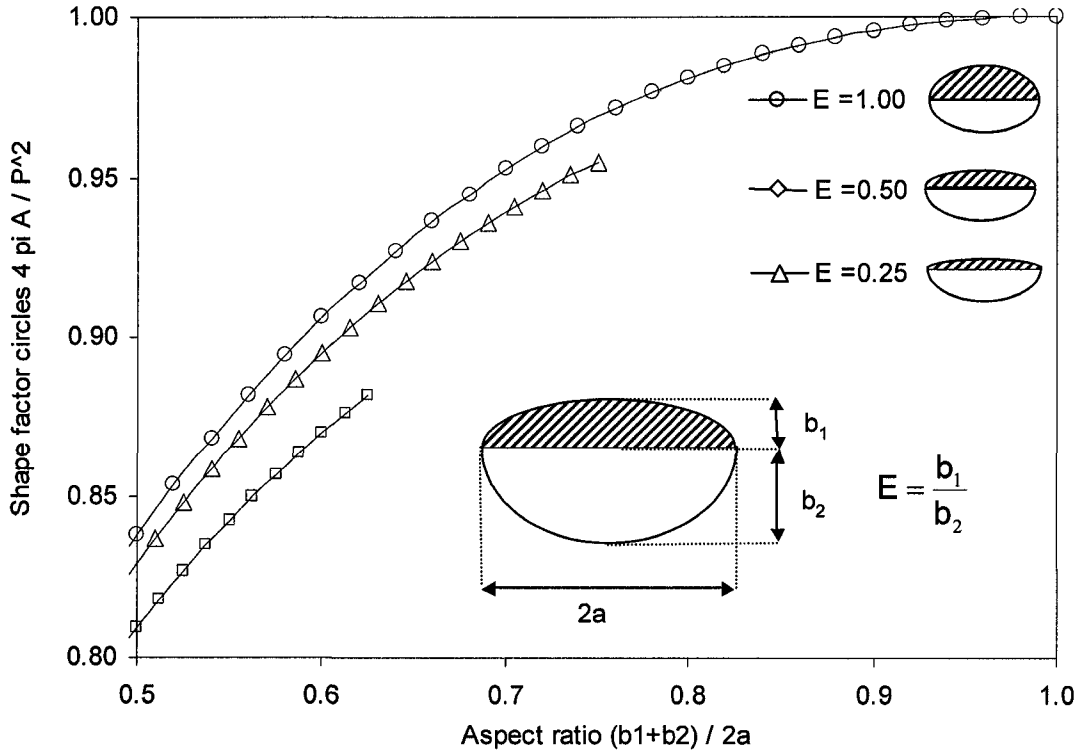

Figure 3.20: Shape factor for ellipsoidal bubbles

A general shape factor for ellipsoidal objects is proposed as one of the selection criteria. The factor is a function of the object parameters A, P and aspect ratio AR (AR = a/b).

$$SF_{elipse} = \frac{4\pi A_{ellipse}}{P_{ellipse}^{\ 2}} = \frac{4a \cdot b}{2 \cdot \left(a^2 + b^2\right) - \frac{(a-b)^2}{2.2}} \tag{3.3}$$

Substituting a = AR*b, and re-arranging Equation 3.3, results in Equation 3.4, which can be used to identify ellipsoidal objects.

$$SF_{global} = \frac{4\pi A_{object}}{P_{object}^{\ 2}} \left[0.2273 + 0.3863 \cdot \left(AR + \frac{1}{AR} \right) \right] \cdot \tag{3.4}$$

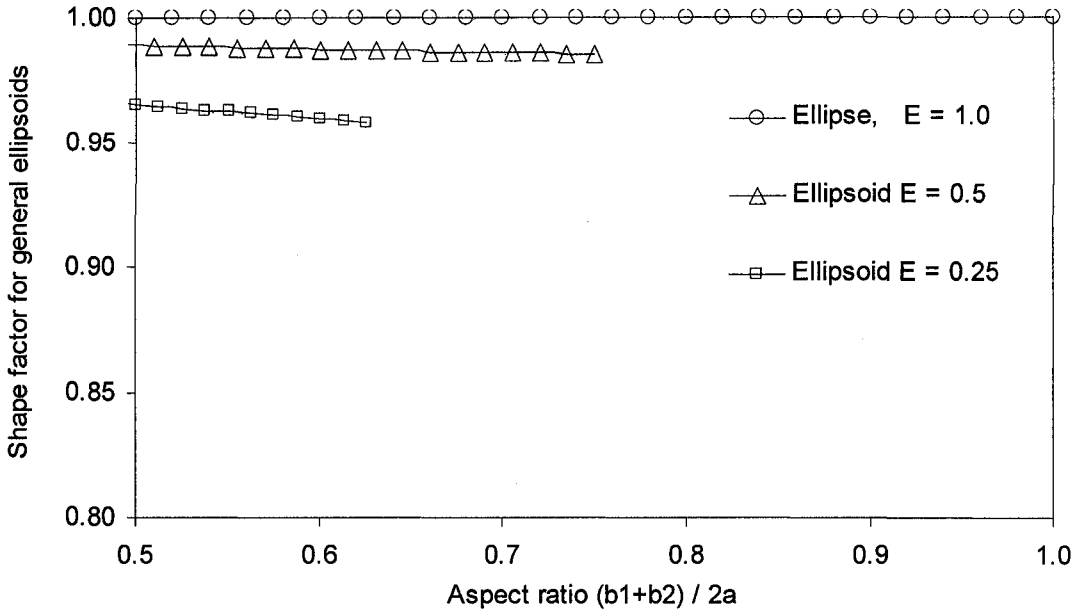

Figure 3.21: Global shape for ellipsoids

As can be seen (Figure 3.21), for ellipsoids the global shape factor is constant regardless of object aspect ratio, and for an object with an E ratio at least 0.25, the criterion which selects all the ellipsoids is 0.95. Applying this model to Figure 3.15, a global shape factor of 0.97 can identify all single bubbles, but the overlapping circles present a global SF factor of 0.99 and cannot be rejected.

Calculations rely on image property measurements, but since objects are represented by square pixels, some bias is present when the object perimeter is measured and thus, it is necessary to develop de-pixelation correction models.

3.2.6- de-pixelation correction for bubble perimeter calculation

Imaged bubbles are represented by square pixels, and geometric property measurements are thus derived from an object with sharp edges (Figure 3.12, binary images). This characteristic makes a disk of actual shape factor 1 appear to have a shape factor of 0.88 (using Empix image processing software). Although this issue has been noted by different researchers (Bailey, 2004; Hernández-Aguilar, 2005), no fundamental analysis has been conducted to correct for sharp edged objects, namely de-pixelation correction. The deviation here is a result of the approximation of the perimeter for an object with sharp edges, which depends on the algorithm used by the image processing software. For example, Matlab measures the Euclidean distance between centers of the external pixels and corners are considered diagonals. Consequently, a 5 pixel diameter circle is 15.71 pixels in perimeter. In contrast, Matlab measures a perimeter of 13.65 pixels i.e., a 13% deviation, because it assumes 4 borders of 2 pixels and 4 corners of $\sqrt{2}$ pixels (12% error).

In general, most of the measurements used in image processing software (area object, major axis, minor axis, convex area, Féret diameters, eccentricity, and orientation) are standard and are reproducible by different image processing software, but perimeter is approximated assuming different models. In Figure 3.22, perimeter calculations of known dimension objects using four image processing software are compared. Results show an underestimation, in all cases of at least 5% relative to true object dimensions.

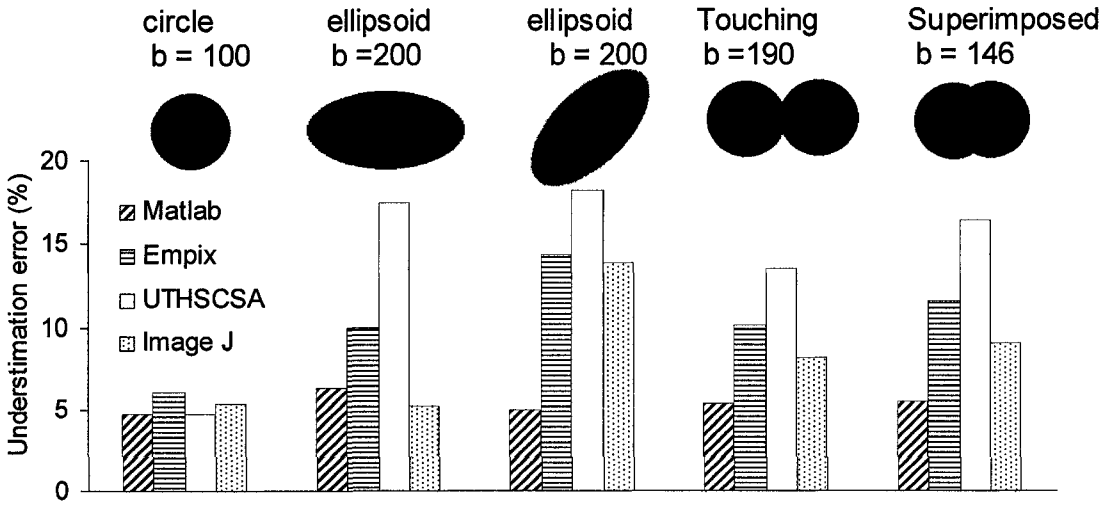

Figure 3.22: Perimeter underestimation using image processing software

The lowest bias (5%) is obtained using Matlab for circles. This bias of 5% is propagated to 10.1% bias once shape factor is calculated, as shown in Figure 3.23 for a set of standard images created using binary matrices. To compare the values with bubble size data, pixel size is set to 28.5 μm (35 pixels/mm).

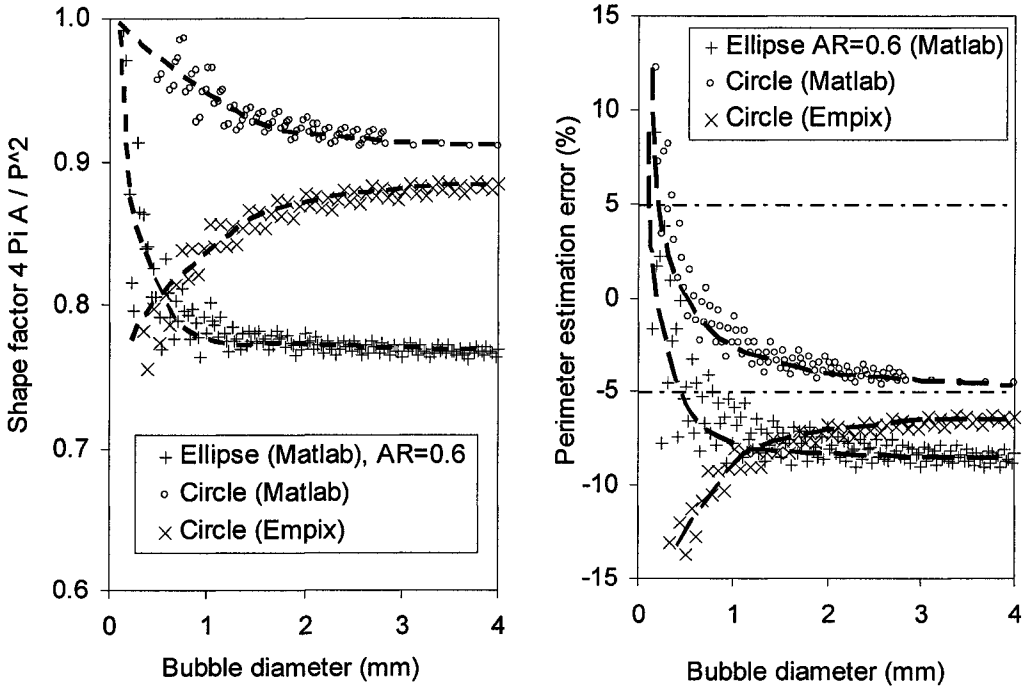

Figure 3.23: Shape factor and perimeter bias for pixelation effect

From Figure 3.23, it can be observed that the bias increases as the object aspect ratio is reduced. Thus, It is necessary to develop a model to correct perimeter measurements, depending on object properties (major axis, minor axis and perimeter measured), and image-processing software used. For this work, a fitting model was adjusted to correct perimeter calculations from standard images of ellipsoids with aspect ratio from 0.5 to 1, and object size from 10 to 300 pixels. The results and the model (Equation 3.5) proposed are shown in Figure 3.24.

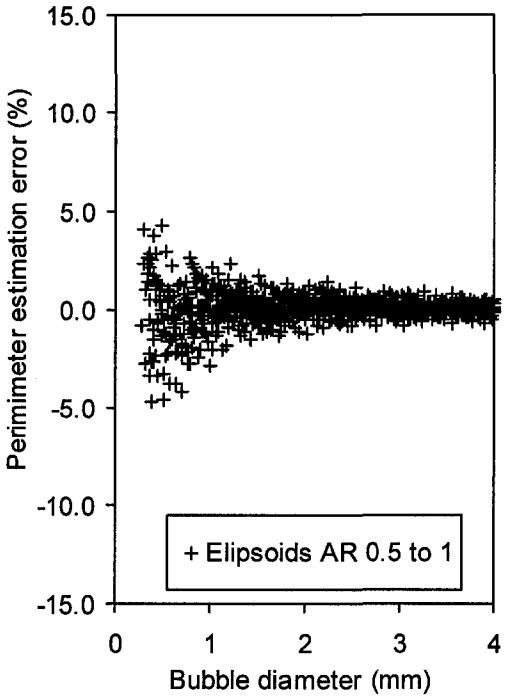

$$P_{corrected} = P_{\substack{measured \\ Matlab}} \cdot \left(\frac{\Phi(AR)}{d^{1.33}} + \Theta(AR) \right) \qquad \text{(Eq. 3.5)}$$

$$\Phi(AR) = 1.67 + 1.36 \cdot AR$$

$$\Theta(AR) = 0.91 - 0.034 \cdot AR + 0.071 \cdot AR^2$$

$$d = \sqrt[3]{a_{Major\_axis}^2 \cdot b_{Minor\_axis}} \qquad \text{(Eq. 3.6)}$$

Where, d corresponds to the equivalent volume (oblate) diameter in pixels

Figure 3.24: Proposed model to correct pixelation effect

Comparing Figures 3.24 and 3.23, it is evident that there is a significant improvement in the accuracy of perimeter estimation from bubble images. In consequence, the precision of identifying single bubbles of ellipsoidal shape, using the general model for shape factor (Equation 3.4), is also enhanced. However, rejected bubbles, mostly bubble clusters, may still affect the accuracy and limit the number of objects tracked. Therefore it is required to develop algorithms to separate and measure single bubbles from a bubble cluster.

3.2.7- bubble cluster separation

For the accepted bubbles, i.e., isolated elliptical objects, the equivalent oblate spheroid diameter is calculated. The resulting diameters are classified in size ranges (bins), and their frequency distribution is plotted as a histogram. An example of selected bubbles (in white) is shown in Figure 3.25(a) and the corresponding number frequency histogram is shown in Figure 3.25b. The Figure shows a bias to smaller sizes because clusters are not counted (they are rejected objects).

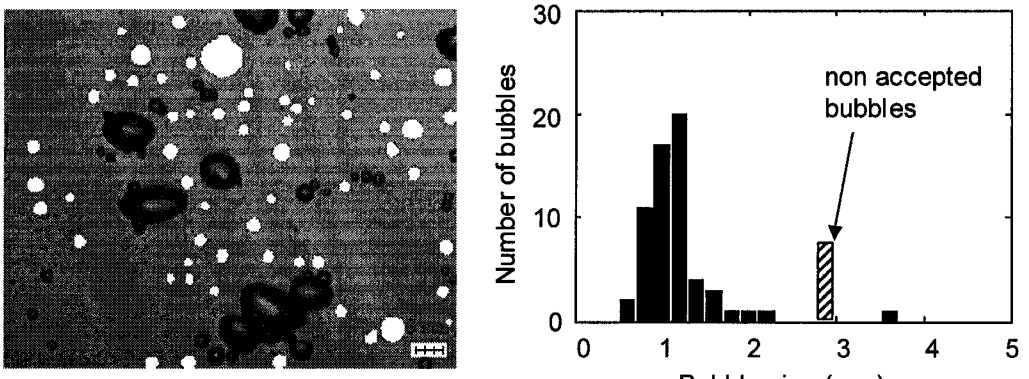

(a) Accepted bubbles in white

(b) Frequency number histogram

Figure 3.25: Selected bubbles and frequency number distribution

Commonly, up to only 30% of the total area of a picture containing bubbles (individual or bubble clusters) is used to measure bubble size, and in some conditions (small bubbles and high air flow rate) as little as 2% of the area is accepted as isolated bubbles. This condition occurring in a sequence of images affects the accuracy of the measurements, and requires a large number of pictures to have enough bubbles to create a repeatable distribution. (Note, simply counting more bubbles does not solve the accuracy problem.) In some cases, regardless of the number of bubbles counted, a significant bias can be produced (e.g., 30% error on the mean value), particularly if the total area of bubbles accepted in a picture is below 10%, as will be demonstrated later (section 3.2.8). An example of the percentage of bubble area accepted is shown in Figure 3.26.

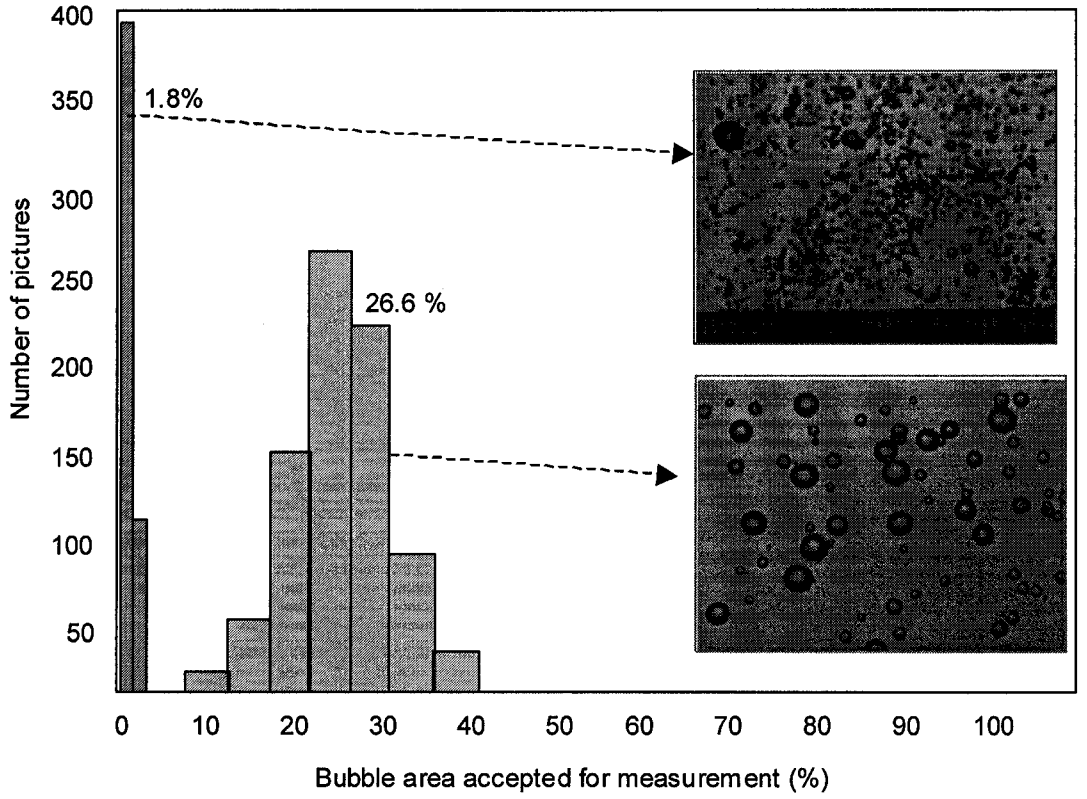

Figure 3.26: Area fraction of bubbles accepted using isolated bubbles

The problems discussed above make image analysis a crucial aspect in the bubble size measurement technique (Gomez et al., 2006), and for current purposes make it difficult to track bubbles in a sequence of images. To tackle some of these difficulties, an enhanced image analysis technique is developed, based on watershed and local thresholding.

Objects not identified as single bubbles, i.e., rejected blobs, correspond to touching or too-close objects (neighbor bubbles), as Figure 3.27 shows in a 3D intensity representation of a selection from Figure 3.4 (a).

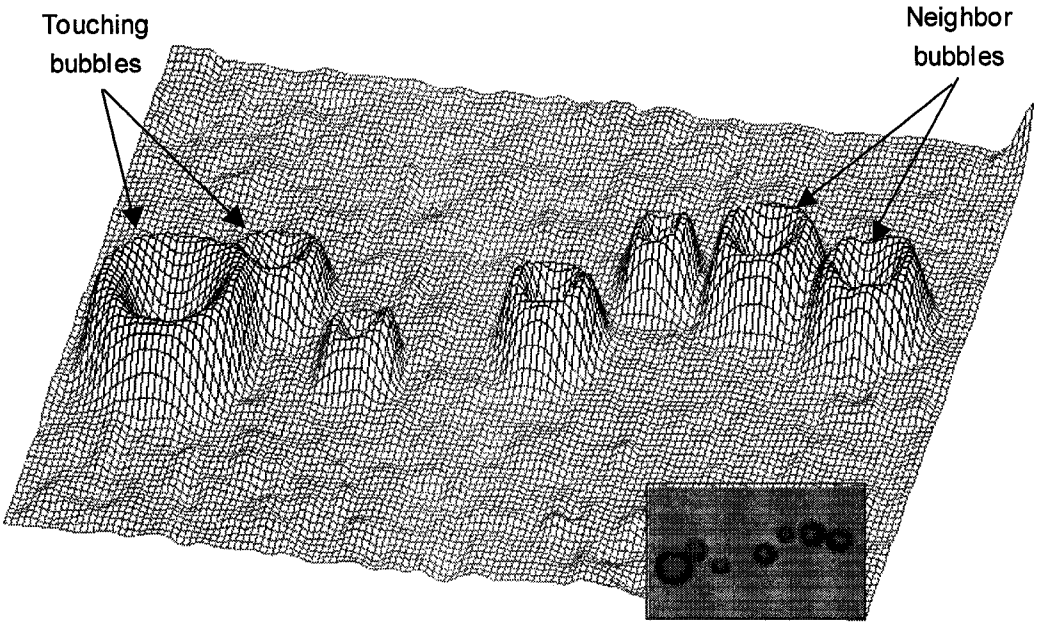

Figure 3.27 Intensity image showing touching and neighbor bubbles

Neighbor bubbles (Figure 3.27), which are not connected in the top part, can be separated using a local threshold. Otherwise, neighbor bubbles can be de-clustered using a watershed algorithm (Acharya and Ray, 2005) and distance transform (Petrou and Bosdogianni, 1999) algorithms. These routines were originally developed for geographical information systems (GIS), and were used to predict water flow in a given topology. In analogy to the situation with mountains and valleys, the technique can be used to identify the more probable border of the object in which "water" can flow. As a result, clusters can be separated.

Once the image has been compensated for uneven light distribution (Figure 3.3), the automatic threshold value has been determined using the Calzado-Acuna algorithm (3.2.1), segmentation performed (3.3.2) and data structure has been created (3.2.4), isolated ellipsoids are identified using the general shape factor criteria. An example of bubbles collected in a flotation system is shown in Figure 3.28 (a), and the selected isolated ellipsoids are drawn in black, Figure 3.28 (b). The remaining non-accepted blobs are processed with a local thresholding, de-clustering some neighbor bubbles. Results are shown in black in Figure 3.28 (c), with the previously isolated

ellipsoids in grey. A new image is created subtracting Figure 3.28(c) from the original image. After applying a filter and removing skeleton objects (lines), segmentation produces isolated bubbles and clusters. A distance transform is applied to each cluster converting a binary matrix into a distance matrix, where a watershed algorithm is applied to separate bubble clusters. The results of this process are shown in black in Figure 3.28 (d), with all previously accepted objects drawn in grey. The procedure is repeated for a sequence of images. The number of bubbles recovered is often double the original number of isolated bubbles, depending on the image characteristics.

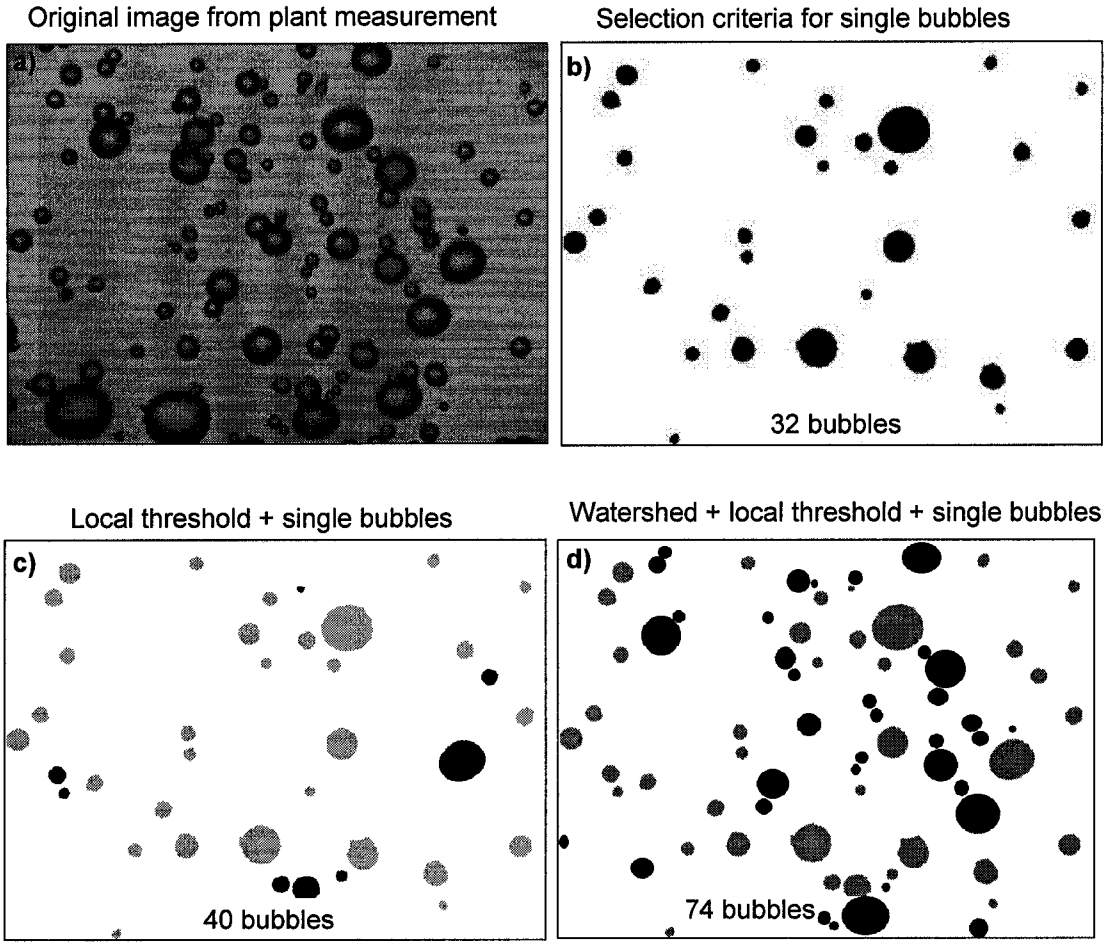

Figure 3.28: Image de-clustering example

The number of bubbles detected can be used as a benchmark parameter. However, this indicator only allows algorithms to be compared, and it does not reflect the

efficiency of isolating bubbles. To evaluate the efficiency to isolate bubbles from a picture containing bubble clusters, it is proposed to use the area fraction of "detected bubbles" relative to the total area of bubbles. In Figure 3.29, the area fraction is 72%, a high efficiency of detecting and isolating bubbles.

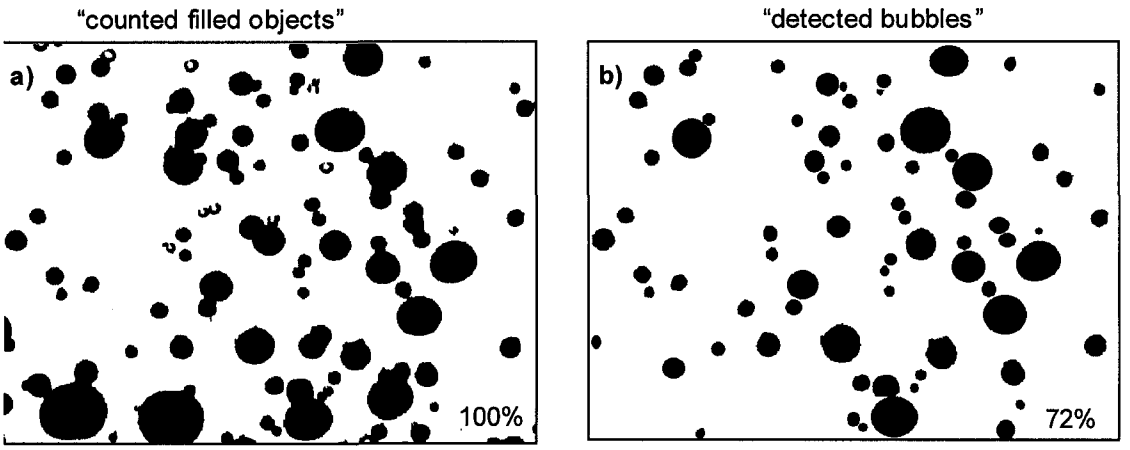

Figure 3.29: Area fraction of detected bubbles

The efficiency to isolate bubbles using the novel algorithms developed is evaluated with image sequences collected in five concentrators in the following section.

3.2.8- enhanced algorithm benchmarking and validation

A comparison of the new techniques developed for bubble isolation is shown in Figure 3.30. The techniques are illustrated on images with a sudden variation in light intensity (Figure 3.7, continuous line). The moving average of 30 pictures of the area fraction of detected bubbles, as the algorithms are added gives the following:

1- Isolated bubbles that match shape factor for ellipsoidal bubbles: 22% accepted.
2- Local threshold on remaining image (objects accepted in 1 are removed): 7% more area isolated. (This algorithm is unaffected by temporal and spatial changes in intensity.)
3- Distance transform and watershed on remaining image (objects accepted in 1 and 2 are removed); 28% more area converted into isolated bubbles.
4- Three algorithms combined: total average area fraction accepted is 57%.

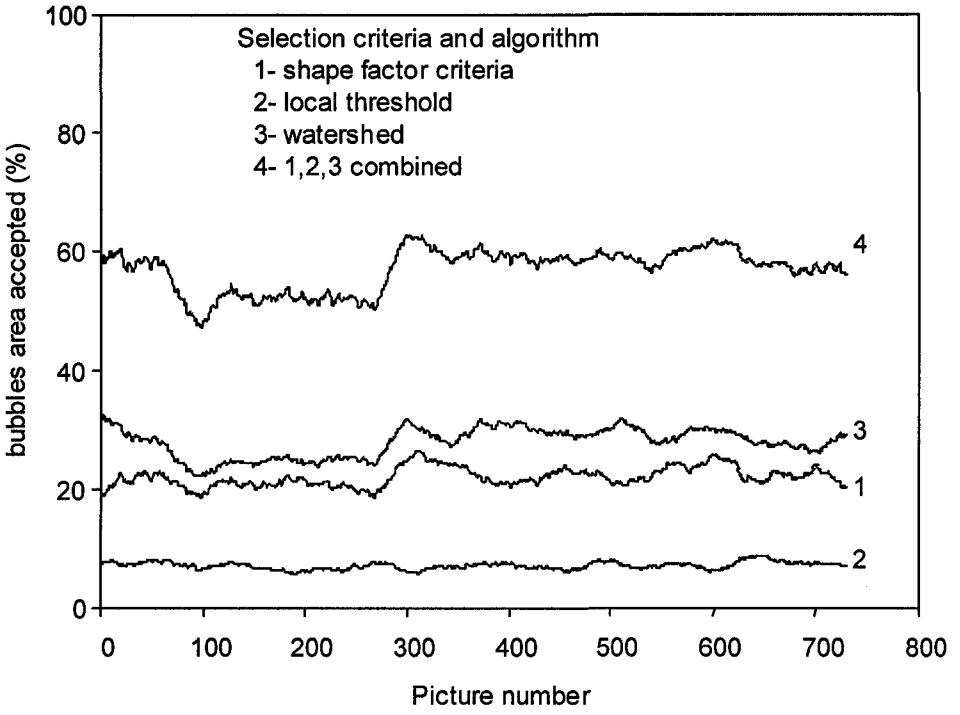

Figure 3.30: Bubble area acceptance (moving average 30 pictures)

Although the average area detected increases from 22% (Figure 3.30, line 1) to 57% (Figure 3.30, line 4), and number of bubbles increase by 230%, there is no significant variation in the mean bubble size (D_{10}) and the Sauter diameter (D_{32}). The mean bubble size diameter has an error of 5.5% comparing routine 1 with 4, while the Sauter diameter error is 4.3%. However, the error on D_{10} may become significant if the detected area is lower than about 10%, as shown in selected tests in Figure 3.21a. Note again that the number of bubbles counted is not related with the measurement accuracy (Figure 3.31b).

To establish the minimum acceptable area fraction of bubbles in a picture to give at the most 5% error on D_{10}, a sampling simulation is conducted for two bubble size distributions, shown in Figure 3.32

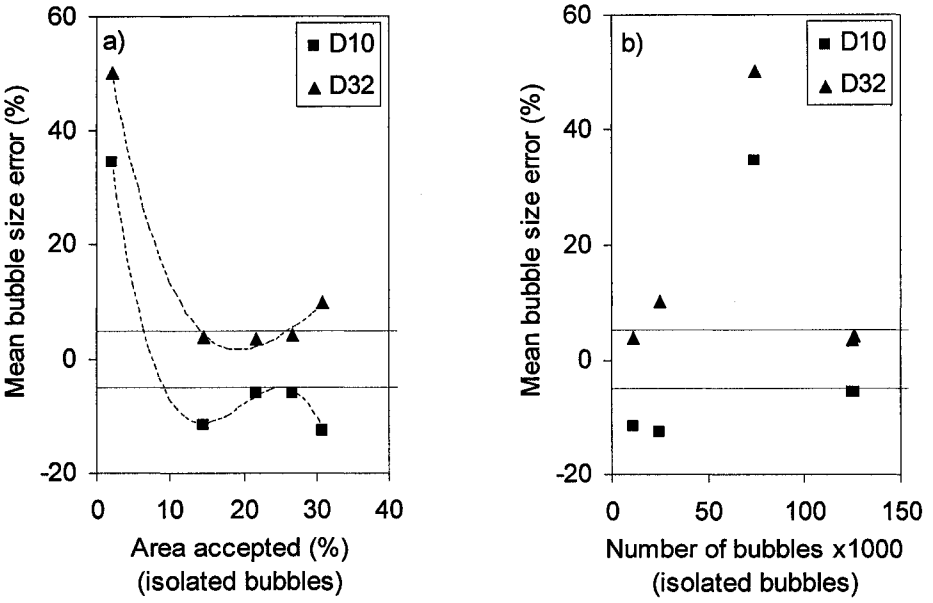

Figure 3.31: Bias measurement in five selected plant test measurements

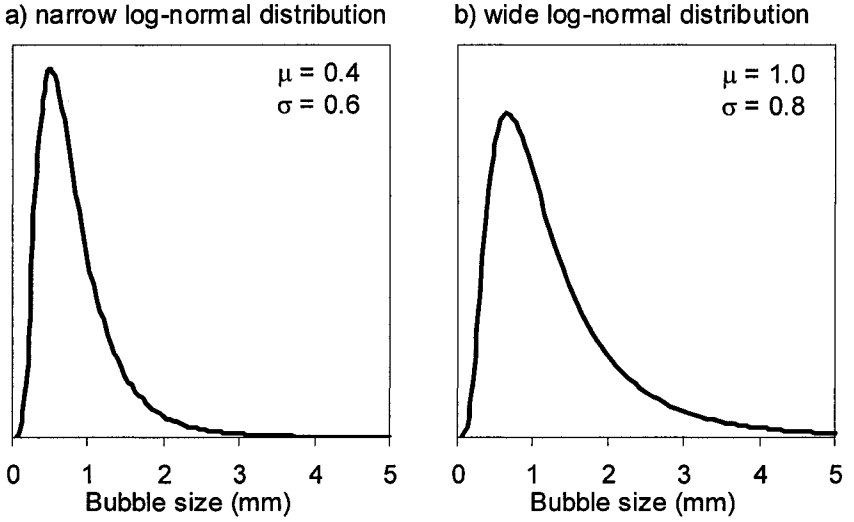

Figure 3.32 Simulated bubble size distributions

To simulate bubble detection, a set of 30 pictures containing 150 bubble diameters is created randomly using a log normal distribution. A random sample of n bubbles is taken for each picture until a given bubble area fraction of the original 150 bubbles is achieved. The given area fraction covered the range from 0.2% to 98%. As a result, an average D_{10} for 30 pictures is obtained and compared with that for the original 150 bubbles (the true D_{10}) to give a D_{10} error. The D_{10} error and standard deviation as a function of the bubble area fraction selected is shown in Figure 3.33.

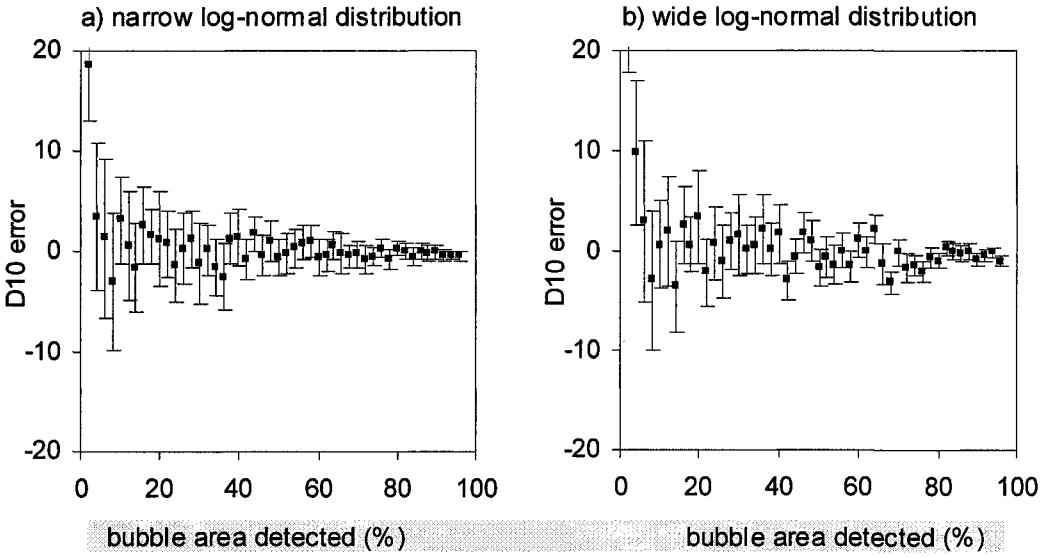

Figure 3.33: Effect of bubble area fraction sampled on D_{10} accuracy

The minimum area required to obtain 5% error in D_{10}, using a narrow distribution (Figure 3.32a), is 40%, while for a wide distribution (Figure 3.32b) it is 60%. Therefore, at least 40% of bubble area is the target to have an accurate measurement of D_{10}.

Comparing the 40% area criterion with previous measurements of bubble size distribution (over 480 flotation machines) using the McGill bubble sizing technique reveals that 35% of the tests are in the acceptable range (≥40%), Figure 3.34.

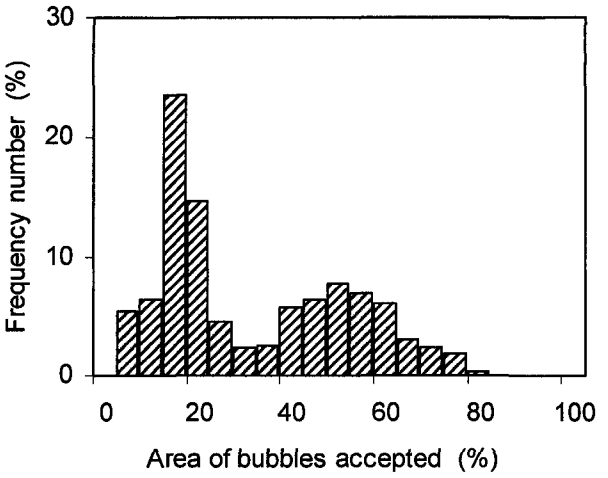

Figure 3.34: Frequency distribution of average bubble area detected from 480 tests on individual flotation cells.

For the present task, the routines and algorithms developed, namely: illumination background compensation, automatic masking removal, automatic thresholding (Calzado-Acuna), particle and noise removal, object perimeter correction, ellipsoidal shape factor measurement, local thresholding and watershed de-clustering, are applied to a sequence of images to construct the data structure (Figure 3.13). The data structure is used to:

1. Track an individual bubble in a picture sequence
2. Construct bubble trajectory in time
3. Compute individual bubble velocity and bubble velocity-size profile
4. Compute bubble size distribution
5. Measure inter-bubble distance and compute volumetric fraction of bubbles

3.3- Tracking of multiple moving objects technique

Bubbles are tracked in image sequences, using the data structure described in Figure 3.13, and a matching criterion based on object geometric properties. To match the same object in consecutive pictures, an incidence value (measurement of similitude) is computed for one selected object in the first picture relative to all objects in the second picture. An example of this procedure is shown in Figure 3.35. In this case, one bubble is selected, the "target bubble", and the incidence value is calculated for the six possible target bubbles in the next image. Given a tolerance value (e.g., 95%), candidate-matching bubbles above the tolerance value are selected. In this case, there are two candidates. The minimum bubble displacement (i.e., object centroid distance of the superimposed images containing the target bubble and the candidate bubbles) is used as a second criterion to select the matching object. In this case the smaller displacement was for the bubble of similitude 98%.

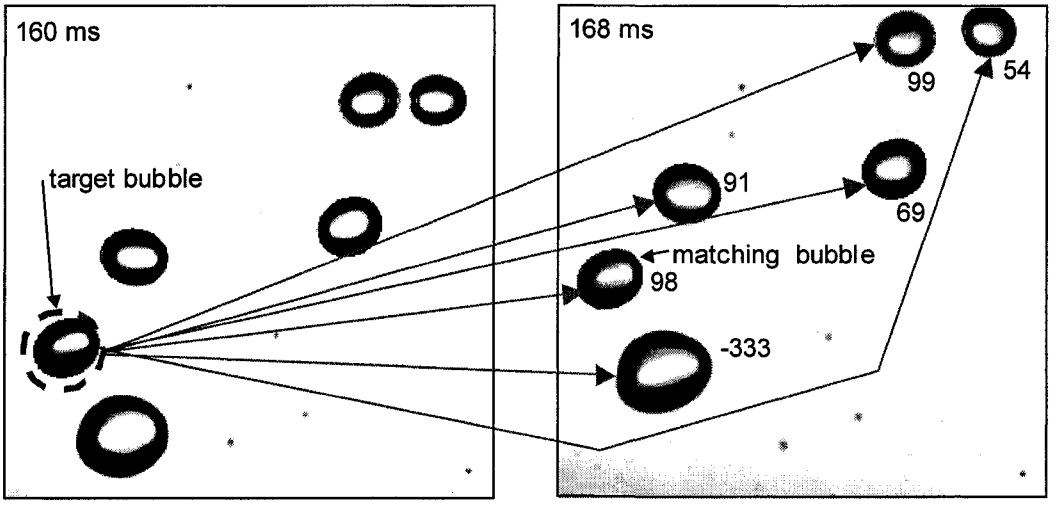

Figure 3.35: Incidence value for two consecutive images.
(Test #69: pictures 160 and 168 ms)

To "visualize" the matching criteria, bubble displacement and incidence values are plotted in Figure 3.36, for the target bubble in Figure 3.35.

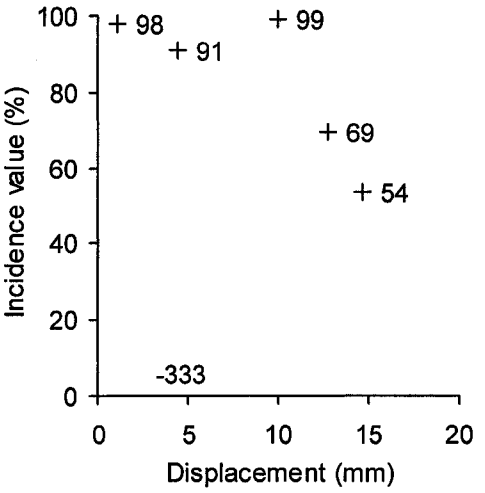

Figure 3.36: Incidence value and displacement for matching bubbles.

To compute the incidence value and later the incidence matrix (Corman et al., 2001), a relationship to measure object similitude (the incidence value function) is proposed. The equation is based on the major axis (a), minor axis (b) and total filled object area (A), (Equation 3.7), and the function is calculated for the target bubble "k" in the picture "j", and bubble "i" in picture "j+1",

$$\psi(j,k,i) = 1 - \left| 1 - \frac{1}{4}\left(\left(\frac{\mathbf{a}\{j,k\}}{\mathbf{a}\{j+1,i\}} \right)^3 + \left(\frac{\mathbf{b}\{j,k\}}{\mathbf{b}\{j+1,i\}} \right)^3 + 2 \cdot \left(\frac{\mathbf{A}\{j,k\}}{\mathbf{A}\{j+1,i\}} \right)^3 \right) \right| \qquad (3.7)$$

This function seems to be suitable for discriminating ellipsoidal objects, and is the result of a series of model evaluations, combining geometric parameters (e.g., perimeter, equivalent diameter). To evaluate the function's ability to discriminate ellipsoids, three target bubbles of aspect ratio 0.5, 0.8 and 1 are compared with ellipsoids of the same major axis but with variable minor axis (aspect ratio varies), as shown in Figure 3.37. The results show that above 95% tolerance value all target bubbles can be matched with the corresponding equivalent bubble geometry.

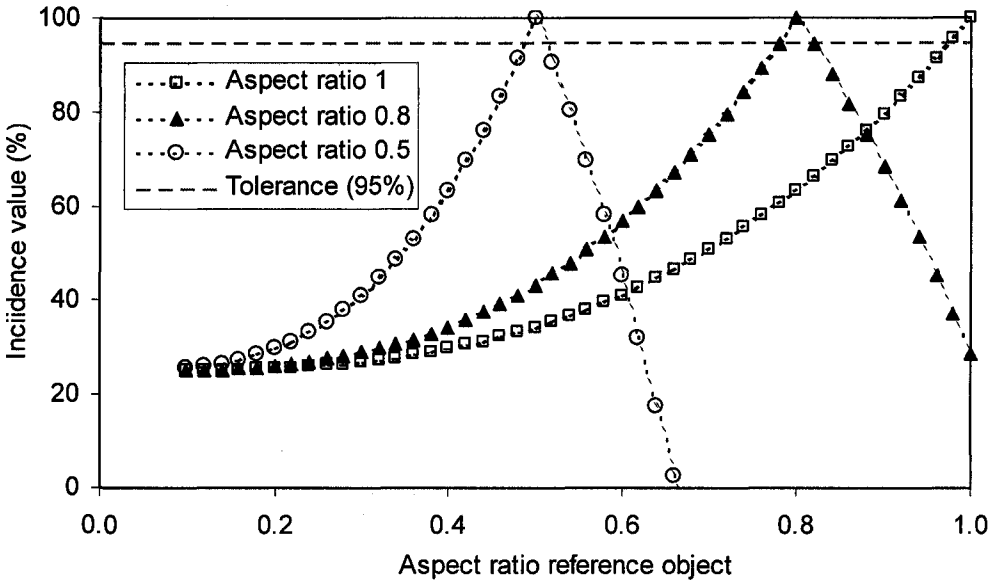

Figure 3.37: Incidence value comparison for ellipsoids

In the case of a large number of bubbles of similar geometry (e.g., aspect ratio 1), the technique is sensitive enough to track a single object, as shown in Figure 3.38. For the target bubble indicated in Figure 3.38 (left) incidence and displacement values are calculated, from which only one object can be selected, indicated by the arrow (right), which is the closest candidate bubble (shortest displacement) with acceptable incidence value (> 95%).

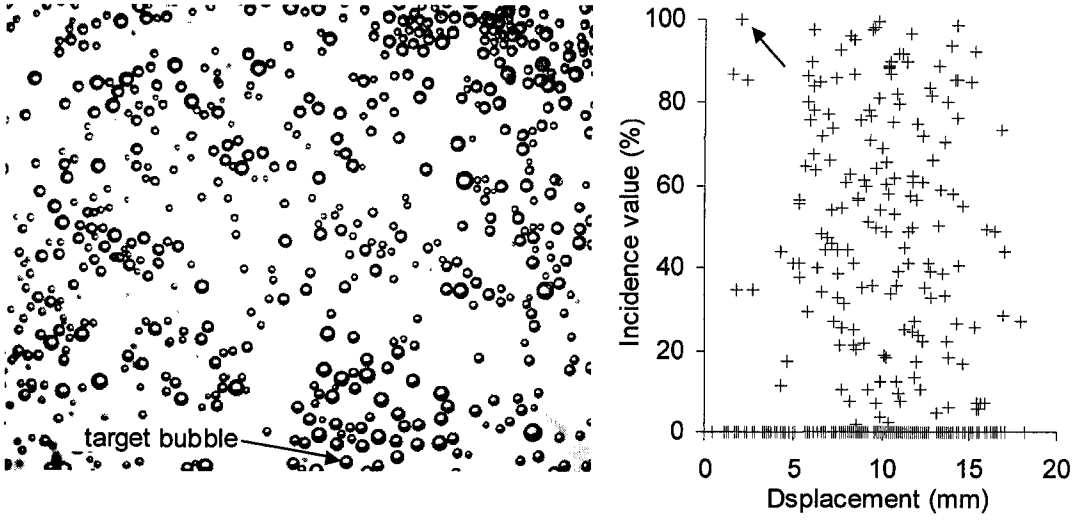

Figure 3.38: Incidence value and bubble for two consecutive images.
(Test #64: pictures 52 ms)

The incidence values and bubble displacement are computed for each bubble in the first picture with all the bubbles in the second of consecutive pictures. Selecting the candidate bubbles, a bubble indices pair or "marriage objects" is obtained, which references the bubble number in the two pictures. The procedure is repeated for every target bubble and repeated for every sequence of image pairs (1 to n-1). These references are added to the data structure, which is used to construct bubble trajectories (section 3.4).

The technique depends on picture resolution and frame rate. Picture resolution determines the precision to evaluate the incidence value (Equation 3.7), the higher the resolution the higher the precision, while the frame rate determines the minimum object displacement. From experimental evidence, it has been determined that to maximize the number of matching bubbles, the object displacement in two consecutive images must be least 0.25 bubble diameter and at the most 1 bubble diameter. This means, for example, a bubble of 1.4 mm (moving at ~35 cm/s) requires a sampling interval of 2 to 4 ms (250 to 500 frames per second).

In some cases, when bubbles are unstable in shape (wobbling bubbles, which are normally larger bubbles (Appendix 1, Figure A1.2)) tracking requires the tolerance parameter to be reduced but still some bubbles cannot be identified and tracked. Figure 3.39 shows changes in incidence value for a wobbling bubble, which was "marked" manually with a specific color. It was followed successfully by the algorithm over most of the time interval.

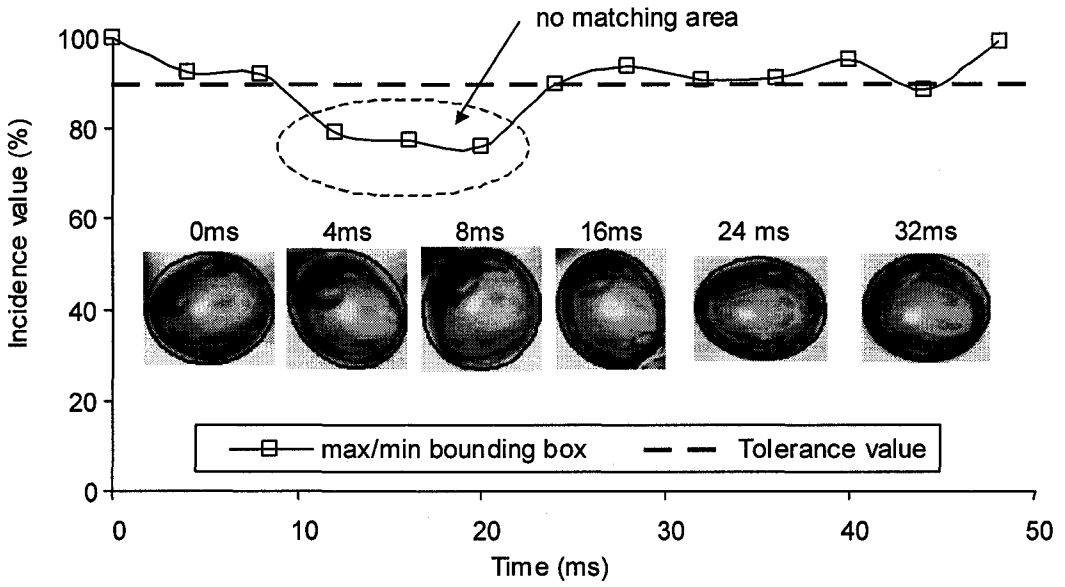

Figure 3.39: Changes in incidence value for wobbling object tracked manually

Normally, 400 to 1000 pictures are collected per test (250 to 1000 frames per second) and the number of matching bubbles varies from 300 to 60,000, which appears to be sufficient to generate bubble velocity vs. size data and construct bubble trajectories. To create a bubble velocity-size profile, bubble velocities (vertical, horizontal and trajectory) are classified in bubble size bin classes. If the bin contains at least 5 elements, mean bubble velocity and 95% confidence interval are calculated (Appendix 2, Table A1.2). Bubble velocity trajectory is constructed from the data structure, which contains indices for matching bubbles in consecutive frames (section 3.4). These new parameters are added to the data structure. An example of bubble velocity (vertical velocity) as a function of bubble diameter, and number of matching bubbles detected is illustrated for two tests in Figure 3.40. As a reference, single bubble velocity is also plotted for distilled water and "contaminated" water (Clift et al., 2005).

Bubble images for both tests were collected in the rectangular column, in which air was injected into tap water containing 0.14 mmol of Polyglycol. The column and sparger descriptions are presented in section 3.5.

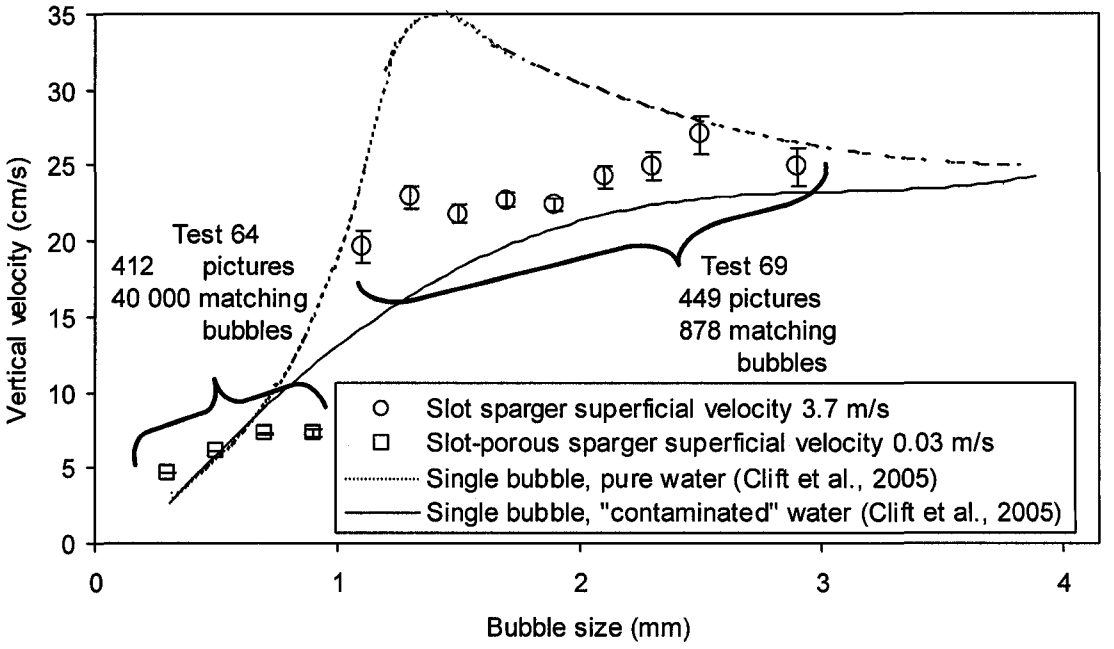

Figure 3.40: Bubble velocity-size profile for two bubble size distributions (Tests #64 and #69)

The tests (in Figure 3.40) correspond to bubble size distributions generated by a slot-porous sparger (a sample picture is shown in Figure 3.38, Test 64), and by a narrow slot sparger (two sample pictures are shown in Figure 3.35, Test 69). Bubble size distributions, for the two cases, are shown in Figure 3.41.

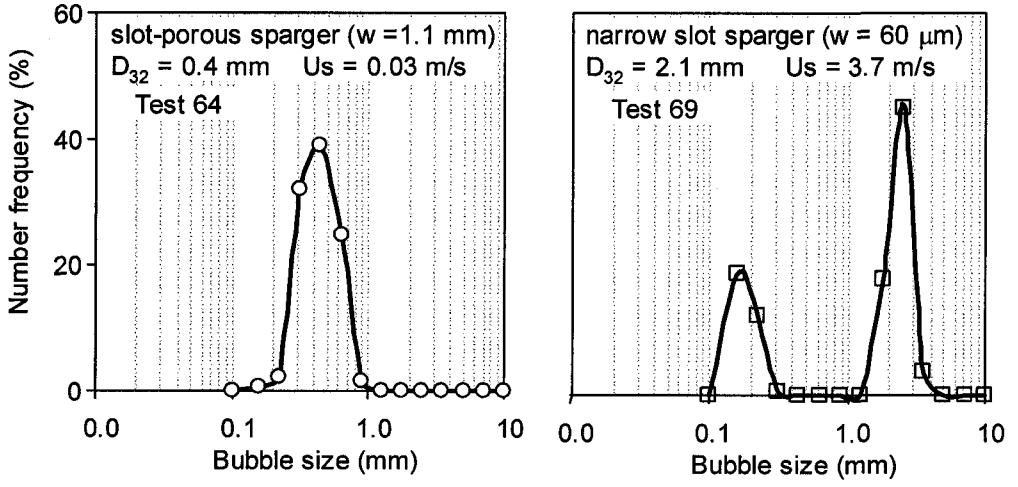

Figure 3.41: Bubble size distribution corresponding to Figure 3.40

The bubble images generated by the slot-porous sparger (section 3.5) have 40,000 matching bubbles with a narrow size distribution, while the slot sparger produced 878 bubbles in a wider (bi-modal) distribution. The average 95% confidence interval on the velocity for the latter test is 0.3 cm/s, which in considered acceptable.

To evaluate the reproducibility of the bubble tracking algorithms, bubble velocity-size profiles were measured using a set of images sampled at different intervals; that is, the same experiment but selected pictures are analyzed. These results (Figure 3.42) show no significant difference for the bubble velocity-size profile measurements; but, as expected, if the frame interval is above 4 ms, significant deviation can be found.

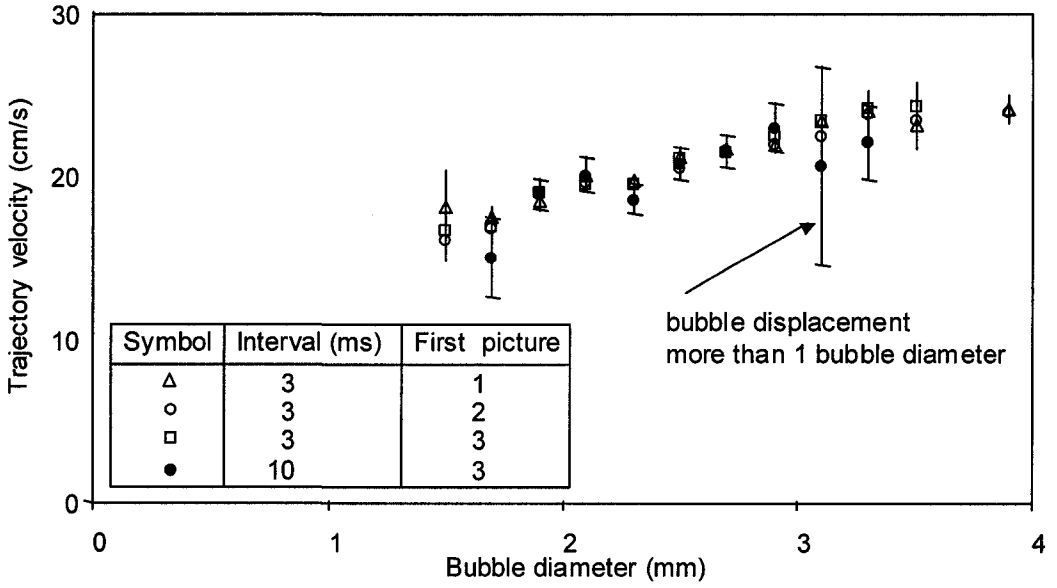

Figure 3.42: Repeat measurements of bubble velocity-size profiles (Test #12)

3.4- Bubble trajectory reconstruction technique

Using the data structure shown in Figure 3.13, and the matching bubble pairs (described in section 3.3), a new data structure is created for each continuous sequence of matching objects (connected bubbles in an image sequence). An example of the values contained in a sequence for a bubble in consecutive pictures, which has 6 matching bubbles (5 bubble pairs), is shown in Table 3. 3.

Table 3.3: Data structure for a sequence of matching bubbles

Parameter	Description	Values for six bubble sequence
x (mm)	Centroid coordinate X	[5.7 5.5 5.4 5.2 5 4.8 4.6 4.4 4.1 3.9 3.7]
y (mm)	Centroid coordinate Y	[2 3 4.1 5.2 6.3 7.5 8.7 9.9 11.1 12.3 13.5]
a (mm)	Minor object radius	[1.5 1.5 1.5 1.4 1.4 1.4 1.4 1.4 1.4 1.4 1.4]
b (mm)	Major object radius	[1.6 1.6 1.7 1.7 1.7 1.7 1.7 1.7 1.7 1.6 1.6]
ms	Elapsed time, ms	[160 164 168 172 176 180 184 188 192 196 200]
pic	Picture number	[38 39 40 41 42 43 44 45 46 47 48]
objn	object index	[2 2 2 2 2 2 2 2 1 1 1]
sim	Incidence value	[97 97 99 99 99 99 96 96 95 99 0]
proximity	Relative displacement	[0.7 0.8 0.8 0.8 0.8 0.8 0.9 0.9 0.9 0.9 0]

(Test #69, sequence 26)

Once the picture number and the object number are identified, bubble trajectory reconstruction is trivial, as shown for a sequence of 10 matching objects for 5 pictures at an interval of 8 ms in Figure 3.43. The parameters of bubble "A" are given in Table 3.3.

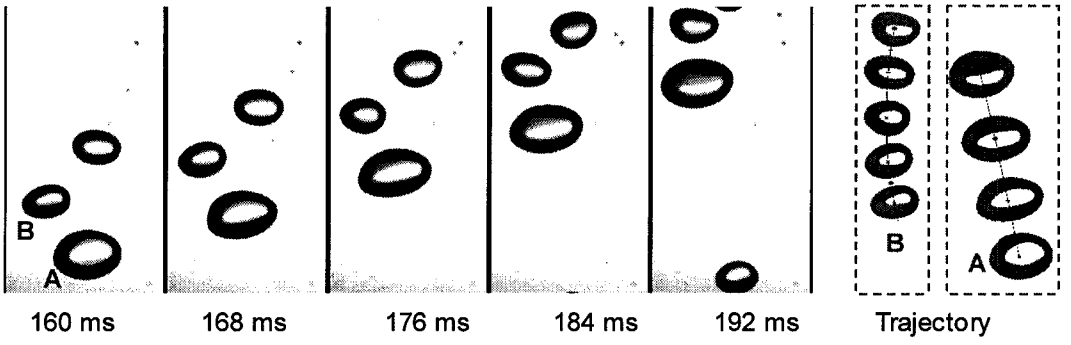

Figure 3.43: Bubble trajectory reconstruction from an image sequence

Bubble geometric properties (from the data structure) can be tracked as the trajectory is constructed, which allows the study of bubble flexing and interactions. An example is shown Figure 3.44, where bubble velocity trajectories at intervals of 4 ms for four selected objects are superimposed on an image at the corresponding time. The interaction of the smallest marked bubble with another bubble affecting its trajectory can be observed.

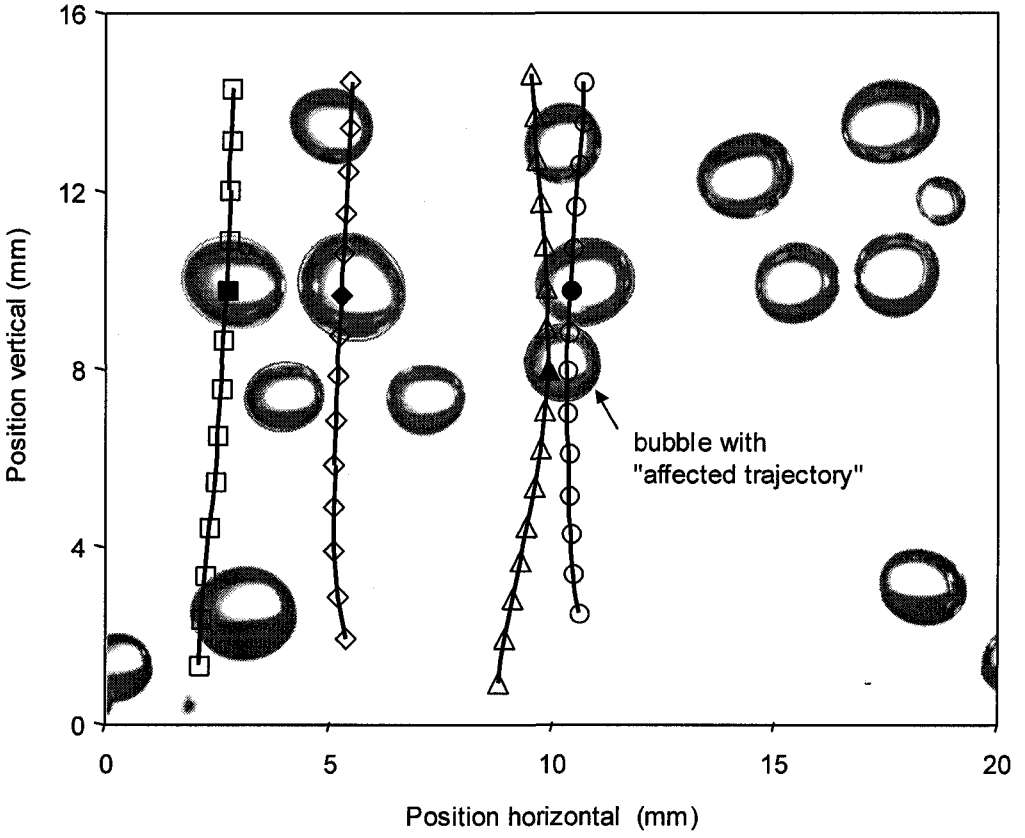

Figure 3.44: Bubble velocity trajectory mapping
(Test #69)

For a system with a large number of bubbles per picture (above 100 bubbles), to "visualize" bubble motion for an individual bubble over a specific time a mapping position plot is used, as shown in Figure 3.45, where position (horizontal or vertical) is plotted in time for all bubbles in a time frame. In this figure, the rectilinear velocities (slopes) are shown from the vertical position plot (top), and bubble oscillation along the vertical axis from the horizontal position plot (bottom); the latter most likely is the consequence of a high level of bubble interactions.

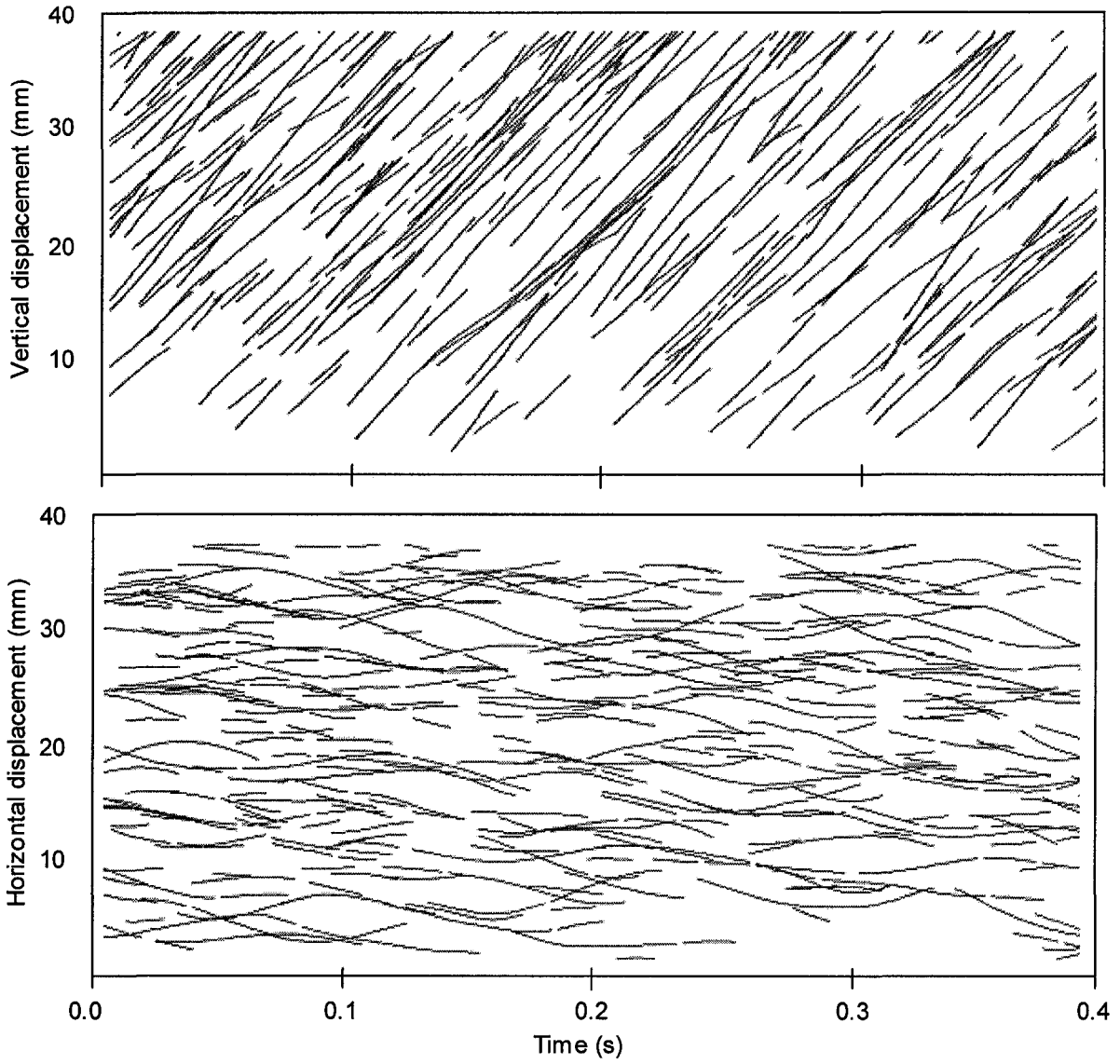

Figure 3.45: Bubble trajectory reconstruction for bubble swarms (Test #11)

In summary, the technique appears to be adequate for bubble velocity studies in bubble swarms; however, validation is required to determine its effectiveness matching the same bubble along a sequence of images.

3.4.1- bubble matching technique validation

To validate the automatic technique for bubble matching, which is the starting point for bubble trajectory reconstruction and velocity-size profile calculations, it is proposed to color mark manually selected bubbles from bubble swarm pictures. A selected bubble is tracked and marked, with the same color, in a sequence of images where the same bubble is present.

To mark a bubble in a given picture the approach is to superimpose the "best" ellipsoid and assign a specific color based on the color map vector (red, green, and blue with 8 bit spectral resolution). For example, to mark a bubble in red the color vector is (255,0,0), and for blue (0,0,255). In this form the ability to selectively mark objects can handle up to 2^{24} combinations. As a result, a color bit map picture (BMP) is generated (Mathworks Inc, 2003), which basically consists of three intensity images, each of them corresponding to colors red, green and blue. To create BMP pictures, the original grey scale images are imported to power point, using a specific Visual Basic routine created in this work (Appendix 2, Table A2.2), from where ellipsoids or other shape objects can be drawn and marked with a selected color. Once the marking process is completed, the power point sequence of images is saved as "TIF" images; this exports separate slides into individual files in BMP format (three intensity images per picture).

To identify a marked object from color pictures, a comparison with the selected color (e.g., (255,0,255)) is applied to the corresponding color intensity image. An example of bubble images, for a selected area, where four bubbles are marked (red, green, blue and magenta) is shown in Figure 3.46.

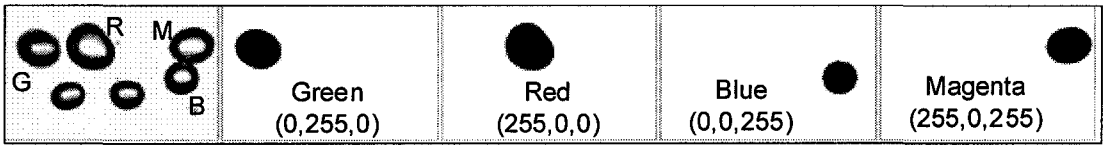

Figure 3.46: Bubble identification based on color "marking" technique

Once the selected bubbles are marked in a series of pictures, bubble identification is trivial, since there is only one object per picture for a given color. A data structure is generated for each picture and object indices are assigned for each color selected. After that, the matching bubble technique is applied and trajectories are constructed. All these operations are executed using specific Matlab routines developed for this research.

Technique validation is based on 16 bubble trajectories color marked manually (181 bubbles). The first 4 bubbles marked (b1 to b4) are shown in a sequence of 8 pictures at an interval of 8 ms (Figure 3.47), from where a visual track can be constructed.

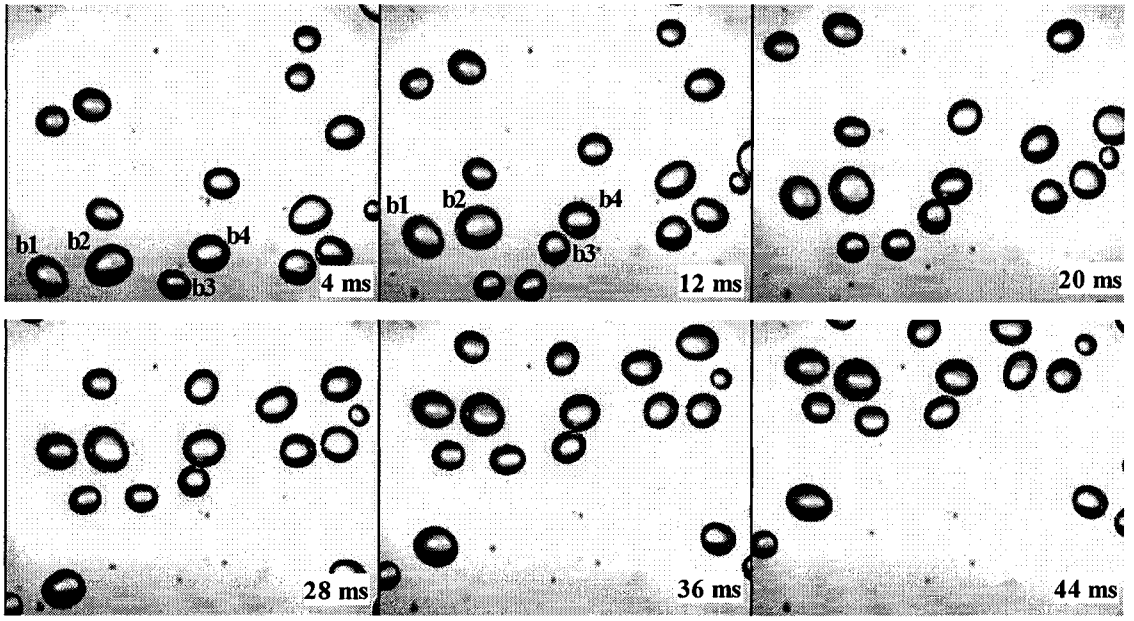

Figure 3.47: Bubble tracking using color "marking" technique

These marked bubbles (181) are identified; employing a selective marking technique, and the resultant trajectory plots are shown in Figure 3.48a. If the same images, containing marked bubbles, are converted into black and white images (binary) and the automatic matching algorithm is applied on these same objects, using a tolerance of 90% (minimum incidence value accepted, Equation 3.7), 76% of the object are detected, as shown in Figure 3.48.b.

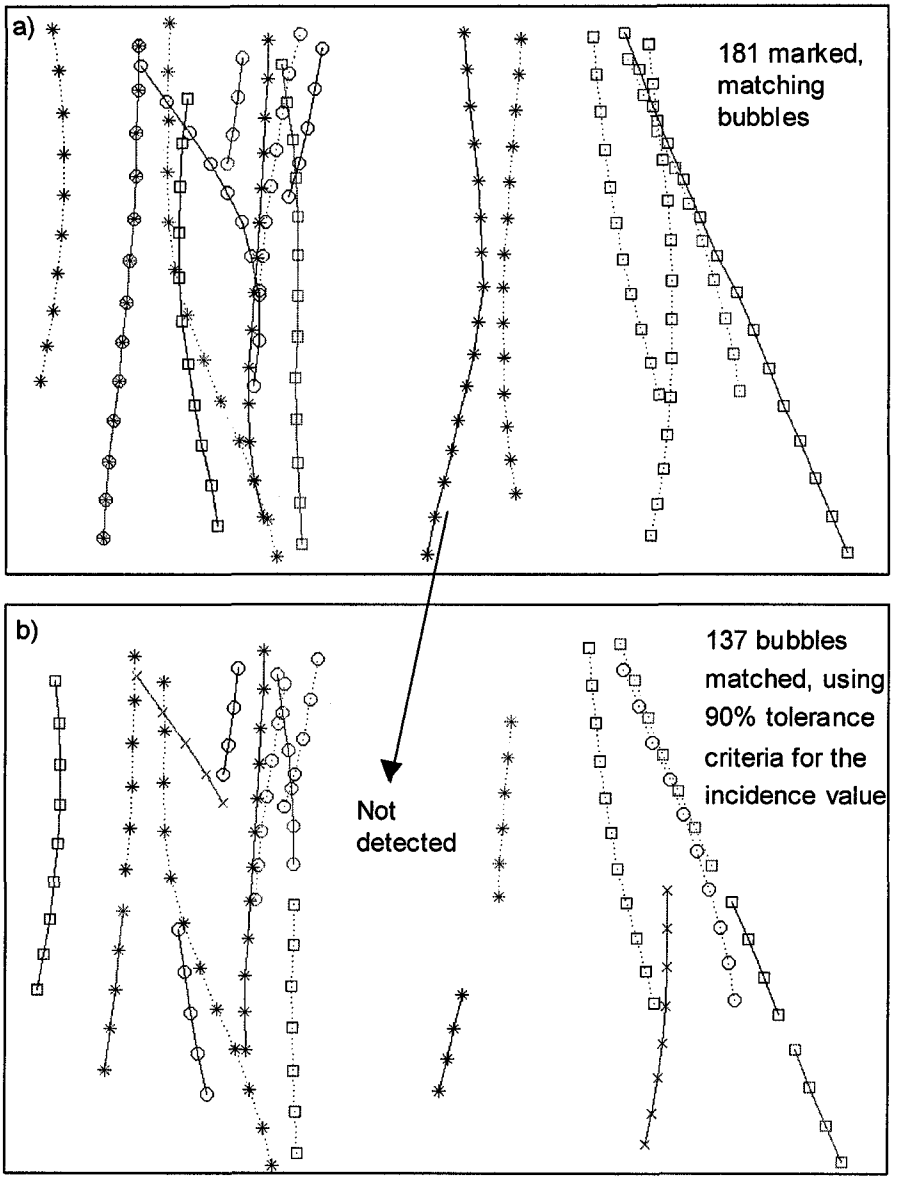

Figure 3.48: Bubble trajectory reconstruction for crowded system
a) manual selection base on color marker, b) automated technique on binary image

To increase the number of objects accepted (matching object efficiency) the tolerance value could be reduced. However, this may degrade the selectivity, especially if the bubbles are similar in size and shape or the distance inter-bubble is close to the bubble diameter; the case, for example, in Figure 3.38.

In this particular set of images, where bubbles are different in shape, and the inter-bubble distance (section 3.7) is larger than the bubble diameter, the tolerance can be reduced to increase the number of matching bubbles. This is illustrated in Figure 3.49 which shows the fraction of detected bubbles, relative to 181 (100% effectiveness), using the automatic matching bubble routines at different levels of tolerance on the black and white images generated from the pictures with color-marked bubbles.

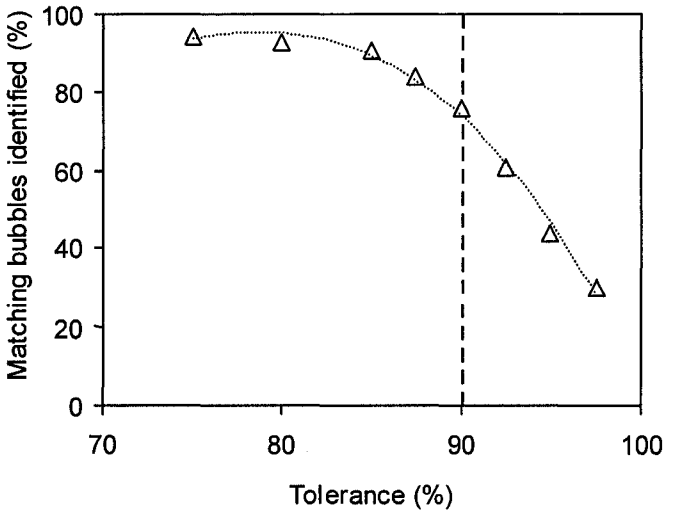

Figure 3.49: Effect of tolerance on the number of matching bubbles.

Normally, 300 to 1000 pictures are collected for bubble velocity measurements. On average, 400 trajectories are identified per test. Each trajectory contains from 5 to 80 connected bubbles. This in considered acceptable, by comparison with single bubble trajectory measurements (Tomiyama, 2002).

A new technique for measuring bubble velocity and trajectories in 2D-bubble swarms has thus been developed to aid the study of bubble motion in swarms. The imaged bubble tracking technique relies on generation of a flat bubble front, which is explained in the following section.

3.5- Generation of a flat front of bubbles

Bubble swarms are generated using narrow slot spargers (Harris et al., 2005), made of stainless steel and a slot-porous sparger (Southern and Wraith, 1990). Two devices were constructed: a single slot sparger (29 mm slot length and 90 μm average width) and a double chamber slot sparger (60 mm slot length each) assembled with one slot of 60 μm average width and the second ~1.1 mm nominal width, filled with a porous material (filter cloth) forming a slot-porous sparger. Sparger details are shown in Figure 3.50 (sparger parts and dimensions are presented in Appendix 3, Figure A3.2).

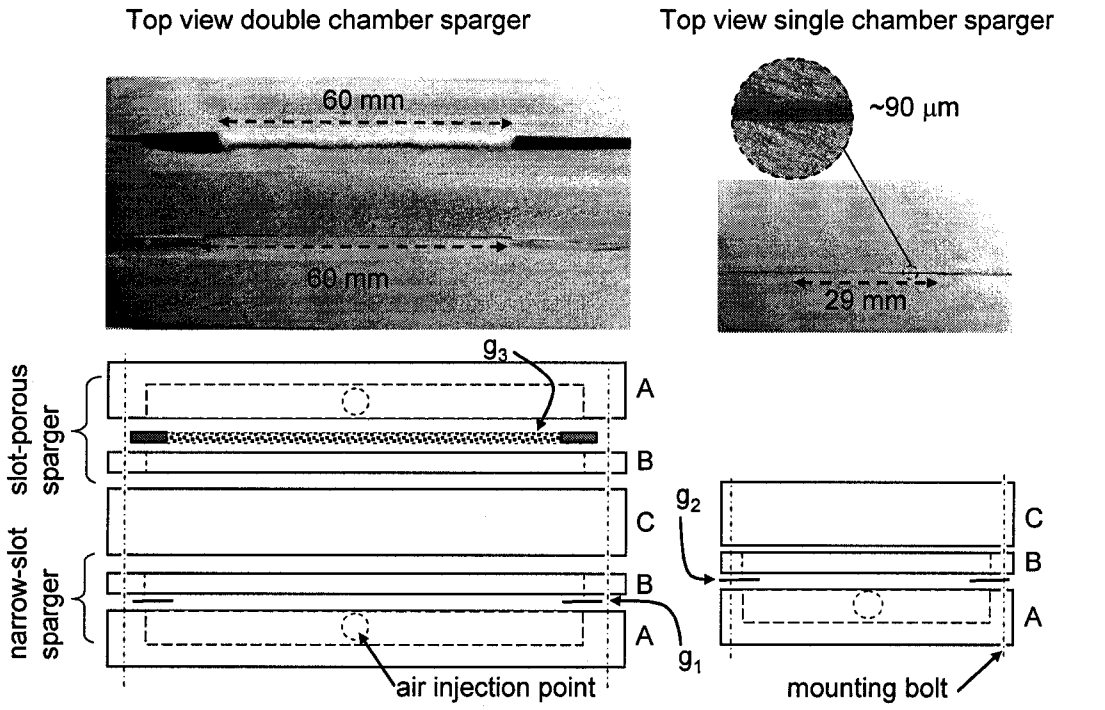

A Air injection chamber (half hollow)
B Air distribution frame (internal holow)
C Blind frame

g_1 Celluloid film (~60 μm)
g_2 Celluloid film (~90 μm)
g_3 Porous material, filter cloth (~1.1 mm)

Figure 3.50: Top view and schematic of bubble generating devices

Gas was injected independently into each sparger; gas flow rate is measured and controlled by two mass flow meters (specification Table A3.3 and calibration Figure A3.1).

The sparger combinations allow generation of various bubble size distributions, chosen to approximate those found in industrial flotation machines (Figure 1.4). For example, using the double slot sparger can create distributions as shown in Figure 3.51. The superficial gas velocity (Us), volumetric gas flow rate divided by slot nominal area, at the slot is 0.3 m/s for the porous-slot sparger and 3.7 m/s for the narrow slot sparger. The distributions were measured in a bubble column, described later (Figure 3.52), with Montreal tap water and 0.2 mmol/L of n-Pentanol as a surfactant.

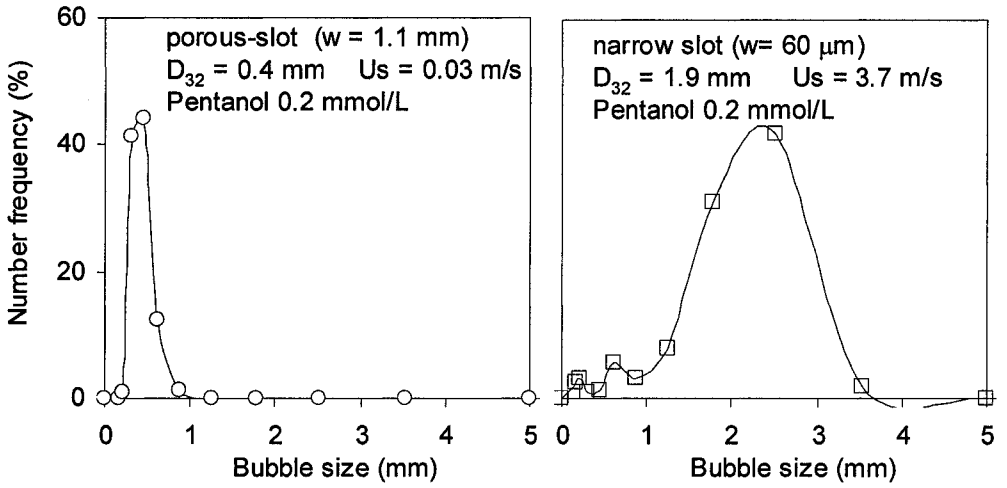

Figure 3.51: Bubble size distributions generated using flat slot sparger (test #65 and 66)

The experiments are conducted in a rectangular transparent column with an inclined top section (15°). Bubble images are collected at three locations (close to the point of generation, at the middle (near top of rectangular section) and in the inclined section), in order to include the effect of possible surfactant accumulation along the column. Column dimensions and example pictures for the three locations are shown in Figure 3.52, where images were collected at the same operating condition (Us, superficial gas velocity 0.9 m/s, tap water 0.01 mmol/L Polyglycol). The viewing

area is also indicated: for top and middle points the viewing area is set to cover half of the column to avoid biasing the measurement (since big bubbles tend to go towards the center). The bottom viewing area is kept in the middle, covering the generating point.

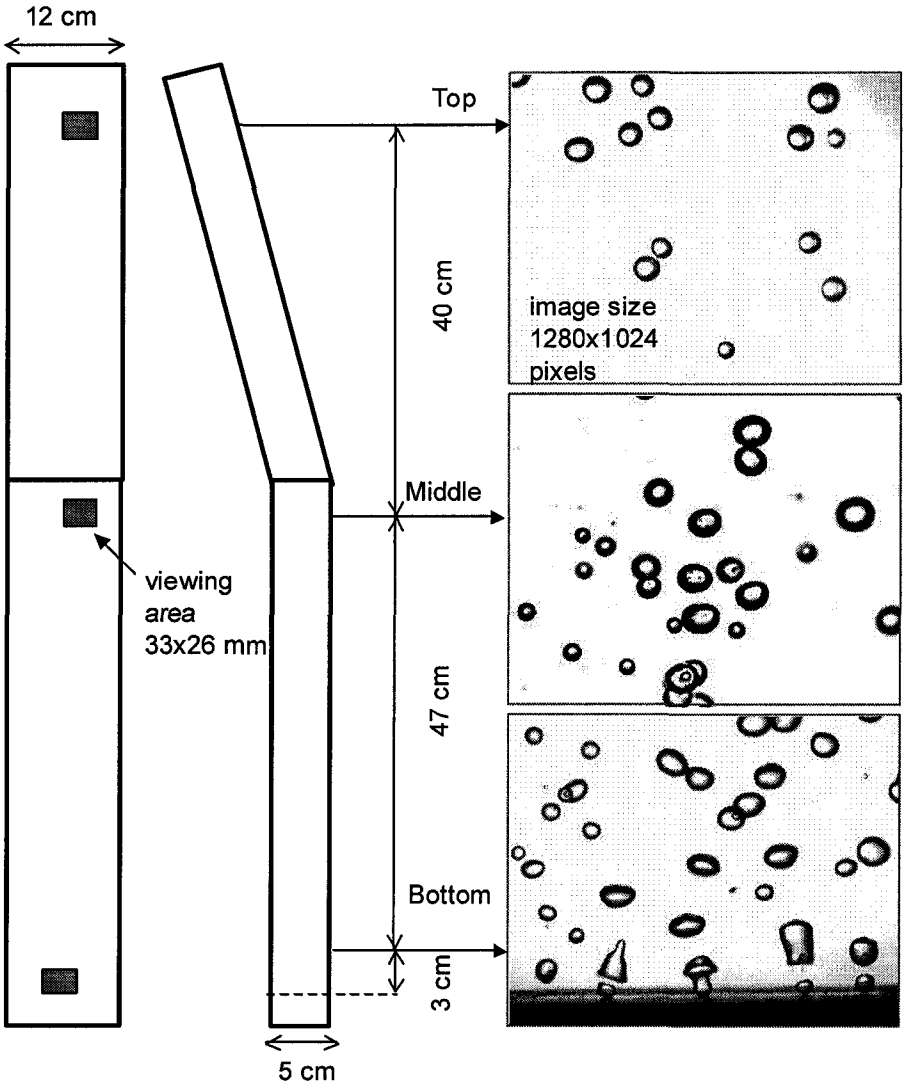

Figure 3.52: Bubble column and sampling points

Both bubble-generating devices produce approximately a 2D (i.e., a flat) bubble swarm, which facilitates bubble tracking measurement in the first 50 cm of the column, as shown in Figure 3.53. After this distance, bubble oscillations, interactions and liquid re-circulation generate axial displacement of bubbles. As a consequence, a bubble plume starts to form (i.e., 3D swarm of bubbles), which makes it difficult to

track trajectories. To avoid this condition, the inclined section forces the plume to spread into single bubble layer again (Hernandez-Aguilar, 2005).

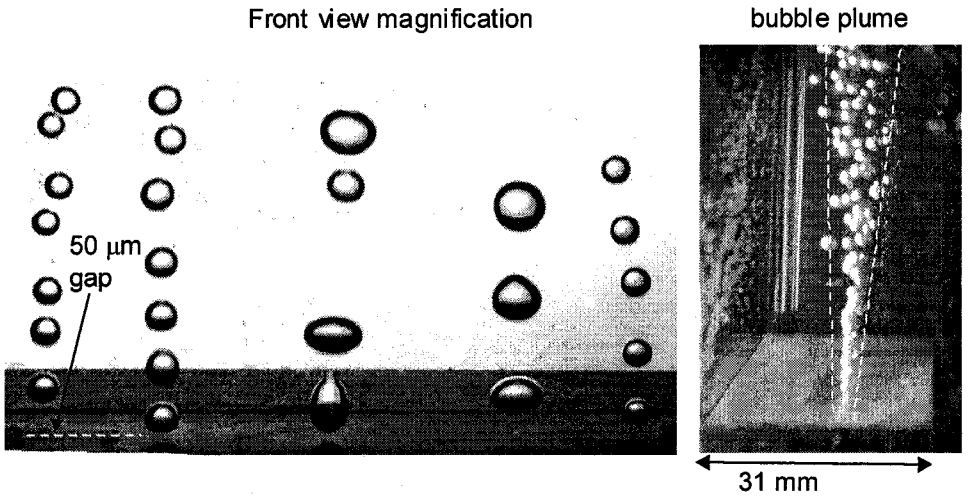

Figure 3.53: Generation of a flat front of bubbles (slot sparger)

Depending on the bubble size distribution, in the middle section the plume can create super-imposed bubbles. This condition is reduced by using a macro lens to reduce the depth of field to 5 mm, as can be observed in the middle picture in Figure 3.52.

As shown in Figure 3.53 left, despite discrete and stable bubble generation nodes being formed, the nodes do not produce the same bubble size. This may occur because of gap imperfections (machine tolerance is about 1 μm) or after the bubble detaches, coalescence occurs by bubble collision, especially when bubble generation rate is high, creating larger bubbles. The latter event is recorded in Figure 3.54 using high-speed cinematography (2000 frames per second).

In Figure 3.54a, bubble generation rate is low enough to avoid bubble collision, while in Figure 3.54b generation is high enough to produce collision and coalescence. This effect can be reduced by surfactant addition (Chapter 4), which confers bubble surface stiffness.

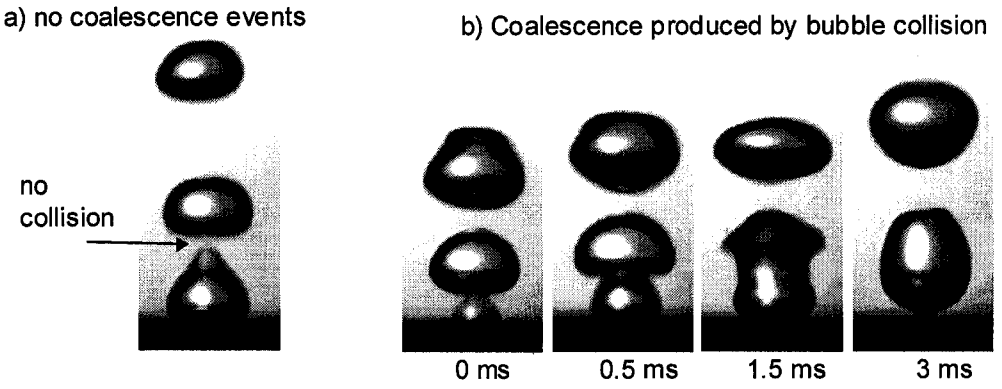

Figure 3.54: Coalescence by bubble collision during generation

Either slot gap "imperfections" or bubble coalescence events cause deviation from mono-size bubbles. But for the purpose of this research, the range in sizes is beneficial as it allows velocity vs. bubble size data to be generated from the same sequence of images.

3.5.1- bubble size distribution type with slot spargers

As air-flow rate increases bubble size tends to increase for most generators (Finch and Dobby, 1990; Nesset et al., 2006) the incidence of bubble collision and coalescence increases, events which together result in bubble size distribution being shifted to larger size. If airflow rate continues increasing bubbles become unstable and small bubbles are produced by coalescence-mediated break-up (Tse et al. 2003). These effects can be controlled by surfactants, which confer bubble stability once they detach from the node. An example of surfactant effect on Sauter mean bubble diameter, at different superficial gas velocities, is shown in Figure 3.55. As gas velocity is increased bubble size continues to increase in water alone but tends to become constant in the presence of frother.

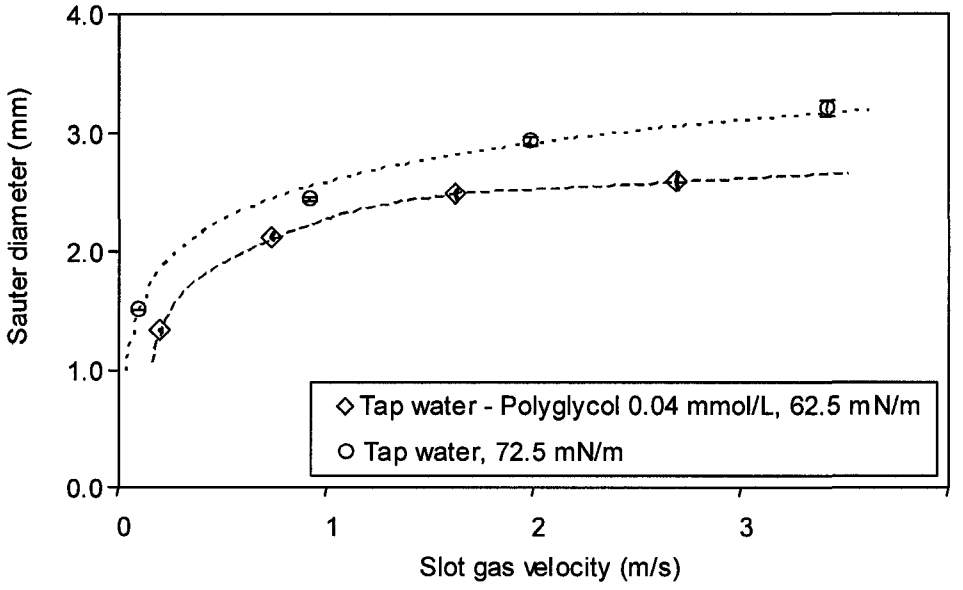

Figure 3.55: Effect of surfactant on bubble size in slot spargers

Bubble size distributions at three levels of superficial gas velocity for a non-coalescence regime are shown in Figure 3.56.

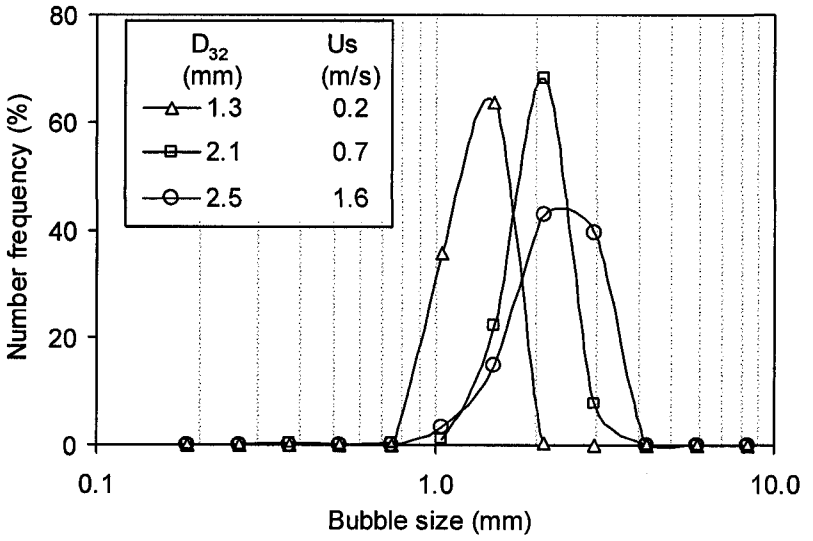

Figure 3.56: Effect of superficial gas velocity on bubble size distributions

For superficial gas velocities above 1.6 m/s, a comparison with and without surfactant is shown in Figure 3.57. From this Figure it can be deduced that bubble size distribution does not seem to be dependant on gas velocity. This is probably

because coalescence is the predominant event. The benefit of this condition is that for a given flow rate, bubble size distribution remains the same but the number of bubbles is higher.

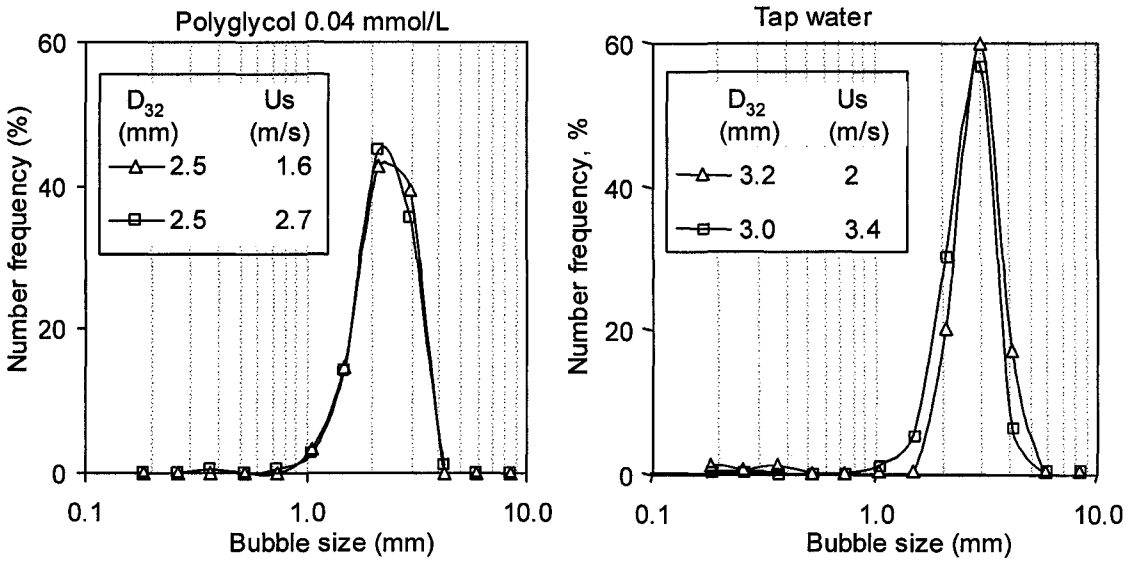

Figure 3.57: Stabilization of bubble size distribution at gas velocities above 1.6 m/s (Test #25, #26, #51, #52)

It is concluded that the technique allows the generation of a flat front of bubbles of various bubble sizes.

3.6- Bubble surface mobility measurement

A bubble rising in a liquid experiences motion in the surface, a layer of liquid sliding from the top of the bubble to the rear (Dukhin et al., 1998). If the liquid contains surfactant molecules, these molecules are transported and accumulated at the bubble rear (wake), called the stagnant zone (Weber, 1975). This creates a concentration profile; as a consequence a surface tension gradient is developed and the associated force starts to "lift" liquid from the bubble rear to the top, the Marangoni effect (Ybert and Meglio, 2000). This force opposes the surface motion, increasing bubble "skin" friction and tending to cause the bubble to behave as a rigid object. As an alternative to this explanation, it has been proposed that frothers increase bubble surface viscosity, which again reduces bubble rise velocity (Zhou et al., 1991).

Both mechanisms, independently or combined, qualitatively explain experimental findings of the surfactant effect on bubble rise velocity (Sam et al., 1996), bubble elasticity upon collision (Malysa et al., 2005) and bubble film thickness (Gélinas et al., 2005). However, there is no technique to measure directly surface mobility on bubbles. To attack this it is proposed, as a first step, to measure surface flows on a static bubble blown in air. A static air bubble created from and remaining in contact with a surfactant solution appears to have a dual water layer surface, an inner layer bound by H-bonding with the adsorbed surfactant (frother) and an outer layer of "free" water (Sarma and Chattopandhyay, 2001; Gélinas et al., 2005). The results from bubbles blown in air can be extrapolated to bubbles blown in water (Finch et al., 2006).

3.6.1- effect of frother on static bubble blown in air

The static bubble generation technique was adapted from that used to measure film thickness on bubbles blown in frother solutions (Gélinas et al., 2005). From that work with different frother types it was observed that:

1- The film is composed of an inner "bound" water layer and a "free" outer layer.
2- The inner film thickness reduces in time until the bubble bursts. Film drainage rate and initial bubble film thickness control this process and determine bubble life time.
3- The bubble surface is in motion with patterns of different textures. This motion is manifested as "random" motion of "packets" of liquid and by light diffraction (surface changes in color).

Bubble surface motion patterns, textures and bubble time life are shown to depend on frother type and concentration. The motion appears to be driven by the Marangoni effect, which in turn depends on the surface tension gradients created, and therefore, depends on frother type and concentration. The motion is induced by gravitational drainage, which creates a surfactant gradient and, as a consequence, the Marangoni effect is induced causing "packets" of liquid to move upwards. The surface becomes rippled or corrugated.

From these observations and interpretations, it is proposed to measure surface motion by tracking and marking "packets" of liquid in time over sections of a bubble surface.

3.6.2- bubble surface motion (velocity) measurement

The velocity of liquid packets moving over the bubble surface is measured by tracking and marking the packets in time over sections of the bubble surface. Bubble surface images are recorded in a digital camera, collected at intervals of 0.1 s. The technique to mark and track the liquid packets is described in section 3.4.1. Experimental set up and camera settings are described in Appendix 3 (Figure A3.3). In Figure 3.58 an example of bubble surface texture is shown for n-Pentanol (6 mmol/L).

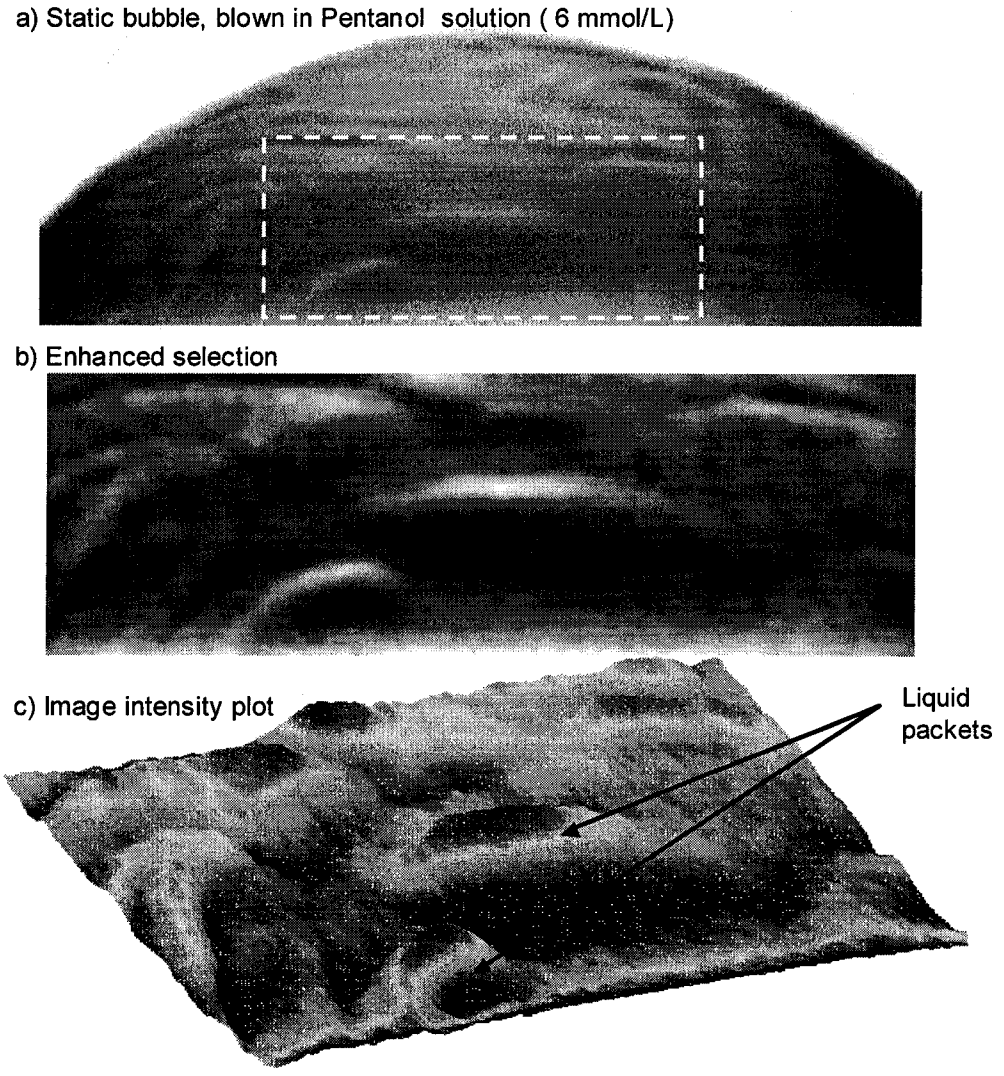

Figure 3.58: Example of bubble surface texture identifying liquid packets.

In Figure 3.58a, a typical static bubble is shown, in which background light is applied to produce "shadows" to reveal the liquid packets. A section is enhanced (Figure 3.58b) by using contrast enhancement and shadow direction transform (Wilcox et al., 2002), and an image intensity plot (Figure 3.58b) is used to embolden the liquid packages. The packages are marked with different colors and tracked on image sequences (technique described in section 3.4.1). An example of a "wave" moving downwards, expanding and then moving upwards is shown in Figure 3.59 for a bubble blown in n-Pentanol solution (6 mmol/L).

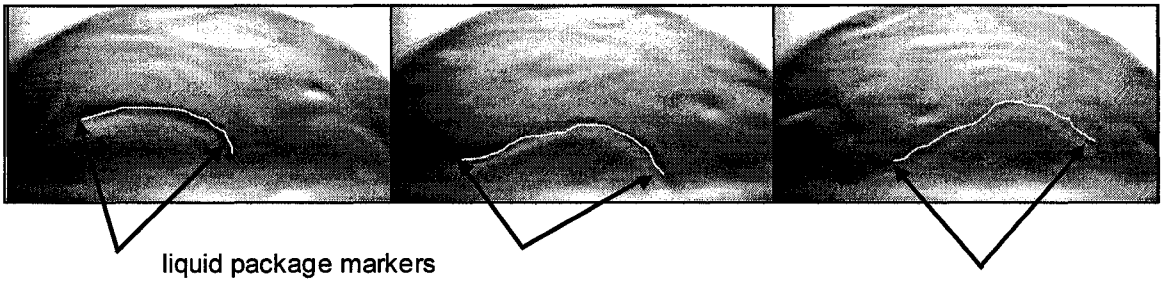

Figure 3.59: Tracking of bubble surface motion on a bubble blown in n-Pentanol

Normally at least 3 to 10 pictures are used to track a liquid packet and 9 to 20 repeat tests on fresh bubbles are done to obtain an average velocity. Figure 3.60 shows some selected trajectories for objects (liquid packets) tracked on the surface of a bubble surface blown in n-Pentanol solution.

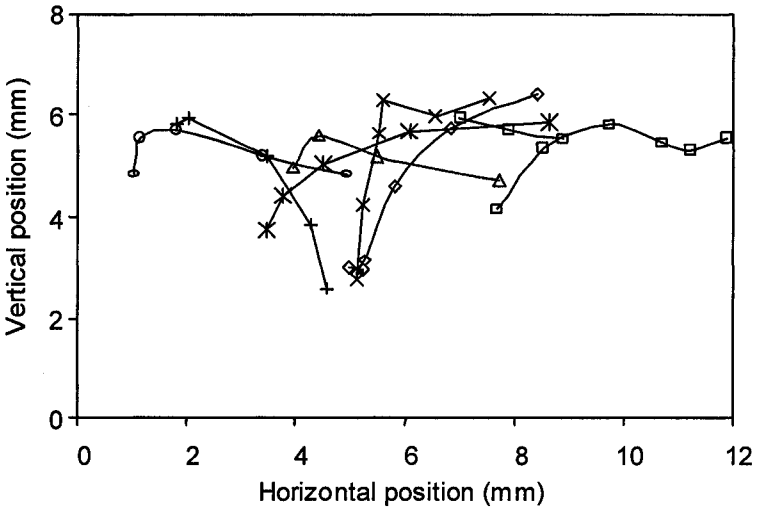

Figure 3.60: Trajectories of selected liquid packets on a bubble surface (same condition as Figure 3.59)

3.7- Bubble interaction characterization technique

According to the literature review (section 2.3), one of the most significant parameters influencing bubble swarm motion appears to be the volumetric fraction of gas. The argument, developed originally for settling particles (Masliyah, 1979) and adapted to bubble swarms by Dobby et al. (1988) is as follows: the higher the gas holdup, the more crowed the bubbles, increasing the extent of interaction and, as a consequence, swarm velocity is reduced. Empirical models try to correlate bubble swarm velocity with gas holdup representing the level of bubble interaction. However, gas holdup is a bulk value and does not provide information related to inter-bubble distance, considered a more direct measurement of the level of interaction. A model and technique is proposed to characterize the level of interactions in a bubble swarm using dimensionless inter-bubble distance. In this model inter-bubble distance is determined from the bubble data structure created with the image processing software developed in section 3.1. In addition, a fundamental model relating gas holdup and inter-bubble distance is developed.

3.7.1- area fraction of gas and inter-bubble distance relationship

An example of two pictures of the same size, containing 4 and 64 uniformly distributed spherical bubbles is shown in Figure 3.61. Bubble radius (r) and minimum inter-bubble distance are arranged to yield the same area fraction of bubbles (29%), which is equivalent to a 2-D gas holdup. Despite both pictures having the same bubble area fraction, the minimum inter-bubble distance is different. Therefore, gas holdup may not be an adequate parameter to measure bubble interactions. If, instead, inter-bubble distance is related with a characteristic bubble dimension, for example bubble radius (r), the resulting dimensionless numbers (d^*) (Equation 3.2) are the same for the two cases. Thus, in this work it is proposed to use the "dimensionless inter-bubble distance" d^* to characterize the level of interaction in a swarm of bubbles, and use it to establish a relationship with bubble swarm velocity.

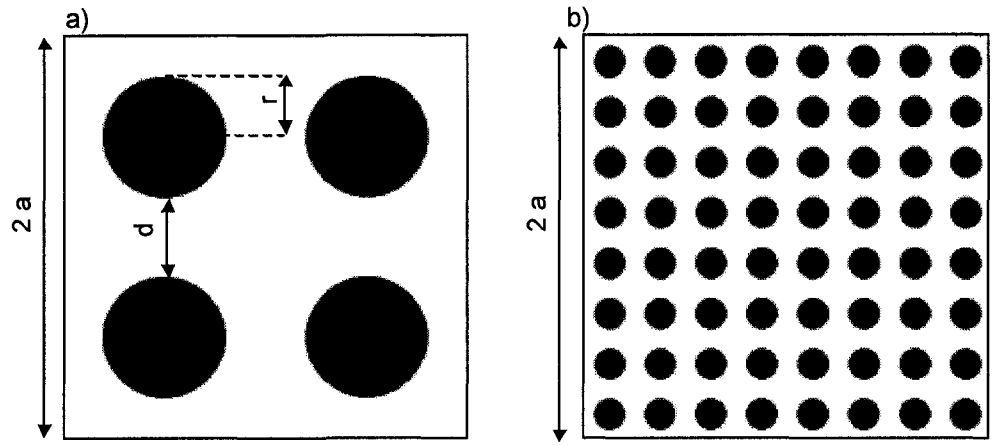

Area fractions of bubbles	= 0.29	Area fractions of bubbles	= 0.29
Radius (r)	= 2 mm	Radius (r)	= 0.5 mm
Box length (2a)	= 13.12 mm	Box length (2a)	= 13.12 mm
Inter-bubble distance (d)	= **2.56** mm	Inter-bubble distance (d)	= **0.64** mm
Number of bubbles	= 4	Number of bubbles	= 64

Figure 3.61: Illustration of bubble interaction distance and fraction of gas relationship

Using image 3.61a, the minimum inter-bubble distance:

$$d = a - 2 \cdot r \tag{3.1}$$

Dimensionless inter-bubble distance:

$$d^* = \frac{d}{r} = \frac{a}{r} - 2, \text{ re-arranged } \frac{r}{a} = \frac{1}{(d^* + 2)} \tag{3.2}$$

If a number (n) of non-superimposed bubbles of radius (r) are uniformly distributed each bubble is bounded by a square of length (a) (i.e., an ideal dispersion) and the area fraction of bubbles $E^{2D}{}_g$ (the subscript 2D indicates 2-Dimensional, i.e., area) can be derived (Equation 3.3):

$$E^{2D}{}_g = \frac{n \cdot \pi \cdot r^2}{n \cdot a^2} \tag{3.3}$$

A relationship, for the ideal dispersion, between dimensionless inter-bubble distance and area fraction of bubbles can be derived by combining Equations 3.2 and 3.3, as presented from Equation 3.4.

$$E^{2D}{}_g = \frac{\pi}{\left(d^* + 2\right)^2} \tag{3.4}$$

Of course, in flotation systems bubbles vary in size, shape and spatial distribution. Therefore these models for an ideal dispersion must be adapted to consider shape and spatial distribution aspects.

Considering that in flotation bubbles are ellipsoidal and the aspect ratio is on average 0.8 (Figure 3.14), a shape correction must be considered to the ideal dispersion result.

A general relationship for the dimensionless inter-bubble distance and area fraction of gas, for ellipses of aspect ratio (AR), is shown in Equation 3.5. The derivation is presented in Appendix 1.1.

$$E_g^{2D} = \frac{\pi}{\left(\frac{d^*}{AR^{2/3}} + 2\right)^2}. \tag{3.5}$$

The bubble imaging technique developed in this work generates 2D images and therefore, a relationship between area fraction and volumetric fraction of gas, in order to determine the level of interaction of bubbles, is required.

3.7.2- area fraction of gas and volumetric fraction of gas relationship

A relationship for oblate spheroid bubbles uniformly distributed in a single layer of bubbles can be derived to connect the area fraction of bubbles on an image with the volumetric fraction of gas, as shown in Equation 3.6. The derivation is presented in Appendix 1.1. It shows that the relationship is independent of the bubble aspect ratio (AR).

$$E_g = \frac{4}{3 \cdot \sqrt{\pi}} \cdot \left(E_g^{2D}\right)^{3/2} \tag{3.6}$$

From stereology (Russ and Dehoff, 1999), the fraction area of one phase in a given image, calculated by the fraction of "hits" of a superimposed grid, is equivalent to the volume fraction. This postulate differs from a system containing bubbles in an ideal dispersion in which the geometry is known. A numeric example is illustrated in Figure 3.62 for bubble of 7 pixels in diameter (the pixel size is 28.6 μm). For digital images, a superimposed grid is represented by pixels.

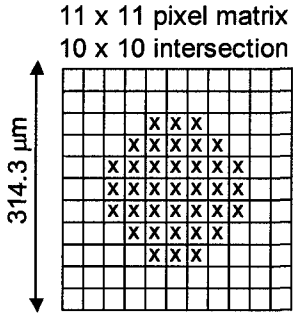

	number of "hits"	number of pixels	area mm	volume mm
Phase (x)	44	37	0.0302	0.863
Total	144	121	0.0988	2.822
Fraction	0.306	0.306	0.306	0.306

Bubble diameter	200 μm
Area fraction	0.318
Volume fraction	0.135

different values

Figure 3.62: Volumetric fraction of gas based on area fraction

Since bubble geometry is known, for an ideal dispersion the relationship described in Equation 3.6 can be used to relate area fraction of bubbles and volumetric fraction of gas.

However, from experimental evidence, bubbles in images are dispersed randomly, and the minimum inter-bubble distance is not uniform. Figure 3.63 illustrates an example of this aspect and also illustrates shape variations. The image was collected under lab conditions using a slot sparger (section 3.6) and in presence of n-Pentanol (0.2 mmol/L). Mean inter-bubble distance is 4.5 mm with a standard deviation of 5.5 mm.

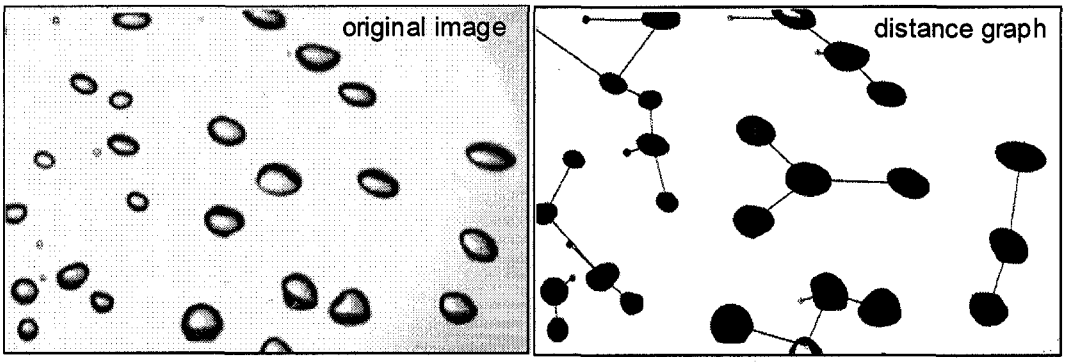

Figure 3.63: Example of random dispersion of bubbles

For a random dispersion, a Poisson distribution can be used to relate 2D measurements (area fraction or number of elements per unit of area) with the volumetric fraction of objects, as derived by Carpat et al. (2002). This model is applicable to spheres in "dilute dispersions", where objects are not superimposed. (Interestingly, Carpat et al. (2002) used the model for a dispersed phase fraction 0.4 to 0.8, which does not correspond to a "dilute" dispersion.) The volumetric fraction range covered in this work, 0.04 to 0.25 (Figure 1.3), is expected to respect the dilute dispersion assumption. The model based on the work of Carpat et al. (2002), (developed in Appendix 1.2) expresses volumetric fraction of gas as a function of area fraction of bubbles, Equation 3.7:

$$E_g = \frac{2}{3} \cdot \frac{D_{10}}{\delta z} \cdot \ln\left(\frac{1}{1-E_g^{2D}}\right) \tag{3.7}$$

where D_{10} is the average bubble diameter and δz is the thickness of the bubble layer. In this case, where an approximately flat front of bubbles is generated, δz is assumed to be equal to the maximum bubble diameter ($d/\delta z = 0.57$, considering the minimum aspect ratio 0.57 ways found experimentally Table A4.1 and A4.2).

There are two ways to calculate the volumetric fraction of bubbles from area fraction: Equation 3.6, for ellipsoidal objects uniformly distributed and Equation 3.7 for a random distribution of spheres. Using Equation 3.5 it is possible to correlate

volumetric fraction of gas with inter-bubble distance, and compare which model conciliates better the experimental measurements. The inter-bubble distance is measured using a new technique proposed in this work in section 3.7.3.

3.7.3- dimensionless inter-bubble inter distance

Measurement of dimensionless inter-bubble distance is based on geometric properties calculated for each bubble: minor axis, major axis, centroid coordinates, which are stored in a data structure (Figure 3.13). Inter-bubble distance is computed using the Euclidian distance, and the equivalent diameter for a sphere of the same volume as an oblate spheroid. Distance bubble-bubble (d_{bb}) is expressed in Equation 3.8, and Figure 3.64 shows an example of distance calculation for an oblate spheroid bubble and a spherical bubble.

$$d_{bb}(i,j) = \sqrt{(Cx(i) - Cx(j))^2 + (Cy(i) - Cy(j))^2} - rj - ri \qquad (3.8)$$

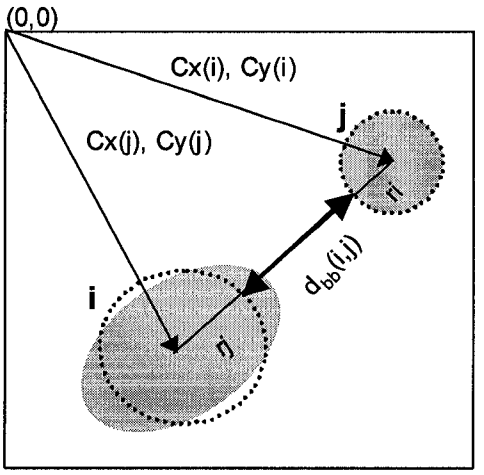

Figure 3.64 Bubble inter-distance

Dividing Euclidian distance $d_{bb}(i,j)$ by the equivalent volume bubble radius, two dimensionless distances are obtained, as indicated in Equation 3.9:

$$d^*(i,j) = \frac{d_{bb}(i,j)}{ri} \qquad d^*(j,i) = \frac{d_{bb}(i,j)}{rj} \qquad (3.9)$$

The calculation is applied for each combination of bubble pairs, resulting in an n x n matrix containing n (n-1) dimensionless distances computed for each bubble. The minimum value is extracted, and the average dimensionless distance is calculated for a given picture. An example of minimum distances is plotted, for one picture, in Figure 3.65, which contains 227 bubbles; the average dimensionless inter-bubble distance, is 0.77

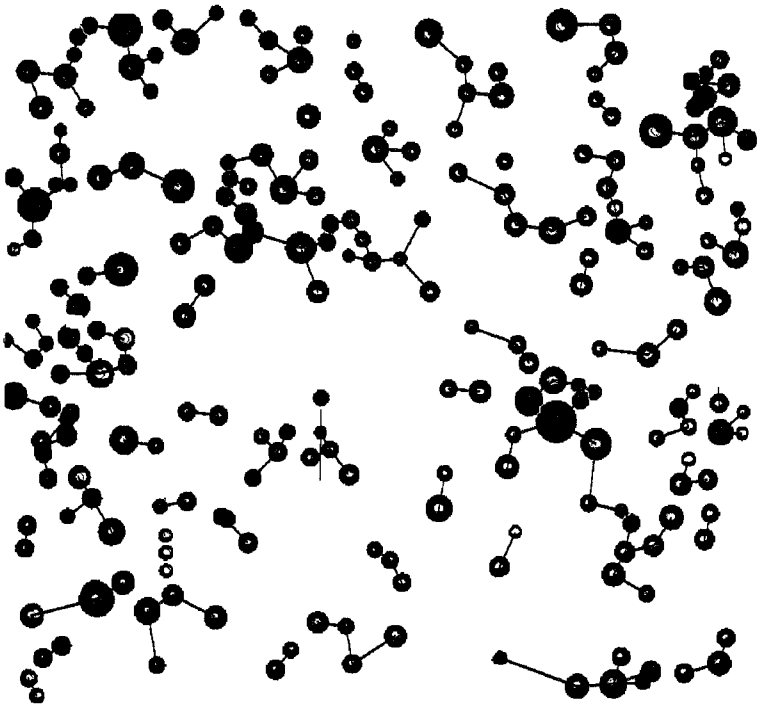

Figure 3.65: Inter-bubble distance computation example

In order to validate this model, a series of 64 experiments were conducted in a laboratory column (Figure 3.52) with porous-slot and slot spargers (Figure 3.50) at various airflow rates, surfactant types (frother) and concentrations (Appendix 4, Table A4.1 and Table A4.2).

3.7.4- model validation

Results of the 64 measurements, using the image analysis tools described in section 3.2, are shown in Figure 3.66. The average dimensionless inter-bubble distance per test and 95% confidence interval is plotted against the fractional area of gas (2-D gas holdup). The theoretical gas holdup calculated from Equation 3.5, for an ideal dispersion (AR 0.8), is included.

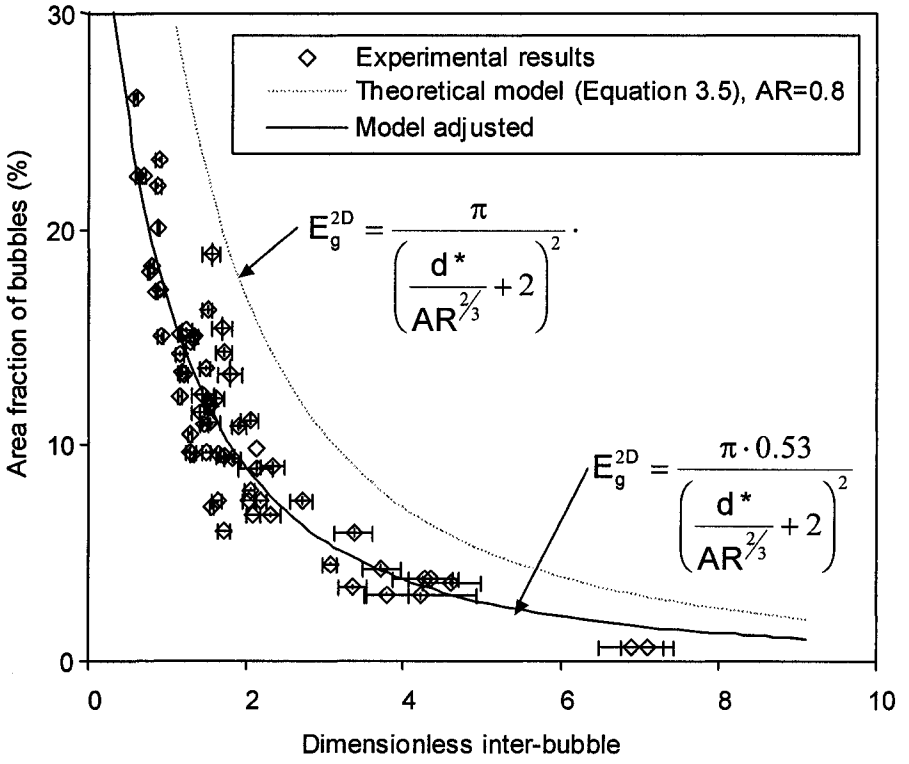

Figure 3.66: Area fraction of bubbles as a function of inter-bubble distance

From Figure 3.66, the ideal dispersion model requires a correction (0.53), because bubbles vary in size and they are randomly dispersed.

Converting the area fraction of gas (E_g^{2D}), measured from the bubble images, to volumetric fraction of gas and plotting against the dimensionless inter-bubble distance, it can be deduced (Figure 3.67) that both models, ideal dispersion of oblate spheroids of aspect ratio 0.8 (Equation 3.10) and the random dispersion model of $d/\delta z = 0.57$ (Equation 3.11), can be used to relate d* and Eg.

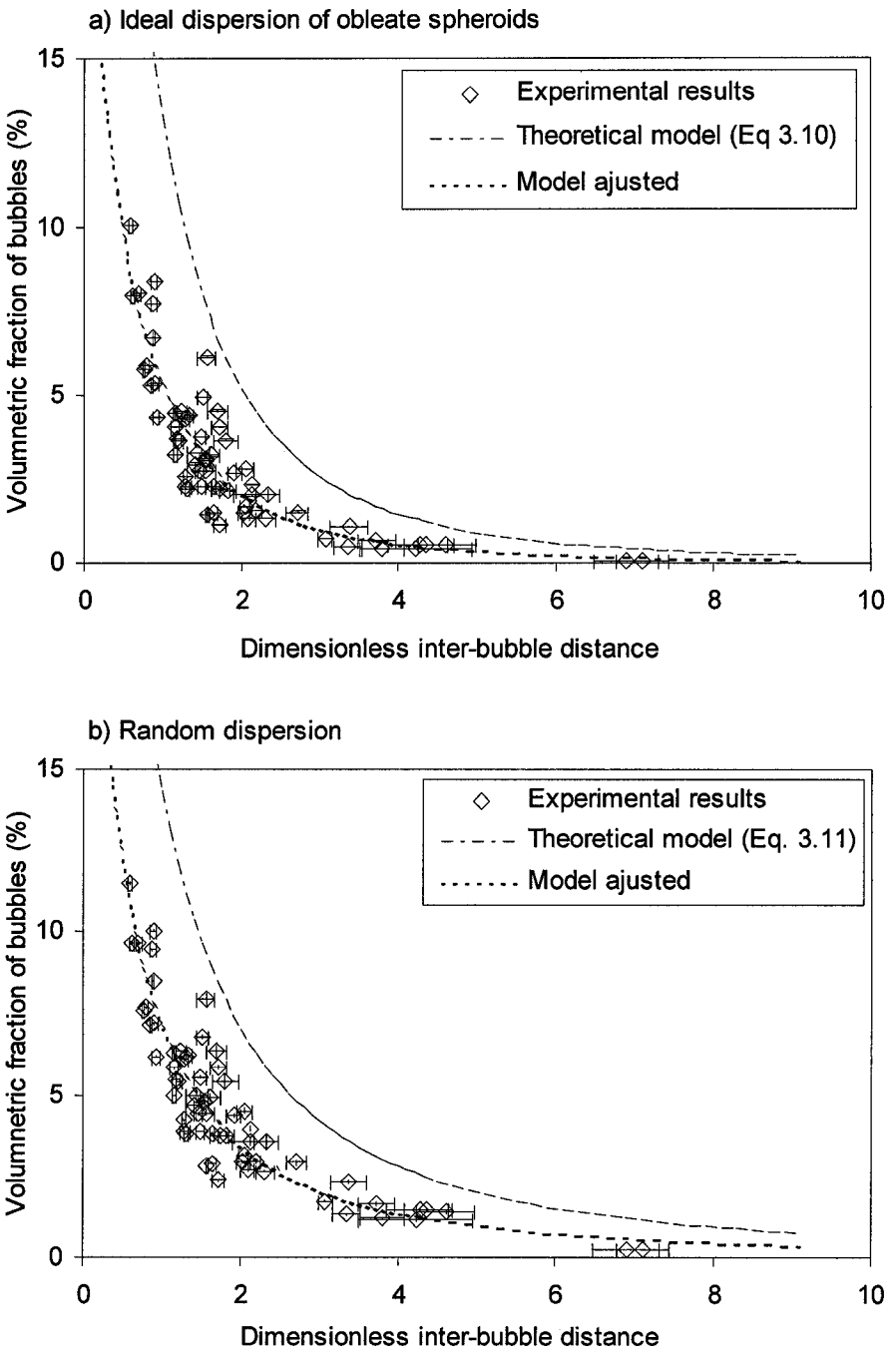

Figure 3.67 Volumetric fraction of gas and relationship to inter-bubble distance

$$E_g = \frac{4}{3 \cdot \sqrt{\pi}} \cdot \left(\frac{\pi}{\left(\frac{d^*}{AR^{2/3}} + 2 \right)^2} \right)^{3/2} \tag{3.10}$$

$$E_g = -\frac{2 \cdot 0.57}{3} \cdot \ln\left(1 - \frac{\pi}{\left(\frac{d^*}{AR^{2/3}} + 2 \right)^2} \right) \tag{3.11}$$

The ideal and random dispersion models are adjusted by one parameter, and the standard deviation for the residuals of the two models is 0.96% and 1.03%, respectively. Thus both theoretical models are suitable to relate dimensionless inter-bubble distance and volumetric fraction of gas.

It is now possible not only to use classical models to evaluate the bubble swarm velocity as a function of gas holdup (Masliyah 1979, Dobby et al., 1988), but also as a function of dimensionless inter-bubble distance. The latter inarguably is the more fundamental parameter (Richardson and Zaki , 1956).

3.8- Conclusions

New image analysis tools have been developed for:

- Compensating uneven intensity lighting
- Masking and removing static objects in digital images
- Thresholding objects using an automatic algorithm (Calzado-Acuna routine)
- Local thresholding to de-cluster touching objects
- Separating bubble clusters using watershed and distance transform algorithm
- Isolating and measuring automatically geometric properties for individual bubbles in a swarm from image sequences or AVI files.
- Tracking moving bubbles and determining individual bubble vector velocity

The image analysis tools increase the detected area of bubbles from typically 30% up to 90%.

From plant measurements, it has been demonstrated that bubbles are best considered as ellipsoidal, with an aspect ratio of 0.8, rather than spherical and, a selection criterion based on shape factor for ellipsoids was substituted for the prior one base on spheres.

A new model for identifying single bubbles from clusters, based on a general shape factor for an ellipsoidal object and appropriate perimeter model, has been developed and evaluated. The new model allows more bubbles to be identified more accurately.

The conversion of a set of images into data structure speeds up computing significantly.

In order to have accurate bubble characterization, image size (i.e., number of pixels), magnification (image resolution) and frame rates must be selected based on the bubble size distribution under study and, for the present purposes, bubble velocity ranges.

The detection limit for minimum bubble size is given by the resolution (minimum object size in pixels that can be detected unambiguously is 7 by 7 pixels). The maximum detectable bubble size is given by image size (in pixels), resolution (pixels/mm), bubble velocity and frame rate.

In order to increase the accuracy of bubble size measurements it is required to identify at least 40% of the area selected as bubbles. Merely counting a large number of objects increases precision of the measurement, but not necessary the accuracy.

CHAPTER 4: Frother effect on bubble behavior: experimental results

In generating bubbles in flotation systems it is almost universal that surfactant (frother) reduces bubble size and stabilizes the bubble size distribution by retarding bubble breakage and coalescence. This effect is a consequence of the adsorption and non-uniform distribution of surfactant on the bubble surface (Krzan et al., 2007) induced by the bubble motion (Dukhin et al.,1998), which confers bubble surface stiffness[1]. Experiments were conducted to demonstrate the effect of surfactants on bubble surface stiffness. Two flotation frother types were tested, n-Pentanol ($C_5H_{11}OH$)and Polyglycol ($H(PO)_7OH$), which are classified as "weak" and "strong", according to previous research in frother classification (Azgomi et al., 2006; Moyo et al., 2006).

4.1- Effect of frother on single bubbles

A comparison was made of single bubbles generated at a capillary in tap water and in the presence of each frother. The growth, detachment and stabilization process were recorded using high-speed cinematography and image analysis to track bubble position and geometric changes (techniques described in Chapter 3). Experimental results reveal that the frothers rapidly dampen changes in bubble shape and oscillation. Figure 4.1 compares the aspect ratio (AR) for bubbles in tap water and a Polyglycol solution of 0.1 mmol/L. Images were collected at intervals of 0.5 ms and bubble object properties were measured frame by frame. Selected pictures are superimposed in Figure 4.1 at intervals of 5 ms to track visually changes in shape.

---

[1] In this work it is proposed to use the term "stiffness" to describe the "macro" effect of surfactant on the bubble surface. The term "rigidity" is used to characterize bubble surface mobility at the "micro" level, as Clift et al. (2005) and Dukhin et al. (1998) refer when a bubble surface behaves as "rigid" in presence of surfactant.

Single bubbles were generated using a 1.2 mm (internal diameter) capillary. Air was injected slowly using a 1 ml syringe, to generate a bubble growth rate of approximately 3.7 ml/min to reproducibly generate a bubble of about 3.6 mm equivalent volume diameter, big enough to easily detect changes in bubble shape.

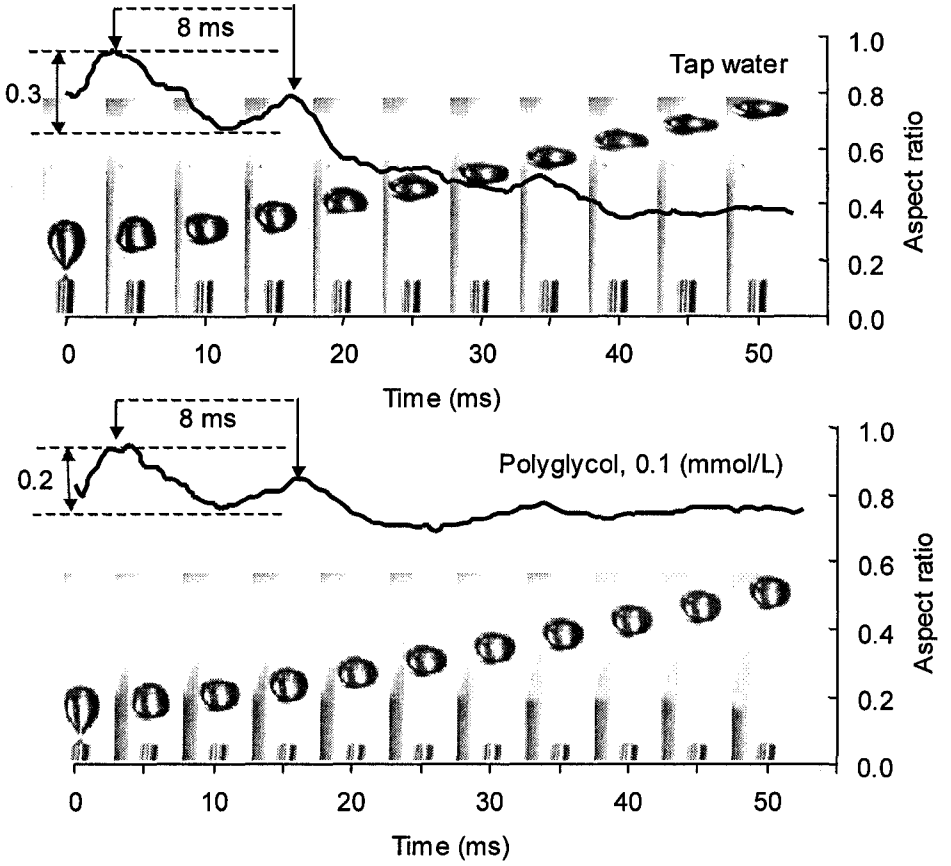

Figure 4.1: Surfactant effect on bubble shape and surface oscillation

The experiment, reproduced three times, was consistent. The conclusions are that:

1- Surfactant compensates the external dynamic forces with surface tension forces created by a concentration gradient in the bubble surface, namely the Marangoni effect (IUPAC, 1997). Thus for the same bubble (equivalent volume diameter 3.6 mm) the aspect ratio in tap water is 0.4 (after ca. 40 ms), while in presence of the surfactant (Polyglycol 10^{-4} mol/L) it is 0.8 (after ca. 30 ms). At this concentration the equilibrium surface tension is 61 mN/m (section 3.6). To compensate the dynamic forces the concentration variation should produce a surface tension difference (i.e., surface pressure) of at least 40 mN/m. Malysa et al. (2005) made similar observation using a smaller bubble (ca. 1.5 mm) which, correspondingly, was less sensitive to a frother effect.

2- Surfactant does not act instantaneously, the effect starting as surfactant accumulates and re-arranges over the bubble surface after the bubble detaches. Finer detail over the initial 10 ms is shown in Figure 4.2, where pictures are at intervals of 0.5 ms. Aspect ratio (AR) and the minor axis are plotted versus time. It is evident that both bubbles evolve over the first 10 ms identically. Thus frother requires "stabilization" time (or "adsorption" time) to produce the effect on the bubble surface, as also observed by monitoring bubble velocity changes (Sam et al., 1996; Ybert and Meglio, 2000; Zhang et al., 2001; Krzan et al., 2007). Surfactant is considered to accumulate on the leading surface and be "displaced" to the bubble rear, as has been interpreted theoretically by Dukhin et al. (1998).

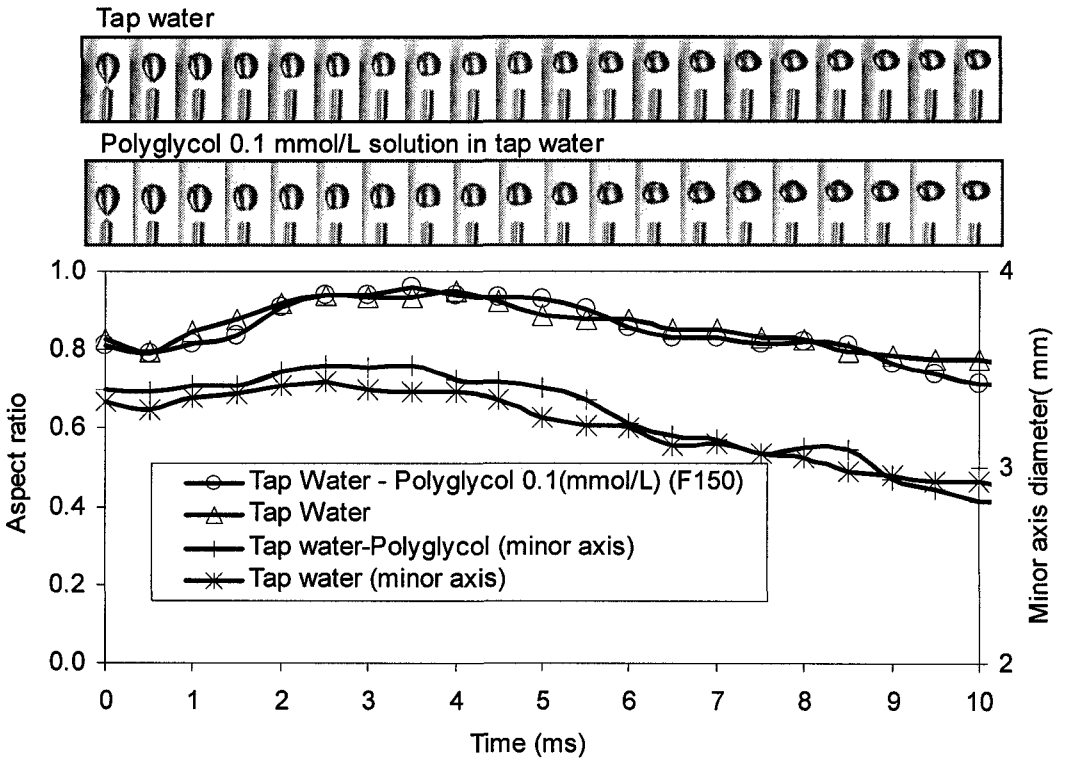

Figure 4.2: Surfactant effect on bubble shape and surface oscillation (10 ms)

3- Bubble shape oscillation amplitude is reduced when surfactant is present, as noted by Malysa et al. (2005), for bubbles colliding with solid surfaces. From Figure 4.1 surfactant reduces the initial amplitude of oscillation of the aspect ratio by approximately 30%, and this is further damped as the bubble rises and accumulates surfactant. However, the surface oscillation frequency appears to be the same (8 ms period); this may indicate that the system harmonics are the same, but the initial energy dissipated is lower in the presence of frother since now the bubble surface resists deformation. Thus, bubble surface stiffness is increased by the accumulation and distribution of surfactant on the bubble surface. That could also mean bubble wobbling (Clift et al., 2005) is reduced.

Salts can have the same effect as surfactants (Hofmeier et al., 1995). Work by Quinn et al. (2006) established that 0.4 mol/L NaCl gave a similar bubble size reduction effect as 8-10 ppm of the common commercial frother (methyl isobutyl carbinol (MIBC)). Figure 4.3 shows that 0.4 mol/L NaCl likewise suppresses the

amplitude of oscillation (dispersion coefficient of the aspect ratio). In the case of salts, surface tension increases over that of water alone, in this case to 72.4 mN/m. This means, regardless of how the surface tension gradient is created, stiffness is conferred to the bubble surface.

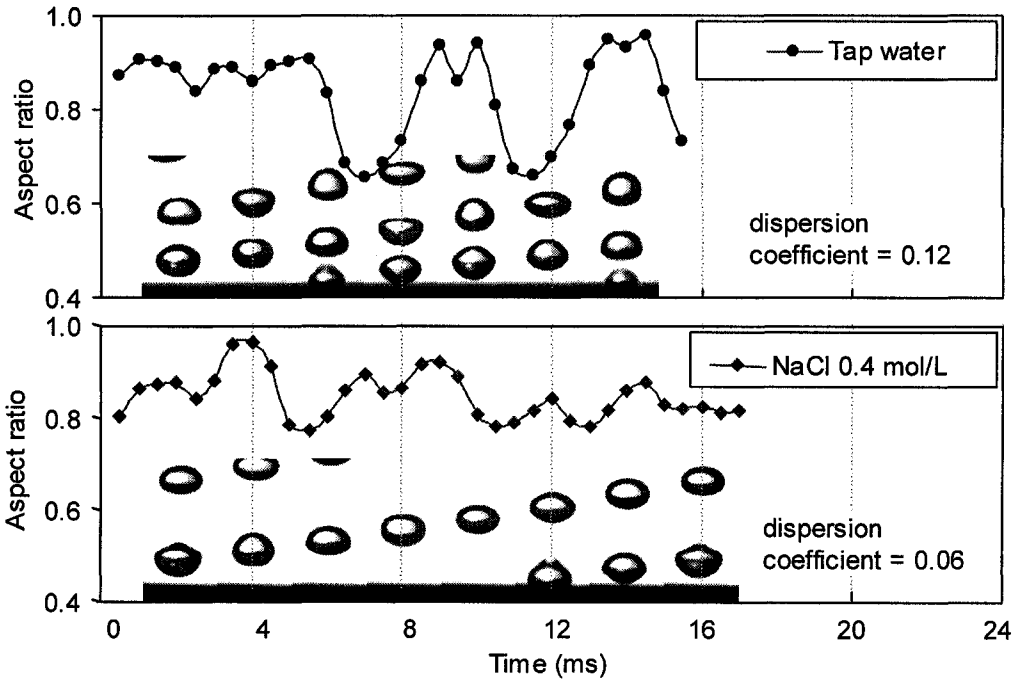

Figure 4.3: Salt effect on bubble oscillation

Bubbles shown in Figure 4.3 were generated using a slot sparger 30 mm in length (described in section 3.5) operating with 8 discrete nodes; Figure 4.3 shows one of these nodes generating a bubble.

4- Surfactant slows the bubble rise velocity (note the lower vertical displacement in presence of surfactant in Figure 4.1 (lower)). This is another indication that frother increases skin friction, as reported by Clift et al. (2005) in "contaminated systems", and reduces surface mobility, due to the "adverse Marangoni effect" as observed by Almatrooshi and Aliborhan (2004). As a consequence, the rise velocity is lower as shown in Figure 4.4. Here, with approximately the same bubble size (diameter 3.6 mm) in both cases, the vertical centroid coordinate is plotted in time for the bubbles

shown in Figure 4.1. The slope corresponds to bubble rise velocity, which is clearly lower in presence of Polyglycol. The slope is calculated after 30 ms, where the aspect ratio has stabilized in both cases and there is sufficient surfactant accumulation to detect differences in velocity.

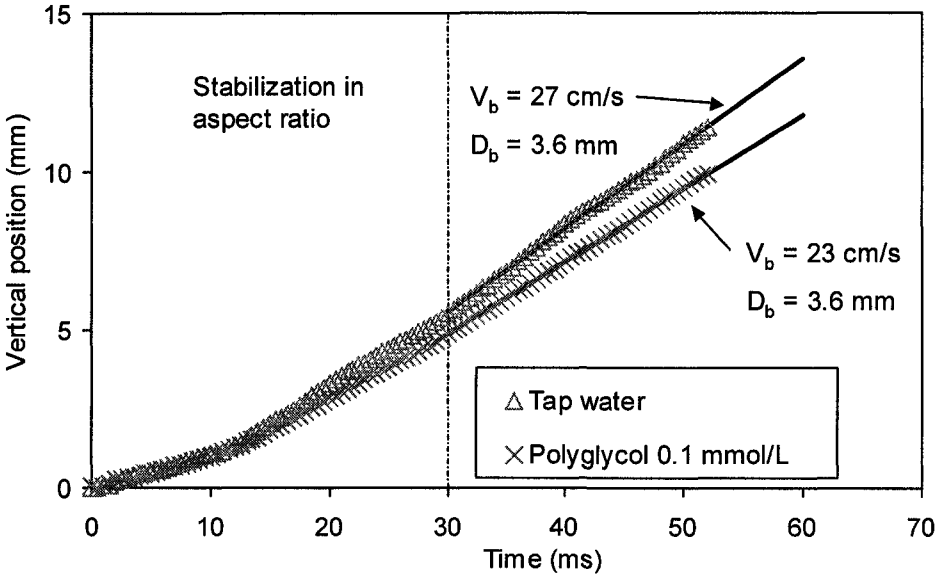

Figure 4.4: Effect of frother on bubble rise velocity

Another consequence of the effect of frother is that bubbles are less likely to coalesce or be deformed during collision with other bubbles or particles (section 4.2). This aspect, in a system of multiple bubbles, stabilizes the bubble size distribution. This is one of the hypotheses proposed in this work: "Once the bubbles are generated, bubble size distribution remains unaffected by the pulp, because of the stability imparted by the frother, but pulp characteristics affect the motion of the bubbles, which is reflected as variation in gas hold-up". This statement is analyzed in the following section.

4.2- Effect of frother on bubble swarms

The hypothesis is that once the bubbles are stabilized with surfactant little subsequent coalescence or break up occurs and the bubble size distribution from then on remains largely unaffected. Coalescence-mediated break-up occurs whenever the bubble surface is not stiff enough to compensate bubble deformation, e.g., upon collision (Tse et al., 2003). Coalescence and/or breakage events occur as in Figure 4.5, which shows bubble growth at a single node in a slot sparger (section 3.5) in tap water. Images were collected using the camera described in section 3.1.

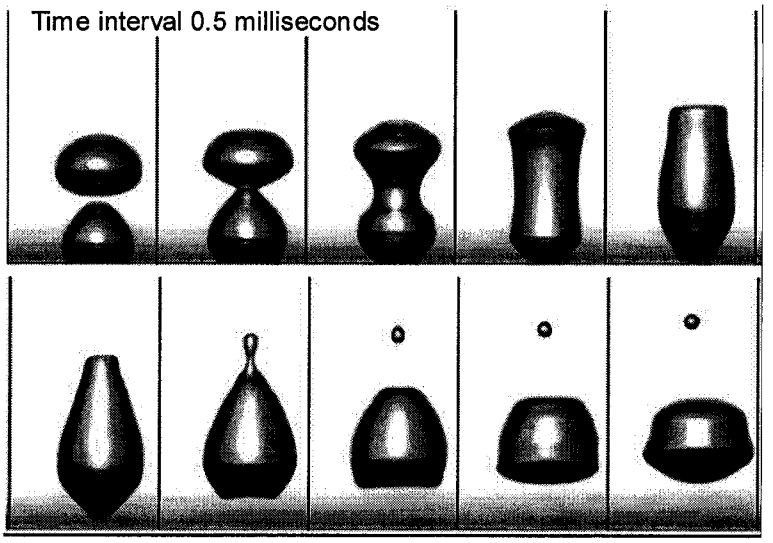

Figure 4.5: Bubble coalescence and breakage events in tap water

4.2.1- bubble size distribution stabilization in presence of frother

That a frother (or strong ionic solution) confers bubble surface stiffness and reduces coalescence and/or breakage is evidenced in Figure 4.6 (data collected in the equipment described in section 3.5), where bubble size distributions are compared for tap water alone and with surfactant at two locations (generation point and 90 cm above the sparger). It can be seen that without frother the bubble size distribution evolves with time (distance), as observed by Polli et al. (2002). In contrast, in the

presence of frother bubble size distribution remains unaffected, at least after the stabilization time required to adsorb sufficient surfactant.

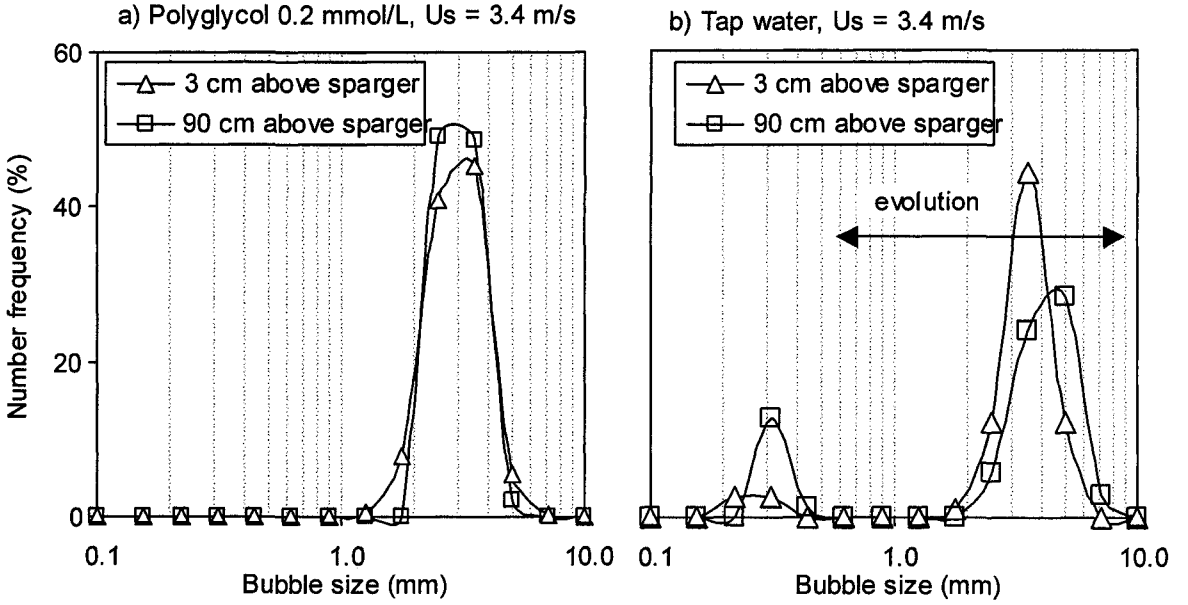

Figure 4.6: Evidence of bubble size distribution stabilization in presence of surfactant
(a)Tests #10,#13 (b) Tests #25,#30

The population of small bubbles at 90 cm above the sparger in Figure 4.6(b), ca. 0.3 mm, is the result of the coalescence-mediated break-up events shown in Figure 4.5.

4.2.2- bubble shape distribution stabilization in presence of frother

The time required to adsorb frother on a bubble surface depends on frother concentration and frother type (Sam et al., 1996; Krzan et al., 2004), and is governed by diffusion (Alves et al., 2005) or boundary layer mass transfer (Zhang et al., 2001). For bubbles in a swarm the same adsorption time concept applies, now showing as a stabilized bubble size distribution. Another illustration is stabilization of bubble shape revealed in Figure 4.7, in which the aspect ratio frequency distribution for a sequence of pictures (total bubbles counted > 1500) is calculated at two locations (equipment described section 3.5).

From Figure 4.6, bubble size distribution, from generation point on, remains unaffected in presence of surfactant but bubble shape is stabilized more gradually (Figure 4.7).

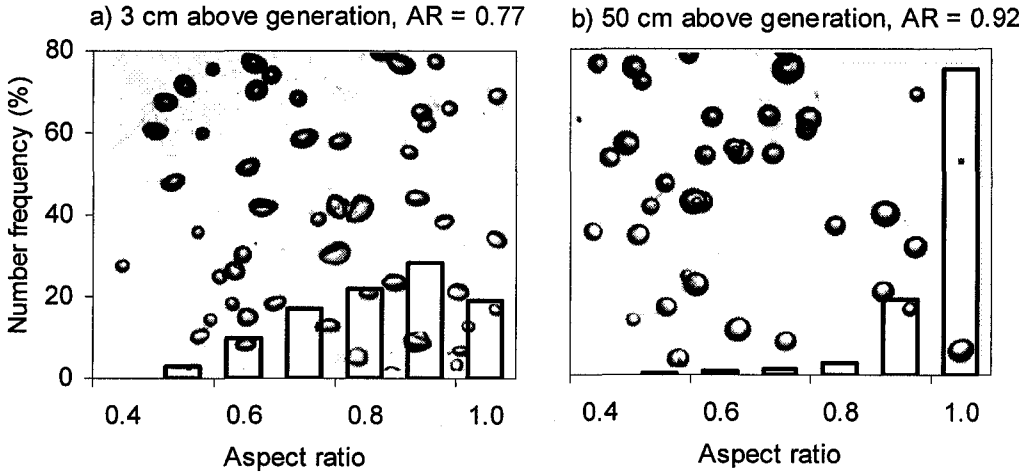

Figure 4.7: Evidence of bubble stabilization in shape in presence Polyglycol (Test #10 and #11)

The shape acquired by a bubble, once at steady state, depends on bubble size and surfactant type and concentration as shown in Figure 4.8 where bubble swarms are generated in three solutions: tap water alone and strong and weak frothers at the same molar concentration. Average and 95% confidence intervals are calculated for the aspect ratio for bubble size bin classes of interval 0.2 mm. Surface tension values were measured using the technique described in section 3.6.

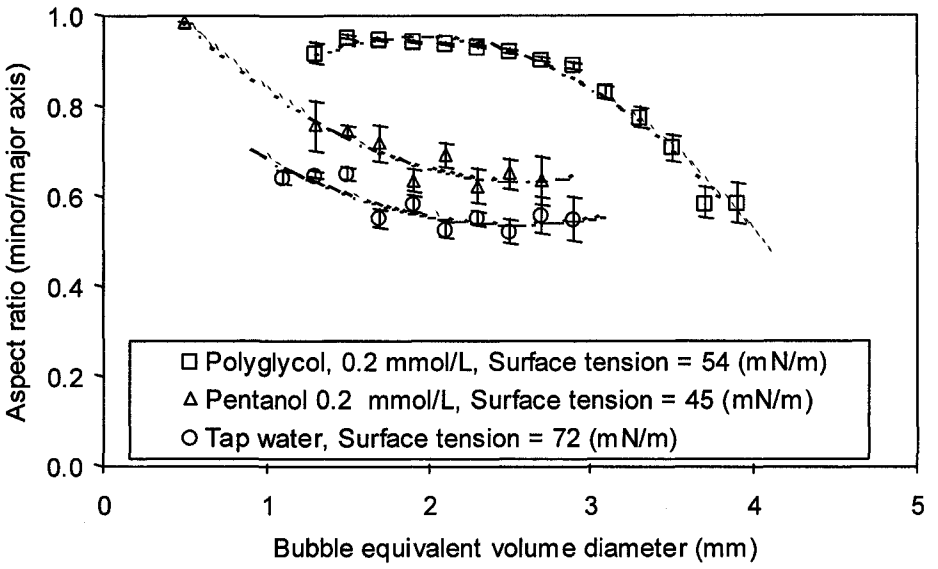

Figure 4.8: Effect of frother type on aspect ratio of bubbles in swarms

From these results the transition in shape (spherical to ellipsoidal) as a function of size appears to be shifted by the frother type, thus bubbles as large as 2.5-3.0 mm can have spherical shape in the presence of Polyglycol, considerably above the value of 1.4 mm typically quoted as being the transition from spherical to non-spherical (ellipsoidal) (Clift et al. 2005).

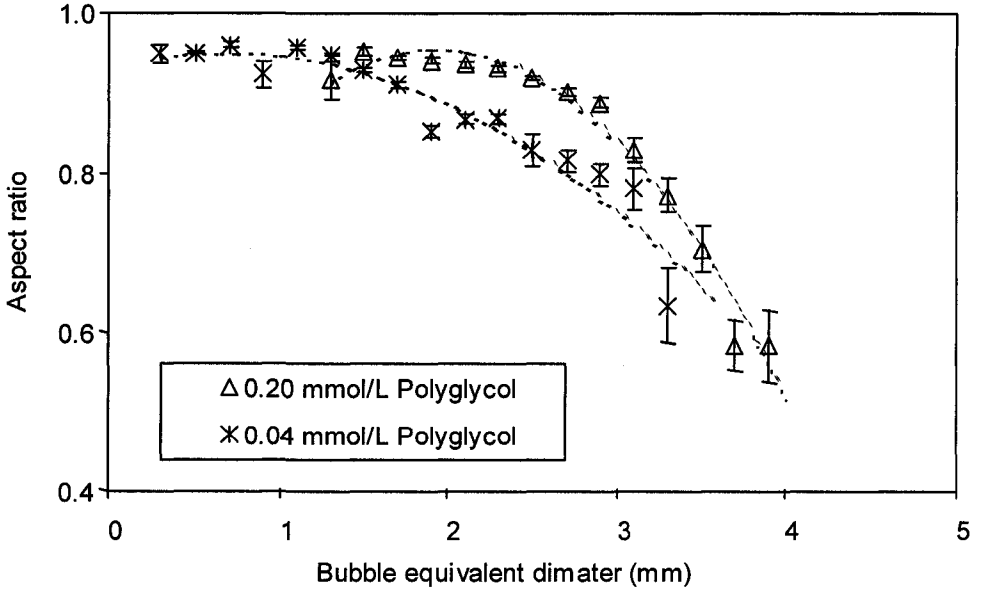

Figure 4.9: Effect of Polyglycol concentration on aspect ratio of bubble swarms

For single bubble studies, bubble shape influences the bubble motion path, as described by Clift et al. (2005). As a bubble changes from spherical to ellipsoidal the rise velocity is reduced because the bubble starts "rocking" (terminal velocity plot for single bubbles in Appendix 1, Figure A1.1), and presents a differing cross-section to the liquid (Tomiyama et al., 2002).

As a consequence, frother has two effects that influence bubble velocity: skin friction (surface mobility is reduced and drag coefficient is increased) and bubble shape, (e.g., shifting the spherical to ellipsoidal transition point). Therefore, bubble swarm velocity measurements should consider and decouple these effects in interpreting frother type effects.

4.3- Frother type effect on bubble surface mobility

Bubble surface mobility measurements, using the technique described in section 3.6, were conducted in tap water alone and the two frother types, n-Pentanol and Polyglycol. These frothers are reported to produce the same bubble velocity at different bubble size (Azgomi et al., 2007), a possible explanation being that frother type may have different effect on skin friction and/or bubble shape.

Surface tension data were measured as a function of molar concentrations for n-Pentanol and Polyglycol using Wilhelmy plate method (Adamson, 1990). The results are shown in Figure 4.10 (Tarkan, 2006). The Szyszkowsky model (Adamson, 1990), for dilute aqueous solutions is used to fit the data and interpolate surface tension values.

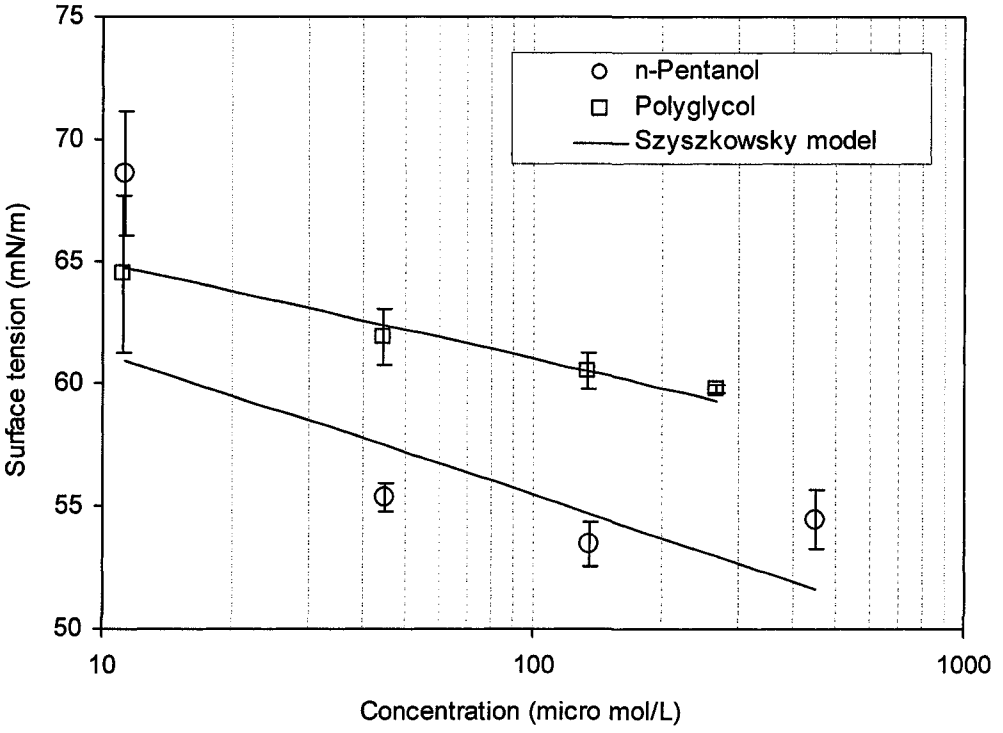

Figure 4.10: Surface tension of Polyglycol and n-Pentanol in tap water (20°C)

A comparison of surface mobility for tap water alone, Polyglycol and n-Pentanol is shown in Figure 4.11. Three pictures are used to show a sequence of motion, with a white marker used to track the moving packets of liquid. Surface tension values, interpolated from Figure 4.10, are noted on Figure 4.11.

A packet of liquid is tracked over 3 to 10 pictures (interval 33 ms) to calculate the average velocity. The measurement is repeated for different packets a total of 9 to 20 times. The results are summarized in Figure 4.12, and the data table is included in Appendix 4.

a) Tap water, σ = 72 mN/m, a = 24 mm, AR= 0.3

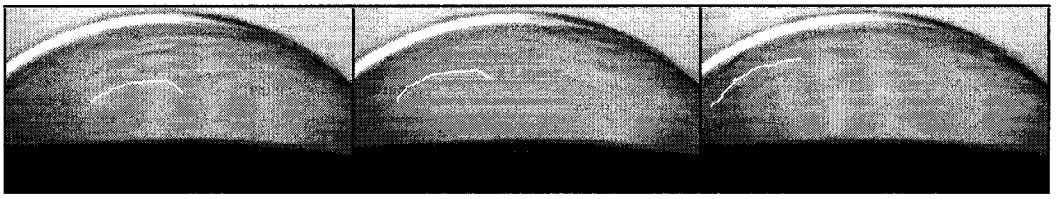

b) 6 mmol/L Polyglycol, σ = 54 mN/m, a = 14 mm, AR= 0.7

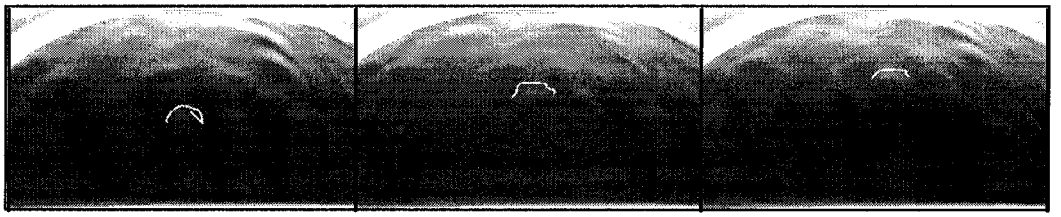

c) 6 mmol/L n-Pentanol, σ = 45 mN/m, a = 18 mm, AR= 0.8

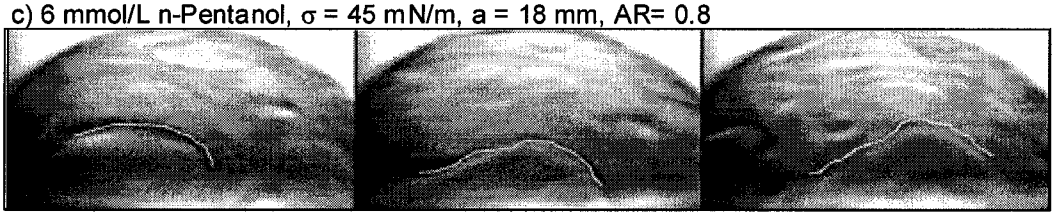

σ : solution surface tension
a : major axis bubble diameter
AR : bubble aspect ratio (minor axis / major axis)

Figure 4.11: Surface texture and tracking for different "liquid packets" on bubbles blown in air (and remaining in contact with solution below)

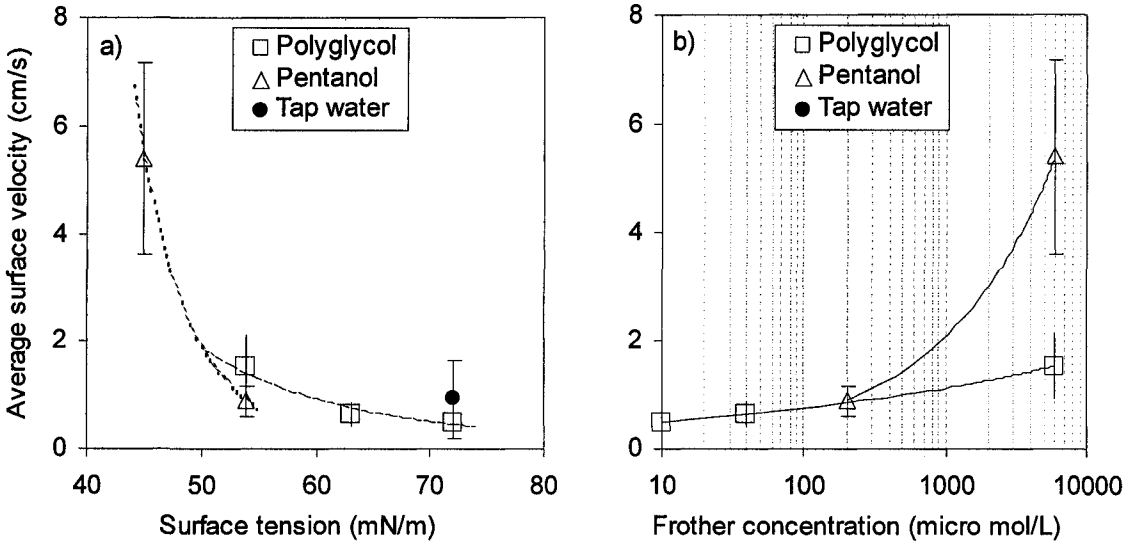

Figure 4.12: Effect of surfactant on average surface velocity

Results in Figure 4.12a show that the average surface velocity seems to depend on surface tension, independent of frother type, although the image texture (Figure 4.11) suggests a difference between the two frothers. These differences in texture may indicate other factors are at play. In addition, surface tension is measured at equilibrium and it does not reveal any effect of distribution of surfactant. A relationship with equilibrium surface tension may be that the larger the equilibrium value the higher is the potential surface tension gradient. Further measurements and texture characterization techniques need to be developed to clarify the observations. From Figure 4.12b, where surface mobility is compared at the same molar concentration, 6 mmol/L, the results seem to reveal the surface velocity for Polyglycol is lower.

Bubble film thickness may also affect surface mobility. Experimental measurement of bubble film thickness revealed its dependency on surfactant type (Gélinas et al., 2005). Finch et al. (2006) showed that Polyglycol had a thicker bubble film (1000 ± 30 nm) than n-Pentanol (< 160 nm). Therefore, surface mobility for bubbles with a thicker film seems to be reduced, according to the experimental measurements of average surface velocity (Figure 4.12).

Surface velocity measurements yielded a high level of dispersion (confidence intervals are large), partly because trajectory velocity values were used (i.e., regardless of the flow direction). Since there are two driving forces that generate surface flow, gravity drainage (flow downwards) and Marangoni flow (flow upwards), it may be more revealing if flows in these two direction vectors are tracked and measured, and these velocities compared among frothers. Another factor that can influence the precision of the technique is the need for orthogonal image correction, which is required to measure velocity over a curved surface. However, as a first approach, the new technique seems to be able to identify texture and measure bubble surface velocity, and suggests that equilibrium surface tension is related to the surface tension gradient and thus appears to be related with the average surface velocity. A subsequent step is to relate these new findings to the question of bubble rise velocity in a swarm.

4.4- Conclusions

When a bubble rises in a solution with surfactant, the surfactant is collected and distributed over the bubble surface generating a concentration gradient, which produces surface pressure, also called Marangoni stress (Ybert and Meglio, 2000), large enough to compensate the dynamic forces. As a consequence the bubble shape tends to remain spherical (Figure 4.1 and 4.8), The effect of surfactant on bubble shape (aspect ratio) is indicative of a non-uniform distribution of surfactant.

The experimental evidence (Figures 4.2 and 4.1) shows that the surfactant adsorption and distribution processes occur after the bubble detaches the generating point. Once the bubble starts to rise, the bubble surface becomes mobile and transports surfactant to the rear. These results confirm the hypothesis, proposed by Dukhin et al. (1998), of surfactant adsorption and distribution on a bubble surface (dynamic adsorption layer), and it is also in agreement with the experimental evidence reported by Malysa et al. (2005).

This non-uniform distribution of surfactant induces the Marangoni effect and confers stiffness (surface rigidity), which increases bubble "skin" friction (reducing bubble rise velocity). The measurement of surface mobility (average surface velocity) on bubbles blown into frother solution may provide experimental measures of Marangoni effect. However, the analogy of a bubble blown in air and a bubble rising in solution must be confirmed.

Frothers appear to accumulate over about a period of ca.10 ms from release, or within about one bubble diameter, using the experiments conducted with Polyglycol (0.1 mmol/L). This may be akin to the adsorption time as reported for single rising bubbles by Sam et al. (1996) and Krzan et al. (2004).

The presence of surfactant reduces bubble coalescence and/or breakage. When bubble swarms are generated, surfactants stabilize the bubble surface and, as a consequence, the bubble size distribution remains stable as the swarm rises (i.e. it does not "evolve"), (for the bubble size range studied 0.1 to 4 mm).

Frothers induce surface flows and textures on bubbles that appear to be dependant on surfactant type. However, further characterization techniques are required for these new observations to be exploited.

CHAPTER 5: Tracking bubble velocity in swarms: experimental results

Experiments to determine the effect of surfactant (concentration and type), bubble interactions and bubble size distribution on bubble velocity in swarms were conducted using the bubble tracking technique developed for 2D bubble swarms (Chapter 3).

The bubble tracking technique allows identification and measurement of individual bubbles velocities in a swarm of bubbles from an image sequence (section 3.3). The images were collected at intervals of 2 ms and bubbles were identified and converted into data structure (sections 3.1 and 3.2). Individual bubble trajectory (section 3.4), inter-bubble distances (section 3.7) and bubble size were computed from the data structure. Bubble velocities are classified by size class at intervals of 0.2 mm, generating a bubble velocity-size relationship.

Slot and porous-slot spargers (Figure 3.50) mounted in a rectangular column (Figure 3.52), were used to generate a 2D array of bubbles. Airflow rate was varied to change bubble size distribution (Figure 3.56) and/or the level of bubble interaction (section 3.7). A combination slot sparger and a porous-slot sparger was used to generate a range of bubble size distributions (e.g., Figure 3.51). Images of the flat front of bubbles were collected at 3 cm and 50 cm above the generating point in order to compare bubble shape stabilization and bubble velocity stabilization (section 4.2). However, in situations when the bubble swarm was too crowded (formation of a more 3D bubble plume), bubbles were directed onto an inclined plane, 90 cm from the generating point, to re-spread them into 2D (Figure 3.52).

5.1- Surfactant effect on bubble velocity reduction in swarms

Individual bubble velocity in swarm was compared for tap water with and with out surfactant (Polyglycol 0.2 mmol/L) (Figure 5.1). Bubble images were collected at 50 cm above the sparger, sufficient distance to stabilize the bubble size distribution in the presence of surfactant. As a reference, single bubble terminal velocity for "clean" and "contaminated" water (Clift et al., 2005) is also plotted. As has been reported for single bubbles, the presence of surfactants reduces bubble terminal velocity (section 4.1). The same effect is evident in the bubble swarm.

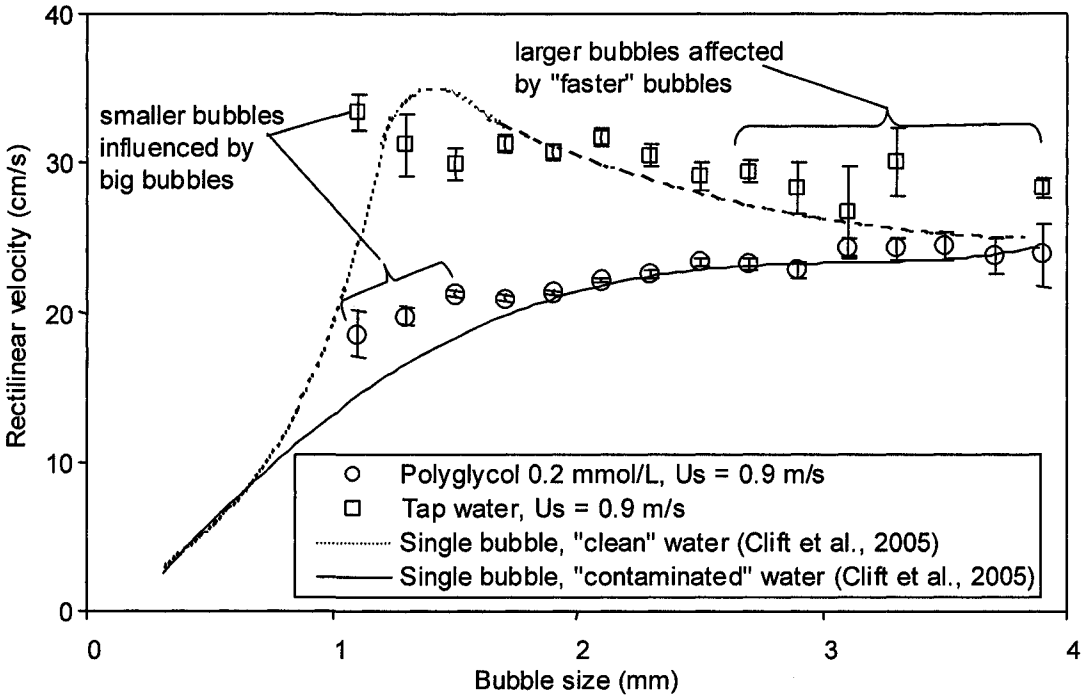

Figure 5.1: Bubble velocity-size profile for tap water and Polyglycol solution (Tests #11 and #28)

For the Polyglycol case, bubbles smaller than 1.8 mm (16% of the population, Figure 5.2) seem to be influenced by the bigger bubbles, i.e., big bubbles appear to drag small bubbles in their wake (Wihelmus, 2001). For the test in tap water, the fastest rising bubbles (1.8-2.5 mm, 36% of the population, Figure 5.2) may be increasing the velocity of the bigger bubbles (> 3 mm). Thus, interactions appear to be significant across the size range (analyzed in section 5.2).

Bubble size distribution (Figure 5.2) for tap water shows a wider distribution than for the Polyglycol solution. The surfactant reduces coalescence and breakage after formation. The reduction in surface tension (60 mN/m) does not seem to influence bubble size formation at a slot, as indicated by the theoretical calculations using the Harris et al. (2005) model in Appendix 1.3.

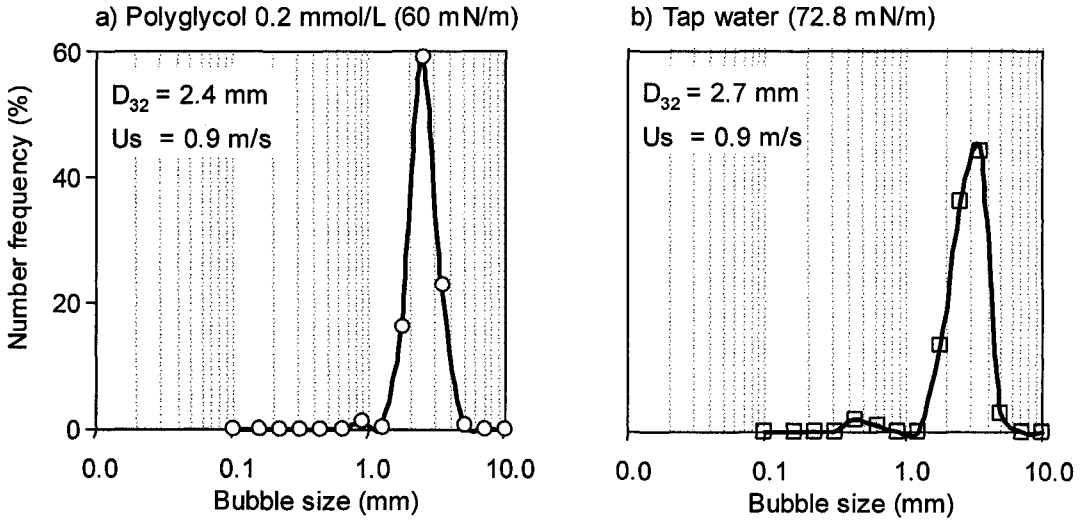

Figure 5.2: Bubble size distribution for Polyglycol solution and tap water (Tests #11 and #28)

Despite this difference in bubble size distribution, the bubble velocity-size profile (Figure 5.1) shows sufficient overlap to compare the two cases.

The reduction in the rectilinear bubble velocity observed for bubbles in Polyglycol solution compared with bubbles in tap water can be a consequence of:

1- Oscillation in bubble trajectory: This effect may be reduced by the presence of surfactant, which helps to maintain bubbles spherical (Figure 4.1). Spherical single bubbles tend to move in a rectilinear path.

2- Surfactant accumulation and reduction in bubble surface mobility: Surfactant re-distribution on the bubble surface increases "skin" friction and, as a consequence, bubble rise velocity is reduced.

3- Bubble interactions: Reduction in velocity makes bubbles come closer together consequently giving a higher level of interaction. The increase in interaction will reduce bubble rise velocity (hindered rise effect). Therefore, bubble inter-distance and bubble velocity-size profiles should be related.

Each possibility is analyzed.

5.1.1- effect of bubble shape on bubble oscillation and bubble path

Bubble shape, size and surface stability determine the degree of oscillation of a single rising bubble (Tsuge and Hibiono, 1977; Tomiyama et al., 2002). As shown in section 4.1, surfactants confer bubble surface stability and tend to keep bubbles spherical (aspect ratio above 0.9 (Clift et al., 2005)), for sizes up to 2 mm or more, as shown in Figure 4.8. As a consequence, the presence of surfactant tends to make single bubbles rise rectilinearly. A change in bubble shape (i.e., to ellipsoidal) produces bubble oscillation and reduction in rise velocity. However in a bubble swarm, where bubble interaction play a role, the effect of bubble oscillation could affect differently the bubble rise rectilinear velocity.

A comparison of aspect ratio distributions for bubbles in Polyglycol solution and tap water is shown in Figure 5.3. In Polyglycol bubbles are more spherical, which should cause less oscillation than for bubbles in tap water.

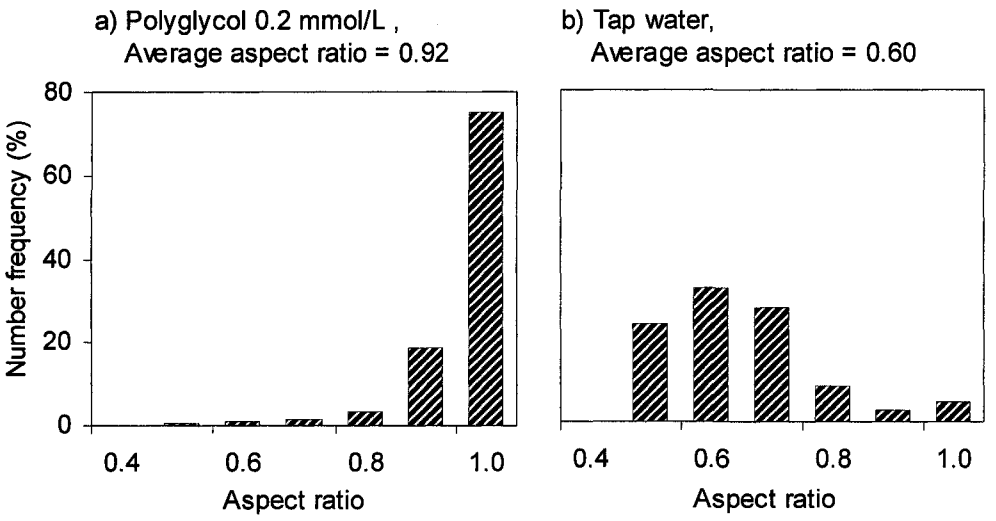

Figure 5.3: Bubble AR frequency distribution for Polyglycol solution and tap water (Tests #11 and #28)

However, comparing the bubble trajectory mapping plots (showing individual bubble trajectories) in Figures 5.4 and 5.5 over a 300 ms time frame, it can be observed that bubbles in Polyglycol solution do oscillate, but the amplitude of oscillation and velocity changes in the horizontal direction are higher for tap water. Alternatively, to characterize horizontal bubble motion a velocity frequency distribution can be created from the data structure. A comparison of horizontal bubble velocity is shown in Figure 5.6 for tap water and Polyglycol 0.2 mmol/L.

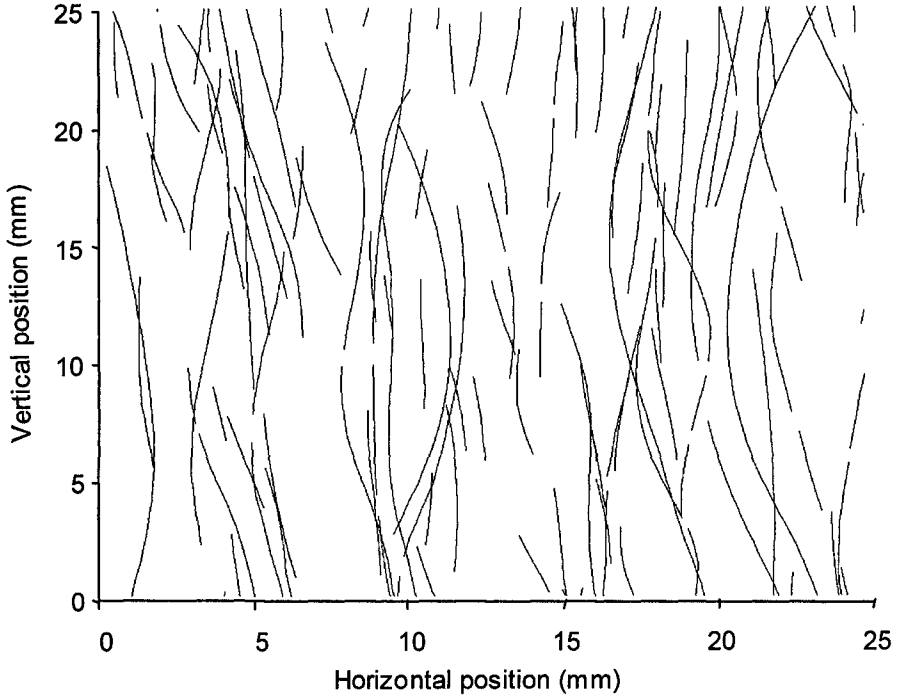

Figure 5.4: Bubble trajectory mapping in Polyglycol solution (0.2 mmol/L)
(Time frame 300 ms, test #11)

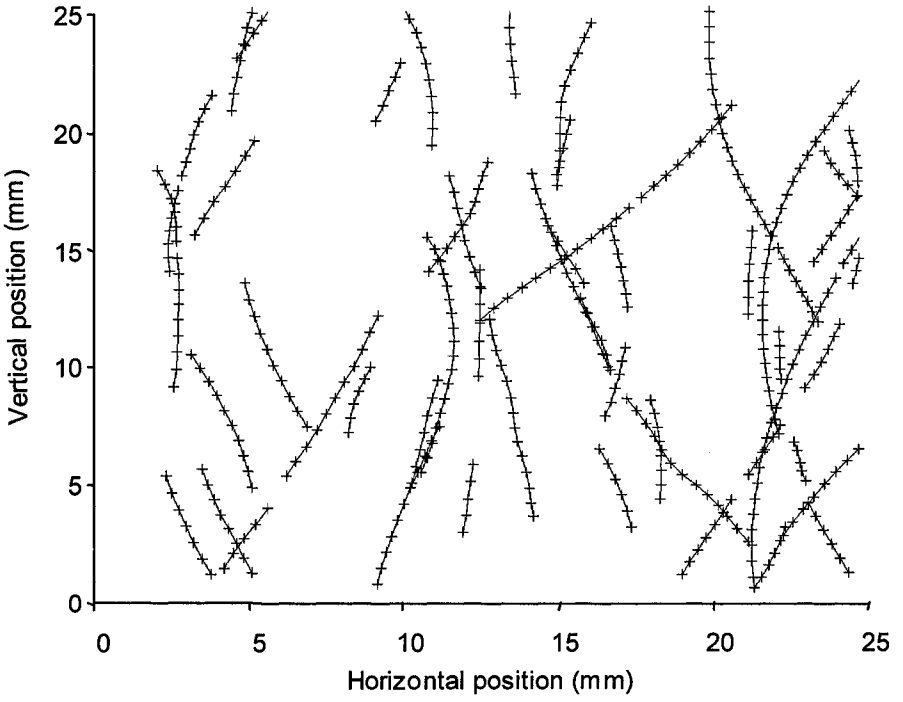

Figure 5.5: Bubble trajectory mapping in tap water
(Time frame 300 ms, test #28)

Figure 5.6 confirms that bubbles in tap water show more oscillation than bubbles in Polyglycol solution. Therefore the differences in velocity observed in Figure 5.1 would seem not to be a consequence of oscillation. The difference may be a consequence of bubble interactions or a reduction in surface mobility or increase in surface viscosity for bubbles in Polyglycol solution, as previously discussed in section 4.3.

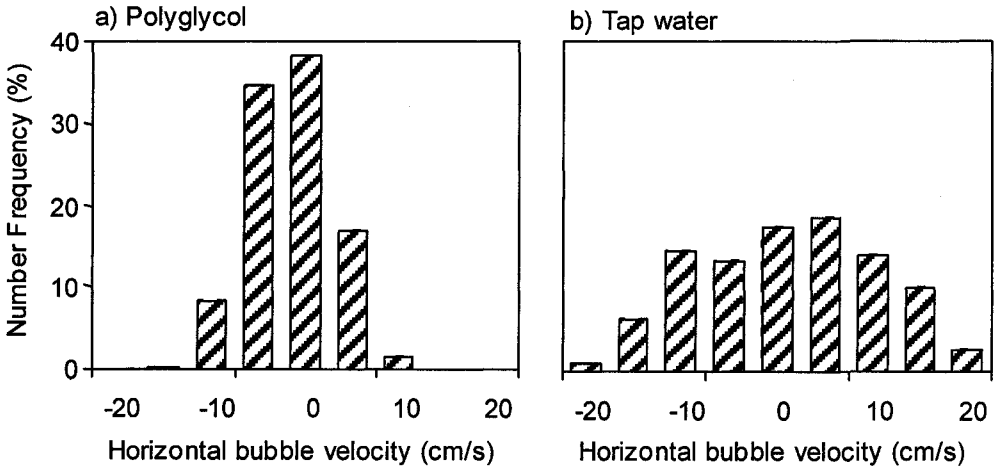

Figure 5.6: Horizontal velocity frequency distribution for bubbles in Polyglycol solution and tap water (Tests #11 and #28)

5.1.2- effect of surfactant accumulation time

On rising bubbles surfactant adsorbs and distributes over the surface, as shown by the experimental evidence in section 4. The surfactant adsorption rate depends on surfactant type and concentration (Ybert and Meglio, 2000; Zhang et al., 2001). For bubble swarms, one expectation is to detect a reduction in bubble rise velocity with the distance as the surfactant is being accumulated, similar to the velocity-distance (time) profile introduced by Sam et al. (1996) for single bubbles.

Bubble velocity-size plots (profiles) were constructed to compare the effect of surfactant accumulation on velocities at two locations (i.e., impact of surfactant accumulation). The comparison was performed at 3 cm and 50 cm above the bubble generating point (Figure 3.52) with bubbles injected into 0.2 mmol/L Polyglycol

solution using a slot sparger of 90 μm gap (Figure 3.50). The results in Figure 5.7 show evidence of a reduction of bubble rise velocity, implying accumulation of surfactant between the 3 and 50 cm rise distance.

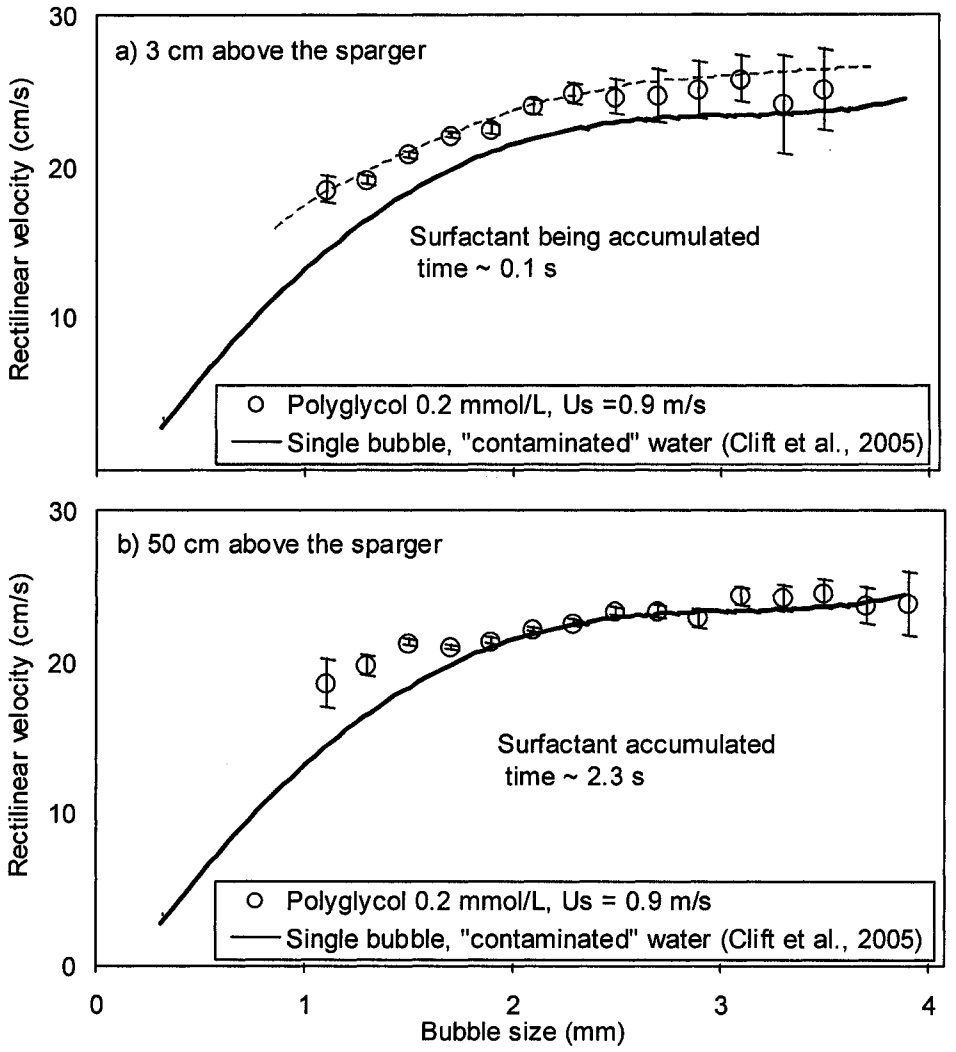

Figure 5.7: Evidence of surfactant accumulation reducing bubble rise velocity.
(Tests #7 and #11)

In Figure 5.7a it can be noted that for bubbles larger than ca. 2.5 mm the velocity varies significantly (large 95% confidence interval). This variation is a consequence of bubble shape (measured by aspect ratio). Bubbles larger than 2.5 mm at 3 cm above the sparger have ellipsoidal shape (aspect ratio < 0.9) and an unstable shape (higher dispersion coefficient for the aspect ratio), while bubbles stabilized by the

surfactant at 50 cm tend to remain spherical and more stable in shape (constant aspect ratio). To demonstrate, aspect ratio and the confidence interval versus bubble size are shown in Figure 5.8 for the two locations. From the insert plot in Figure 5.8, bubble size distribution at 3 cm and 50 cm is practically the same (equivalent volume diameter calculated assuming an oblate spheroid).

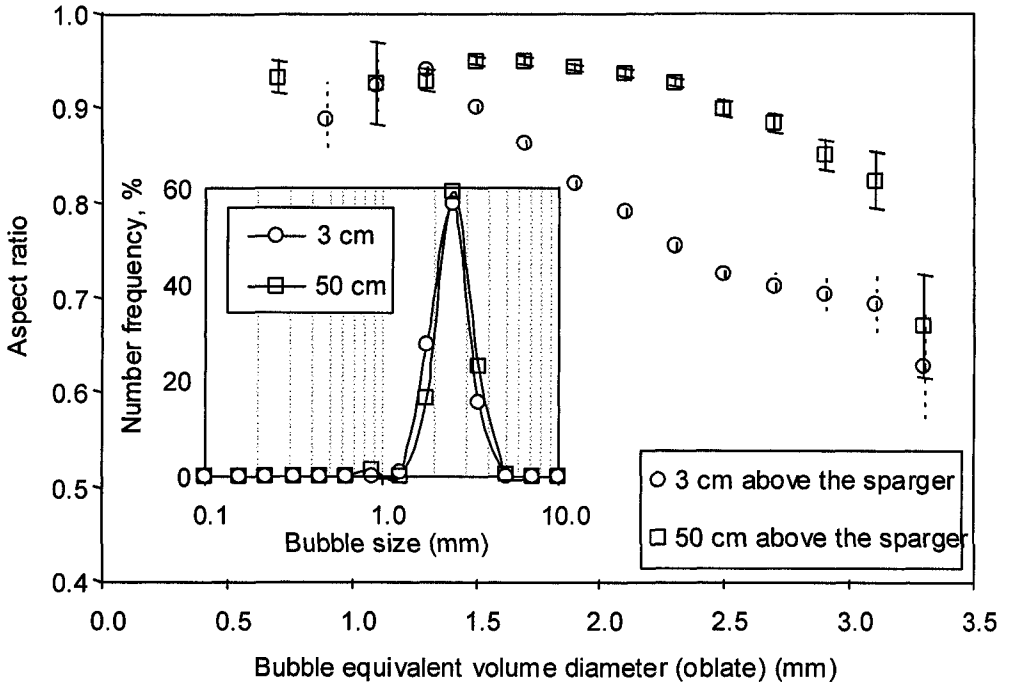

Figure 5.8: Evidence of surfactant conferring bubble shape stability as swarm rises (Tests #7 and #11)

Aspect ratio distributions for bubbles in Polyglycol solution and tap water are also shown in Figure 5.9. The changes in shape as bubbles rise are indicative that frother is being accumulated (and distributed) with time, which decreases surface mobility and as a consequence, bubble rise velocity is reduced.

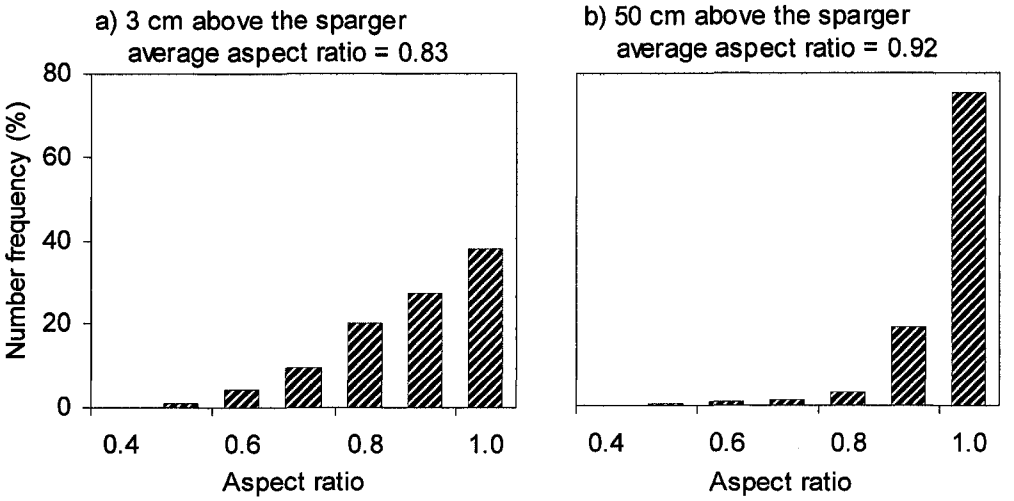

Figure 5.9: Evidence of surfactant changing bubble shape (AR) as swarm rises (Tests #7 and #11)

5.1.3- effect of surfactant concentration

Comparing bubble velocity-size profiles at two concentrations of surfactant 50 cm from the generating point (approximately 2.2 s after generation) also reveals the effect of surfactant accumulation on bubble rise velocity. Compared to Figure 5.10a, the velocity for bubbles > 1.8 mm is significantly lower than in Figure 5.10b for the lower concentration. The small bubbles (0.2 to 0.5 mm) in swarms are strongly affected by the faster rising, larger bubbles (Figure 5.10b). Small bubbles are effectively "carried" by bigger bubbles. The bubble interaction factor seems to be significant in swarm bubble motion, which will be reviewed later in the thesis (section 5.2).

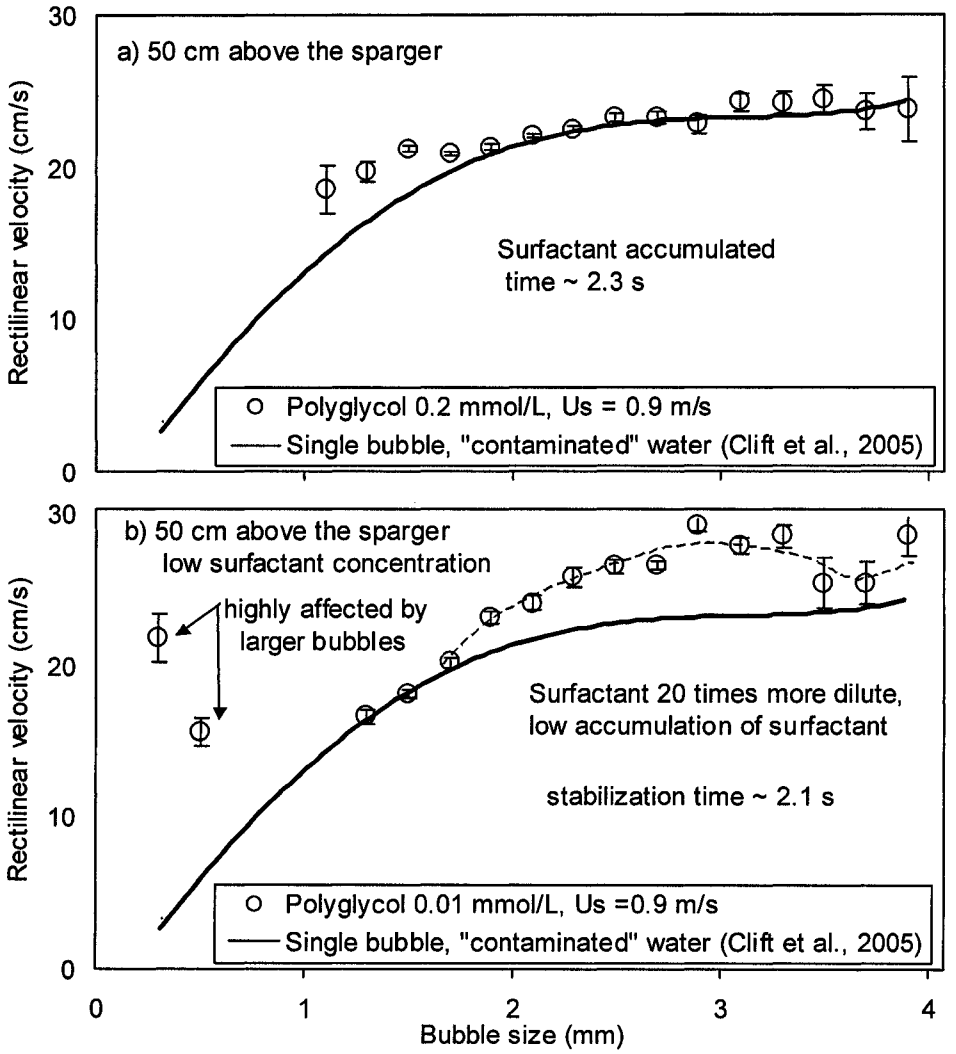

Figure 5.10: Evidence of surfactant concentration reducing bubble rise velocity
(Tests #18 and #11)

The presence of small bubbles created by breakage in the low frother concentration case (Figure 5.11a), as discussed in section 4.2.1, can be observed; high surfactant concentration reduces bubble breakage (Figure 5.11b).

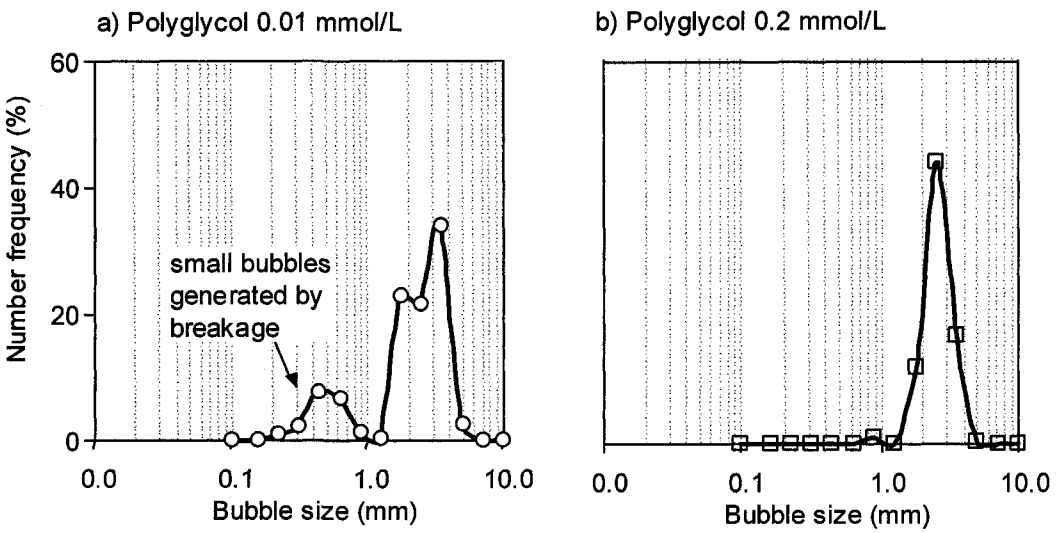

Figure 5.11: Evidence of surfactant accumulation effect on BSD.
(Tests #18 and #11)

The experimental evidence, summarized in Table 5.1, shows that surfactant is accumulated over time on the bubble surface (stabilization time), reducing the bubble velocity-size profile. The Table also shows the surfactant confers bubble shape stability (aspect ratio close to 0.9). With these results and the experiments shown in Figure 4.8, it is possible to conclude that the surfactant is distributed on a bubble surface creating a concentration and surface tension gradient, that makes the bubble spherical and stiffer.

Table 5.1: Effect of surfactant on bubble rise velocity profile

Test type	Stabilization time s	Polyglycol concentration mmol/L	AR	Figure
Reference test at 50 cm from the sparger	~2.3	0.2 (80 ppm)	0.92	5.7b
1- Stabilization time at 3 cm from the sparger	~0.1	0.2 (80 ppm)	0.83	5.7a
2- Frother concentration 50 cm from the sparger	~2.1	0.01 (5.4 ppm)	0.60	5.9

Ultimately, the reduction of the on bubble velocity-size profile is a consequence of the increment in skin friction created by surfactant accumulation and distribution over the bubble surface as the bubble rises. The reduction in velocity may also increase bubble interactions, which can affect the bubble velocity-size profile.

5.2- Effect of bubble inter-distance and BSD type on bubble swarms

To analyze the effect of bubble interactions (bubble collisions and wake effect) on bubble velocity-size profile, measurements were conducted at two levels of interactions and bubble size distribution type (narrow, wide and bimodal).

5.2.1- comparison of similar BSDs at two level of interactions

Two similar bubble size distributions were generated at two airflow rates in order to compare the effect of bubble interactions on the bubble velocity-size profile. To characterize the level of interaction, the mean dimensionless inter-bubble distance (d*), described in section 3.7.2, was used. The bubble swarms were injected in a 0.2 mmol/L Polyglycol solution, and the bubble images were collected at 50 cm from the sparger to allow bubble surfaces to stabilize. The superficial gas velocity in the slot was set at two levels, 0.9 m/s and 2.2 m/s. The results are shown in Figure 5.12.

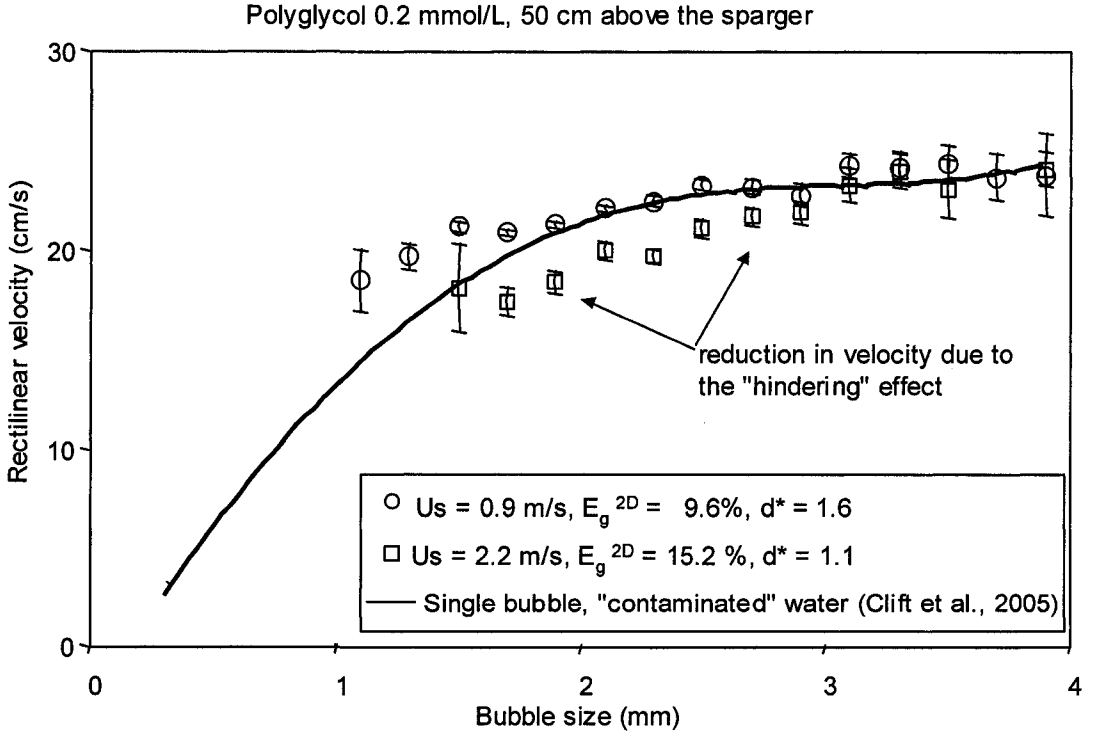

Figure 5.12: Effect of bubble interaction on bubble velocity-size profile (similar BSD) (Tests #11and #12)

The bubble size distributions and the corresponding aspect ratio distribution (bubble shape) are shown in Figure 5.13 and Figure 5.14, respectively. These results show that the population of bubbles has the same average aspect ratio (0.92) i.e., same bubble shape (Figure 5.14). Sauter diameter (D_{32}), for bubbles generated at higher superficial gas velocity (2.2 m/s), is 15% larger than at the lower velocity. However, from the bubble size distribution shown in Figure 5.13 and bubble velocity-size profile shown in Figure 5.12 both populations overlap enough to make a comparison.

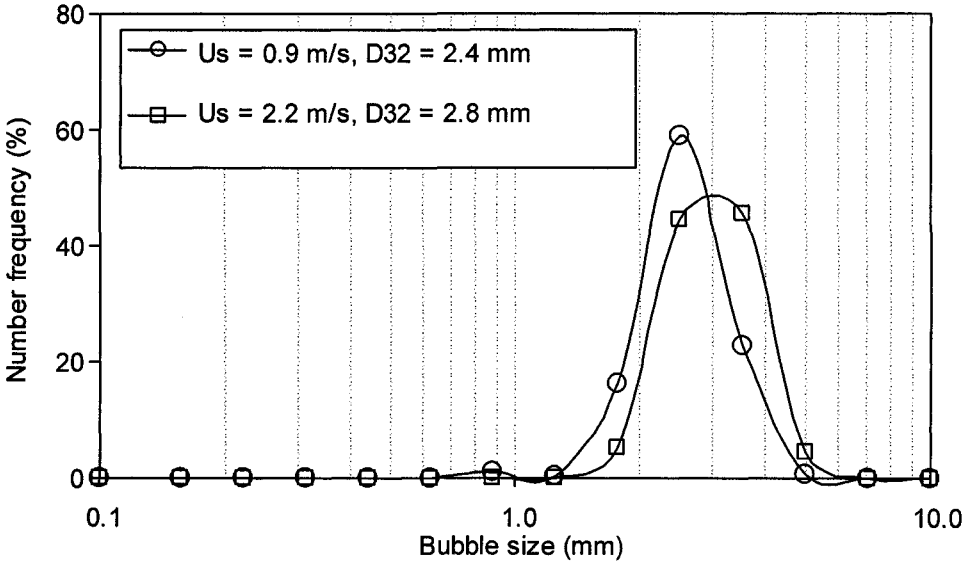

Figure 5.13: BSD at two levels of bubble interactions
(Tests #11and #12)

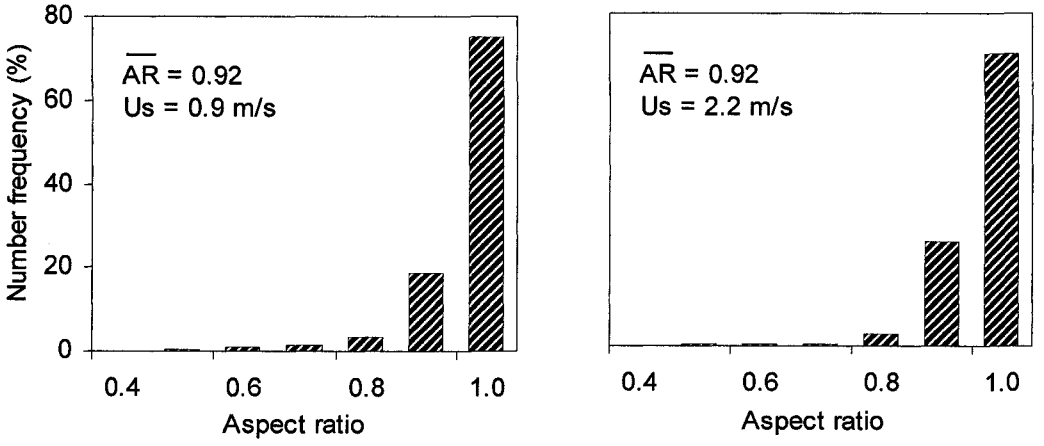

Figure 5.14: Bubble AR frequency distributions at two levels of interactions
(Tests #11and #12)

The experiment revealed that the bubble velocity-size profile was reduced as the bubble interaction increased. The average reduction (taking the velocity ratios in each bubble size class) is 0.93. This result is in agreement with the fundamental models, e.g. proposed for settling particles (rigid surface) by Richardson and Zaki (1954) and its adaptation for bubble swarms by Dobby et al. (1988). According to the model proposed by Dobby et al. (1988), for a mono size distribution, the expected reduction in velocity for the conditions presented in Figure 5.13 is 0.91. In actual bubble size distributions some bubbles seem to be influenced by other bubbles (faster rising bubbles dragging smaller bubbles in the wake), as shown in Figure 5.1 and 5.10. This effect is also noted for wide bubble size distributions, as analyzed in section 5.2.2.

5.2.2- comparison of a narrow and a wide bubble size distribution

Bubble velocity-size profiles were measured for two bubble size distributions (narrow and wide) in order to compare the effect of BSD type on bubble motion. The superficial gas velocity in the slot was set to 0.2 m/s and 1.0 m/s producing a dimensionless bubble inter-distance of 0.9 and 1.7, respectively. Bubble images were collected at 6 cm above the sparger and these bubbles were dispersed in a 0.04 mmol/L Polyglycol solution. The conditions give sufficient time and surfactant concentration to create spherical and stable bubble size distributions. The results are shown in Figure 5.15.

The bubble size distribution generated and the aspect ratio distribution (bubble shape) for the two gas velocity conditions are shown in Figure 5.16 and Figure 5.17, respectively. These results show that bubble shapes are spherical (average aspect ratio > 0.91), and the narrow bubble size distribution overlaps with the wide distribution. Examples of images for the two bubble size distributions are shown in Figure 5.18

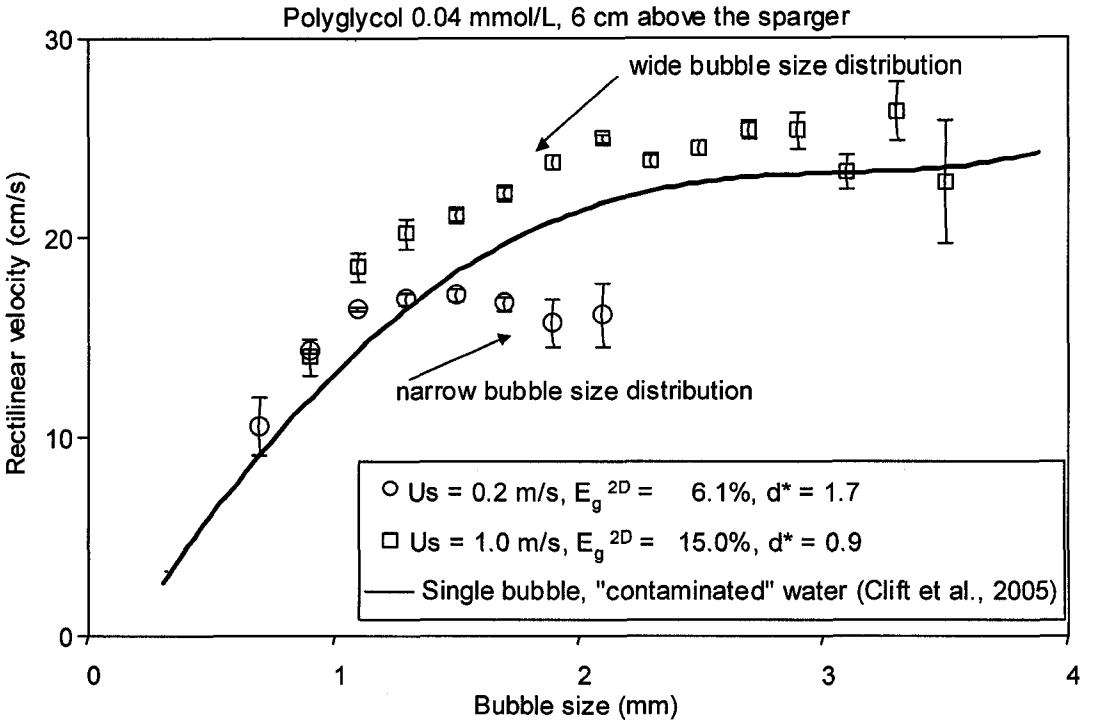

Figure 5.15: Bubble velocity-size profile comparison for narrow and wide BSDs (Tests #49and #51)

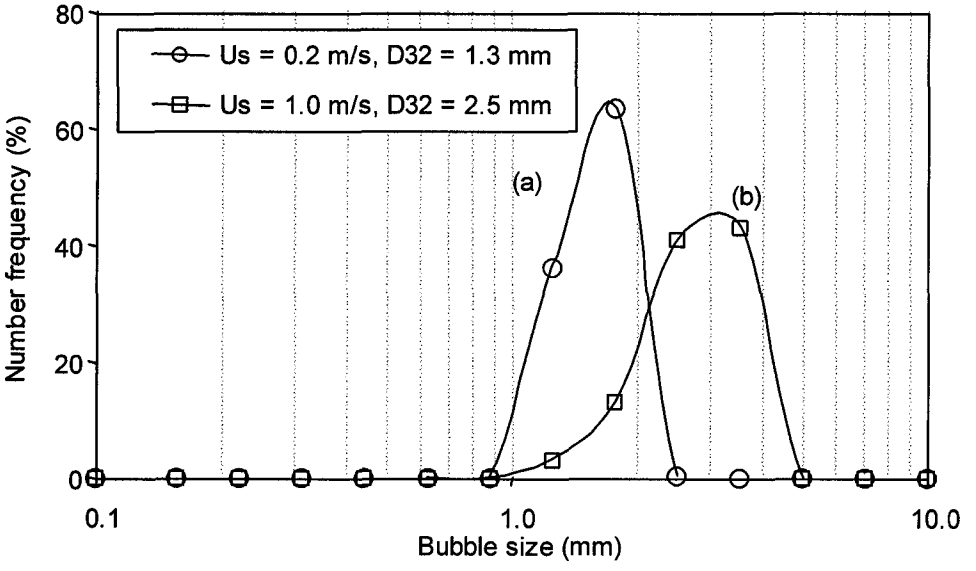

Figure 5.16: Wide and narrow BSDs at two levels of superficial gas velocity (Tests #49 and #51)

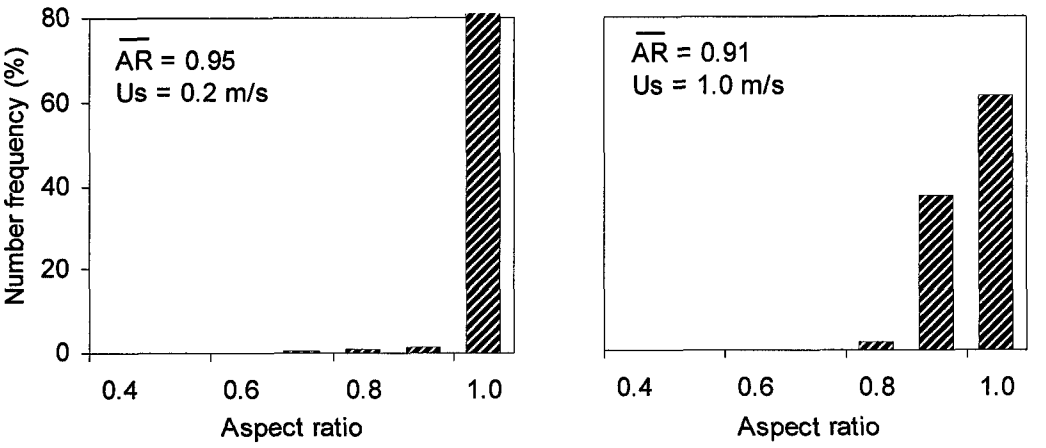

Figure 5.17: Bubble AR frequency distributions for wide and narrow BSDs (Tests #49and #51)

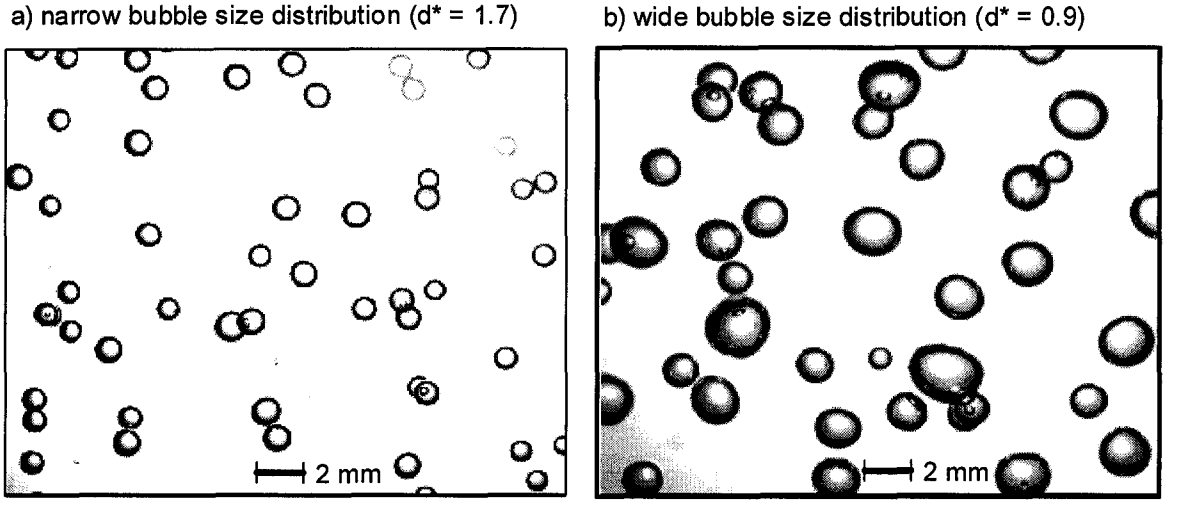

Figure 5.18: Image examples of narrow and wide BSDs (Tests #49 and #51)

The results in Figure 5.15 reveal that the bubble velocity-size profile was dependent on bubble size distribution type. For the narrow bubble size distribution (Figure 5.16a), despite the low level of interaction (or larger bubble inter-distance, d* = 1.7), slower rising bubbles (below 1.4 mm) reduced the rise velocity of larger bubbles (1.4-2.2 mm); this suggests a hindering effect, where the predominant population of small bubbles (77% below 1.4 mm) restrict the motion of the larger ones.

In contrast, for the wide bubble size distribution (Figure 5.16b) and high level of interaction (or shorter bubble inter-distance d* = 0.9), larger bubbles (predominant population (84%) above 2.5 mm) increased the rising velocity of bubbles in the range 1.4-2.2 mm. This could be a consequence of: a) bubbles being drawn into the bubble wake, in analogy to experimental evidence found by Krishna et al. (1999) for large bubbles (3-6 mm) rising in swarms; or b) a hindering effect, where larger bubbles "push" smaller bubbles increasing their rising velocity. These two effects are discussed in following section 5.2.3.

5.2.3- comparison of a narrow and a bimodal bubble size distributions

To study the effect of bubble wake (Fujiwara et al., 2004) and the hindering effect on bubble velocity-size profile, a bimodal bubble size distribution at low level of interaction (d* = 2.7) was compared with a narrow bubble size distribution at higher level of interaction (d* = 0.9). To generate a bimodal BSD the narrow-slot sparger was used (Figure 3.50), and the superficial gas velocity (Us) was set to 1.9 m/s. The narrow BSD was generated using the porous-slot sparger and the superficial gas velocity (Usp) was set to 0.03 m/s. A 0.1 mmol/L Polyglycol solution was used and bubble images were collected at 90 cm above the sparger in the inclined section (Figure 3.52), in order to reduce the number of superimposed bubbles (reduce crowding). The bubble velocity-size profile results are shown in Figure 5.19 and bubble size distributions in Figure 5.20.

The aspect ratio distributions (bubble shape) are shown in Figure 5.21; the average aspect ratio for both bubble size distributions is above 0.9 (bubbles are considered spherical).

An example of selected pictures for the two bubble size distributions is shown in Figure 5.22.

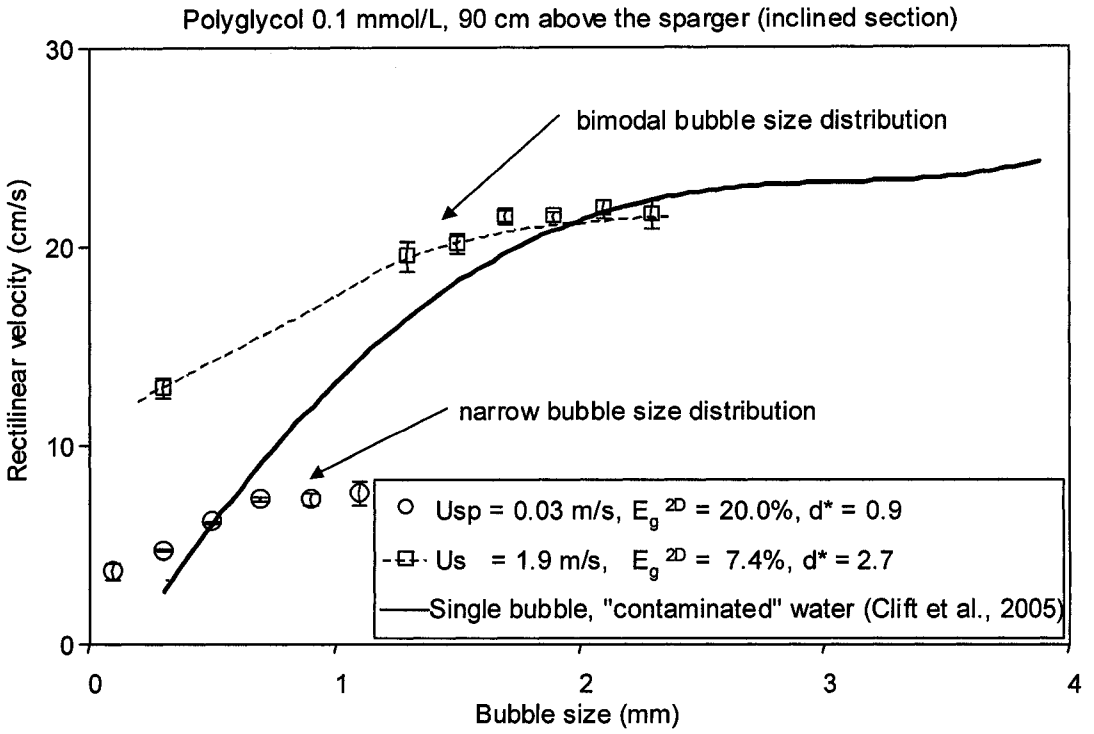

Figure 5.19: Bubble velocity-size profile comparison for narrow and bimodal BSDs (Tests #64 and #68)

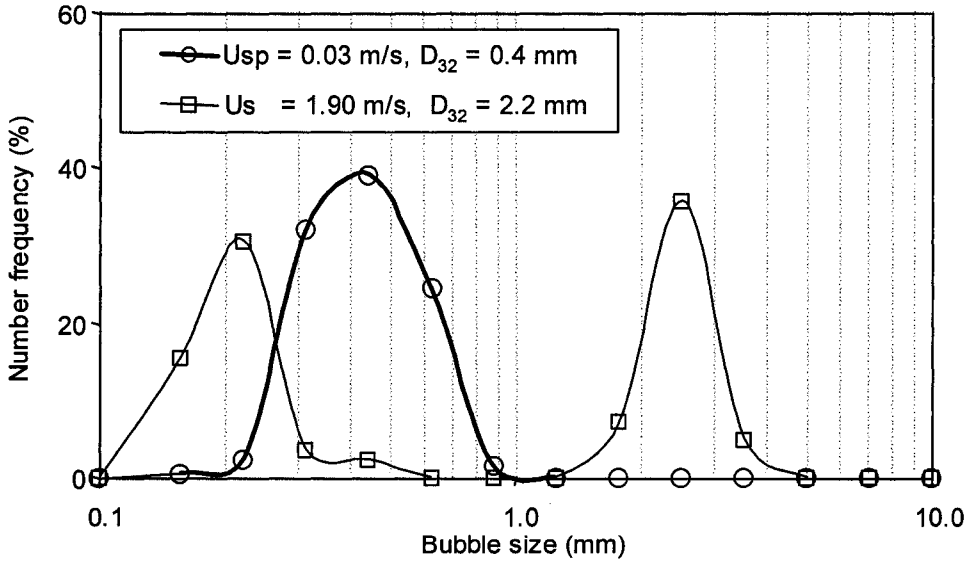

Figure 5.20: Narrow and bimodal bubble size distributions (Tests #64 and #68)

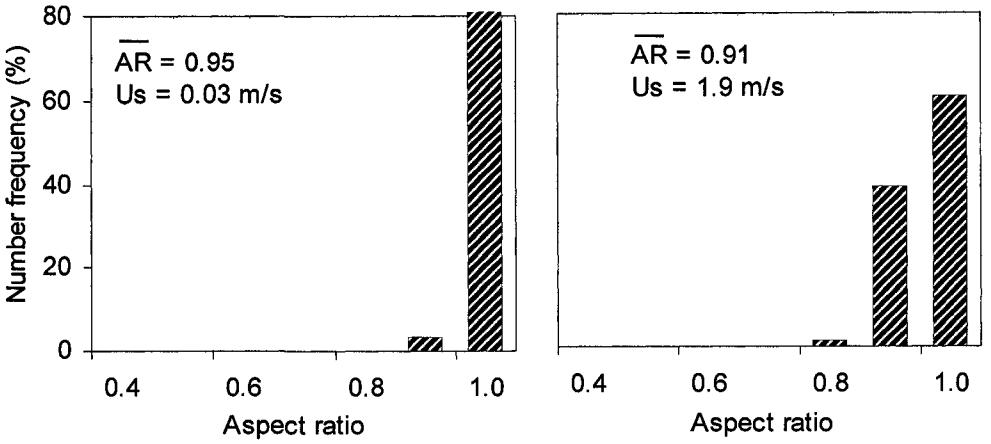

Figure 5.21: Bubble AR frequency distributions for narrow and bimodal BSDs (Tests #64 and #68)

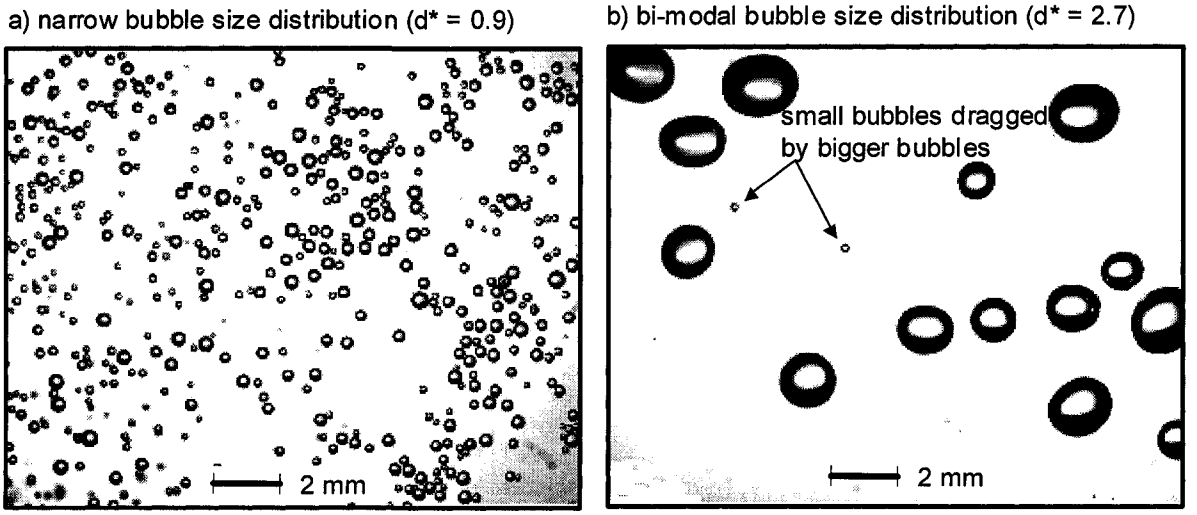

Figure 5.22: Image example of narrow and bimodal BSDs (Tests #64 and #68)

The results (Figure 5.19) imply that small bubbles in the bimodal bubble size distribution are dragged into the bubble wake even with the relatively low level of interaction (bubble inter-distance d*= 2.7). For the narrow bubble size distribution, the hindering effect tends to reduce bubble rise velocity for the larger bubbles at both levels of interaction: a) low level of interaction (d*=1.7) show in Figure 5.15, and b) high level of interaction (d*=0.9) shown in Figure 5.19.

5.2.4- bubble inter-distance and gas holdup relationship validation

The dimensionless bubble inter-distance and the area fraction of gas were measured directly on a sequence of bubble images at three concentration levels of surfactant (0.01, 0.02 and 0.20 mmol/L). The measurements and the 95% confidence interval are shown in Figure 5.23.

From these results, it can be concluded that the dimensionless bubble inter-distance parameter can be used as a direct measurement of the level of bubble interactions in bubble swarms.

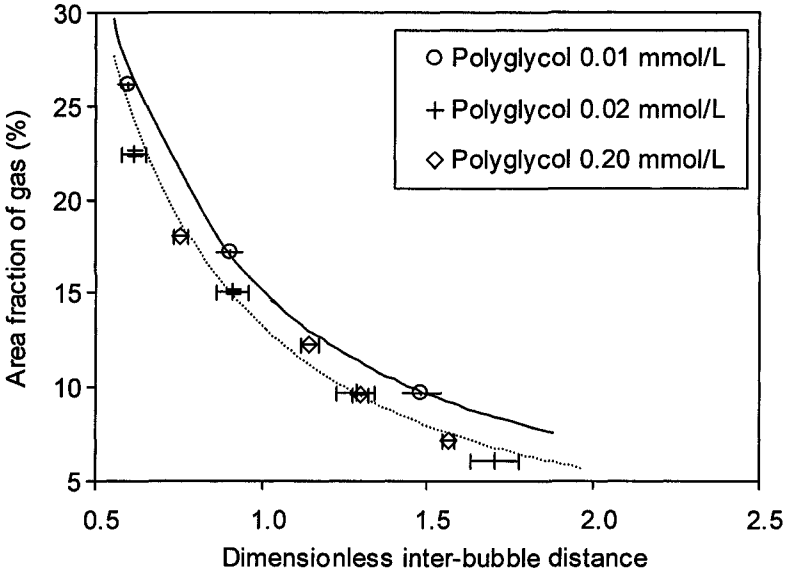

Figure 5.23: Dimensionless bubble inter-distance and area fraction of gas relationship for Polyglycol solutions
(Tests: 7-10, 48-51,15-17)

5.3- Effect of frother type on bubble motion in swarms

Experiments with Polyglycol and n-Pentanol solutions (i.e. a, strong v/s weak frother) were conducted to determine any effect of frother type on bubble motion.

5.3.1- effect of Polyglycol and n-Pentanol solutions on bubble motion at the same superficial gas velocity and D_{32} ~3 mm

A comparison of bubble velocity-size profile between Polyglycol and n-Pentanol solutions at the same molar concentration (0.2 mmol/L) is shown in Figure 5.24 (at this concentration both frothers reduce bubble size in flotation systems). The superficial gas velocity (Us) was set to 2.0 m/s in a 90 μm slot sparger for both experiments. Bubble images were collected at 50 cm above the sparger, sufficient distance to stabilize the bubble size distribution in the presence of surfactant (Figure A4.1). As a reference, single bubble terminal velocity for "clean" and "contaminated" water (Clift et al., 2005) is also plotted.

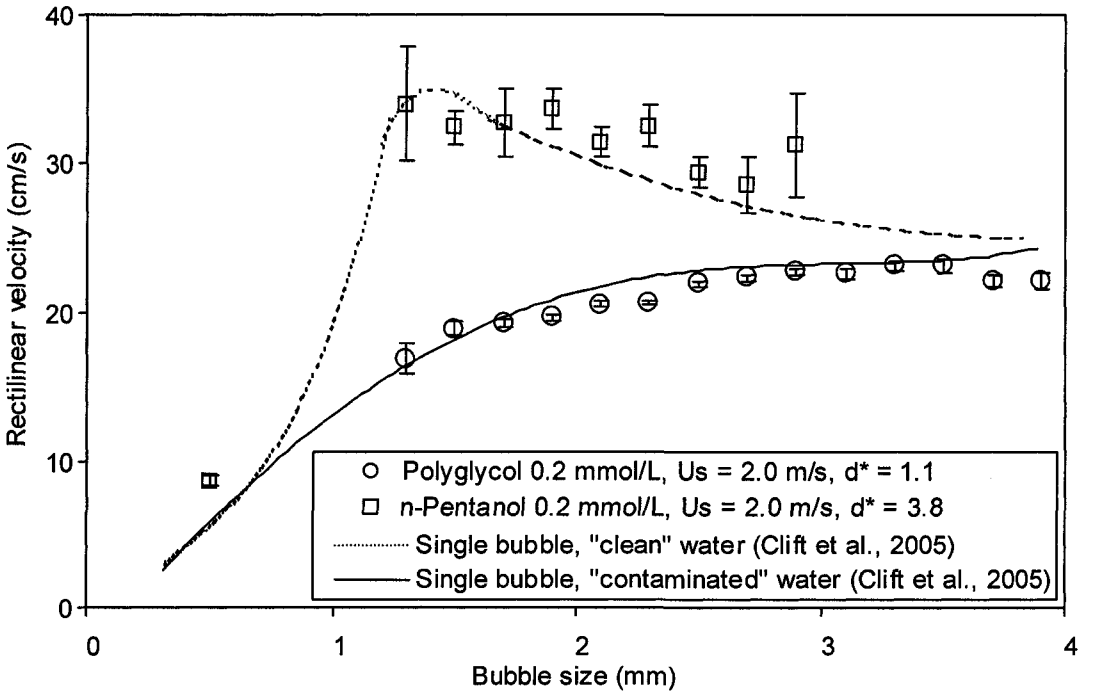

Figure 5.24: Bubble velocity-size profile for rising bubbles in Polyglycol and n-Pentanol solutions (same superficial gas velocity and sparger type).
(Test #12 and #41)

The resulting bubble size distributions are shown in Figure 5.25. The Sauter diameters are similar (~3 mm), but bubble shape (aspect ratio) are significantly different as shown in Figure 5.26.

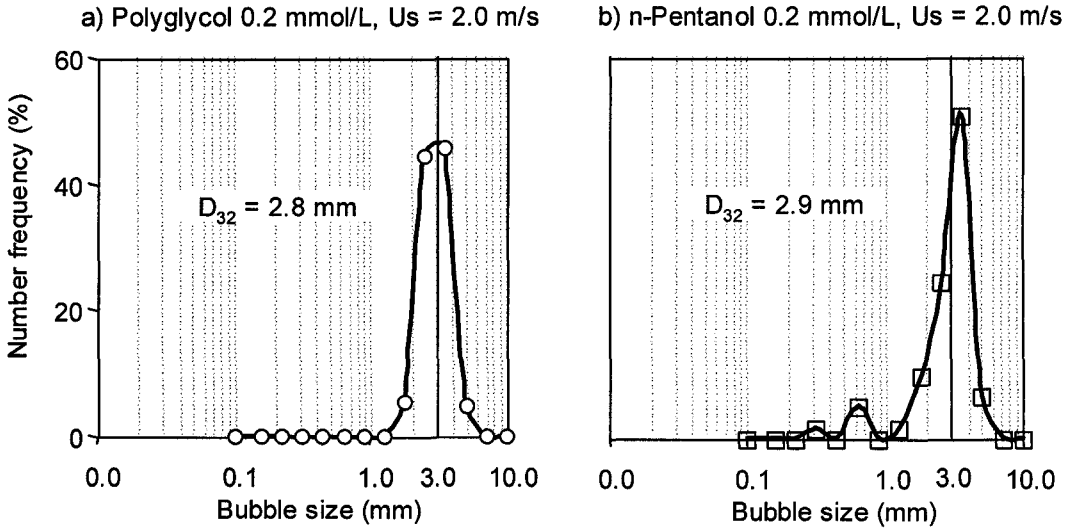

Figure 5.25: Frequency size distributions for bubbles in Polyglycol and n-Pentanol solutions (Test #12 and #41)

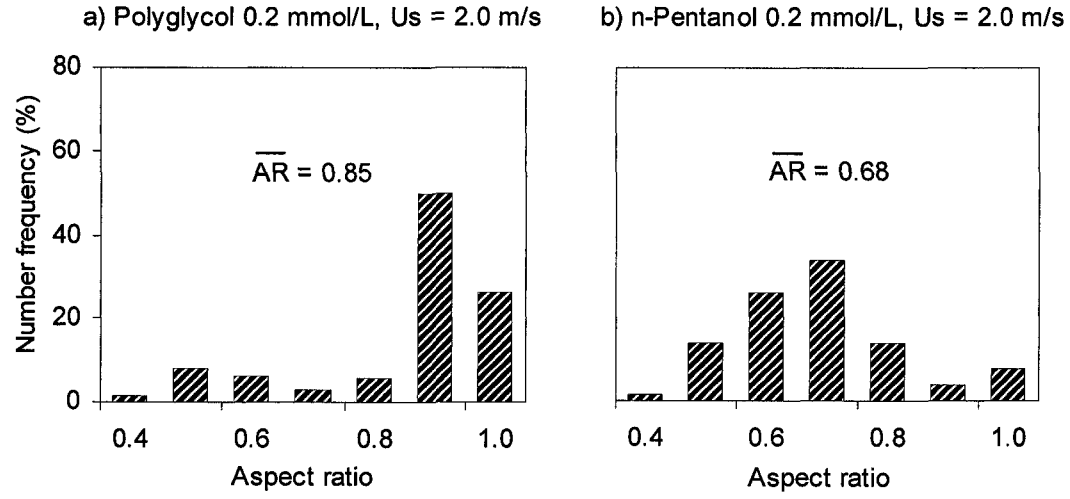

Figure 5.26: AR frequency distributions for bubbles in Polyglycol and n-Pentanol solutions (same Us). (Test #12 and #41)

As discussed in Section 5.1.1, a low aspect ratio (< 0.9) creates bubble oscillation, which can be characterized by a horizontal bubble velocity frequency plot. A comparison of these velocities is shown in Figure 5.27. Bubbles in n-Pentanol solution evidence more oscillation (Figure 5.27b) than bubbles rising in Polyglycol

solutions (Figure 5.27a), which is consistent with the aspect ratio shown in Figure 5.26. The results in n-Pentanol are similar to those in water only (Figure 5.1 and 5.3).

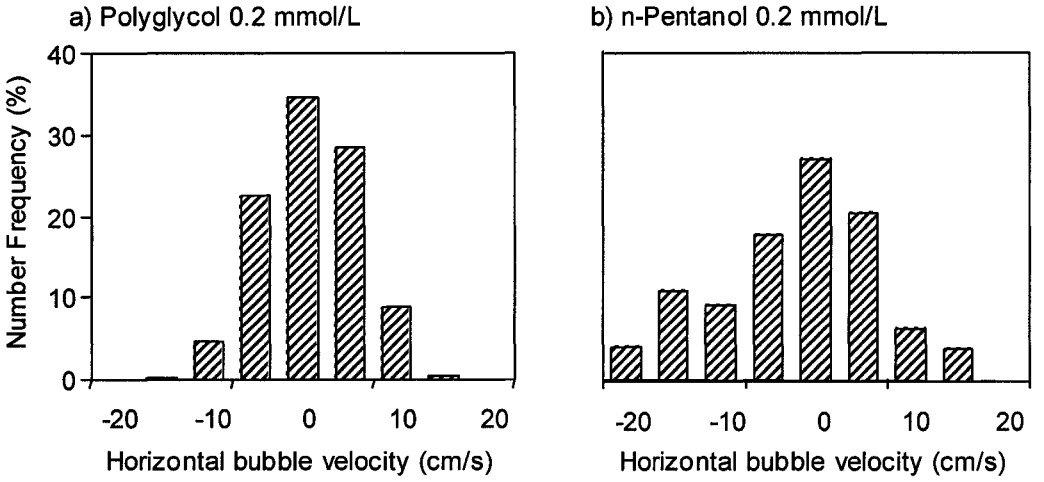

Figure 5.27: Horizontal velocity frequency distributions for rising bubbles in Polyglycol and n-Pentanol solutions
(Tests #12 and #41)

These results show that bubbles in Polyglycol rise slower than in n-Pentanol for otherwise similar conditions. In deed in n-Pentanol the effect is little different from water alone despite the fact this concentration is quite sufficient to reduce bubble size (an important function of frother) (Nesset et al., 2007; Azgomi et al., 2007). As a consequence frother type appears to be a new factor influencing bubble motion.

The results are in broad agreement with the observation of Azgomi et al. (2006, 2007). They noted that low concentrations of Polyglycol produced coarser bubbles than high concentration of n-Pentanol but the gas holdup were similar. The explanation, based on swarm velocity, inferred that bubbles in Polyglycol rise more slowly than in n-Pentanol. Interestingly their results for n-Pentanol implied bubble rising at the same speed as it in water alone, again, consistent with the current findings.

However, the dimensionless bubble inter-distance (d*) for bubbles in Polyglycol solution was 1.1 (Eg = 15%), while for n-Pentanol solution was d* = 3.8 (Eg = 3.1). The difference in d* may influence bubble rise velocity i.e., there may be

superimposed effects. To decouple from the inter-distance effect, experiments at the same superficial gas velocity, bubble size distribution and dimensionless bubble inter-distance are required. To achieve these conditions it was necessary to generate small bubbles < 0.8 mm, for which in theory (Dukhin et al., 1998) surfactant does not affect the rising velocity. The limited experimental evidence (Okazaki, 1962; Clift et. al, 2005) for single bubbles (< 0.8 mm) suggests rising velocity is not affected by surfactants, but the number of measurement are few. There is also notable scatter in these data as shown in Clift et al. (2005) With the new technique to track multiple moving bubbles of different sizes simultaneously, it is possible more conveniently now to test the theory.

5.3.2- effect of Polyglycol and n-Pentanol solutions on bubble motion at same dimensionless bubble inter-distance (d*) D_{32} ~0.4 mm

A comparison of bubble velocity-size profile between Polyglycol and n-Pentanol solutions at the same bubble size distribution, aspect ratio and dimensionless bubble inter-distance (level of interactions) was performed. To create these conditions, narrow bubble size distributions of small bubbles (D_{32} = 0.4 mm) were generated using a porous-slot sparger (Figure 3.50), at a the superficial gas velocity (Usp) set to 0.03 m/s. Bubble images were collected at 90 cm above the sparger along the inclined section (column top section, Figure 3.52), both sufficient distance to stabilize the bubble size distribution and using the slope section helped reduce the number of overlapping bubbles. The bubble velocity size-profile plots (Figure 5.28) considered over 40,000 matching bubbles for Polyglycol and over 60,000 bubbles for n-Pentanol. As a reference, single bubble terminal velocity for "contaminated" water (Clift et al., 2005) is also plotted. The results are shown in Figure 5.28.

The resulting bubble size distributions are similar, as shown in Figure 5.29, and the Sauter diameters are the same (D_{32} ~0.4 mm).

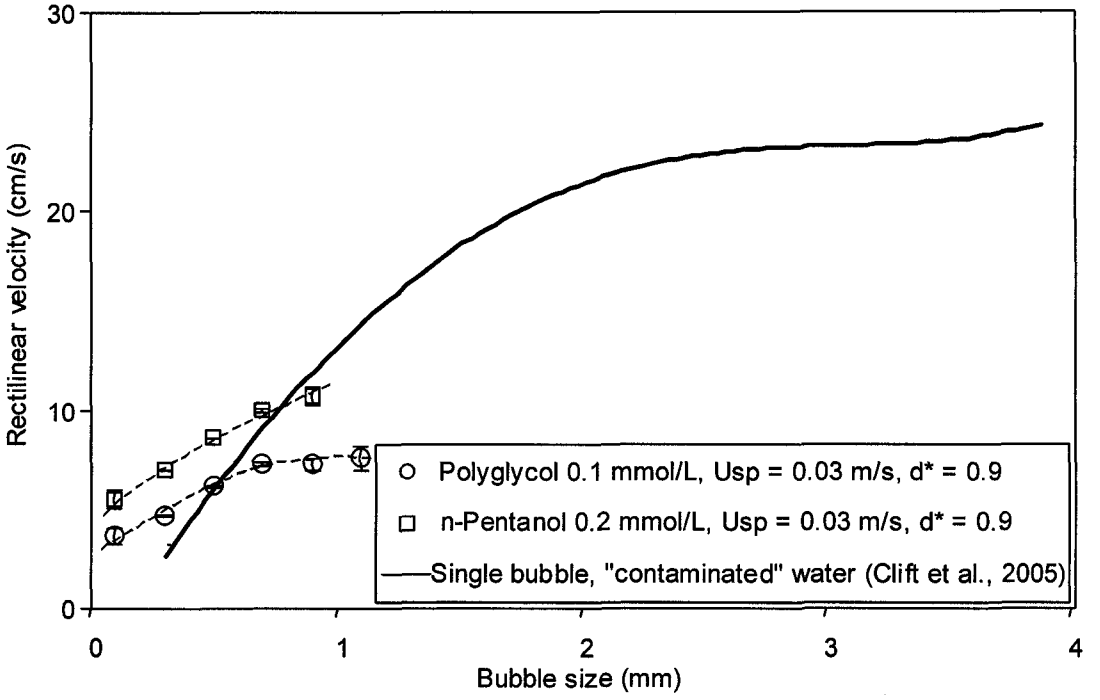

Figure 5.28: Bubble velocity-size profile for rising bubbles in Polyglycol and n-Pentanol solutions (same superficial gas velocity, bubble inter-distance and BSD).
(Test #64 and #66)

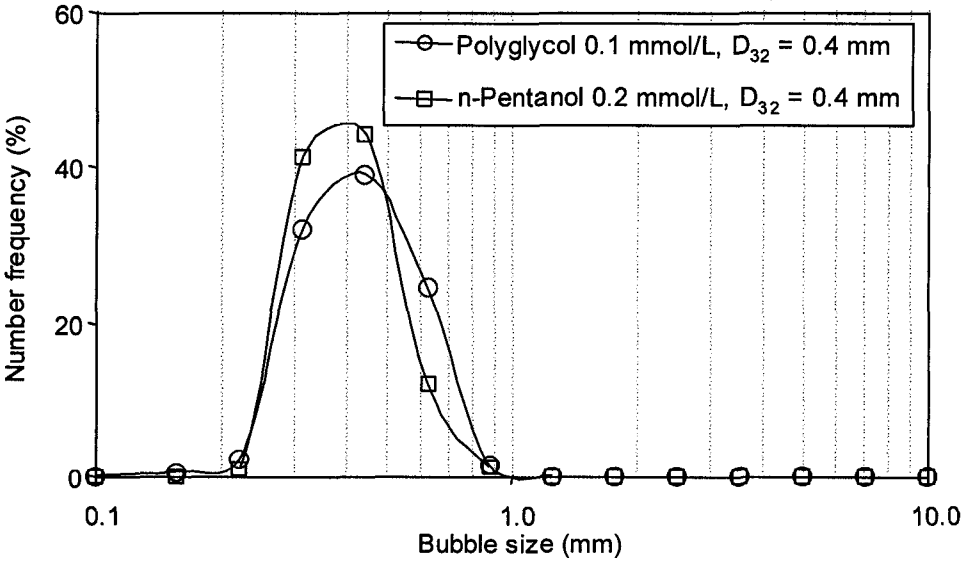

Figure 5.29: Frequency size distributions for bubbles in Polyglycol and n-Pentanol solutions (same d*)
(Test #64 and #66)

Bubble aspect ratio distribution (bubble shapes) are also the same as shown in Figure 5.30.

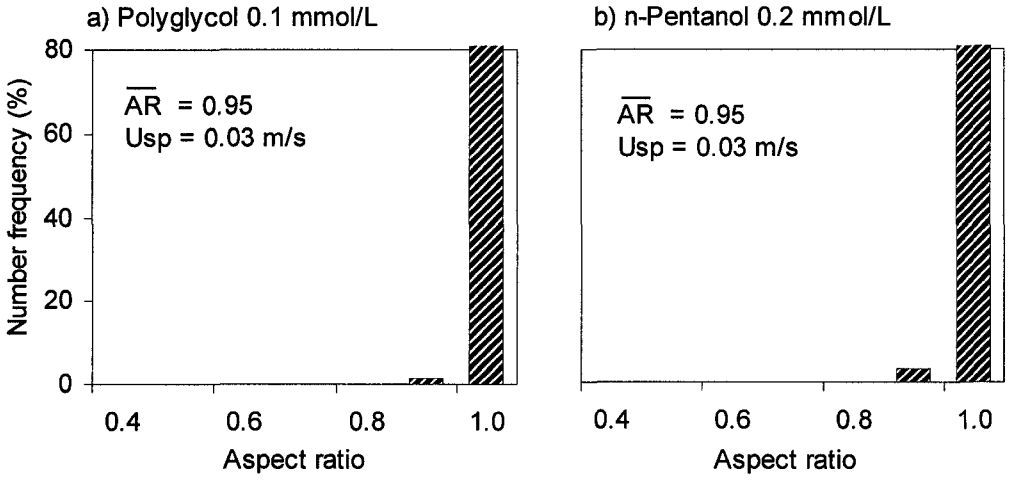

Figure 5.30: AR frequency distributions for bubbles in Polyglycol and n-Pentanol solutions (same d*). (Test #64 and #66)

Selected pictures bubbles are shown in Figure 5.31, which demonstrate visually the similarity of the distribution generated for the two frother types.

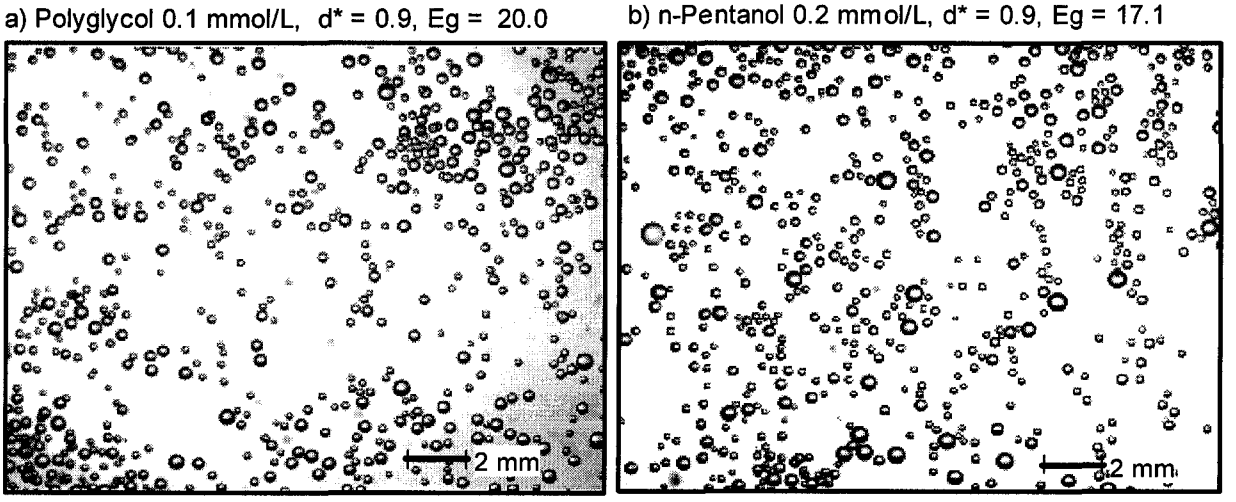

Figure 5.31: Image example of narrow and bimodal BSDs (Test #64 and #66)

These results show that bubbles in Polyglycol solution again rose slower than in n-Pentanol with now the same bubble size distribution, aspect ratio, dimensionless bubble inter-distance and gas flow rate. This difference correspond to the observation of Azgomi et al. (2007) in order to explain the similar gas holdup in n-Pentanol with small bubbles and in Polyglycol with large bubbles it meant that the small bubbles in n-Pentanol rose at the same speed as the large bubbles in Polyglycol. Or, to generalize, bubbles (of equal size) rise more slowly in Polyglycol than in n-Pentanol, i.e., as found here.

This confirms that frother type appears to be a new factor influencing bubble motion. More revealing, surfactant type affects bubble rise velocity for small bubbles (< 0.8 mm). This observation suggest that the surfactant gradient / surface rigidity model (Dukhin et al. (1998)) is not the complete explanation. In addition it is suggested, surface viscosity may play a role (Levich, 1962; Zhou et al., 1991).

5.4- Conclusions

The effects of frother type, concentration, adsorption time, level of interaction, bubble aspect ratio distribution and bubble size distribution on bubble velocity-size profile were studied for bubble swarms dispersed in tap water, Polyglycol and n-Pentanol solutions. The experiments were conducted in a bubble column, operated batch, and approximating flotation bubble size distribution conditions. Individual bubble velocity, tracking and characterization were determined using the techniques developed in this research. The main conclusions for a 2D bubble swarms and bubble sizes from 0.1 to 4 mm are:

- Bubble motion in a swarm can be characterized by a velocity-size profile. The velocity-size profile is dependent on surfactant (type, concentration and accumulation time), bubble size distribution, and bubble inter-distance.

- Presence of surfactants reduces bubble rise velocity in swarms in the same manner as for single bubble (focusing for now on bubbles above 0.8 mm). Bubble distribution type (i.e., narrow, wide, bimodal) alters bubble motion either increasing velocity (wake effect) or reducing velocity (hindering effect) depending on the dominant bubble size class.

- Bubble size distribution type determines the bubble velocity-size profile. The interaction effect (or hindering effect) is more significant for narrow bubble size distributions than for wide distributions. The predominant bubble size class appears to determine the motion of the remaining bubbles regardless of the level of interactions, i.e., if the predominant bubble population is small (slow velocity) the swarm velocity will be reduced; but if there is a high population of larger bubbles (above 1.4 mm) dominates, the swarm velocity tends to increase.

- Accumulation and importantly distribution of surfactant occur after the bubbles start (as was the case for single bubbles). The experimental evidence showing bubble aspect ratio distribution evolving from ellipsoidal shape (AR<0.9) to spherical supports this claim. The effect of surfactant accumulation on bubble velocity-size profile was demonstrated by tracking individual bubble velocities at different distance after generation.

- An experiment generating the same bubble size distribution, level of interaction and gas flow rate, was performed to compare frother type, Polyglycol vs. n-Pentanol. The results showed that surfactant type affected rising velocity even for bubbles below 0.8 mm. This seems in disagreement with previous authors (Dukhin et al., 1998; Clift et al., 2005), who propose that surface mobility for small bubbles is not affected by surfactant. However, it is possible that a different mechanism, i.e., surface viscosity, plays a role in bubble motion and this becomes evident for bubbles smaller than 0.8 mm.

CHAPTER 6: Conclusions, contributions and future work

6.1- Conclusions

This thesis has addressed the characterization of bubble motion in bubble swarms under flotation related conditions (notably presence of frother), and development of the necessary techniques. Following the structure of the thesis the main conclusions are:

CHAPTER 1:

- Fundamental of the flotation models have been restricted to mono-sized bubbles, basically for the lack of measurement techniques to characterize bubble motion in swarms. The techniques developed in this work provide valuable new information to improve flotation models.

- Surfactant plays a significant role in both stabilizing bubble shape and reducing surface wobbling, factors that could affect flotation efficiency. As a consequence, using the techniques to characterize bubble surface mobility, bubble shape oscillation, and bubble velocity in swarms, may provide useful insight into the effect of frother type and concentration on flotation performance.

CHAPTER 2:

- Previous studies on bubble swarm velocity have focused on average velocity measurement, and there are no studies on individual bubble motion in presence of surfactants. The developed techniques for bubble tracking in swarms, constitute unique tools that may be applied not only in flotation related conditions but in bubbling reactors in general or other dispersions (droplets in solvent extraction and particle settling)

CHAPTER 3:

- New image analysis tools have been developed for isolating, tracking moving bubbles and determining individual bubble velocity from bubble swarm image sequences using high-speed cinematography.

- A technique for tracking and trajectory construction of individual bubbles in swarms has been developed. The technique allows the establishment of velocity size relationships.

- A new model for isolating single bubbles from clusters, based on a general shape factor for an ellipsoidal object and a perimeter model, has been developed. The new model allows more bubbles to be identified and reduces the pixelation effect of digitized objects.

- A novel technique for determining average dimensionless bubble inter-distance in bubble swarms has been developed. As a result, a new model for relating the average dimensionless bubble inter-distance and area fraction of bubbles has been developed and evaluated for bubble swarms.

- A technique for generating bubble swarms in a 2D plane and controlling bubble size distribution using slot and porous-slot spargers has been developed to aid characterization of bubble motion in swarms.

- A new technique for measuring and characterizing bubble surface mobility on a bubble blown in frother solution has been developed. The technique allows tracking moving packets of liquid on a bubble surface.

- It is shown that to increase the accuracy of bubble size measurements it is required to identify at least 40% of the area selected as bubbles.

CHAPTER 4:

- Experimental evidence shows that surfactant accumulation occurs after the bubble detaches the generating point, and re-distribution takes place on the surface, corroborating the dynamic adsorption layer theory of Dukhin et al. (1998).

- When a bubble rises surfactant is distributed over the bubble surface generating a surface tension gradient, which produces surface pressure that compensates dynamic distorting forces. As a consequence bubble shape tends to spherical in presence of frother, as demonstrated experimentally in this work for single bubbles and bubbles in a swarm.

- The measurement of surface mobility (average surface velocity) on air bubbles blown in frother solution provides experimental evidence of the mechanisms by which surfactants reduce bubble rise velocity and its dependency on frother type. However, the analogy of a bubble blown in air and a bubble rising in solution must be confirmed.

- The presence of surfactant reduces bubble coalescence and/or breakage. Surfactants stabilize the bubble size distribution which remains stable as the swarm rises.

CHAPTER 5:

The bubble velocity tracking technique for 2D bubble swarms was applied to study the effect on bubble velocity-size profile of the following: frother type (Polyglycol and n-Pentanol), frother concentration, frother adsorption time, bubble size distribution type (narrow, wide, and bimodal), dimensionless bubble inter-distance (d*), and bubble aspect ratio distribution. The relevant conclusions are:

- A bubble swarm describes a velocity size-profile, which is determined by the bubble size distribution. The predominant bubble size class establishes the motion of the remaining bubbles.

- The effect of the dimensionless bubble inter-distance (interaction effect or the hindering effect) on the bubble velocity size-profile is only significant for narrow bubble size distributions.

- Accumulation and distribution of surfactant occur as bubbles rise in a swarm. This experimental evidence supports the dynamic adsorption layer theory for bubbles in swarms.

- The effect of surfactant on bubble generation and motion was successfully decoupled to study the effect of frother type on bubble motion in swarms.

- The surfactant type is a factor in controlling velocity. In n-Pentanol the velocity was little different from water alone while in Polyglycol the velocity approximated that in "contaminated" systems

- Surfactant type also seems to be a factor determining bubble rise velocity even for bubbles below 0.8 mm, despite that surface mobility for small bubbles is considered not to be affected by surfactant. It is possible that surface viscosity plays a role in bubble motion.

6.2- Claims to original research

1- Development and validation of bubble swarm characterization techniques:

- bubble identification in swarms from multiple images based on:
  - automatic thresholding (Calzado-Acuna)
  - watershed algorithm (Forbes-Acuna)
  - background compensation algorithm
  - automatic masking of fixed objects
  - shape factor model for ellipsoids as a function of object size

- bubble tracking and individual velocity measurement in a swarm of bubbles
- bubble inter-distance measurement in swarms
- bubble surface mobility characterization (surface flows on an air bubble)
- generation of flat front of bubbles (2D swarm) using slot spargers suited to testing the measurement techniques.
- control of the bubble size distribution covering the range found in industrial flotation units.

2- Measurement of individual bubble rise velocity and tracking of bubble trajectory in a 2 D swarm of bubbles.

3- Measurement of bubble surface oscillation (bubble wobbling) on single bubbles and individual bubbles in a swarms.

4- Measurement of Marangoni flow on bubble surface blown in air.

6.3- Contribution to knowledge

- Provided experimental evidence of surfactant type effect on bubble rise velocity in swarms using direct bubble velocity measurements.

- Demonstrated experimentally the effect of frother on reducing coalescence-induced break up reduction and bubble size distribution stabilization.

- Provided experimental evidence to support the dynamic adsorption layer theory for rising bubbles in solutions containing surfactants for both single bubbles and bubbles in swarms.

- Provided experimental evidence of the effect of surfactant type on bubble surface flow (Marangoni flow) on static bubbles blown in air.

- Established the dependency of the bubble velocity-size profile on bubble size distribution type and demonstrated that the hindering effect is only important for narrow bubble size distributions.

- Evidenced the effect of surfactant type on bubble rise velocity for bubbles smaller than 0.8 mm, introducing that surface viscosity may play a role determining bubble drag coefficient.

- Developed and validated experimentally a mathematical relationship between bubble inter-distance and gas holdup.

6.4- Recommendations

Develop and validate a model to establish the relationship among gas holdup, gas velocity and bubble size distribution, based on the bubble velocity-size profile using a population balance approach. It is proposed to use bubble velocity profile instead of an average swarm velocity to interpret bubble swarm behavior.

Utilize and select the bubble swarm image sequences and the bubble tracking measurement results (bubble position and geometry in time) generated in this work to predict and validate bubble wake structure using the images containing interacting bubbles.

Establish criteria to determine the minimum number of bubbles required to describe a bubble size distribution, under flotation related conditions, in order to standardize the McGill bubble sizing technique and reduce the number of images collected. In addition, incorporate the image analysis techniques developed in Matlab for this thesis into the McGill bubble sizing technique, which may increase the accuracy.

Extend the 2D bubble swarm characterization technique to 3D using synchronized cameras starting with dilute bubble swarms. The findings of this work can thus be tested on the three dimensional case.

REFERENCES

Acharya, T., Ray, A.,K., 2005. Image Processing: Principles and Applications. Wiley Inter-science, pp. 131-156.

Adamson, A. W., 1990. Physical Chemistry, 5th Edition, Wiley Publication, New York.

Ahmed, N., Jameson, G.J., 1985. The effect of bubble size on rate of flotation of fine particles. International Journal of Mineral Processing, Vol. 14, pp. 195-215.

Almatroushi, E., Borhan, A., 2004. Surfactant effect on the buoyancy-driven motion of bubbles and drops in a tube. Anna, N.Y. Acad. Sci. 1027, pp. 330-341.

Alves, S.,S., Orvalho, S.P., Vasconcelos, J., M., T., 2005. Effect of bubble contamination on rise velocity and mass transfer. Chemical Engineering, Vol. 60, pp. 1-9.

Azgomi, F., Gomez, C. O. and J. A. Finch, 2006. Characterizing frothers using gas holdup. Interfacial Phenomena in Fine Particle Technology, 6th UBC-McGill-UA International Symposium on Fundamentals of Mineral Processing (Eds. Z. Xu and Q. Liu), COM 2006, Montreal, Oct 1-4, pp. 429-442.

Azgomi, F., Gomez, C. O. and J. A. Finch, 2007. Correspondence of gas holdup and bubble size in presence of different frothers. International Journal of Mineral processing, Vol. 83 (1-2, 4), pp. 1-11.

Bailey, M., 2004. Analysis of bubble size distributions using the McGill bubble size analyzer. Master Thesis. Department of Mining, Metals and Materials Engineering, McGill University.

Bailey, M., Gomez, C., Finch J.A, 2005. A method of bubble diameter assignment. Minerals Engineering, Technical note, Vol.18, pp. 119-123.

Banisi, S., Finch, J. A., 1994. Technical note reconciliation of bubble size estimation methods using drift flux analysis. Minerals Engineering, Technical note, Vol.17, No 12, pp.1555-1559.

Banisi, S., Finch, J. A., Laplante, A.R., 1995. Effect of solid particles on gas hold-up in Flotation columns: I - Measurement. Chemical Engineering Science, Vol. 50 (14), pp. 2329-2334.

Barigou, M., Greaves, M., 1992, Bubble-size distributions in a mechanically agitated gas-liquid contactor. Chemical Engineering Science, Vol. 47 (8), pp. 2009-2025.

Barnard, R., W., Pearce, K., Schovanec, L., 2001. Inequalities for the perimeter on an ellipse. Journal of Mathematical Analysis and Applications, Vol. 260, pp. 295-306.

Becker, S., De Bie H., Sweeney, J., 1999. Dynamic flow behaviour in bubble columns. Chemical Engineering Science, Vol. 54, Issue 21, pp. 4929-4935.

Behkish, A., 2004. Hydrodynamic and mass transfer parameters in large-scale slurry bubble column reactors. PhD Thesis. Department of Chemical Engineering, University of Pittsburgh.

Boyer, C., Duquenne, A-M., Wild, G., 2002. Measuring technique in gas-liquid and gas-liquid-solid reactors. Chemical Engineering Science, Vol. 57, pp. 3185-3215.

Buwa, V., Ranade, V., 2002. Dynamic of gas-liquid flow in a rectangular bubble column: experiments and single/multi-group CFD simulations. Chemical Engineering Science, Vol. 57, pp. 4715-4736.

Carpat, H., Young, L., Zech, Y., 2002. Voronoi imaging methods for measurement of granular flows. Experiments in Fluids, Vol. 32, pp. 121-135.

Southern, S.M., Wraith A.E., 1990. Gas dispersion at diffuser sources for steel making. Proceedings of Developments in Ladle Steel Making and Continuous Casting, Hamilton, Ont., Canada, 26-29 August 1990, CIM, Montreal, Quebec, pp. 1-18.

Chen S., Wang, M., 2005. Seeking multi-thresholding directly from support vectors for image segmentation. Neurocomputing, Vol 67, pp. 335-344.

Chen, F., Gomez, C.O. and Finch, J.A., 2001. Technical Note: Bubble Size Measurement in Flotation Machines. Minerals Engineering, 14 (4), pp 427-432.

Cheng, D., Burkhardt H., 2003. International Journal of Thermal Sciences, Vol 42, pp. 647-655.

Cheng, D-C, Burkhardt, 2006. Template-base bubble identification and tracking in image sequences. International Journal of Thermal Science, Vol. 45, pp. 321-330.

Cheng, T., Holthan, P.,N.,1995. The particle detachment process in flotation. Minerals Engineering, Vol. 8 (8), pp. 883-891.

Clift, R., Grace, J.R., Weber, M.E., 2005. Bubbles, Drops and Particles, Academic Press, New York, 2nd edition.

Colella, D., Vinci D., Bagatin R., Masi, M., Abu-Bakr E., 1999. A study on coalescence and breakage mechanisms in three different bubble columns. Chemical Engineering Science. Vol. 54, pp. 4767-4777.

Corman , T.,Leiserson, C.,Rivest R., Stien, C., 2001, Introduction to Algorithms, Second Edition, MIT Press, Cambridge, Massachusetts, pp. 531

Dahlke R., Acuña C., A., Girgin H., Gomez, C., O., Finch, J., A., 2004. Raglan Gas Dispersion Measurements. Technical Report, Mining Metals Materials Engineering Department, McGill University.

De Swart, J.W.A., Van Vliet R.E., Krishna, R., 1996. Size, structure and dynamics of Large bubbles in a two-dimensional slurry bubble column. Chemical Engineering Science. Vol. 51 (20), pp. 4619-4629.

Deen, N. G., Hjertager, B. H., Solberg, T., 2000. Comparison of PIV and LDA measurement methods applied to gas-liquid flow in a bubble column, 10th Int. Symp. on Appl. of Laser Techniques to Fluid Mech., Lisbon, Portugal.

Deen, N.G., J. Westerweel and E. Delnoij, 2002. Two-Phase PIV of Bubbly Flows: Status and Trends, Chem. Eng. Technol. 25, pp. 97-101.

Deglon, D.A., Egya-Mensah, D., Franzidis J.P., 2000. Review of hydrodynamics and gas dispersion in flotation cells on South African platinum concentrators. Minerals Engineering, Vol. 13 (3), pp. 235-244.

REFERENCES

Dobby, G. S., Yianatos, J. B., and Finch, J. A., 1988. Canadian Metallurgy Quarterly, Vol. 27(2), pp. 85-90.

Doucet, J., Gomez, C. O. and J. A. Finch, 2006. Tools and strategies for optimizing gas distribution in industrial flotation banks. Mineral Process Modeling, Simulation and Control (Eds. T. Yalcin and H. Shang), Conference Proceedings, Laurentian University, June 6-7, pp 313-328

Dukhin, S.S., Miller, R., Loglio, G., 1998. Physico-chemical hydrodynamics of rising bubbles. Studies in Interfacial Science Vol.6: Drops and Bubbles in Interfacial Research. D. Mubius and R. Miller Editors, Elsevier Science.

Empix, Inc., 2002. Northern Eclipse help reference manual, version 6.0, www.empix.com

Finch, J.A., and Dobby, G.S., 1990. Column flotation. Pergamon Press: Elmsford, New York, pp. 23-24.

Finch, J.A., Gelinas S., Moyo P., 2006. Frother-related research at McGill University Minerals Engineering, Vol. 19 , pp. 726-733.

Fujiwara A., Danmoto Y., Hishida K., Maeda M., 2004. Bubble deformation and flow structure measured by double shadow images and PIV/LIF. Experiments in Fluids, Vol. 36, pp 157-165. DOI 10.1007/s00348-003-0691-0

Gandhi, B., Prakash, A., Bergougnou, M.A., 1999. Hydrodynamic behavior of slurry bubble column at high solids concentrations. Powder Technology, Vol. 103, pp. 80-94.

Gelinas S., Finch J.A. and Gouet-Kaplan M., 2005. Comparative real-time characterization of frother bubble thin films. Journal of Colloid and Interface Science, 291(1), 187-191.

Gomez, C.O, Acuna C.A., Girgin E.H., Finch J.A., 2006. Bubble distributions in laboratory flotation machines measurement and evolution with increasing gas velocity. International Mineral Processing Congress.

Gomez, C.O., Finch, J.A., 2002. Gas dispersion measurements in flotation machines, Technical paper, CIM Bulletin, Vol. 95 (1066), pp. 73-78.

Gomez, C.O., Finch, J.A., 2002. Gas dispersion measurements in flotation machines. CIM Bulletin, Vol. 95 (1066), pp. 73-78.

Gorain, B.K., Napier-Munn, T.J., Franzidis, J.P., and Manlapig, E.V., 1998. Studies on impeller type, impeller speed and air flow rate in an industrial scale flotation cell. Part 5: validation of k-s b relationship and effect of froth depth. Minerals Engineering, Vol. 11 (7), pp. 615-626.

Gorain, B.K., Franzidis, J.P., Manlapig, E.V., 1995. Studies on impeller type, impeller speed and air flow rate in an industrial scale flotation cell - Part 1: effect of bubble size distribution. Minerals Engineering, Vol. 8, pp. 615-635.

Grau R.A., 2006. An investigation of the effect of physical and chemical variables on bubble generation and coalescence in laboratory scale flotation cells. Dissertation for the degree of Doctor of Science in Technology. Department of Material Science and Engineering, Helsinki University of Technology.

Grau, R.A., Heiskanen, K., 2002. "Visual technique for measuring bubble size in flotation machines." Minerals Engineering, Vol. 15, pp. 507-513.

Grau, R.A., Heiskanen, K., 2003. Gas dispersion measurements in a flotation cell. Minerals Engineering, Vol. 16, pp.1081-1089.

Guet, S., Fortunati, R.,V., Mude, R., Ooms, G., 2003. Bubble velocity size measurement with a four point optical fiber probe. Part. Part. Syst. Charact., Vol. 20, pp. 219-230.

Guthrie R., I., L., Bradshaw, A., V., 1973. Spherical capped gas bubbles rising in aqueous media. Chemical Engineering Science, Vol. 28(1), pp. 191-203.

Harris, R., Ng, K.W., Wraith, A.E., 2005. Spargers for controlled bubble size by means of the multiple slot disperser (MSD). Short communication. Chemical Engineering Science, Vol. 60(11), pp. 3111-3115

Hernandez-Aguilar, J.R., 2004a. An imaging technique for sizing bubbles In flotation systems. Ph. D. Thesis. Department of Mining, Metals and Materials Engineering, McGill University.

Hernandez-Aguilar, J.R., Gomez, C.O. and Finch, J.A., 2002. A Technique for the direct measurement of bubble size distribution in industrial flotation cells. Proceedings 34th Annual Meeting of the Canadian Mineral Processors, CIM, pp. 389-402.

Hibiki, T., Ishii M., 2002. Interfacial area concentration of bubbly flow system. Chemical Engineering Science, Vol. 57, pp. 3967 - 3977.

Hofmeier, U., Yaminsky, V. V., Christenson, H. K., 1995. Observations of solute effects on bubble formation. Journal of Colloid and Interface Science, Vol. 174 (1), pp. 199-210.

Honkanen, M., Saarenrinne, P., Stoor, T., Niinim, J., 2005. Recognition of highly overlapping ellipse-like bubble images. Meas. Sci. Technol. Vol. 16, pp. 1760-1770.

Huang Q., Gao, W., Cai, W., 2005. Thresolding technique with adaptive window selection for uneven lighting image. Pattern Recognition Letters, Vol. 26, pp. 801-808.

IUPAC, 1997. Compendium of Chemical Terminology, second edition, section 51, pp. 1218

Jameson, G.J. and Allum, P., 1984. "A survey of bubble sizes in industrial flotation cells." Report to Australian Mineral Industries Research Association Limited.

Kluytmans, J.H.J., Wachem, B.G.M. van, Kuster, B.F.M., Schouten, J.C., 2002. Image analysis to quantify sizes, velocities, interfacial areas, and coalescence behavior of gas bubbles in a 2D bubble column, Meas. Sci. Tech, Chapter 2.

Krasowska M., Malysa K., 2007. Kinetics of bubble collision and attachment to hydrophobic solids: I. Effect of surgace roughness. Int. J. Miner Process. Vol. 81, pp. 205-216.

Krishna, R., Urseanu, M.,I., van Baten, J.,M., Ellenberger, J., 1999. Rise velocity of a swarm of large gas bubbles in liquids. Chemical Engineering Science, Vol. 54, pp.171-183.

Krzan M., Lunkenheimer K., Malysa K., 2004. On the influence of the surfactant's polar group on the local and terminal velocities of bubbles. Colloids and Surfaces A: Physicochem. Eng. Aspects, 250, pp. 431-441.

Krzan M., Zawala J., Malysa K., 2007. Development of steady state adsorption distribution over interface of a bubble rising in solutions of n-alkanols (C5,C8) and n-alkyltrimethylammonium bromides (C8,C12,C16), Colloids Surf. A: Physicochem. Eng. Aspects, Vol. 298 (1-2), pp. 42-51.

Laakkonen, M., Moilanen, P., Aittamaa, J., 2005. Local bubble size distributions in agitated vessels. Chemical Engineering Journal, Vol. 106, pp. 133-143.

Lammers, J.H. "The stability of bubbly flows." Published by the University of Twente, Netherlands, 1994.

Lee, D.J., Luo, X., Fan, L.S., 1999. Gas disengagement technique in a slurry bubble column operated in the coalesced bubble regime. Chemical Engineering Science, Vol. 54, pp. 2227-2236

Leifer, I., De Leeuw, G., Kunz, G., Cohen, L.H., 2003. Calibrating optical bubble size by the displaced-mass method. Chemical Engineering Science, Vol. 58, pp. 5211-5216.

Levich, V.G.,1962. Physico-Chemical Hydrodynamics, Prentice-Hall, Englewood Cliffs, New York.

Lin T-J, Reese J, Hong T, Fan L-S, 1996. Quantitative analysis and computation of two-dimensional bubble columns. AIChE Journal. Vol. 42, No. 2, pp. 301–318

Malysa K., Krasowska, M., Krzan M., 2005. Influence of surface active substances on bubble motion and collision with various interfaces. Advances in Colloid and Interface Science 114-115, pp. 205-225.

Masliyah, J.H., 1979. Hindered settling in multi-species particle system, Chemical Engineering Science, Vol. 34, pp. 1166-1168.

Mathworks Inc., 2003a. The language of technical computing: Programming. Version 7, pp. 1.1- 2.82.

Mathworks Inc., 2003b. Image Processing Toolbox for use with MatLab, User's Guide, Version 4.

Mena, P.C., Ruzicka M.C., Rocha, F.A., Teixeira J.A., Drahos, J., 2005. Effect of solids on homogeneous-heterogeneous flow regime transition in bubble columns. Chemical Engineering Science, Vol. 60, pp. 6013-6026.

Miyahara, T., Hamaguchi, M., Sukeda,Y., Takahashi, T., 1986. Size of bubbles and liquid circulation in a bubble column with a draught tube and a sieve plate. Canadian Journal of Chemical Engineering , Vol. 64 , pp. 718 -725.

Moyo, P., Gomez, C. O. and J. A. Finch, 2006. Characterization of frothers by water carrying rate. Interfacial Phenomena in Fine Particle Technology, 6th UBC-McGill-UA International Symposium on Fundamentals of Mineral Processing (Eds. Z. Xu and Q. Liu), COM 2006, Montreal, Oct 1-4, pp. 429-442.

Mudde R.,F., 2005. Gravity-driven bubble flow. Annu. Rev. Fluid Mech., Vol. 37, pp. 393-423.

Munholand L., Soucy, G., 2005, Comparison of four conductivity needle probe designs for determination of bubble velocity and local gas holdup. Review of Scientific Instruments, Vol. 76 (095101), pp. 1-6.

Nesset, J.E., Hernandez-Aguilar, J.R., Acuna, C.A., Gomez, C.O., Finch, J.A., 2006. Minerals Engineering, Vol. 19, pp. 807-815.

Nguyen A.V., H.S. Schulze, 2004. Colloidal science of flotation, Surfactant science series, Ed. Marcel Dekker.

Nguyen-Van A., Kmet, S., 1994. Probability of collision between particles and bubbles in flotation: the theoretical inertialess model involving a swarm of bubbles in pulp phase. International Journal of Mineral Processing, Vol. 40, pp. 155-169.

Nicklin, D.J., 1962. Two-phase bubble flow. Chemical Engineering Science, Vol. 17, pp. 693-702

Nishino K., Kato H., Torii K., 2000. Stereo imaging for simultaneous measurement of size and velocity of particles in dispersed two-phase flow. Measurement Science and Technology, Volume 11, Issue 6, pp. 633-645.

Okazaki, S., 1962. The velocity of air bubble ascending in aqueous solution of surface active substance and inorganic electrolyte. Kolloid-Zeitschrift und Zeitschrift für Polymere, Band 185-Heft 2, pp.154-157.

Otsu, N., 1979. A threshold selection method from gray-level histogram. IEEE Transactions on Systems, Man, and Cybernetics, Vol. 9(1), pp. 62-66.

Petrou, M., Bosdogianni, P., 1999, Image Processing: The Fundamentals, Wiley.

Pfleger, D., Gomes, S., Gilbert, N., Wagner, H.-G., 1999. Hydrodynamics simulations of a laboratory scale bubble columns fundamental studies of Eulerian-Eulerian modelling approach. Chemical Engineering Science, Vol. 54, pp. 5091-5099.

Polli, M.,Di-Stanislao, M., Bagatin, R., Abu Bakr, E., Masi, M., 2002. Bubble size distribution in the sparger region of bubble columns. Chemical Engineering Science, Vol. 57, pp. 197-205.

Prasser, H.M., Eckhard Krepper, Dirk Lucas, 2002. Evolution of the two-phase flow in a vertical tube decomposition of gas fraction profiles according to bubble size classes using wire-mesh sensors. International Journal of Thermal Sciences Vol. 41, pp. 17-28.

Pratt W.,2002. Digital Image Processing: PIKS Inside, Third Edition, John Wiley & Sons, Inc.

Quinn, J. J., Gomez, C. O. and Finch, J. A., 2006. Exploring the Effect of Salts on Gas Dispersion in Flotation Systems, JKMRC International Student Conference, Brisbane, March 7-8, pp. 57-70.

Rao, S., R., 2003. Surface Chemistry of Froth Flotation. Kluwer Academic/Plenum Publishers; 2nd Rev edition.

Richardson J.F., Zaki W.N., 1954, Chemical Engineering Science, Vol. 3, pp. 65-73.

Risso, F., Ellingsen K., 2002. Velocity fluctuations in a homogeneous dilute dispersion of high Reynolds-number rising bubbles. J. Fluid Mech, Vol. 453, pp. 395-410.

Robinson, J.V., 1946. The rise of air bubbles in lubricating oils. Journal of Physical Chemistry, Vol. 51 (2), pp. 431-437.

Rosenfeld, A., 2000. Survey image analysis and computer vision. Computer Vision and Image Understanding, Vol. 78, pp. 222-302.

Russ, J., C., Dehoff, R. T., 1999. Practical Stereology. Second Edition, Plenum press, New York.

Sam A., Gomez, C.O., Finch J.A.,1996. Axial velocity profiles of single bubbles in water/frother solutions, International Journal of Mineral Processing, Vol. 47, p. 177-196.

Sarma K.,T., Chattopandhyay,A.,2001. Langmuir, vol. 17, pp. 6399-6403.

Schäfer, R., Merten, C., Eigenberger, G., 2001. Bubble size distributions in a bubble column reactor under industrial conditions. Experimental Thermal and Fluid Science. Vol. 26, pp.595-604.

Shen, G., Finch J.A., 1996. Bubble swarm velocity in a column. Chemical Engineering Science, Vol. 51 (14), pp. 3665-3674.

Sriram K., Mann, R., 1976. Dynamic gas disengagement a new technique for assesing the behaviour of bubble columns. Chemical Engineering Science, Vol. 32, pp. 571-580.

Tao, D., 2004. Role of bubble size in flotation of coarse and fine particles-A Review. Separation Science and Technology, Vol. 39 (4), pp. 741-760.

Tarkan H.M., Post doc, Department of Mining, Metals and Materials Engineering, McGill University, personal communication, 2006.

Tizhoosh, H., R., 2005. Image thresholding using type II fuzzy sets. Pattern Recognition, Vol. 38, pp. 2363-2372.

Tomiyama, A., Celata, G.P., Hosokawa S., Yoshida, S.,2002. Terminal velocity of single bubbles in surface tension force dominant regime. International Journal of Multiphase Flow, Vol. 28, 1497-1519.

Tse, K. L., Martin T., McFarlane, C. M., Nienow A.W., 2003. Small bubble formation via a coalescence dependent break-up mechanism. Chemical Engineering Science, Vol. 58, pp. 275 - 286.

Tsuge H., Hibino S.I., 1977, Journal of Chemical Engineering of Japan, Vol. 10 (1), pp. 66-68.

Uribe-Salas, A., Lira-Gómez, P., Pérez-Garibay, R., Nava-Alonso, F., Magallanes-Hernández, L., Lara-Valenzuela, C., 2003. Overloading of gas bubles in column flotation of coarse particles and effect upon recovery. Int. J. Miner. Process., Vol 71, pp. 167-178.

Ventura-Medina E., Cilliers J.J, 2002. A model to describe flotation performance based on physics of foams and froth image analysis, Int. J. Miner. Process. 67, pp. 79- 99.

Wallis G.B.,1969, One-dimension two phase flow, McGraw-Hill, New York.

Wang Q., Chi Z., Zhao R., 2002, Image thresholding by maximizing the index of nonfuzziness of the 2-D grayscale histogram, Computer Vision and Image Understanding, 85, pp. 100-116.

Warsito, Ohkawa M., Kawata N., Uchida S., 1999. Cross-sectional distributions of gas and solid hold-ups in slurry bubble column investigated by ultrasonic computed tomography. Chemical Engineering Science Vol. 54, pp. 4711-4728.

Weber, M., E., 1974. The effect of surface active agents on mass transfer from spherical cap bubbles. Chemical Engineering Science, Vol. 30, pp. 1507-1510.

Wilcox D., Dove B., McDavid D., Greer D., UTHSCSA Image Tool v 3.00 software, 2002. The University of Texas Health Science Center in San Antonio.

Wilhelmus, A., G., 2001. PhD Thesis. Path and wake of a rising bubble. Twente University Netherland.

Ybert, C., di Meglio,J.-M., 2000. Ascending air bubbles in solutions of surface-active molecules: Influence of desorption kinetics. The European Physical Journal E, Vol. 3, pp. 143-148.

Yianatos, J.B., Bergh, L.G., Condori P. and Aguilera J., 2001. Hydrodynamic and Metallurgical Characterization of Industrial flotation banks for control purposes. Minerals Engineering, Vol. 14 (9), pp. 1033-1046.

Yianatos, J.B., Finch, J.A., Dobby G.S., Manqiu Xu,1998. Journal of Colloid and Interface Science, Vol. 126 (1), pp.37-44.

Zaruba, A., Krepper, E., Prasser, H.-M., Reddy Vanga B.N., 2005. Flow measurement and Instrumentation, Vol. 16, pp. 277-287.

Zhang Y., McLaughlin J.,B., Finch, J.,A., 2001, Bubble velocity profile and model of surfactant mass transfer to bubble surface. Chemical Engineering Science, Vol. 56, pp. 6605-6616.

Zhou, Z.A., Egiebor, N.O., Plitt, L.R., 1991, Effect of frother on bubble rise velocity in a flotation column-I single bubble system, In G.E. Agar, B.J. Hulus and S.B. Hyma (eds.), Column '91, CIM, Canada, pp. 249-255

APPENDIX 1: Calculations, tables and plots

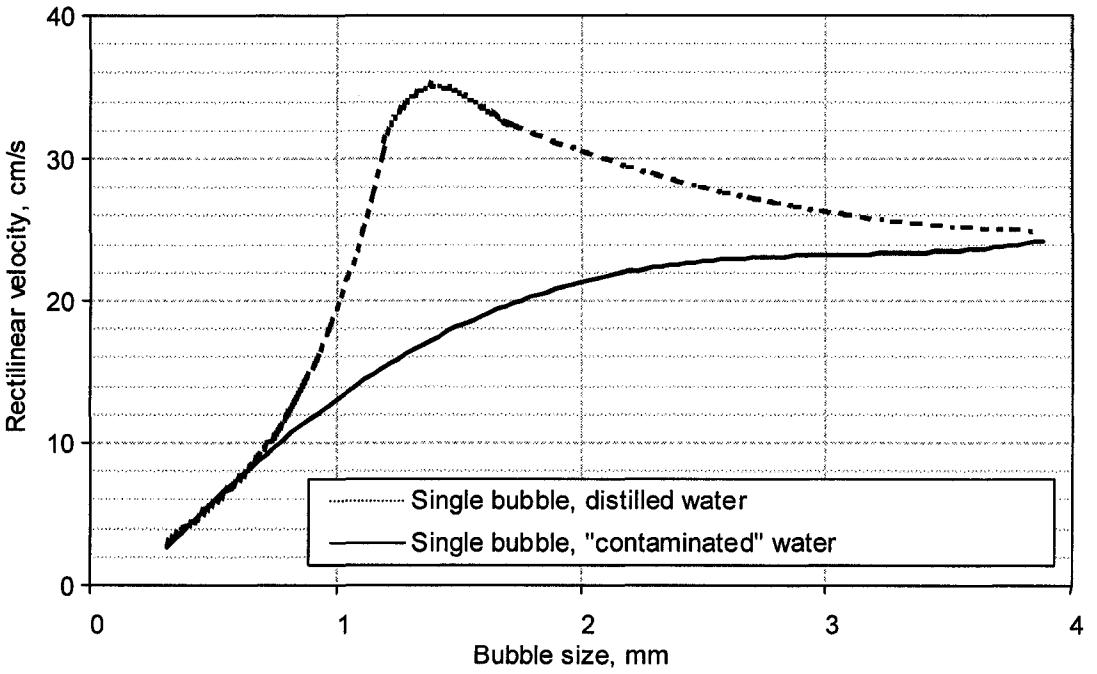

Figure A1.1: Terminal velocity of a single bubble as a function of the spherical equivalent diameter (Converted into data vector from Clift et al., 2005, p. 172)

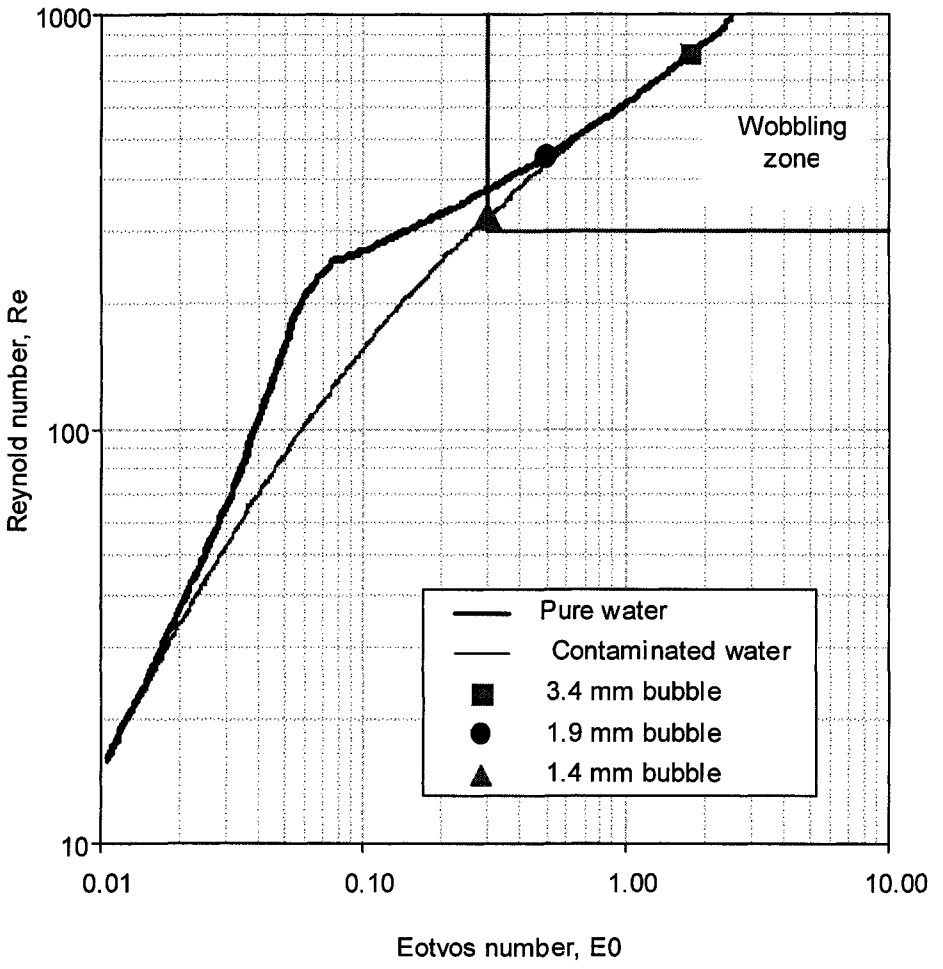

Figure A1.2: Wobbling zone for single bubble

Range of Re, Eo and We for bubbles in flotation related conditions:

Parameter		minimum	maximum
Re	Reynolds number	1	1300
Eo	Eotvos number	0.002	3
We	Webers number	0.0001	8

Table A1.1: Research groups in gas dispersion measurements

Research Group	Name, Location	Selected publication(s)
HUT	Helsinki University Technology, Helsinki, Finland.	Grau and Heiskanen, 2003
JK-MRC	Julius Kruttschnitt Mineral Research Center, Brisbane, Australia.	Gorain et al., 1998
McGill	McGill University, Montreal, Quebec, Canada.	Gomez and Finch, 2002; Nesset et al., 2006
UCT	University of Cape Town, Cape Town, South Africa.	Deglon et al., 2000
UTFSM	Universidad Técnica Federico Santa María, Valparaíso, Chile.	Yianatos et al., 2001

Table A1.2: 95% Confidence interval

Number of measurements	T-student 95% confidence	Confidence Interval 95% x standard deviation
2	12.7	8.98
3	4.3	2.48
4	3.2	1.59
5	2.8	1.24
6	2.6	1.05
7	2.4	0.92
8	2.4	0.84
9	2.3	0.77
10	2.3	0.72
15	2.1	0.55
30	2.0	0.37
50	2.0	0.28
100	2.0	0.20
200	2.0	0.14
1000	2.0	0.06

Appendix 1.1: Volumetric fraction of gas and inter-bubble distance for ellipsoidal bubbles in an ideal dispersion.

Given an ideal dispersion of ellipsoidal bubbles:

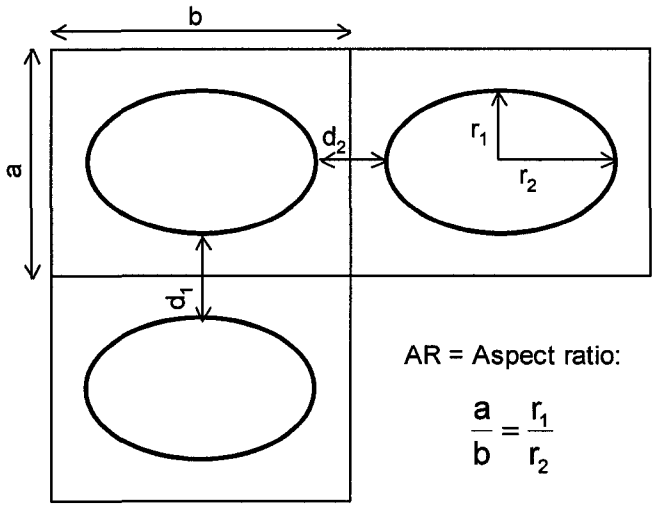

Figure A1.3: Ideal dispersion of ellipsoidal bubbles of aspect ratio AR

Bubble inter-distances are:

$$d_1 = a - 2\,r_1, \text{ and } d_2 = b - 2\,r_2 \qquad \text{(A1.1.1)}$$

Substituting b and r_2 with the aspect ratio equations (AR) in d_2 yields:

$$d_2 = \frac{a}{AR} - 2\cdot\frac{r_1}{AR} = \frac{1}{AR}\cdot(a - 2\cdot r_1) = \frac{d_1}{AR} \qquad \text{(A1.1.2)}$$

Therefore, for the given geometry the minimum inter-bubble distance for an ideal dispersion of ellipsoidal bubbles is d_1. Assuming oblate spheroid bubbles the equivalent bubble diameter (d_e, characteristic diameter) corresponds to:

$$d_e = \sqrt[3]{r_1\cdot(r_2)^2} = r_1\cdot AR^{-\frac{2}{3}} \qquad \text{(A1.1.3)}$$

Thus the dimensionless bubble inter-distance corresponds to:

$$d^* = \frac{a}{d_e} - \frac{2 \cdot r_l}{d_e} = a \cdot AR^{\frac{2}{3}} - 2 \cdot r_l \cdot AR^{\frac{2}{3}} \qquad \text{(A1.1.4)}$$

The area fraction of gas for an ideal dispersion of ellipsoidal bubbles (Figure A1.3) corresponds to:

$$E_g^{2D} = \frac{area\_ellipsoid}{area\_rectangle} = \frac{r_l \cdot \left(\frac{r_l}{AR}\right) \cdot \frac{\pi}{4}}{a \cdot \left(\frac{a}{AR}\right)} = \frac{\pi}{4} \cdot \left(\frac{r_l}{a}\right)^2 \qquad \text{(A1.1.5)}$$

Re-arranging equation A1.1.4 as a function of r_l/a, the result is:

$$\frac{r_l}{a} = \frac{1}{\frac{d^*}{AR^{\frac{2}{3}}} + 2} \qquad \text{(A1.1.6)}$$

Substituting A1.1.6 in A1.1.5, the resulting relationship is expressed as

$$E_g^{2D} = \frac{\pi}{4} \cdot \left(\frac{1}{\frac{d^*}{AR^{\frac{2}{3}}} + 2} \right)^2$$

Appendix 1.2: Volumetric fraction of gas and bubble and area fraction of gas relationship for random dispersions

According to Carpat et al. (2002), the density of objects in a random distribution is described in A1.2.1:

$$\eta = \frac{4}{\pi \cdot d^2} \cdot \left(1 - \exp\left(\frac{3}{2} \cdot E_g \cdot \frac{\Delta z}{d}\right)\right) \qquad \text{(A1.2.1)}$$

$$\eta = \frac{n}{A} \qquad \text{(A1.2.2)}$$

$$E_g^{2D} = \frac{\frac{n \cdot \pi \cdot d^2}{4}}{A} \qquad \text{(A1.2.3)}$$

Combining A1.2.2 and A1.2.3 and replacing η in A1.2.1, the resulting equation is:

$$1 - E_g^{2D} = \exp\left(\frac{3}{2} \cdot E_g \cdot \frac{\Delta z}{d}\right) \qquad \text{(A1.2.4)}$$

Finally, arranging equation A1.2.4, E_g is given by

$$E_g = \frac{2}{3} \cdot \frac{d}{\Delta z} \cdot \ln\left(\frac{1}{1 - E_g^{2D}}\right) \qquad \text{(A1.2.4)}$$

Nomenclature:

η	density of feature point (number of bubbles/area picture)
E_g	volumetric fraction of gas
Δz	depth of the dispersion (mm)
n	number of elements (bubbles) in the dispersion
A	area picture (mm^2)
E_g^{2D}	area fraction of bubbles
d	bubble mean diameter (mm)

Appendix 1.3: Effect of surface tension on bubble size generated on slot sparger.

The distance inter-nodes model for slot spargers proposed by Harris et al. (2005) can be written as:

$$\lambda = 17.2 \cdot \omega \cdot \left(\frac{\rho_l}{\rho_g}\right)^{0.16} \cdot \left(\frac{U_s^2 \cdot \omega \cdot \rho_l}{\sigma_l}\right)^{-0.25}, \qquad \text{(A1.3.1)}$$

and, the model bubble volume is:

$$V = 0.86\left(U_s \cdot \omega \cdot \lambda\right)^{6/5} \cdot g^{-3/5}, \qquad \text{(A1.3.2)}$$

where

λ	distance inter nodes, m
ω	slot opening width, m
ρ_l	liquid density, Kg/m3
ρ_g	gas density, Kg/m3
σ_l	interfacial tension, N/m
U_s	superficial gas velocity at the slot, m/s
V	bubble volume, m^3

Assuming that a slot sparger is operated at the same conditions, but with a liquid of surface tension, the relationship for the distance inter-nodes, using A1.3.1, for two surface tensions σ_l and σ_2 is:

$$\frac{\lambda_1}{\lambda_2} = \left(\frac{\sigma_2}{\sigma_1}\right)^{1/4}, \text{ and } \quad \frac{V_1}{V_2} = \left(\frac{\lambda_1}{\lambda_2}\right)^{6/5}$$

Therefore, the effect of surface tension on bubble diameter is:

$$\frac{V_1}{V_2} = \left(\frac{\sigma_2}{\sigma_1}\right)^{6/20}, \text{ and } \frac{d_1}{d_2} = \left(\frac{\sigma_2}{\sigma_1}\right)^{1/10}$$

As a consequence a change in surface tension from 72 dynes/cm to 60 dynes/cm creates a variation in size of 2%.

APPENDIX 2: Software: description, codes, manuals references

Table A2.1: Matlab routines implement for image analysis

Matlab Routine	Description
McGill_avi_2_tif	Converts AVI files into TIF files naming automatically based on user define name or AVI file name.
McGill_avi_folder_2_tif	Converts multiple AVI files into TIF organized into subfolders named from the AVI filename.
McGill_im_compensation	Removes uneven background distribution, for a given folder containing TIF files.
McGill_IMAGE2TIF_Binary	Converts TIF files (grey scale) into binary image base on selectable threshold algorithms (manual, average, Otsu, Calzado-Acuna).
McGill_im_automasking	Removes static objects from a sequence of images containing moving objects.

Table A2.2: Visual basic code to export images into Power Point

```
Sub Import_TIF_2_PPT() ' *Insert in the first slide
' Macro created by Claudio Auna / June 2006
' McGill University, J.A. Finch´s Research group
 root = "C:\root_folder"  ' root folder containing images subfolder
 sfold = "folder1"        ' subforlder containing TIF files
 outfolder = "F:\output"  ' output folder for ppt files containig images
 szx = 720                ' picture size horizonal
 szy = 534                ' picture size vertical
 root2 = root + "\" & sfold
 path_file = root2 & "\*.tif"
 f = Dir(path_file)
 i = 2
 Do Until f = ""
  fname = f
  sf = root2 & "\" & fname
  ActiveWindow.View.GotoSlide Index:=ActivePresentation.Slides.Add(Index:=i,&
  Layout:=ppLayoutText).SlideIndex
  ActiveWindow.Selection.SlideRange.Shapes.AddPicture(FileName:=sf, &
  LinkToFile:=msoFalse, SaveWithDocument:=msoTrue, Left:=0, Top:=0, Width:=szx, &
  Height:=szy).Select
  i = i + 1
  f = Dir
 Loop
 outname = outfolder & "\" & sfold & ".ppt"
 ActivePresentation.SaveAs FileName:=outname
End Sub
```

Table A2.3: Data structure parameters

Parameter	description
a	minor radius
b	major radious
A	total area (filled objected)
P	perimeter
Cx	centroid in x axis
Cy	centroid in y axis
x	left corner coordinate of the bounding box
y	upper corner coordinate of the bounding box (top of the is 1 and bottom is maximum pixel size)
H	bounding box height.
W	bounding box width
SF	shape factor for ellipsoids
AR	aspect ratio
AreaR	area ratio object to ellipsoid (a,b)
holes	number of holes
pos	vector containing bounding box coordinates [x y H W]
bw	Binary matrix containing a picture of the selected bubble
v(i,1)	reserved for future calculations
milisecs	elapsed time
next	index of a matching bubble in the next picture
seconds	elapsed tieme
VX	vector containing horizontal velocity for all bubbles in the current picture matching the corresponding marriage on the next picture..
VY	vector containing vertical velocity for all bubbles in the current picture matching the corresponding marriage on the next picture.s
V0	Trajectory velocity = $(Vx^2 + Vy^2)^{0.5}$
Similitud	Similitude value for matching bubbles

APPENDIX 3: Hardware specifications and equipment setup

Table A3.1: High speed camera specifications

Model	TroubleSooter HR
Sensor	CMOS array up to 1280 x 1024 pixels, 8 bit resolution (monochrome)
Shutter speed	1x ,2x ,3x ,4x ,5x, 10x and 20x the recording rate
Recording rate (fps)	16000, 8000, 4000, 2000, 1000, 500, 250, 125 (image size depends on recording rate)
Playback rates	1 to 1000 (selectable)
Display	Built in 5" LCD color digital display
Lens mounts	Standard C-mount, 1/4-20 tripod
I/O connectors	USB 2.0 port, compact flash memory.
Power supply	Four (4) D-Cell batteries or 110/220 VAC adapter

Recording rate (fps) and image size configurations

Frames Per Second	Sensor	Standard Memory - 1gb	
Recording Rate	Resolution	Total Frames	Record Time (Sec)
125	1280 x 1024	1,022	8.2
250	1280 x 1024	1,022	4.1
500	1280 x 1024	1,022	2.0
1000	1280 x 512	2,044	2.0
2000	1280 x 256	4,088	2.0
4000	1280 x 128	8,176	2.0
8000	1280 x 64	16,352	2.0
16000	1280 x 32	32,704	2.0
125	640 x 480	4,368	34.9
250	640 x 480	4,368	17.5
500	640 x 480	4,368	8.7
1000	640 x 480	4,368	4.4
125	320 x 240	17,472	139.8
250	320 x 240	17,472	69.9
500	320 x 240	17,472	34.9
1000	320 x 240	17,472	17.5
2000	320 x 240	17,472	8.7

Table A3.2: Macro lens specifications

Manufacture	Nikon
Model	AF MICRO NIKKOR
Focal distance	60 mm
Aperture	f/2.8
Maximum reproduction ratio	1:1
Minimum focal distance	20 cm

Table A3.3: Mass Flow meter controller specifications

Parameter	MKS	Sierra
Range standard (cm^3/min)	0-5000	0-500
Accuracy	± 1% FS	± 1% FS
Resolution	0.2% FS	n.a.
Time response	2 s	1 s
Model	Mass Flo-Controller	840D-L-1-V1

*FS: Full scale (range)

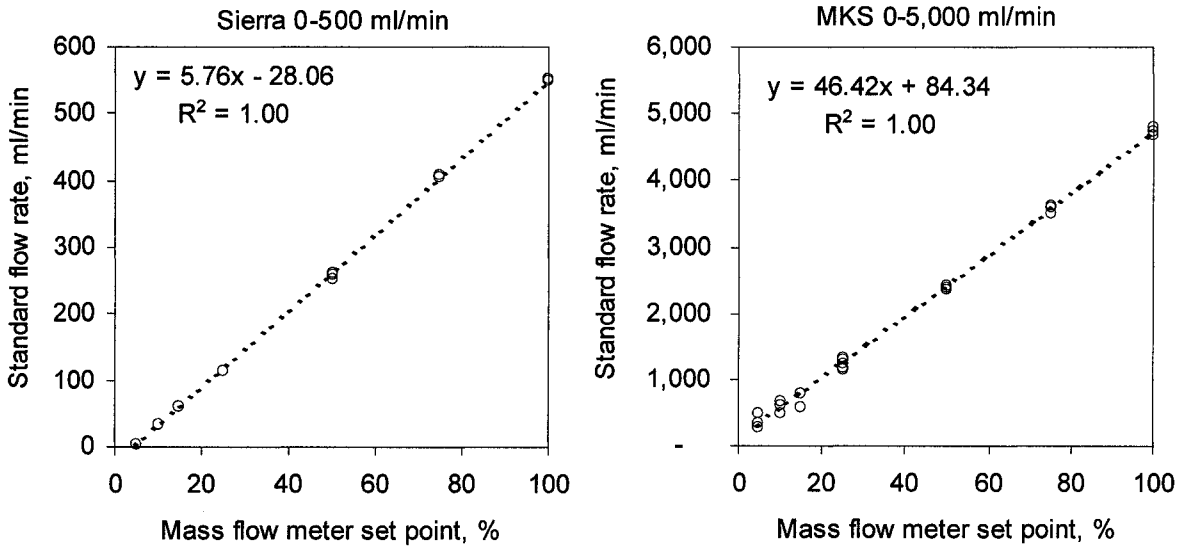

Figure A3.1: Mass flow meter calibrations
* Method: Inverted burette (50, 500, 1000 ml)

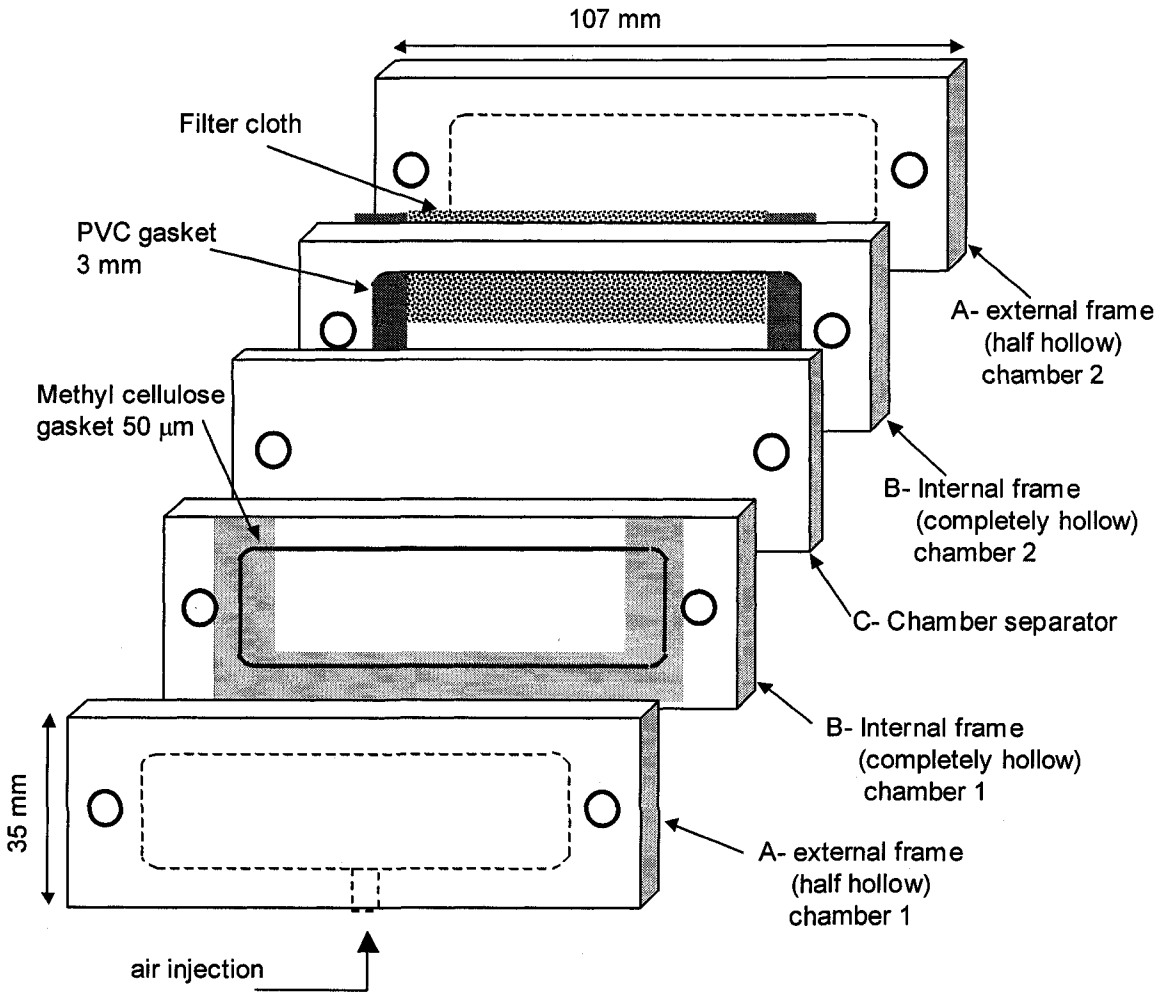

Figure A3.2: Double chamber slot sparger details

Bubble surface mobility equipment setup

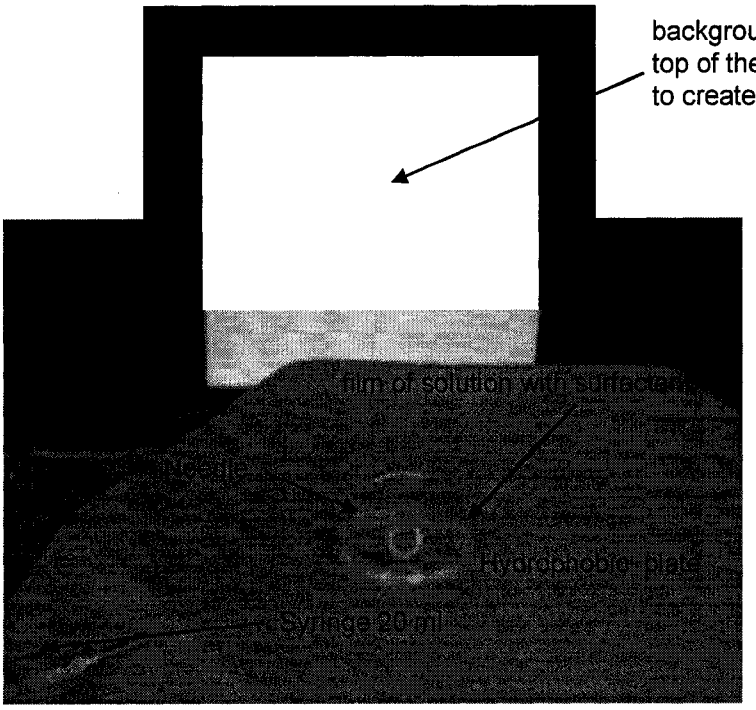

CAMERA SETTINGS:
- Camera Canon GL2
- Focal distance 35 cm
- Magnification lenses x4
- Shutter speed 1000
- diaphragm automatic (TV mode)

Air bubble blown in a liquid film (detail)

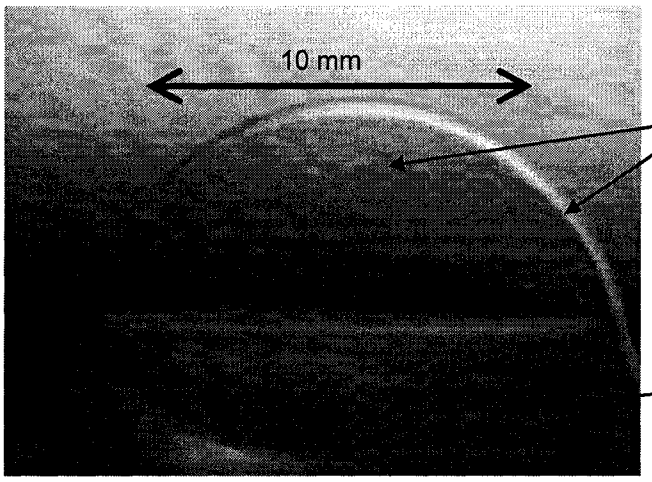

Figure A3.3: Surface mobility equipment setup and specification

APPENDIX 4: Experimental results

Table A4.1: Experimental result summary (test #7 -#30)

#	Test	dsp	Surfactant	conc.	D10	D32	Eg	d*	AR	Us	Usp
		cm		mmol/L	mm	mm	%			m/s	m/s
7	60529_E50	3	Polyglycol	0.2	2.0	2.2	7.1	1.6	0.83	0.9	
8	60529_E52	3	Polyglycol	0.2	2.3	2.5	9.6	1.3	0.80	1.3	
9	60529_E56	3	Polyglycol	0.2	2.4	2.6	12.3	1.1	0.78	2.0	
10	60529_E58	3	Polyglycol	0.2	2.5	2.8	18.0	0.8	0.77	3.4	
11	60529_E60	50	Polyglycol	0.2	2.2	2.4	9.6	1.6	0.92	0.9	
12	60529_E62	50	Polyglycol	0.2	2.5	2.8	15.2	1.1	0.92	2.0	
13	60529_E66	90	Polyglycol	0.2	2.6	2.7	10.5	1.3	0.94	3.4	
14	60529_E69	90	Polyglycol	0.2	2.6	2.7	4.5	3.1	0.94	0.9	
15	60530_E10	3	Polyglycol	0.01	2.7	3.1	26.1	0.6	0.82	3.4	
16	60530_E12	3	Polyglycol	0.01	2.4	2.6	9.7	1.5	0.84	0.9	
17	60530_E14	3	Polyglycol	0.01	2.7	3.0	17.2	0.9	0.81	2.0	
18	60530_E16	50	Polyglycol	0.01	2.0	2.7	11.9	1.5	0.92	0.9	
19	60530_E18	90	Polyglycol	0.01	2.9	3.1	9.5	1.7	0.92	3.4	
20	60530_E19	90	Polyglycol	0.01	2.6	2.8	3.0	4.2	0.92	0.9	
21	60530_E21	90	Polyglycol	0.01	3.3	3.6	11.0	1.5	0.90	4.8	
22	60530_E22	90	Polyglycol	0.01	4.2	5.1	12.4	1.4	0.86	9.6	
23	60530_E23	90	Polyglycol	0.04	2.7	3.0	13.4	1.2	0.91	3.4	
24	60530_E24	90	Polyglycol	0.1	2.9	3.2	11.5	1.4	0.91	3.4	
25	60530_E83	3	Tap water	0	2.8	3.2	18.3	0.8	0.73	3.4	
26	60530_E84	3	Tap water	0	2.7	3.0	10.9	1.5	0.70	2.0	
27	60530_E90	50	Tap water	0	3.0	3.3	14.3	1.7	0.57	3.4	
28	60530_E93	50	Tap water	0	2.4	2.7	3.8	4.4	0.60	0.9	
29	60530_E97	90	Tap water	0	2.8	3.2	3.8	4.3	0.71	0.9	
30	60530_E98	90	Tap water	0	2.9	3.8	8.9	2.1	0.71	3.4	

Nomenclature:

- dsp distance above the slot sparger (cm)
- conc. surfactant concentration (mmol/L)
- D10 mean bubble size (mm)
- D32 bubble Sauter diameter (mm)
- Eg Area fraction of gas (%)
- d* dimensionless inter-bubble distance
- AR bubble aspect ratio (minor / major axis)
- Us superficial gas velocity in the slot sparger (m/s)
- Usp superficial gas velocity in the porous-slot sparger (m/s)

Table A4.2: Experimental result summary (test #31 -#70)

#	Test	dsp	Surfactant	conc.	D10	D32	Eg	d*	AR	Us	Usp
		cm		mmol/L	mm	mm	%			m/s	m/s
31	60531_E11	90	Tap water	0	2.1	3.0	3.7	4.6	0.82	0.9	
32	60531_E13	90	Tap water	0	3.2	3.6	9.0	2.3	0.71	3.4	
33	60531_E15	90	Pentanol	0.2	3.1	4.8	15.4	1.7	0.75	9.6	
34	60531_E17	90	Pentanol	0.2	2.0	2.4	4.3	3.7	0.86	0.9	
35	60531_E19	90	Pentanol	0.2	2.7	3.1	5.9	3.4	0.79	2.0	
36	60531_E20	90	NaCl	400	2.2	2.5	9.4	1.8	0.93	0.9	
37	60531_E22	90	Pentanol	0.2	2.8	3.1	11.2	2.0	0.78	3.4	
38	60531_E24	90	NaCl	400	3.1	3.6	13.3	1.8	0.90	6.4	
39	60531_E26	90	NaCl	400	2.9	3.2	12.2	1.6	0.91	3.4	
40	60531_E29	50	Pentanol	0.2	1.5	2.7	3.5	3.3	0.82	0.9	
41	60531_E32	50	Pentanol	0.2	2.5	2.9	3.1	3.8	0.69	2.0	
42	60531_E35	50	Pentanol	0.2	2.6	3.2	6.8	2.3	0.73	3.4	
43	60531_E41	3	Pentanol	0.2	2.2	2.4	7.9	2.0	0.74	0.9	
44	60531_E43	3	Pentanol	0.2	2.6	2.9	14.2	1.1	0.71	2.0	
45	60531_E45	3	Pentanol	0.2	2.7	2.9	22.5	0.7	0.73	3.4	
46	60531_E67	3	NaCl	400	1.5	1.5	0.6	6.9	0.71	0.2	
47	60531_E73	3	Tap water	0	1.5	1.5	0.6	7.1	0.75	0.1	
48	60531_E75	3	Tap water	0	2.0	2.4	7.4	2.2	0.74	0.9	
49	60603_E09	3	Polyglycol	0.04	1.3	1.3	6.1	1.7	0.95	0.2	
50	60603_E10	3	Polyglycol	0.04	2.0	2.1	9.7	1.3	0.92	0.7	
51	60603_E11	3	Polyglycol	0.04	2.3	2.5	15.0	0.9	0.91	1.6	
52	60603_E12	3	Polyglycol	0.04	2.2	2.5	22.4	0.6	0.90	2.7	
53	60604_E45	25	Polyglycol	0.04	1.8	2.1	15.3	1.2	0.92	2.0	
54	60604_E47	25	Polyglycol	0.04	1.9	2.3	15.1	1.3	0.92	0.9	
55	60604_E49	25	Polyglycol	0.04	1.4	1.5	7.4	1.6	0.95	0.2	
56	60604_E51	25	Polyglycol-Gly	0.04	2.2	2.6	23.2	0.9	0.89	2.0	
57	60604_E53	25	Polyglycol-Gly	0.04	2.1	2.3	13.6	1.5	0.90	0.9	
58	60604_E56	25	Polyglycol-Gly	0.04	1.3	1.3	6.8	2.1	0.97	0.2	
59	60604_E58	25	Polyglycol-Gly	0.04	1.8	1.9	13.3	1.2	0.95	0.6	
60	60604_E60	25	Polyglycol-Gly	0.04	2.4	2.7	22.0	0.9	0.90	2.0	
61	60604_E61	25	Polyglycol-Gly	0.04	2.2	2.3	14.8	1.3	0.92	0.9	
62	60604_E63	25	Polyglycol-Gly	0.04	1.9	2.1	11.8	1.5	0.94	0.6	
63	60604_E65	25	Polyglycol-Gly	0.04	1.4	1.4	7.4	2.0	0.97	0.2	
64	60607_E00	90	Polyglycol	0.1	0.4	0.4	20.0	0.9	0.95	0.0	0.03
65	60607_E09	90	Pentanol	0.2	1.5	1.9	16.3	1.5	0.76	3.7	0.00
66	60607_E11	90	Pentanol	0.2	0.3	0.4	17.1	0.9	0.95	0.0	0.03
67	60607_E84	90	Tap water	0	1.5	2.0	10.9	1.9	0.77	2.5	0.13
68	60607_E90	90	Polyglycol	0.1	1.1	2.2	7.4	2.7	0.91	1.9	0.00
69	60607_E92	90	Polyglycol	0.1	1.4	2.1	9.9	2.1	0.91	3.7	0.00
70	60607_E98	90	Polyglycol	0.1	1.6	2.0	15.0	1.3	0.90	6.9	0.03

*** Nomenclature in Table A4.1**

Table A4.3: Bubble surface velocity results

Solution	Concentration mmol/L	Surface Tension nN/m	Avg. Surface velocity cm/s	95% Confidence interval cm/s	number of measurements
Plant solution		-	0.48	0.10	20
N-Pentanol	0.20	54	0.88	0.28	15
N-Pentanol	6.00	45	5.40	1.80	15
Polyglycol	0.04	63	0.63	0.22	13
Polyglycol	0.01	72	0.50	0.25	9
Polyglycol	6.00	54	1.53	0.60	9
Tap water	0.00	72	0.92	0.73	10

* Experimental bubble surface tracking (manual marking), Jeniffer Radman (McGill, Summer student report, 2006)

* Surface tension measurements conducted Dr. Mustafa Tarkan (internal communication, 2006)

Surface tension values

$$\tau_{solution} = \tau_{water} \cdot (1 - B \cdot Ln\left(1 + \frac{c}{a}\right))$$

where,

B, a: fitting parameters

c: molar concentration

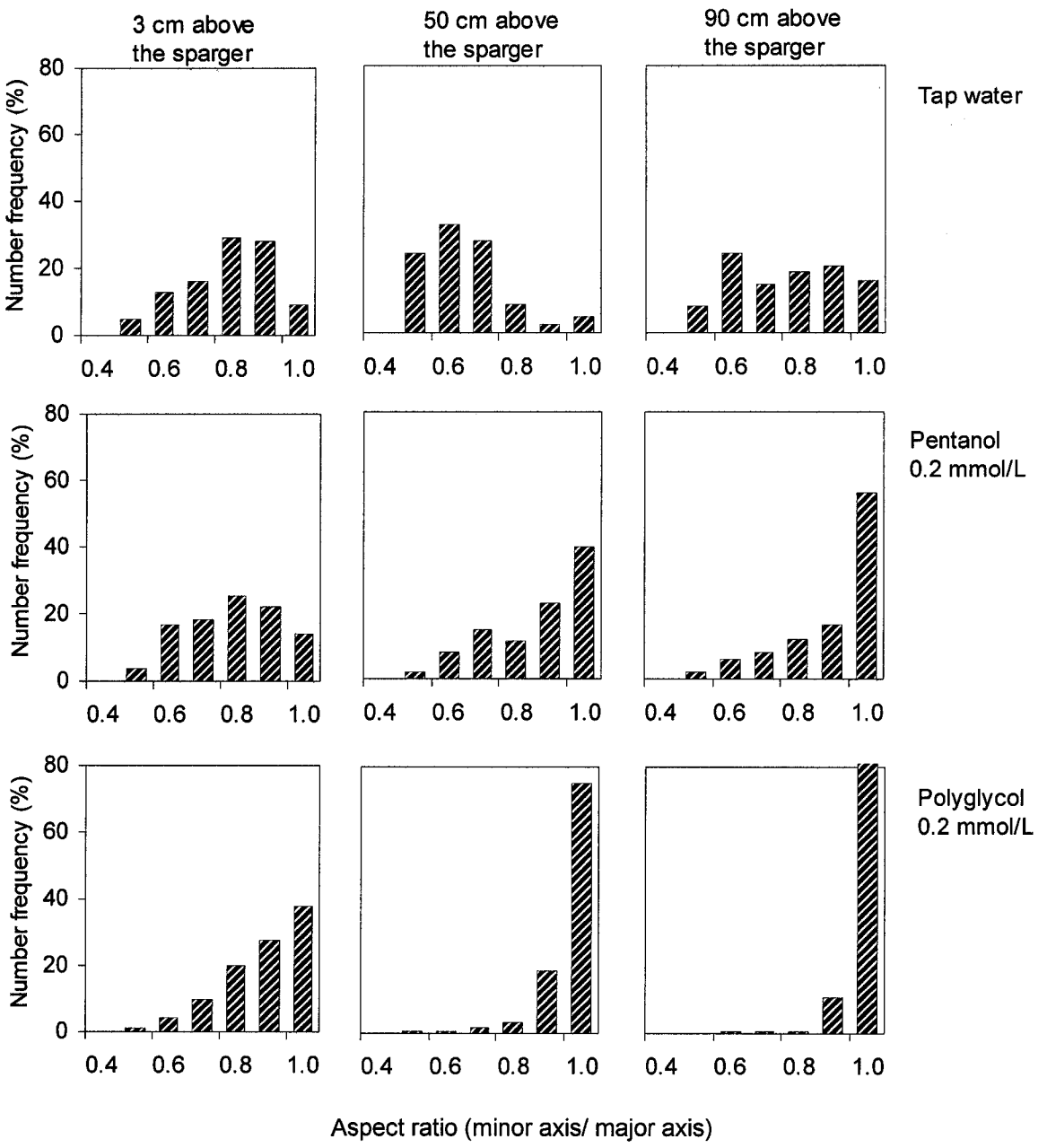

Figure A4.1: Comparison of bubble shape stabilization at 3, 50, and 90 cm above the sparger for tap water, Pentanol (0.2 mmol/L) and Polyglycol (0.2 mmol/L).
(Tests: # 48, #28, #29, #43, #40, #34, #7, #11, #14)

Table A4.4: Test #7, Polyglycol 0.2 mmol/L, Us = 0.9 m/s (3 cm)

#7 Polyglycol 0.2 mmol/L

Test: 60529_E50

Distance from sparger 3 cm

Sparger type:narrow slot: w = 60 um, L = 60 mm

Bubble rectilinear velocity profile

Db (mm)	VY (cm/s)	Confidence interval (95%)	Number of bubbles
0.1	-	-	0
0.3	-	-	0
0.5	-	-	0
0.7	-	-	0
0.9	-	-	0
1.1	18.4	0.85	61
1.3	19.0	0.29	779
1.5	20.7	0.25	1230
1.7	22.0	0.22	1590
1.9	22.4	0.28	1030
2.1	23.9	0.48	421
2.3	24.7	0.68	205
2.5	24.5	1.10	82
2.7	24.6	1.73	32
2.9	25.0	1.87	23
3.1	25.7	1.50	28
3.3	24.0	3.20	7
3.5	25.0	2.62	6
3.7	-	-	0
3.9	-	-	0

Average velocity (cm/s)	21.7
Number of bubbles	5,494
Number of pictures	543

Bubble size distribution

Db (mm)	Number of bubbles	Frequency %	Cummulative %
0.16	0	0.0	0.0
0.22	0	0.0	0.0
0.31	0	0.0	0.0
0.44	0	0.0	0.0
0.63	0	0.0	0.0
0.88	0	0.0	0.0
1.25	19	0.6	0.6
1.77	811	27.4	28.0
2.50	1674	56.5	84.5
3.54	454	15.3	99.8
5.00	6	0.2	100.0
7.07	0	0.0	100.0
10.00	0	0.0	100.0

Mean bubble size, D10 (mm)	2.04
Sauter diameter, D32 (mm)	2.22
Mean aspect ratio	0.83
Gas fraction area (%)	7.1
Bubble inter-distance	1.57
Number of bubbles	2,964
Number of pictures	65
Calibration (pixels/mm)	9.4
Resolution (mm)	0.11
Picture size (pixels)	480x640

Table A4.5: Test #10, Polyglycol 0.2 mmol/L, Us = 3.4 m/s (3 cm)

#10 Polyglycol 0.2 mmol/L

Test: 60529_E58

Distance from sparger 3 cm

Sparger type:narrow slot: w = 60 um, L = 60 mm

Bubble rectilinear velocity profile

Db (mm)	VY (cm/s)	Confidence interval (95%)	Number of bubbles
0.1	-	-	0
0.3	-	-	0
0.5	-	-	0
0.7	-	-	0
0.9	-	-	0
1.1	-	-	0
1.3	-	-	0
1.5	22.0	1.50	58
1.7	24.6	1.89	39
1.9	27.0	2.37	59
2.1	24.0	2.57	38
2.3	24.3	2.93	41
2.5	23.8	2.53	18
2.7	27.7	3.25	14
2.9	21.7	4.33	9
3.1	20.4	1.52	8
3.3	-	-	0
3.5	-	-	0
3.7	33.7	4.56	4
3.9	23.5	4.39	3

Average velocity (cm/s)	24.5
Number of bubbles	291
Number of pictures	170

Bubble size distribution

Db (mm)	Number of bubbles	Frequency %	Cummulative %
0.16	0	0.0	0.0
0.22	0	0.0	0.0
0.31	0	0.0	0.0
0.44	0	0.0	0.0
0.63	0	0.0	0.0
0.88	0	0.0	0.0
1.25	3	0.5	0.5
1.77	49	7.8	8.2
2.50	259	41.0	49.2
3.54	286	45.3	94.5
5.00	34	5.4	99.8
7.07	1	0.2	100.0
10.00	0	0.0	100.0

Mean bubble size, D10 (mm)	2.54
Sauter diameter, D32 (mm)	2.83
Mean aspect ratio	0.77
Gas fraction area (%)	18.0
Bubble inter-distance	0.76
Number of bubbles	632
Number of pictures	21
Calibration (pixels/mm)	9.4
Resolution (mm)	0.11
Picture size (pixels)	480x640

Table A4.6: Test #11, Polyglycol 0.2 mmol/L, Us=0.9 m/s (50 cm)

#11 Polygcol 0.2 mmol/L, Us = 0.9 m/s

Test: 60529_E60

Distance from sparger 50 cm

Sparger type:narrow slot: w = 60 um, L = 60 mm

Bubble rectilinear velocity profile

Db (mm)	VY (cm/s)	Confidence interval (95%)	Number of bubbles
0.1	-	-	0
0.3	-	-	0
0.5	-	-	0
0.7	-	-	0
0.9	-	-	0
1.1	18.5	1.55	14
1.3	19.7	0.63	158
1.5	21.2	0.24	846
1.7	20.9	0.18	1470
1.9	21.3	0.18	2070
2.1	22.1	0.16	2280
2.3	22.5	0.22	1420
2.5	23.3	0.29	967
2.7	23.2	0.40	648
2.9	22.8	0.56	290
3.1	24.3	0.61	169
3.3	24.2	0.74	115
3.5	24.4	0.92	67
3.7	23.7	1.17	41
3.9	23.8	2.09	21

Average velocity (cm/s)	22.0
Number of bubbles	10,576
Number of pictures	388

Bubble size distribution

Db (mm)	Number of bubbles	Frequency %	Cummulative %
0.16	0	0.0	0.0
0.22	0	0.0	0.0
0.31	0	0.0	0.0
0.44	0	0.0	0.0
0.63	0	0.0	0.0
0.88	25	1.1	1.1
1.25	4	0.2	1.3
1.77	359	16.1	17.4
2.50	1316	59.1	76.5
3.54	509	22.9	99.4
5.00	13	0.6	100.0
7.07	0	0.0	100.0
10.00	0	0.0	100.0

Mean bubble size, D10 (mm)	2.18
Sauter diameter, D32 (mm)	2.38
Mean aspect ratio	0.92
Gas fraction area (%)	9.6
Bubble inter-distance	1.64
Number of bubbles	2,226
Number of pictures	47
Calibration (pixels/mm)	9.4
Resolution (mm)	0.11
Picture size (pixels)	480x640

Table A4.7: Test #12, Polyglycol 0.2 mmol/L, Us=2.0 m/s (50 cm)

#12 Polyglycol 0.2 mmol/L

Test: 60529_E62

Distance from sparger 50 cm

Sparger type:narrow slot: w = 60 um, L = 60 mm

Bubble rectilinear velocity profile

Db (mm)	VY (cm/s)	Confidence interval (95%)	Number of bubbles
0.1	-	-	0
0.3	-	-	0
0.5	-	-	0
0.7	-	-	0
0.9	-	-	0
1.1	-	-	0
1.3	16.9	1.04	42
1.5	18.9	0.50	205
1.7	19.3	0.27	648
1.9	19.6	0.20	1390
2.1	20.5	0.18	1750
2.3	20.6	0.18	1910
2.5	21.9	0.21	1670
2.7	22.3	0.22	1470
2.9	22.7	0.24	1090
3.1	22.6	0.34	646
3.3	23.1	0.38	451
3.5	23.1	0.47	289
3.7	22.1	0.42	273
3.9	22.1	0.56	154

Average velocity (cm/s)	21.3
Number of bubbles	11,988
Number of pictures	421

Bubble size distribution

Db (mm)	Number of bubbles	Frequency %	Cummulative %
0.16	0	0.0	0.0
0.22	0	0.0	0.0
0.31	0	0.0	0.0
0.44	0	0.0	0.0
0.63	0	0.0	0.0
0.88	2	0.1	0.1
1.25	1	0.0	0.1
1.77	122	5.3	5.4
2.50	1024	44.3	49.7
3.54	1054	45.6	95.4
5.00	107	4.6	100.0
7.07	0	0.0	100.0
10.00	0	0.0	100.0

Mean bubble size, D10 (mm)	2.54
Sauter diameter, D32 (mm)	2.77
Mean aspect ratio	0.92
Gas fraction area (%)	15.2
Bubble inter-distance	1.14
Number of bubbles	2,310
Number of pictures	51
Calibration (pixels/mm)	9.4
Resolution (mm)	0.11
Picture size (pixels)	480x640

Table A4.8: Test #13, Polyglycol 0.2 mmol/L, Us=3.4 m/s (90 cm)

#13 Polyglycol 0.2 mmol/L

Test: 60529_E66

Distance from sparger 90 cm

Sparger type:narrow slot: w = 60 um, L = 60 mm

Bubble rectilinear velocity profile

Db (mm)	VY (cm/s)	Confidence interval (95%)	Number of bubbles
0.1	-	-	0
0.3	-	-	0
0.5	-	-	0
0.7	-	-	0
0.9	-	-	0
1.1	-	-	0
1.3	24.0	1.53	18
1.5	29.6	1.23	75
1.7	30.1	0.52	267
1.9	30.1	0.36	615
2.1	30.9	0.30	958
2.3	32.2	0.25	1180
2.5	32.0	0.27	1350
2.7	32.6	0.27	1420
2.9	32.6	0.29	1110
3.1	34.5	0.40	557
3.3	34.2	0.54	305
3.5	33.7	0.84	145
3.7	32.7	0.91	139
3.9	33.8	0.93	101

Average velocity (cm/s)	32.2
Number of bubbles	8,240
Number of pictures	491

Bubble size distribution

Db (mm)	Number of bubbles	Frequency %	Cummulative %
0.16	0	0.0	0.0
0.22	0	0.0	0.0
0.31	0	0.0	0.0
0.44	0	0.0	0.0
0.63	0	0.0	0.0
0.88	0	0.0	0.0
1.25	0	0.0	0.0
1.77	0	0.0	0.0
2.50	401	49.3	49.3
3.54	396	48.6	97.9
5.00	17	2.1	100.0
7.07	0	0.0	100.0
10.00	0	0.0	100.0

Mean bubble size, D10 (mm)	2.60
Sauter diameter, D32 (mm)	2.69
Mean aspect ratio	0.94
Gas fraction area (%)	10.5
Bubble inter-distance	1.28
Number of bubbles	814
Number of pictures	43
Calibration (pixels/mm)	9.4
Resolution (mm)	0.11
Picture size (pixels)	480x640

Table A4.9: Test #18, Polyglycol 0.01 mmol/L, Us=0.9 m/s (50 cm)

#18 Polyglycol 0.01 mmol/L

Test: 60530_E16

Distance from sparger 50 cm

Sparger type:narrow slot: w = 60 um, L = 60 mm

Bubble rectilinear velocity profile

Db (mm)	VY (cm/s)	Confidence interval (95%)	Number of bubbles
0.1	-	-	0
0.3	21.8	1.56	9
0.5	15.6	0.90	79
0.7	-	-	0
0.9	-	-	0
1.1	-	-	0
1.3	16.6	0.51	281
1.5	18.1	0.25	512
1.7	20.2	0.34	619
1.9	23.1	0.42	450
2.1	24.1	0.49	379
2.3	25.8	0.64	317
2.5	26.5	0.42	553
2.7	26.6	0.27	784
2.9	29.2	0.35	539
3.1	27.9	0.55	292
3.3	28.5	0.77	99
3.5	25.4	1.66	24
3.7	25.4	1.37	18
3.9	28.5	1.26	45

Average velocity (cm/s)	24.0
Number of bubbles	5,000
Number of pictures	517

Bubble size distribution

Db (mm)	Number of bubbles	Frequency %	Cummulative %
0.16	0	0.0	0.0
0.22	3	0.9	0.9
0.31	8	2.3	3.2
0.44	27	7.7	10.9
0.63	23	6.6	17.5
0.88	4	1.1	18.6
1.25	1	0.3	18.9
1.77	80	22.9	41.8
2.50	75	21.5	63.3
3.54	119	34.1	97.4
5.00	9	2.6	100.0
7.07	0	0.0	100.0
10.00	0	0.0	100.0

Mean bubble size, D10 (mm)	2.00
Sauter diameter, D32 (mm)	2.71
Mean aspect ratio	0.92
Gas fraction area (%)	11.9
Bubble inter-distance	1.52
Number of bubbles	349
Number of pictures	21
Calibration (pixels/mm)	39.5
Resolution (mm)	0.03
Picture size (pixels)	1280x1024

Table A4.10: Test #25, Tap water, Us=3.4 m/s (3 cm)

#25 Tap water

Test: 60530_E83

Distance from sparger 3 cm

Sparger type:narrow slot: w = 60 um, L = 60 mm

Bubble rectilinear velocity profile

Db (mm)	VY (cm/s)	Confidence interval (95%)	Number of bubbles
0.1	-	-	0
0.3	-	-	0
0.5	-	-	0
0.7	-	-	0
0.9	-	-	0
1.1	-	-	0
1.3	-	-	0
1.5	-	-	0
1.7	-	-	0
1.9	30.8	15.90	4
2.1	26.1	3.40	14
2.3	-	-	0
2.5	28.0	13.50	3
2.7	30.8	2.35	11
2.9	28.6	5.40	3
3.1	29.5	8.62	5
3.3	23.3	9.69	4
3.5	-	-	0
3.7	-	-	0
3.9	-	-	0

Average velocity (cm/s)	28.1
Number of bubbles	44
Number of pictures	381

Bubble size distribution

Db (mm)	Number of bubbles	Frequency %	Cummulative %
0.16	0	0.0	0.0
0.22	5	3.5	3.5
0.31	5	3.5	7.0
0.44	0	0.0	7.0
0.63	0	0.0	7.0
0.88	0	0.0	7.0
1.25	0	0.0	7.0
1.77	2	1.4	8.5
2.50	23	16.2	24.6
3.54	84	59.2	83.8
5.00	23	16.2	100.0
7.07	0	0.0	100.0
10.00	0	0.0	100.0

Mean bubble size, D10 (mm)	2.79
Sauter diameter, D32 (mm)	3.18
Mean aspect ratio	0.73
Gas fraction area (%)	18.3
Bubble inter-distance	0.79
Number of bubbles	142
Number of pictures	16
Calibration (pixels/mm)	38.9
Resolution (mm)	0.03
Picture size (pixels)	1280x1024

Table A4.11: Test #28, Tap water, Us=0.9 m/s (50 cm)

#28 Tap water, 0.9 m/s

Test: 60530_E93

Distance from sparger 50 cm

Sparger type:narrow slot: w = 60 um, L = 60 mm

Bubble rectilinear velocity profile

Db (mm)	VY (cm/s)	Confidence interval (95%)	Number of bubbles
0.1	-	-	0
0.3	-	-	0
0.5	-	-	0
0.7	-	-	0
0.9	-	-	0
1.1	33.4	1.16	38
1.3	31.2	2.05	22
1.5	29.9	1.12	83
1.7	31.3	0.58	103
1.9	30.7	0.55	138
2.1	31.7	0.61	119
2.3	30.5	0.76	121
2.5	29.1	0.91	64
2.7	29.4	0.78	44
2.9	28.3	1.77	28
3.1	26.7	3.11	8
3.3	30.0	2.26	5
3.5	-	-	0
3.7	-	-	0
3.9	28.3	0.72	5

Average velocity (cm/s)	30.6
Number of bubbles	778
Number of pictures	381

Bubble size distribution

Db (mm)	Number of bubbles	Frequency %	Cummulative %
0.16	0	0.0	0.0
0.22	0	0.0	0.0
0.31	0	0.0	0.0
0.44	2	2.0	2.0
0.63	1	1.0	2.9
0.88	0	0.0	2.9
1.25	0	0.0	2.9
1.77	14	13.7	16.7
2.50	37	36.3	52.9
3.54	45	44.1	97.1
5.00	3	2.9	100.0
7.07	0	0.0	100.0
10.00	0	0.0	100.0

Mean bubble size, D10 (mm)	2.41
Sauter diameter, D32 (mm)	2.71
Mean aspect ratio	0.60
Gas fraction area (%)	3.8
Bubble inter-distance	4.35
Number of bubbles	102
Number of pictures	16
Calibration (pixels/mm)	38.9
Resolution (mm)	0.03
Picture size (pixels)	1280x1024

Table A4.12: Test #30, Tap water, Us=3.4 m/s (90 cm)

#30 Tap water

Test: 60530_E98

Distance from sparger 90 cm

Sparger type:narrow slot: w = 60 um, L = 60 mm

Bubble rectilinear velocity profile

Db (mm)	VY (cm/s)	Confidence interval (95%)	Number of bubbles
0.1	-	-	0
0.3	-	-	0
0.5	-	-	0
0.7	-	-	0
0.9	-	-	0
1.1	-	-	0
1.3	-	-	0
1.5	-	-	0
1.7	-	-	0
1.9	40.6	4.38	3
2.1	31.8	2.29	3
2.3	-	-	0
2.5	35.6	5.08	8
2.7	39.1	2.46	10
2.9	37.7	1.70	25
3.1	39.8	1.45	19
3.3	37.2	1.94	20
3.5	36.1	1.18	12
3.7	36.7	2.40	6
3.9	35.9	2.42	6

Average velocity (cm/s)	37.5
Number of bubbles	112
Number of pictures	159

Bubble size distribution

Db (mm)	Number of bubbles	Frequency %	Cummulative %
0.16	0	0.0	0.0
0.22	0	0.0	0.0
0.31	9	17.0	17.0
0.44	1	1.9	18.9
0.63	0	0.0	18.9
0.88	0	0.0	18.9
1.25	0	0.0	18.9
1.77	0	0.0	18.9
2.50	4	7.5	26.4
3.54	17	32.1	58.5
5.00	20	37.7	96.2
7.07	2	3.8	100.0
10.00	0	0.0	100.0

Mean bubble size, D10 (mm)	2.94
Sauter diameter, D32 (mm)	3.84
Mean aspect ratio	0.71
Gas fraction area (%)	8.9
Bubble inter-distance	2.11
Number of bubbles	53
Number of pictures	7
Calibration (pixels/mm)	38
Resolution (mm)	0.03
Picture size (pixels)	1280x1024

Table A4.13: Test #41, n-Pentanol 0.2 mmol/L, Us=2.0 m/s (50 cm)

#41 Pentanol 0.2 mmol/L, Us = 2 m/s

Test: 60531_E32

Distance from sparger 50 cm

Sparger type:Double chamber: slot (w=60 um) / porous (w=1.1 mm), L =60 mm

Bubble rectilinear velocity profile

Db (mm)	VY (cm/s)	Confidence interval (95%)	Number of bubbles
0.1	-	-	0
0.3	-	-	0
0.5	8.7	0.29	34
0.7	-	-	0
0.9	-	-	0
1.1	-	-	0
1.3	34.0	3.84	4
1.5	32.4	1.17	45
1.7	32.7	2.25	32
1.9	33.7	1.38	28
2.1	31.4	1.01	50
2.3	32.5	1.40	38
2.5	29.4	1.01	49
2.7	28.6	1.89	23
2.9	31.3	3.49	7
3.1	-	-	0
3.3	-	-	0
3.5	-	-	0
3.7	-	-	0
3.9	-	-	0

Average velocity (cm/s)	29.0
Number of bubbles	310
Number of pictures	511

Bubble size distribution

Db (mm)	Number of bubbles	Frequency %	Cummulative %
0.16	0	0.0	0.0
0.22	0	0.0	0.0
0.31	1	1.6	1.6
0.44	0	0.0	1.6
0.63	3	4.9	6.6
0.88	0	0.0	6.6
1.25	1	1.6	8.2
1.77	6	9.8	18.0
2.50	15	24.6	42.6
3.54	31	50.8	93.4
5.00	4	6.6	100.0
7.07	0	0.0	100.0
10.00	0	0.0	100.0

Mean bubble size, D10 (mm)	2.48
Sauter diameter, D32 (mm)	2.89
Mean aspect ratio	0.69
Gas fraction area (%)	3.1
Bubble inter-distance	3.79
Number of bubbles	61
Number of pictures	21
Calibration (pixels/mm)	42.1
Resolution (mm)	0.02
Picture size (pixels)	1280x1024

Table A4.14: Test #49, Polyglycol 0.04 mmol/L, Us=0.2 m/s (6 cm)

#49 Polyglycol 0.04 mmol/L, Us = 0.2 m/s

Test: 60603_E09

Distance from sparger 3 cm

Sparger type:Double chamber: slot (w=60 um) / porous (w=1.1 mm), L =60 mm

Bubble rectilinear velocity profile

Db (mm)	VY (cm/s)	Confidence interval (95%)	Number of bubbles
0.1	-	-	0
0.3	-	-	0
0.5	-	-	0
0.7	10.5	1.44	13
0.9	14.3	0.15	1550
1.1	16.4	0.07	6980
1.3	16.9	0.29	477
1.5	17.1	0.31	333
1.7	16.7	0.35	183
1.9	15.7	1.19	9
2.1	16.1	1.57	6
2.3	-	-	0
2.5	-	-	0
2.7	-	-	0
2.9	-	-	0
3.1	-	-	0
3.3	-	-	0
3.5	-	-	0
3.7	-	-	0
3.9	-	-	0

Average velocity (cm/s)	16.1
Number of bubbles	9,551
Number of pictures	381

Bubble size distribution

Db (mm)	Number of bubbles	Frequency %	Cummulative %
0.16	0	0.0	0.0
0.22	0	0.0	0.0
0.31	0	0.0	0.0
0.44	0	0.0	0.0
0.63	0	0.0	0.0
0.88	0	0.0	0.0
1.25	116	36.4	36.4
1.77	202	63.3	99.7
2.50	1	0.3	100.0
3.54	0	0.0	100.0
5.00	0	0.0	100.0
7.07	0	0.0	100.0
10.00	0	0.0	100.0

Mean bubble size, D10 (mm)	1.31
Sauter diameter, D32 (mm)	1.33
Mean aspect ratio	0.95
Gas fraction area (%)	6.1
Bubble inter-distance	1.71
Number of bubbles	319
Number of pictures	16
Calibration (pixels/mm)	53
Resolution (mm)	0.02
Picture size (pixels)	1280x1024

Table A4.15: Test #51, Polyglycol 0.04 mmol/L, Us=1.0 m/s (6 cm)

#51 Polyglycol 0.04 mmol/L, Us = 1 m/s

Test: 60603_E11

Distance from sparger 3 cm

Sparger type:Double chamber: slot (w=60 um) / porous (w=1.1 mm), L =60 mm

Bubble rectilinear velocity profile

Db (mm)	VY (cm/s)	Confidence interval (95%)	Number of bubbles
0.1	-	-	0
0.3	-	-	0
0.5	-	-	0
0.7	16.1	0.24	4
0.9	14.0	0.89	24
1.1	18.5	0.72	54
1.3	20.2	0.75	130
1.5	21.1	0.38	472
1.7	22.2	0.39	332
1.9	23.8	0.32	586
2.1	25.0	0.22	861
2.3	23.9	0.30	551
2.5	24.5	0.32	411
2.7	25.4	0.43	149
2.9	25.4	0.91	51
3.1	23.3	0.82	39
3.3	26.3	1.45	34
3.5	22.8	3.08	10
3.7	19.6	3.19	6
3.9	-	-	0

Average velocity (cm/s)	23.5
Number of bubbles	3,714
Number of pictures	370

Bubble size distribution

Db (mm)	Number of bubbles	Frequency %	Cummulative %
0.16	0	0.0	0.0
0.22	0	0.0	0.0
0.31	0	0.0	0.0
0.44	0	0.0	0.0
0.63	0	0.0	0.0
0.88	0	0.0	0.0
1.25	3	3.0	3.0
1.77	13	13.0	16.0
2.50	41	41.0	57.0
3.54	43	43.0	100.0
5.00	0	0.0	100.0
7.07	0	0.0	100.0
10.00	0	0.0	100.0

Mean bubble size, D10 (mm)	2.30
Sauter diameter, D32 (mm)	2.50
Mean aspect ratio	0.91
Gas fraction area (%)	15.0
Bubble inter-distance	0.91
Number of bubbles	100
Number of pictures	15
Calibration (pixels/mm)	53
Resolution (mm)	0.02
Picture size (pixels)	1280x1024

Table A4.16: Test #64, Polyglycol 0.14 mmol/L, Usp=0.03 m/s (90 cm)

#64 Polyglycol 0.14 mmol/L

Test: 60607_E00

Distance from sparger 90 cm

Sparger type:Double chamber: slot (w=60 um) / porous (w=1.1 mm), L =60 mm

Bubble rectilinear velocity profile

Db (mm)	VY (cm/s)	Confidence interval (95%)	Number of bubbles
0.1	3.6	0.38	61
0.3	4.7	0.02	22300
0.5	6.1	0.02	16300
0.7	7.3	0.07	1340
0.9	7.3	0.29	67
1.1	7.5	0.59	13
1.3	-	-	0
1.5	-	-	0
1.7	-	-	0
1.9	-	-	0
2.1	-	-	0
2.3	-	-	0
2.5	-	-	0
2.7	-	-	0
2.9	-	-	0
3.1	-	-	0
3.3	-	-	0
3.5	-	-	0
3.7	-	-	0
3.9	-	-	0

Average velocity (cm/s)	5.4
Number of bubbles	40,081
Number of pictures	412

Bubble size distribution

Db (mm)	Number of bubbles	Frequency %	Cummulative %
0.16	20	0.5	0.5
0.22	92	2.3	2.7
0.31	1304	32.0	34.7
0.44	1597	39.2	73.9
0.63	1004	24.6	98.5
0.88	61	1.5	100.0
1.25	0	0.0	100.0
1.77	0	0.0	100.0
2.50	0	0.0	100.0
3.54	0	0.0	100.0
5.00	0	0.0	100.0
7.07	0	0.0	100.0
10.00	0	0.0	100.0

Mean bubble size, D10 (mm)	0.37
Sauter diameter, D32 (mm)	0.42
Mean aspect ratio	0.95
Gas fraction area (%)	20.0
Bubble inter-distance	0.88
Number of bubbles	4,078
Number of pictures	17
Calibration (pixels/mm)	65.6
Resolution (mm)	0.02
Picture size (pixels)	1280x1024

Table A4.17: Test #65, n-Pentanol 0.2 mmol/L, Us=3.7 m/s (90 cm)

#65 Pentanol 0.20 mmol/L

Test: 60607_E09

Distance from sparger 90 cm

Sparger type:Double chamber: slot (w=60 um) / porous (w=1.1 mm), L =60 mm

Bubble rectilinear velocity profile

Db (mm)	VY (cm/s)	Confidence interval (95%)	Number of bubbles
0.1	-	-	0
0.3	9.5	0.93	17
0.5	13.4	1.14	86
0.7	14.9	0.68	79
0.9	15.1	1.20	81
1.1	19.1	4.95	11
1.3	16.7	5.15	7
1.5	20.6	1.11	23
1.7	21.6	1.72	32
1.9	22.3	5.23	9
2.1	11.6	3.01	3
2.3	20.9	5.23	3
2.5	-	-	0
2.7	-	-	0
2.9	-	-	0
3.1	-	-	0
3.3	-	-	0
3.5	-	-	0
3.7	-	-	0
3.9	-	-	0

Average velocity (cm/s)	15.7
Number of bubbles	351
Number of pictures	473

Bubble size distribution

Db (mm)	Number of bubbles	Frequency %	Cummulative %
0.16	6	2.7	2.7
0.22	7	3.1	5.8
0.31	2	0.9	6.7
0.44	3	1.3	8.0
0.63	13	5.8	13.8
0.88	7	3.1	17.0
1.25	18	8.0	25.0
1.77	70	31.3	56.3
2.50	94	42.0	98.2
3.54	4	1.8	100.0
5.00	0	0.0	100.0
7.07	0	0.0	100.0
10.00	0	0.0	100.0

Mean bubble size, D10 (mm)	1.53
Sauter diameter, D32 (mm)	1.87
Mean aspect ratio	0.76
Gas fraction area (%)	16.3
Bubble inter-distance	1.50
Number of bubbles	224
Number of pictures	19
Calibration (pixels/mm)	65.6
Resolution (mm)	0.02
Picture size (pixels)	1280x1024

Table A4.18: Test #66, n-Pentanol 0.2 mmol/L, Usp=0.03 m/s (90 cm)

#66 Pentanol 0.20 mmol/L

Test: 60607_E11

Distance from sparger 90 cm

Sparger type:Double chamber: slot (w=60 um) / porous (w=1.1 mm), L =60 mm

Bubble rectilinear velocity profile

Db (mm)	VY (cm/s)	Confidence interval (95%)	Number of bubbles
0.1	5.5	0.47	152
0.3	6.9	0.02	50200
0.5	8.6	0.03	9730
0.7	10.0	0.10	718
0.9	10.7	0.48	13
1.1	-	-	0
1.3	-	-	0
1.5	-	-	0
1.7	-	-	0
1.9	-	-	0
2.1	-	-	0
2.3	-	-	0
2.5	-	-	0
2.7	-	-	0
2.9	-	-	0
3.1	-	-	0
3.3	-	-	0
3.5	-	-	0
3.7	-	-	0
3.9	-	-	0

Average velocity (cm/s)	7.2
Number of bubbles	60,813
Number of pictures	302

Bubble size distribution

Db (mm)	Number of bubbles	Frequency %	Cummulative %
0.16	1	0.0	0.0
0.22	26	1.1	1.1
0.31	1020	41.3	42.4
0.44	1091	44.2	86.6
0.63	303	12.3	98.8
0.88	29	1.2	100.0
1.25	0	0.0	100.0
1.77	0	0.0	100.0
2.50	0	0.0	100.0
3.54	0	0.0	100.0
5.00	0	0.0	100.0
7.07	0	0.0	100.0
10.00	0	0.0	100.0

Mean bubble size, D10 (mm)	0.35
Sauter diameter, D32 (mm)	0.40
Mean aspect ratio	0.95
Gas fraction area (%)	17.1
Bubble inter-distance	0.85
Number of bubbles	2,470
Number of pictures	12
Calibration (pixels/mm)	65.6
Resolution (mm)	0.02
Picture size (pixels)	1280x1024

Table A4.19: Test #68, Polylycol 0.1 mmol/L, Us=1.9 m/s (90 cm)

#68 Polyglycol 0.1 mmol/L, Us = 1.9 m/s

Test: 60607_E90

Distance from sparger 90 cm

Sparger type:Double chamber: slot (w=60 um) / porous (w=1.1 mm), L =60 mm

Bubble rectilinear velocity profile

Db (mm)	VY (cm/s)	Confidence interval (95%)	Number of bubbles
0.1	-	-	0
0.3	12.9	0.49	120
0.5	-	-	0
0.7	-	-	0
0.9	15.9	2.17	4
1.1	18.4	3.39	11
1.3	19.5	0.77	49
1.5	20.1	0.49	115
1.7	21.5	0.34	215
1.9	21.5	0.29	299
2.1	21.9	0.48	114
2.3	21.6	0.70	45
2.5	22.3	4.03	7
2.7	-	-	0
2.9	-	-	0
3.1	-	-	0
3.3	-	-	0
3.5	-	-	0
3.7	-	-	0
3.9	-	-	0

Average velocity (cm/s)	20.2
Number of bubbles	979
Number of pictures	666

Bubble size distribution

Db (mm)	Number of bubbles	Frequency %	Cummulative %
0.16	34	15.5	15.5
0.22	67	30.6	46.1
0.31	8	3.7	49.8
0.44	5	2.3	52.1
0.63	0	0.0	52.1
0.88	0	0.0	52.1
1.25	0	0.0	52.1
1.77	16	7.3	59.4
2.50	78	35.6	95.0
3.54	11	5.0	100.0
5.00	0	0.0	100.0
7.07	0	0.0	100.0
10.00	0	0.0	100.0

Mean bubble size, D10 (mm)	1.09
Sauter diameter, D32 (mm)	2.15
Mean aspect ratio	0.91
Gas fraction area (%)	7.4
Bubble inter-distance	2.70
Number of bubbles	219
Number of pictures	27
Calibration (pixels/mm)	65.6
Resolution (mm)	0.02
Picture size (pixels)	1280x1024

Table A4.20: Test #69, Polyglycol 0.14 mmol/L, Us=3.7 m/s (90 cm)

#69 Polyglycol 0.14 mmol/L, Us = 3.7 m/s

Test: 60607_E92

Distance from sparger cm

Sparger type:narrow slot: w = 60 um, L = 60 mm

Bubble rectilinear velocity profile

Db (mm)	VY (cm/s)	Confidence interval (95%)	Number of bubbles
0.1	-	-	0
0.3	-	-	0
0.5	-	-	0
0.7	-	-	0
0.9	-	-	0
1.1	19.6	1.10	37
1.3	22.9	0.72	76
1.5	21.8	0.55	161
1.7	22.7	0.45	228
1.9	22.4	0.43	185
2.1	24.2	0.78	98
2.3	24.9	0.92	41
2.5	27.0	1.25	13
2.7	24.0	1.76	10
2.9	24.9	1.26	29
3.1	-	-	0
3.3	-	-	0
3.5	-	-	0
3.7	-	-	0
3.9	-	-	0

Average velocity (cm/s)	22.8
Number of bubbles	878
Number of pictures	449

Bubble size distribution

Db (mm)	Number of bubbles	Frequency %	Cummulative %
0.16	26	19.1	19.1
0.22	17	12.5	31.6
0.31	1	0.7	32.4
0.44	0	0.0	32.4
0.63	0	0.0	32.4
0.88	0	0.0	32.4
1.25	0	0.0	32.4
1.77	25	18.4	50.7
2.50	62	45.6	96.3
3.54	5	3.7	100.0
5.00	0	0.0	100.0
7.07	0	0.0	100.0
10.00	0	0.0	100.0

Mean bubble size, D10 (mm)	1.39
Sauter diameter, D32 (mm)	2.08
Mean aspect ratio	0.91
Gas fraction area (%)	9.9
Bubble inter-distance	2.13
Number of bubbles	136
Number of pictures	18
Calibration (pixels/mm)	65.6
Resolution (mm)	0.02
Picture size (pixels)	1280x1024